THE MICROSTRUCTURE OF WELD METALS IN LOW ALLOY STEELS

GRAEME STUART BARRITTE

EMMANUEL COLLEGE

CAMBRIDGE

A dissertation submitted for the
Degree of Doctor of Philosophy
at the University of Cambridge.

April 1982.

DEDICATED TO MY PARENTS

ON THE MICROSCOPICAL STRUCTURE OF IRON AND AND STEEL

...." It is quite probable that the individual character of these constituents may be modified by the presence of small quantitites of sulphur, phosphorous or other impurities.... this question would require special investigation ....."

H.C. SORBY SPRING 1885

In "SORBY'S COLLECTED WORKS" No. 79 Vol. II
UNIVERSITY OF SHEFFIELD

PREFACE

This dissertation describes work carried out in the Department of Metallurgy and Material Science at the University of Cambridge under the supervision of Dr D.V. Edmonds (October 1978 to September 1979) and subsequently Professor R.W.K. Honeycombe, F.R.S. (October 1979 to October 1981). Except where acknowledgement and reference to previous work has been made, the work described is original and has been done without collaboration. The dissertation does not exceed 60,000 words and no part has been, or will be, submitted for a degree, diploma or other qualification at any other University.

G.S.Barritte,
April 1982

ACKNOWLEDGEMENTS

I would like to thank Professor R.W.K. Honeycombe F.R.S. for the provision of laboratory facilities and for his continued advice and encouragement. I am grateful to other members of the alloy steels research group in particular Dr's Howell, Ricks and Bhadeshia for many stimulating discussions and the benefit of their experience. Acknowledgement is also due to the assistant staff of the Metallurgy department, in particular Mr J. Leader for his invaluable practical assistance, Mr B. Barber and Mr M. Swann for advice and assistance with photography and Mrs V. Kohler for her help with the Quantimet. I am indebted to Dr D.V. Edmonds and Dr H.K.D.H. Bhadeshia for patiently reading the original text and their many and useful comments. I would also like to thank Mrs V. Rule for her cheerful and patient typing of the manuscript and Mr A. Benteley for proof reading the final text.

This work was supported by the Science Research Council, to whom I am grateful for the provision of a maintainance grant, and the Welding Institute who sponsored the research as a case award. I am indebted to my friends at the Welding Institute, particularly Messrs G. Hall, N. Tebbit, K. Tiplady, P. Kerr, and Mrs S. Stevans for their invaluable practical assistance and ever cheery support and encouragement during the course of this research. Similarly Dr's D.J. Abson and R.E. Dolby and Messrs. P.H.M. Hart and R. Pargeter are thanked for many discussions on the subject of weld metal microstructure and toughness.

Finally, only I know how grateful I am to my wife, Anne, for her patience and encouragement.

THE MICROSTRUCTURE OF WELD METALS IN LOW ALLOY STEELS

SUMMARY

The microstructure of High Strength Low-Alloy steel weld metals has been investigated using a variety of techniques including transmission electron microscopy, incorporating energy dispersive X-ray analysis, and high- speed dilatometry.

The nature of the constitutent commonly termed acicular ferrite, which is known to confer good toughness and strength in these materials, has been shown to comprise intragranularly nucleated Widmanstatten ferrite. Weld metal inclusions have been demonstrated to be the primary sites for the intragranular nucleation events and it is believed that the inclusions act to reduce the energy barrier to nucleation by providing a high energy interface which is destroyed during nucleation. The fine interlocking nature of the microstructure is attributed to sympathetic nucleation of ferrite on inclusion nucleated laths.

The proportion of the acicular ferrite constituent in the final microstructure is found to be a complex function of cooling rate, alloy composition, inclusion content and the austenite grain size of the weld deposit. These latter three parameters appear to be interrelated in many instances due to the nature of the alloying elements considered.

The dilatometric investigation of the decomposition of austenite in H.S.L.A. weld metals, under both isothermal and continuous cooling treatments, seems to be consistent with recent fundamental theories of phase transformations in steels. The general concept that two 'C' curves exist (ie. describing diffusional and shear transformations respectively) and can accurately describe transformations in steels is supported. The application of a thermodynamic analysis to transformations occurring on continuous cooling has introduced the concept of an 'effective' bainite start temperature to describe the condition of the austenite remaining untransformed during heat treatment.

At the cooling rate and alloy composition considered in these weld materials, transformation has been shown to proceed at temperatures consistently higher than this calculated bainite start temperature at all stages of transformation. The morphology of the upper bainite microstructure has been investigated and shown to be consistent with a mechanism involving displacive sub-units of bainitic ferrite.

CONTENTS

CHAPTER I

INTRODUCTION

1.1. INTRODUCTION

The fusion welding of steels encompasses one of the broadest fields of Metallurgy. It brings together many aspects of Science and Engineering design, placing these disciplines at the front of commercial development. The principles of steelmaking, casting technology and physical metallurgy all combine to produce a complex problem which must be solved by the consumables manufacturer. As if not content, technology has then demanded of these materials stringent mechanical properties and set them to work often in extremely severe operating conditions.

The development of High Strength Low Alloy (H.S.L.A.) steels has been one of the major breakthroughs in metallurgy over the last ten years. Combinations of controlled rolling and microalloying additions have systematically improved the mechanical properties in these low carbon steels to meet the rigorous demands of the pipeline and offshore industries. The next section will describe the metallurgical background to the welding of these steels.

1.2 METALLURGICAL BACKGROUND

In response to the development in wrought steels, welding technology has so far kept pace with the ever increasing demands for

improved mechanical properties in weld materials. This has been achieved in H.S.L.A. weld metals by promoting the development of the so called 'ACICULAR FERRITE' microstructural constituent, as shown in Fig.1.1. This fine grained component has been shown to be both stronger and tougher than predominantly grain boundary nucleated microstructures, as illustrated in Fig. 1.2. Since in these materials, the study of microstructure is synonymous with investigations into their mechanical properties, any fundamental study into the development of microstructure can contribute directly to achieving the goals of stronger, tougher weld materials.

An additional factor in determining the toughness of these materials is the presence of a significant volume fraction of non-metallic inclusions.

Since the early metallographic studies of wrought iron revealed the presence of numerous and often large inclusions, as for example shown in Fig.1.3, metallurgists have sought to reduce the total numbers present in structural materials. In wrought steels, the overall relationship which has been determined in many studies linking the volume fraction of inclusions with toughness is given in Fig.1.4. Typically, decreasing the inclusion volume fraction has usually been associated with increasing toughness. In marked contrast, however, this is not generally the case in weld materials. Ito & Nakanishi (1976) detailed a unique relationship, linking inclusion volume fraction and toughness in submerged arc weld metals, which is given in Fig.1.5. Initially, as in wrought materials, a decrease in inclusion volume fraction is associated with increasing toughness. Maximum toughness is achieved at a critical inclusion volume fraction, and, if further reduced, toughness is impaired.

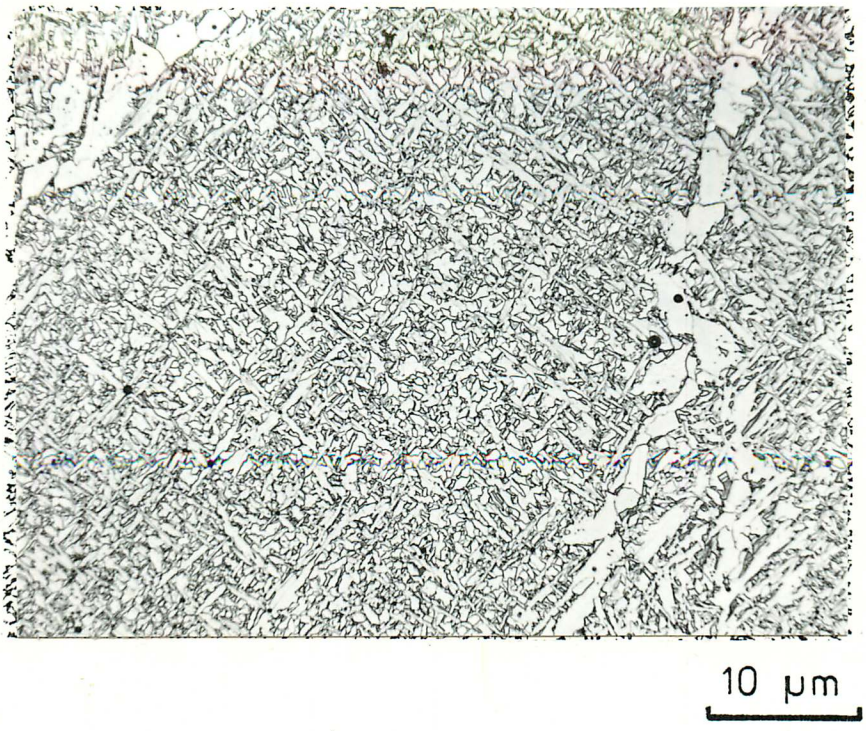

Fig.1.1 Typical example of the microstructure commonly termed 'ACICULAR FERRITE'
(Courtesy D.J. Abson, The Welding Institute)

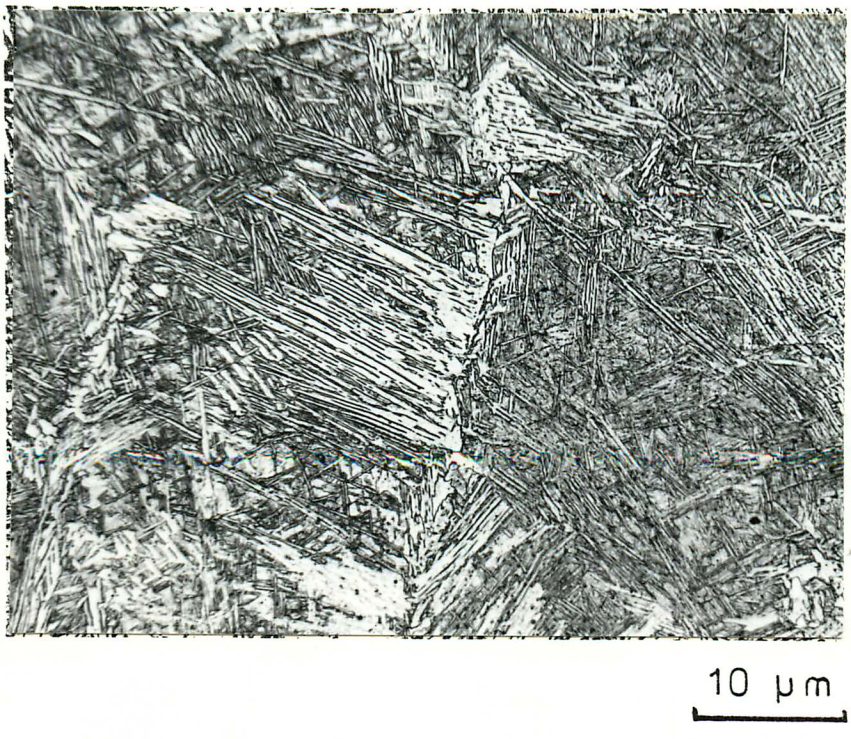

Fig.1.2 Typical example of the microstructure previously termed 'FERRITE SIDE PLATES' or more recently 'FERRITE WITH ALIGNED M-A-C' (martensite -austenite-carbide).
(Courtesy D.J. Abson, The Welding Institute).

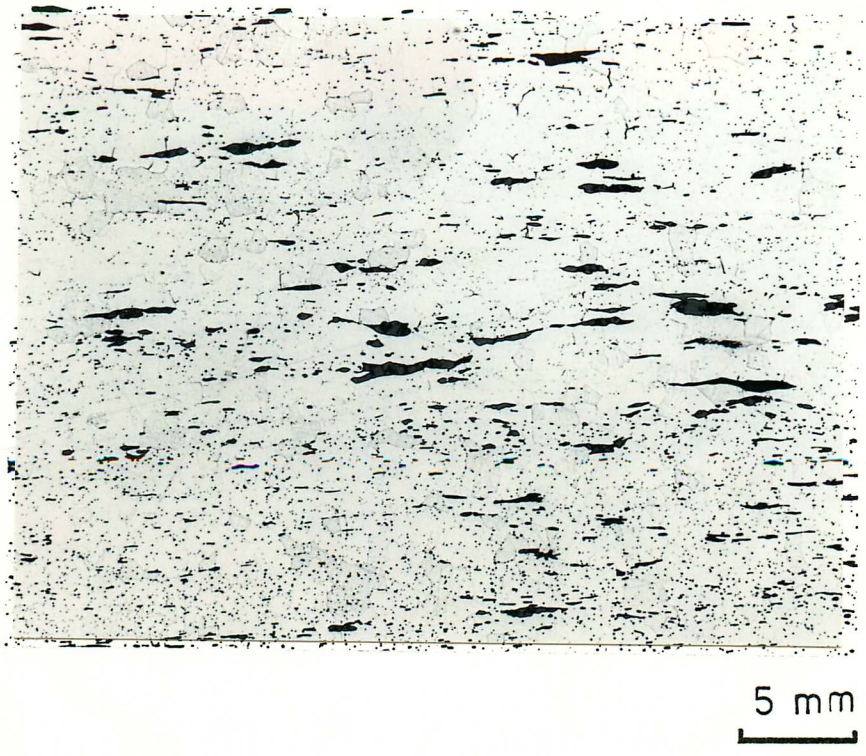

Fig.1.3 Microstructure of a wrought iron girder supporting the central arch, Corn Exchange, Cambridge. The inclusions comprise sulphide, phosphide and silicate types.

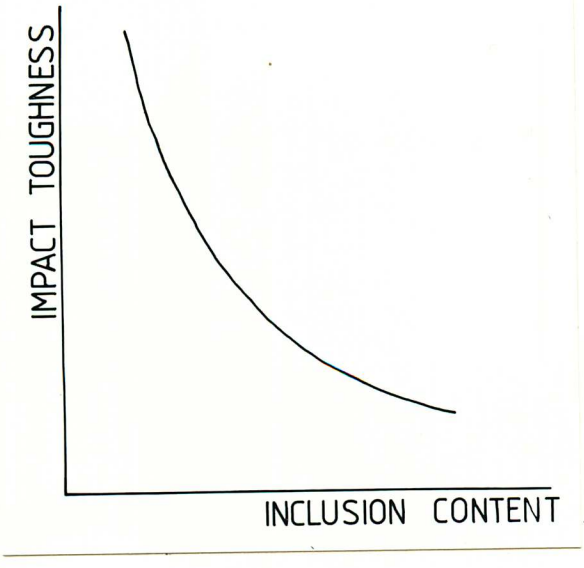

Fig.1.4 The effect of inclusion content on impact toughness in wrought steel.

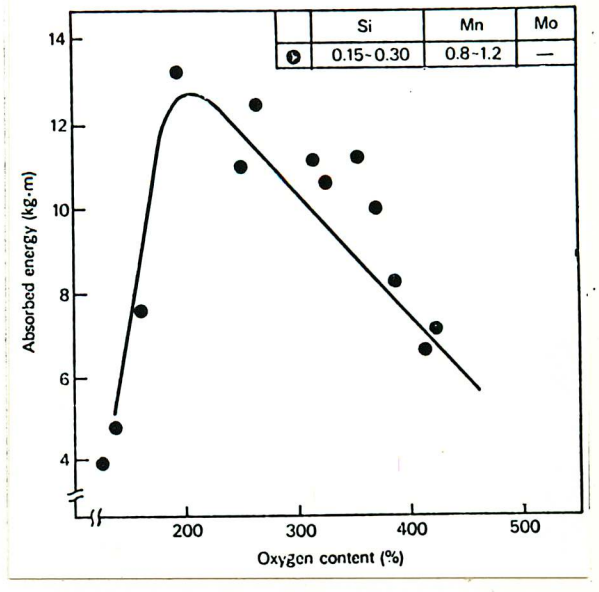

Fig.1.5 Relationship between toughness and inclusion content determined experimentally in submerged arc weld metal, after Ito and Nakanishi (1976).

Ito & Nakanishi (1976) noted that the microstructural component present in a given weld metal was dependent on the inclusion volume fraction - the acicular ferrite constitutent being present only over a limited oxygen range. It is the explanation of this so-called 'OXYGEN EFFECT' i.e. the relationship between microstructure, toughness and inclusion volume fraction, that is central to the work described in this investigation.

The conference 'TRENDS IN STEELS AND CONSUMABLES FOR WELDING' (1978) focussed attention on recent developments in welding and material requirements for the 1980's. In particular, the discussion sections following that conference highlighted many of the points which needed clarifying with respect to microstructure.

Both North (1978) and Garland (1978) pointed to the confusion regarding the terminology used to describe the microstructure of as-deposited steel weld metals. It was clear that the terms acicular ferrite, Widmanstatten ferrite and bainite had often been almost interchangeable in previous investigations; thus, there was a need for a systematic study of microstructure per se. Such an investigation is described in Chapters 2, 4 and 5, where the techniques of weld quenching, transmission electron microscopy and high speed dilatometry have all been used to characterise commercial weld metals. In addition, Chapter 5 presents a thermodynamic analysis based on the recent work of Bhadeshia, which attempts to quantify, thermodynamically, the development of microstructure in these weld materials.

Experimental evidence presented at the conference suggested that weld metal inclusions were having a pronounced effect on the development of microstructure. However, it was clear [viz the written contributions of Cochrane (1978) and Abson (1978.1)] that no general consensus of opinion could be established between the various authors

as to the role of inclusions, and, as Garland commented'....THE WHOLE OXYGEN SITUATION NEEDS VERY CAREFUL ATTENTION'. Since the medium oxygen regime (CIRCA 0.03% O_2) is known to confer the optimum mechanical properties in weld materials, the whole of Chapter 6 is devoted to a study of the nature and development of acicular ferrite. A model is described to assess the relative free energy barriers for the possible modes of formation of this constitutent and T.E.M. is used to clarify its microstructural development.

Work published during the course of this research, Farrar & Watson (1979), suggested that inclusions could have a role to play in determining matrix chemistry. This possibility is examined in Chapter 7, where a STEM/EDS technique has been used to characterise both the inclusion chemistry and its effect on local and matrix composition.

Finally, having established the major parameters involved in the development of microstructure in H.S.L.A. steel weld metals, the work in Chapter 8 examines several factors which can promote the development of the desired acicular ferrite constituent. Specifically, the role of oxygen and manganese will be reviewed in both manual metal arc and submerged arc weld metals. The role of preheat, parent plate deoxidation practice and facetting of inclusions will be briefly examined, and possible crystallographic aspects of ferrite nucleation on inclusions discussed. Chapter 9 will present the conclusions and suggestions for further work.

1.3 SOLIDIFICATION STRUCTURE OF WELD METALS

Any investigation into the study of microstructure in ferrous materials must include an accurate description of the parent austenite. In the case of weld materials, this also involves describing the

solidification process which has been summarised recently by Widgery (1974), whose work will form the basis of this brief review.

Because of the high thermal gradient present, cellular solidification is usually favoured in submerged arc and manual metal arc weld deposits. This results in the familiar columnar structure usually found in the final microstructure. An additional factor which has been established in these materials is the epitaxial growth of solidifying grains from those in the base materials.

The solidification process of these low carbon weld metals can best be summarised in Fig.1.6. Initially, the delta ferrite grains form epitaxially at the fusion boundary. They grow in a columnar manner towards the centre of the weld pool, separated by high angle boundaries, and accompanied by solvent segregation (e.g. sulphur). These columnar delta ferrite grains are highly textured, since <100> directions are favoured growth directions in these cubic materials. As the temperature falls, austenite nucleates on these boundaries and also grows in a columnar manner. Thus, in the final as-deposited microstructure of a weld metal, two columnar grain structures are present. Using solute sensitive etches, Widgery (1974) showed (Fig.1.7) that prior delta boundaries could be revealed (arrowed) and that these boundaries were independent of the prior austenite boundaries which are generally outlined by the presence of proeutectoid ferrite (e.g. at A and B). The relationship between these delta and austenite boundaries is still not clearly understood, and is one of the areas where a detached study is recommended.

Summarising, the result of the solidification process is to establish a series of columnar austenite grains prior to the decomposition reaction, which is the subject of the research described in this thesis.

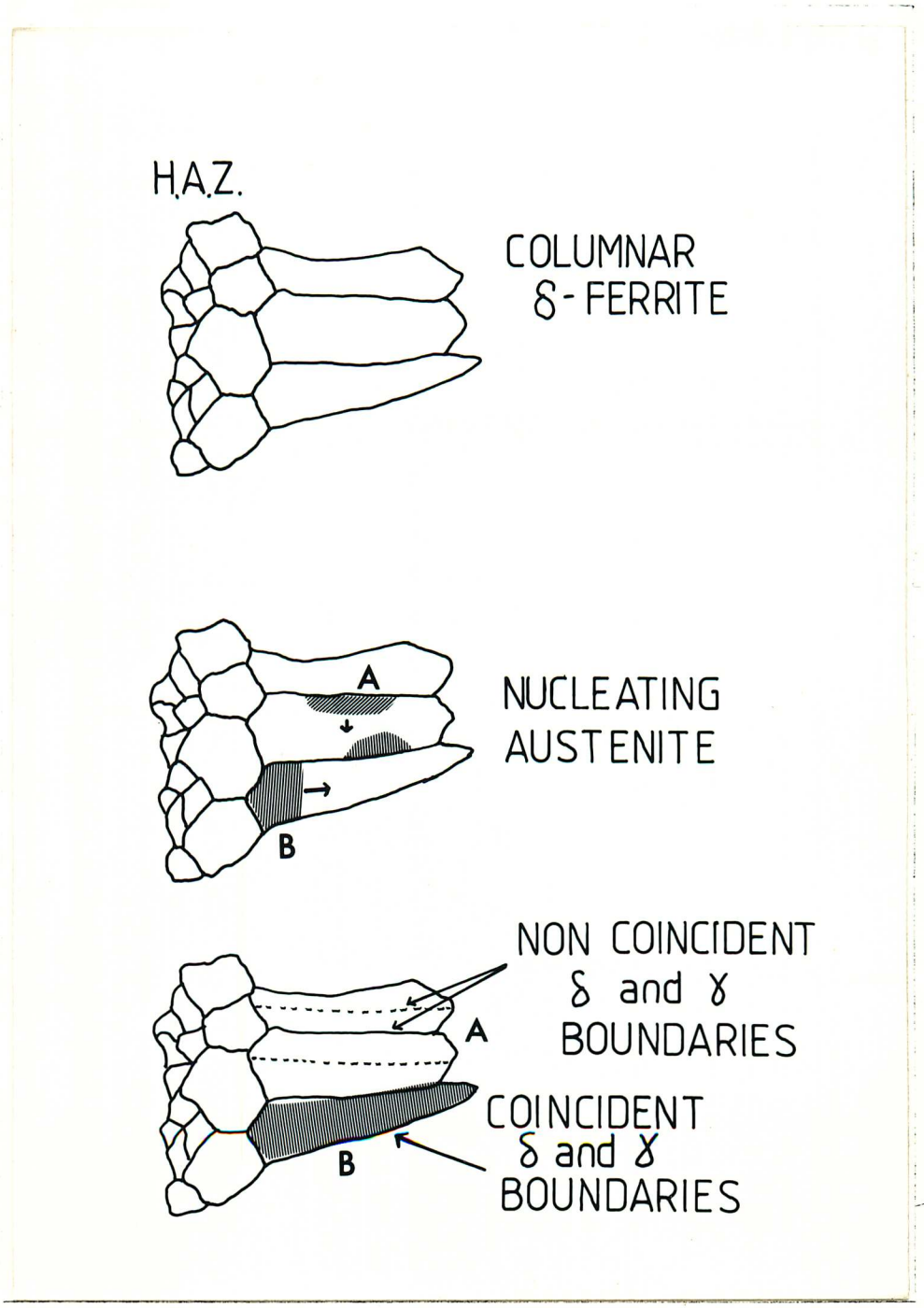

Fig.1.6 The solidification sequence for low carbon weld metals deposited using submerged arc or manual metal arc welding processes.

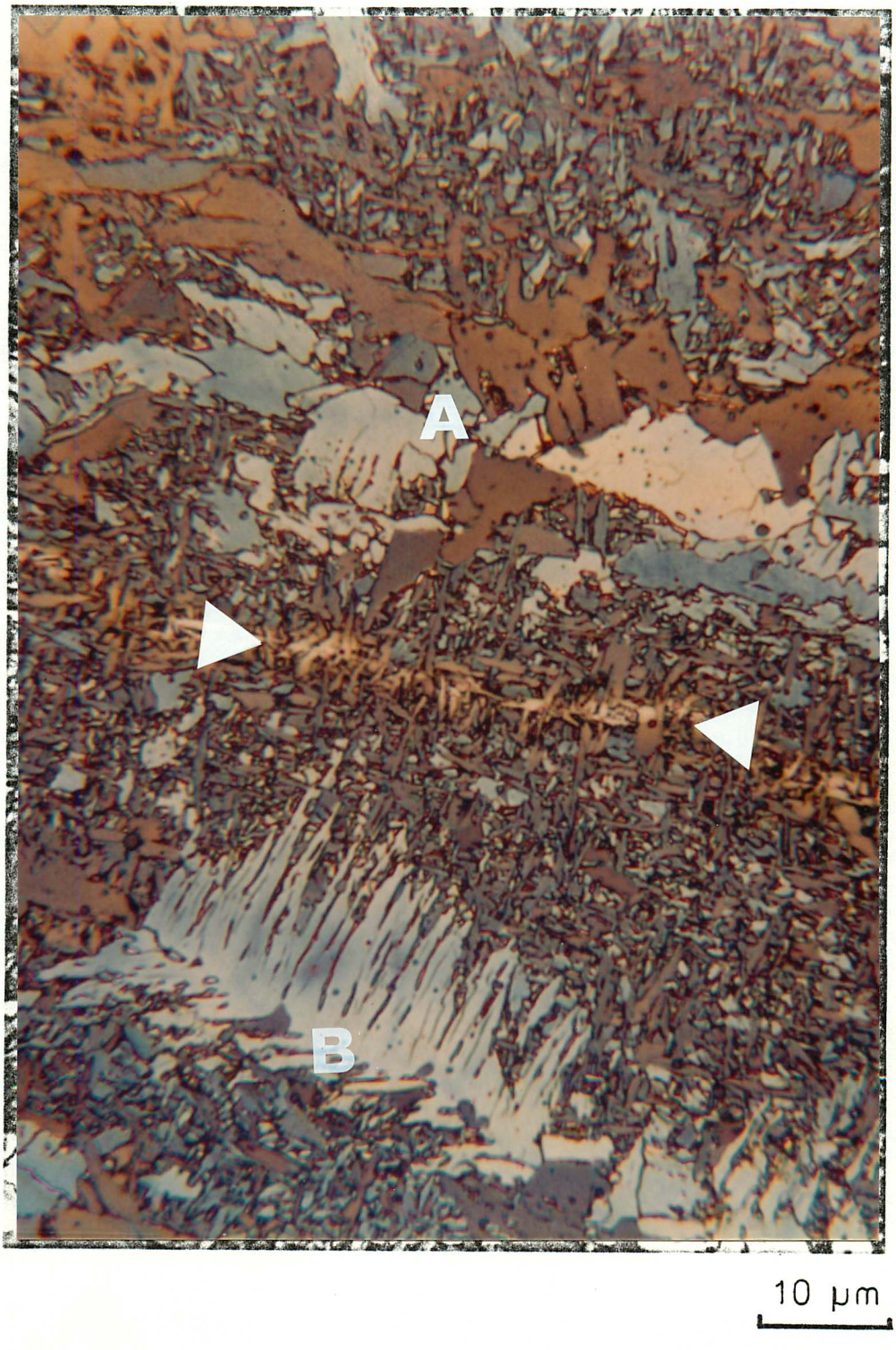

Fig.1.7 Microstructure of a typical submerged arc weld etched in Klems reagent. Following a light pre-etch in nital, the solute sensitive reagent reveals prior delta ferrite boundaries (as arrowed) in addition to the prior austenite grain boundaries, eg at A and B. (After Widgery (1974), courtesy D.J. Abson, The Welding Institute).

CHAPTER 2

THE DECOMPOSITION OF AUSTENITE IN FERROUS ALLOYS

2.1 INTRODUCTION

The decomposition of austenite is probably one of the most important phase transformations in physical metallurgy. The industrial significance of iron-based alloys reflects the degree of scientific interest in the various transformation mechanisms by which this decomposition can occur and the various morphologies and mechanical properties so produced.

This chapter will review the literature concerning the austenite decomposition reactions in ferrous alloys. Particularly relevant is the recent literature regarding the proeutectoid ferrite transformation in low alloy steels. This is the predominant microstructure observed in H.S.L.A. steel weld metals and therefore central to the work described in this dissertation. The ferrite morphologies observed in commercial weld metals formed during continuous cooling will be compared with those obtained in isothermal heat treatment in comparable wrought steels.

As further background, it is useful to consider the general characteristics of solid state transformation, as summarised by Christian (1965). These are best termed CIVILIAN and MILITARY and are as follows:

(a) Civilian Processes

The characteristics of thermally activated reactions are:-

(1) There is usually an incubation period before transformation commences.

(2) The degree of transformation is independent of temperature and will continue until equilibrium is reached.

(3) There is no correspondence between the initial and final sites of atoms, since diffusion during the transformation destroys any such correspondence.

(4) The final composition of the product phase may differ from the parent phase because of the diffusional processes involved.

(5) The effect of applied stress is to increase the rate of reaction.

(b) Military Processes

The characteristics of these reactions are:-

(1) The degree of transformation is dependent on temperature.

(2) There is a definite correspondence between the product and parent phases, since no diffusion occurs during the transformation and atoms are transferred across the interface in an orderly manner.

(3) There is no change in chemical composition between the product and parent phases during transformation.

(4) The effect of applied stress is to increase the degree of transformation.

In the light of recent research, it is important to note that such a strict division is not always permissible, as 'SOLDIERS MAY SOMETIMES BE OUT OF STEP AND CIVILIANS MAY SOMETIMES FORM PARAMILITARY ORGANISATIONS' (Christian, 1965).

2.2 THE DECOMPOSITION OF AUSTENITE IN FERROUS ALLOYS

2.2.1. THE PROEUTECTOID FERRITE REACTIONS

Aaronson (1962) has provided an extensive survey of the early literature regarding the proeutectoid ferrite and cementite reactions in ferrous alloys, which will form a framework for this review. It is now

generally accepted that, initially, nucleation of proeutectoid ferrite will occur at austenite grain boundaries. Classically, following the proposal of Smith (1953), nucleation was thought to take place with the ferrite nucleus forming a partially coherent interface with one of the adjacent austenite grains. The orientation relationship across this low energy interface would be the Kurdjumov-Sachs (1930) relationship, where

$$(111)_\gamma \quad // \quad (110)_\alpha$$

$$[110]_\gamma \quad // \quad [111]_\alpha$$

The growth of ferrite subsequently occurs into the other austenite grain by the movement of the more mobile incoherent boundary. Zener (1949) and subsequently Atkinson et al (1973) showed that the thickening rate of these allotriomorphs was consistent with growth involving the volume diffusion of carbon in austenite. Though it is now recognised (eg Hillert (1962)) that, in many cases, the ferrite nucleus has an orientation relationship with both austenite grains, the classical model still forms a useful basis for further discussion.

The various morphologies which ferrite develops during the proeutectoid reaction were examined by Mehl and Dubé (1951) and finally summarised by Aaronson (1962) in the form of the Dubé morphological classification system. This scheme is shown in Fig.2.1, where the following components can be described. (It should be noted that this scheme is quite arbitrary and therefore does not contribute directly to a study of mechanisms.)

(a) GRAIN BOUNDARY ALLOTRIOMORPHS

- nucleating and growing preferentially along grain boundaries.

(b) WIDMANSTATTEN SIDEPLATES

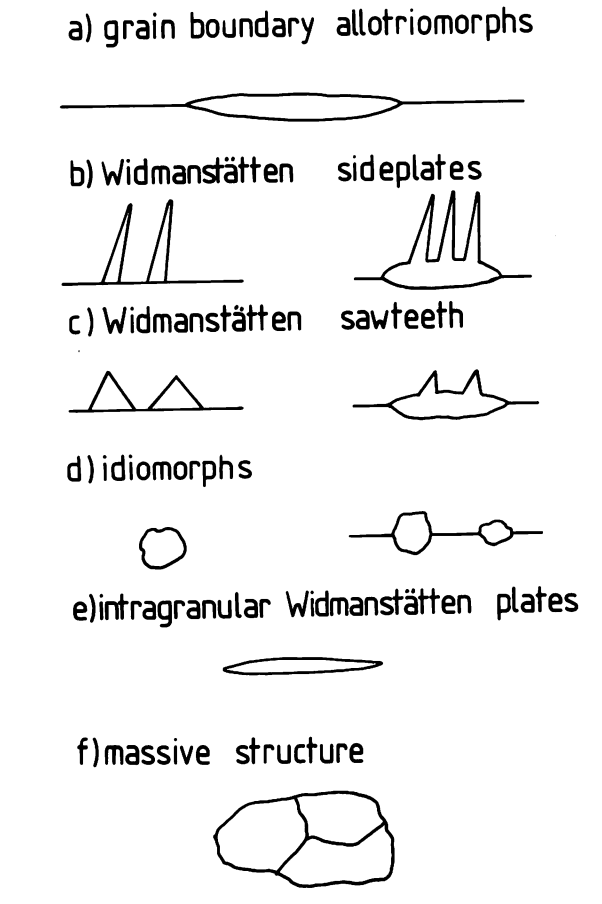

Fig.2.1 The Dubé morphological classification system

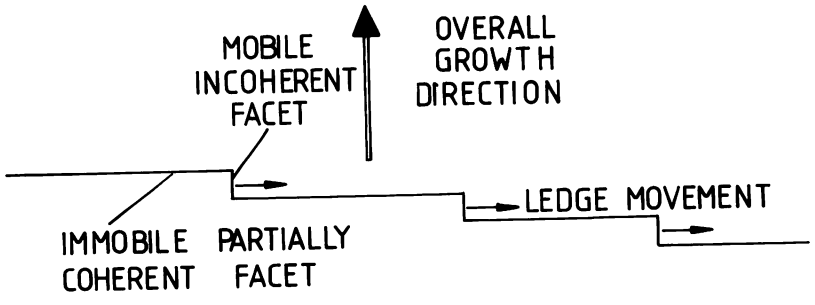

Fig.2.2 The ledge mechanism (Aaronson, 1962)

-nucleating directly at grain boundaries (primary plates) or from grain boundary allotriomorphs (secondary plates).

(c) WIDMANSTATTEN SAWTEETH

- having triangular cross-section in the plane of polish which again can be primary sawteeth or secondary sawteeth.

(d) IDIOMORPHS

- equiaxed ferrite which can be intragranularly or grain boundary nucleated.

(e) INTRAGRANULAR WIDMANSTATTEN PLATES

- nucleating within the austenite grains.

(f) MASSIVE STRUCTURES

- not constituting a fundamental morphology, being the result of impingement.

The relative proportion of these variants in any given system can be rationalised as follows. At relatively high temperatures (slow cooling rates in continuous cooling), incoherent growth is favourable, since the supersaturation is low. At lower temperatures (faster cooling rates in continuous cooling), partially coherent growth modes are favoured, since the supersaturation is high.

The mechanism of growth of Widmanstatten ferrite (ie. primary and secondary sideplates and intragranular plates) remains controversial.

One school of thought considers that the plates develop by a diffusional ledge mechanism, which is illustrated in Fig.2.2. This was initially proposed by Aaronson (1962) and subsequently refined (1969) to form a general theory of precipitate morphology. The interphase boundary between austenite and ferrite was considered to comprise of partially coherent regions and incoherent ledges. The partially coherent regions were considered immobile and to offer a barrier to growth normal to the boundary, whereas the disordered structure of the ledge allows it to migrate along the immobile boundary, displacing it

perpendicular to the interface. The rate of growth of these ledges was modelled by Jones and Trivedi (1971) as a function of the ledge height and interledge spacing. The development of secondary Widmanstatten sideplates was modelled by Townsend and Kirkaldy (1968), who extended the complex perturbation theory of Mullins and Sekerka (1965). In this manner, Widmanstatten plates were thought to develop from protuberances in the austenite/ferrite interface. The overall features of the reaction were controlled by carbon diffusion in austenite moderated by the effect of surface tension.

Kinsman et al (1975) studied the formation of ferrite sideplates in iron-carbon alloys, using thermionic electron emission microscopy. Experimentally, they observed growth ledges on the broad faces of Widmanstatten ferrite plates, and claimed that the measured velocity of these ledges corresponded to those calculated using the analysis of Jones and Trivedi (1971). Further, since the ledges were observed to lengthen at rates controlled by the diffusion of carbon in austenite, they claimed that the disordered nature of the riser was justified. Fig.2.3 shows the thickening kinetics they observed for the growth of Widmanstatten plates in a low carbon steel. The observed rate was clearly less than that allowed by the theoretical diffusion controlled rate (upper curve) and was clearly discontinuous, which they attributed to the passage of superledges along the broad faces of the plates. They concluded that the F.C.C./B.C.C. interface was indeed partially coherent and represented a barrier to growth normal to the interphase boundary. In the case of secondary sideplates, they proposed that the most important source of ledges was the concave junction between the sideplates and the grain boundary allotriomorphs from which they developed. It should also be noted that their experimental evidence included excellent examples of the surface relief which accompanied the transformation products investigated. They concluded that the

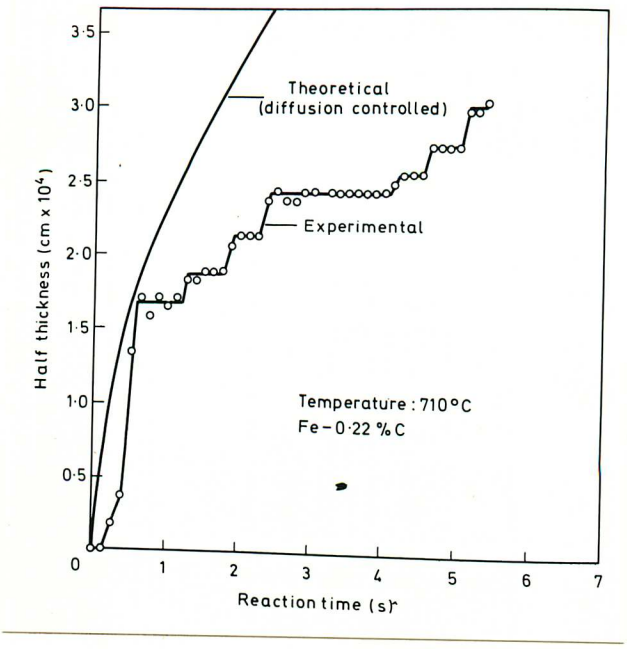

Fig.2.3 Thickening kinetics observed for the growth of Widmanstätten plates in a low carbon steel, after Kinsman et al., (1975).

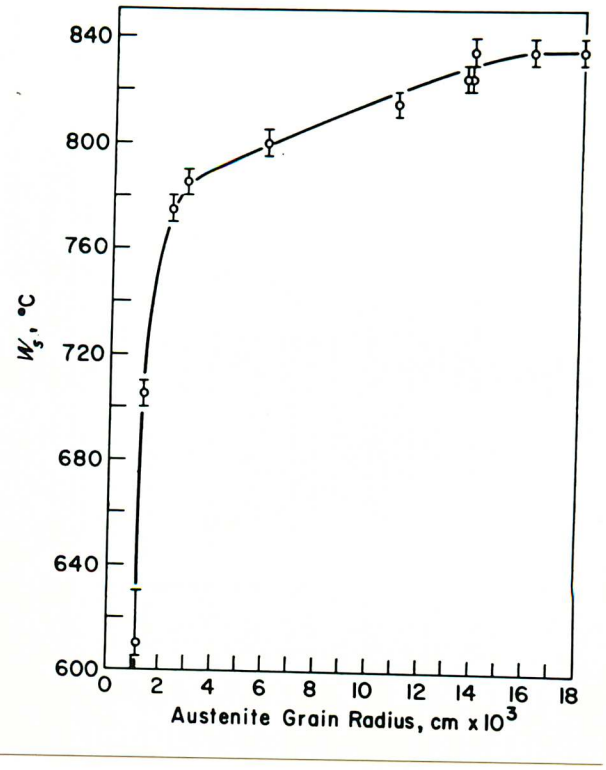

Fig.2.4 The influence of austenite grain size on the Widmanstätten ferrite start temperature (W_s), after Krahe et al., (1972).

observation of these surface tilts was not necessarily indicative of a military type of transformation, and only indicates the presence of a partially coherent boundary.

The influence of austenite grain size on the Widmanstatten ferrite start temperature has been the subject of many investigations. Early work in this field has been reviewed by Krahe et al (1972) and these experimental observations are summarised in Fig.2.4 for a plain carbon steel. The Widmanstatten ferrite start temperature was observed to vary between 600°C and 840°C over a range of austenite grain sizes between 10 μm and 200 μm. It should be noted that over the range generally encountered in weld materials, 100 μm, there is little variation with temperature. Krahe et al (1972) have claimed that these observations can be incorporated into the general theory of precipitate morphology, Aaronson (1962) (1969).

The nature of the partially coherent austenite/ferrite interface has been investigated by Aaronson and co-workers. Atkinson et al (1973) showed that the F.C.C./B.C.C. interface could be modelled geometrically and that for the N-W or K-S orientation relationships noted that only 8% of the atoms in the boundary could be regarded as coherent. However, with the introduction of monatomic steps in the interface, the proportion of coherent atom sites increased to 25%. Subsequently, Russell et al (1974) introduced a series of misfit dislocations beteeen the areas of coherency, resulting in a classic partially coherent boundary. Neither the structural ledges (which were coherent) or the misfit dislocation (whose Burgers vector lay in the boundary plane) could participate in the growth process.

Rigsbee and Aaronson (1979.1) extended the results of Hall et al (1972) and Russell et al (1974) for a spread of orientations in the N-W to K-S region and a range of lattice parameter ratios between the FCC and BCC phases. Summarising, they concluded that regions of good atomic

matching exist in the interface for all orientation relationships in the N-W to K-S orientation regions and for a wide range of lattice parameter ratios. They proposed that these structural ledges can account for the irrational habit plane observed (see Lui et al (1972)) for Widmanstatten ferrite. Further, they show that the introduction of triatomic structural ledges increases the overall coherency of the interface. Finally, since the misfit dislocations and structural ledges are immobile, they conclude that FCC - BCC transformation cannot be displacive in nature.

In a comparison paper, Rigsbee and Aaronson (1979) investigated the interfacial structure of the broad faces of Widmanstatten ferrite plates, using a weak beam technique. They concluded that the interfacial structure contained a single array of parallel misfit dislocation (20 Å apart) and structural ledges (50 Å apart). The dislocations were mixed in character, with their Burgers vectors lying in the habit plane of the interface, thus again concluding that, since a glissile dislocation structure is required for a displacive mechanism, the transformation was diffusional in nature.

The opposing school of thought regards the transformation to Widmanstatten ferrite as having characteristics which they believe are unmistakably martensitic in character.

Early work with this view, eg Ko and Cottrell (1952), established that the ferrite transformation product gave rise to relief effects on a prepolished surface. Further work by Ryder and Pitsch (1966) showed that the crystallography of this reaction was in general agreement with the phenomenological theory of martensite formation, Bowles and Mackenzie (1954). Watson and McDougall (1973) established that the plates produced an invariant plane strain (I.P.S.) form of shape deformation, and implied that the growth mechanism had martensitic characteristics. It should be noted (see Aaronson, (1962)) that the

observation of these surface reliefs is itself not disputed for the Widmanstatten ferrite reaction. However, there is clear disagreement over the significance of such effects. Christian (1962) and Bhadeshia (1979) believe that the existence of an I.P.S. shape change implies definitive evidence for a displacive growth mechanism. (It must also be realised, however, that this does not imply that carbon diffusion cannot accompany, and even control, the overall transformation.). In contrast, Aaronson and co-workers, eg (1962) (1969), claim that the I.P.S. shape change does not necessarily define the nature of the transformation mechanisms. They claim that relief arises due to the existence of a sessile semi-coherent interface, though it must be stated that, as Bhadeshia (1980.2) has pointed out, the diffusional school consistently fails to explain the mechanism of relief production. Since this point is purely a matter of interpretation, it is difficult to envisage how it will be resolved in future.

A further point to be considered is the nature of the ferrite/austenite interface. Rigsbee and Aaronson (1979.1), (1979.2) concluded that a displacive transformation was impossible, since the interfacial structure is comprised of coherent structural ledges and sessile dislocations. In contrast, Bhadeshia (1980.2) proposes that these structural ledges would be better regarded as coherency dislocations which accompany shear transformation, and are therefore glissile, leading to the formation of an I.P.S. shape change effect.

Though the relief effects and interfacial structure have been subject to two different interpretations, a third objection to the shear mechanism for Widmanstatten ferrite formation has recently been resolved.

Aaronson et al (1975) have proposed that for a displacive mechanism there is insufficient driving force to account for the strain energy which arises from the shape change. Bhadeshia (1980.2), in an effort to

resolve this question, investigated the existence of a 'crystallographic' degeneracy in the FCC/BCC system. This was considered compatible with the simultaneous and back-to-back growth of mutually accommodating plates. Adjacent plates are of the same crystallographic orientation, but their shape strains mutually accommodate, giving rise to the tent shaped relief observed. In a further analysis, Bhadeshia (1981.1) established the precise thermodynamic conditions for the formation of Widmanstatten ferrite. The strain energy question was rationalised, and it seems unlikely that this objection itself is a limiting feature for the proposed displacive nature of the transformation.

Summarising, Widmanstatten ferrite formation was considered to involve the growth of mutually accommodating plates in a back to back manner. The plates form with an equilibrium carbon content, and hence the growth rate is carbon diffusion controlled, but an atomic correspondence is maintained with respect to the iron atoms.

Recent work on the nature of the FCC/BCC interface, eg Ecob and Ralph (1980), (1981) and Howell et al (1981), has indicated that the nature of the partially coherent boundary is considerably more complex than that proposed by Rigsbee and Aaronson (1979.1).

It is important to note that in their model, Rigsbee and Aaronson (1979.2) identify the interphase boundary of minimum energy by maximisation of the interfacial coherency between the phases. They thus step the interface and introduce misfit dislocations to increase the degree of interfacial coherency. In contrast, Ecob and Ralph (1980), (1981) have shown that a purely geometrical quantity, designated the R parameter, represents the most appropriate quantity to describe the lowest energy interface between the phases. This quantity varies as the energy of interaction of the interfacial dislocations, and can be used to determine the interface with the overall minimum energy. This

analysis thus accounts for the contribution of the interfacial dislocations to the energy of the interface, which is not included in the Rigsbee and Aaronson model.

The lowest value of R (corresponding to the minimum interfacial energy) is predicted to be (111) FCC for orientations in the N-W to K-S range, and for any deviations from this plane, they concur with Rigsbee and Aaronson (1979.1) that structural ledges must be incorporated into the interface.

2.2.2 THE PROEUCTECTOID CEMENTITE REACTION

The morphology and kinetics of the proeutectoid cementite reaction has received relatively little attention in comparison with the ferrite reaction. Aaronson (1962) has documented the major morphological variants of proeutectoid cementite, indicating some of the similarities with the ferrite microstructures. However, he also noted the confusion that existed (and still does) in the factors controlling the mechanism of growth of the various constituents.

2.2.3. THE PEARLITE REACTION

The pearlite reaction is most conveniently described as a lamellar eutectoid reaction occurring by the co-operative growth of ferrite and cementite behind an incoherent boundary. It has been the subject of many extensive reviews, eg Hillert (1962), since Sorby first identified the constituent in plain carbon steels.

Since the two product phases have different carbon contents, a local rearrangement can be achieved in three principal ways.

(1) Diffusion of carbon in austenite ahead of the interface.

(2) Diffusion of carbon in the austenite/pearlite interface

(3) Diffusion of carbon in the ferrite behind the interface.

Quantitative analysis of the growth rates of pearlite, eg. Cahn and Hagel (1962), indicated that the transformation proceeded faster than that allowed by volume diffusion of carbon. These observations led both Cahn and Hagel (1962) and Hillert (1962) to conclude that an interfacial diffusion pathway was likely. The view of Darken and Fisher (1962) that a ferrite gap existed between the cementite lamellae and austenite interface, which led then to conclude that the transformation was controlled by the diffusion of carbon in the ferrite behind the interface, has been refuted by Dippenar and Honeycombe (1973). In this latter study, cementite was shown to be continuous up to the austenite interface.

Nucleation of pearlite, like that previously discussed for proeutectoid ferrite, occurs preferentially at austenite grain boundaries. It now seems accepted that either cementite or ferrite can nucleate the initial pearlite nodule. Two main ferrite/cementite orientation relationships are observed in pearlite (Dippenar and Honeycombe (1973)), depending on the condition of the prior austenite boundary. If pearlite nucleated directly on the austenite grain boundary, a Pitsch-Petch orientation relationship was observed; however, when the austenite boundary was coated with a proeutectoid layer of cementite, a Bagaryatski orientation relationship was observed.

2.2.4. THE BAINITE TRANSFORMATION

For many years, the mechanism of formation, and even the identification, of the bainite constituent in steel represented one of the great debates in metallurgical literature, eg. Hehemann et al (1970), Kennon (1974), Christian (1965). The choice of mechanism lay again between a diffusional mechanism proposed by Aaronson and co-workers and a displacive mode of transformation as discussed by Oblak, Hehemann and Wayman and co-workers.

Classically two variants are generally recognised, designated upper and lower bainite, which reflects the difference in carbide distribution. At high temperatures, interlath cementite was observed between the bainite ferrite laths, whereas at lower temperatures, intralath cementite was present within the bainite ferrite laths. Other bainite morphologies have been observed, eg. granular bainite reported by Habraken and Economopoulos (1967), and the confusion regarding definitions and terminology prompted Aaronson (1969) to propose three principal definitions, which can be summarised as follows.

1. MICROSTRUCTURAL DEFINITION

Microstructuraly, bainite was defined as a non-lamellar eutectoid reaction.

2. KINETIC DEFINITION

Kinetically, bainite was regarded as having a distinct 'C' CURVE, and above a critical temperature (the bainite start temperature), the product was not observed.

3. SURFACE RELIEF DEFINITION

In this last definition, bainite was loosely described as any product which, under isothermal heat treatment conditions, gave rise to surface tilts on a prepolished surface.

Much of the early literature on the mechanism of formation of this constitutuent has been recently reviewed in a complete and definitive study of the bainite reaction (Bhadeshia (1979)). The basis of this present review will be to consider briefly the early work in this field, before considering the implications of the more recent work in detail. It must be noted that the problems discussed in section 2.2 regarding interpretation of surface relief effects and the nature of the interfacial structure also apply to the following section.

Observations by Ko and Cottrell (1952) that the formation of bainite was accompanied by surface relief effects led to the proposal

that the reaction was displacive in character. Further work by Matas and Hehemann (1961) and Goodenow et al (1965) concluded that in both upper and lower bainite, the bainitic ferrite formed initially with a carbon supersaturation. In lower bainite, this was subsequently relieved by precipitation of initially e-carbide (resulting finally in cementite) within the bainitic ferrite, whereas in upper bainite carbon diffusion to the remaining austenite resulted in precipitation of cementite at the bainite ferrite boundaries. Goodenow et al (1965) and subsequently Oblak and Hehemann (1967) reported that the morphology of bainite comprised individual sub-units, which were the elementary growth units whose repeated nucleation and martensitic growth could account for the overall reaction kinetics. The development of microstructure was considered to be controlled by either the removal of carbon from the bainitic ferrite and/or the relaxation of transformation strain.

The diffusional mechanism, based on the work of Aaronson and co-workers, proposes that the bainitic ferrite component develops by a classic ledge mechanism over the whole range of transformation temperatures. The characteristic bay in the T.T.T. curve is considered to arise due to a solute drag concept. Alloying elements which decrease the carbon activity in austenite, eg Mo, are considered to give rise to an enhanced drag effect on the austenite /ferrite interface, therefore reducing the overall reaction kinetics. In contrast, elements which have only a small effect on reducing the carbon activity, eg Mn, or raise this parameter, eg. Si, should not give rise to this drag effect. The so-called 'incomplete reaction phenomenon' of the bainite is not considered to be a general characteristic. Finally, a thermodynamic analysis has been presented, Aaronson and Kinsman (1967) , which was claimed to invalidate the displacive sub-unit mechanism.

It is now appropriate to review the recent literature regarding the bainite transformation which has clarified many of the problems discussed above.

Bhadeshia and Edmonds (1979), (1980) investigated the morphology of bainite in a medium carbon silicon steel. The advantage of this system is that due to the presence of 2% Si, carbide precipitation is inhibited and retained austenite observed in the final microstructure. The morphology of a complete sheaf of upper bainite which they observed is shown in Fig.2.5. Each sheaf is comprised of a group of individual sub-units separated by films of retained austenite. These observations themselves are quite convincing evidence for the martensitic sub-unit mechanism which the authors support. Further, the observation of two distinct 'C' curves for the upper and lower bainite reactions in this system (and thus three minima in the overall reaction kinetics) is clearly incompatible with a solute drag effect, which can only explain one such bay. A more recent analysis has refuted the solute drag model on a thermodynamic basis (Bhadeshia (1981.4)). The incomplete reaction phenomenon the authors observed was shown to be incompatible with a diffusional mechanism of formation, since, after long holding at the reaction temperature, a pearlite reaction was observed after the bainite reaction.

Subsequent work on this system, eg Bhadeshia and Edmonds (1980) and Bhadeshia and Waugh (1981), has shown that two further characteristics of the bainite transformation can be directly understood if a displacive mechanism is involved. Bhadeshia (1979) has established an advanced thermodynamic analyis of the austenite to bainite transformation. The principle of this analysis is to define a To temperature, where stress -free austenite and ferrite of the same composition have equal free energy. Any displacive transformation must therefore occur below this temperature. Similarly, a no-substitutional temperature can be

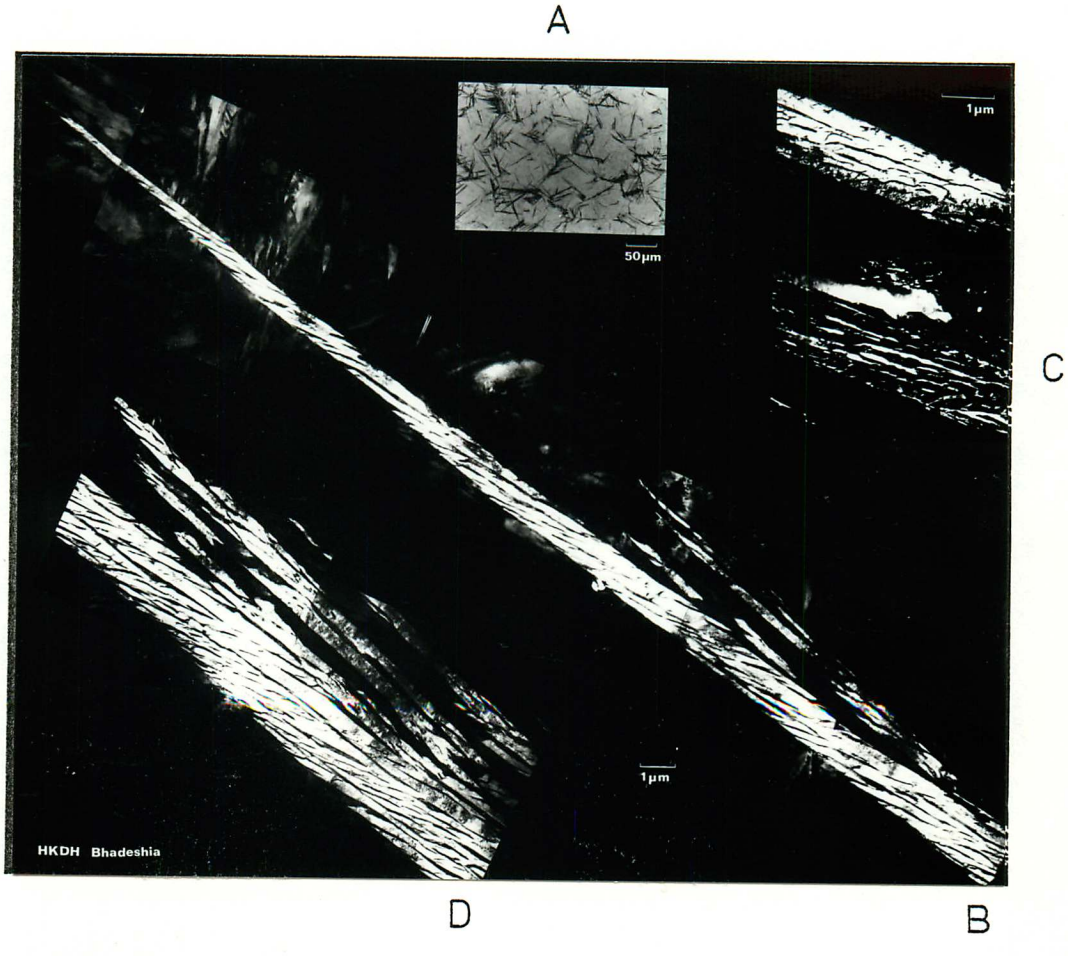

Fig. 2.5 The morphology of upper bainite observed by Bhadeshia and Edmonds (1979) in a C/Mn/Si steel

(A) Optical micrograph
(B) and (D) Electron micrographs indicating the sheaf substructures of upper bainite
(C) Corresponding retained austenite dark field image.

established, and the locus of these points is summarised in Fig.2.6 as a function of temperature and carbon content. Using the dilatometric data obtained for the upper and lower bainite reactions, the carbon content of the residual austenite could be calculated at the termination of the bainite reaction and plotted with respect to the To and Ae_3 curves. Reasonable agreement was achieved between the To curve and the experimentally determined carbon contents, indicating that the termination of the bainite reaction occurred when the residual austenite composition approached the To curve.

On this basis, the degree of transformation to bainite would clearly be sensitive to carbide precipitation reactions since they would allow <u>further</u> transformation to bainitic ferrite as the composition of the residual austenite would again be reduced below the To line. Further if an inhomogenous distribution of carbon existed (as proposed by Bhadeshia and Edmonds, (1979)), the degree of transformation would exceed that calculated on the basis of the <u>average</u> carbon content of the residual austenite. Direct evidence for the existence of such an inhomogenous distribution of carbon has now been experimentally determined (Bhadeshia and Waugh, (1981)), further characterising the incomplete reaction phenomenon. A second implication of this latter work was that a full supersaturation of carbon existed during the growth of the bainitic ferrite.

Considering the weight of recent experimental evidence, coupled with the advanced thermodynamic analysis of the bainite reaction previously described, it seems reasonable that the characteristics of the bainite reaction are best described by a displacive mechanism.

The transition from upper bainite to lower bainite, and indeed the lower bainite transformation itself, has also recently received much attention. The usual morphological features associated with the lower bainite transformation are plates of bainitic ferrite with internal

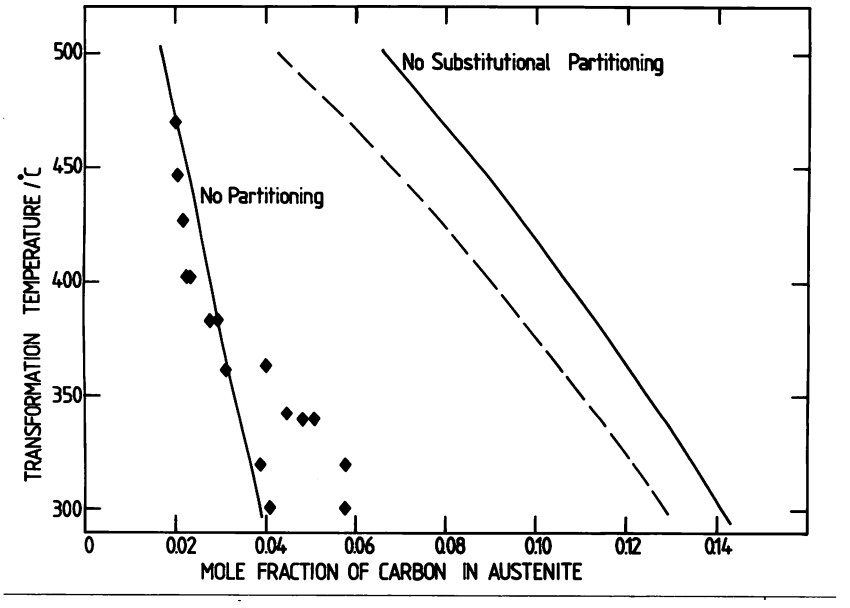

Fig.2.6 Summary of the advanced thermodynamic analysis due to Bhadeshia (1979). The No partitioning curve (To) is in reasonable agreement with the dilatometric analysis (♦) which indicates the carbon content of the austenite at the termination of the bainite reaction. The dashed curve indicates the position of the substitutional partitioning curve allowing for strain and interfacial energy contributions.

carbides. In general, a single crystallographic orientation of precipitates is observed such that their habit plane makes an angle of 60° with the major plate axis.

The significance of this carbide precipitation during the lower bainite transformation has been investigated by Bhadeshia (1980.1). The conclusions of that investigation can best be summarised as follows.

1). Cementite nucleates and grows from within supersaturated ferrite.

2). The observed cementite crystallography was inconsistent with the proposed interphase precipitation mechanism, where it was thought that precipitation occurred at the bainitic ferrite/austenite interface (Aaronson et al 1978).

3). The same crystallographic observations suggested that the characteristic single carbide variant was not directly related to the lattice invariant shear occurring during the transformation (Srinivasan and Wayman, 1968)

4). The most likely cause of the single carbide variant was thought to be due to the total transformation strain associated with the formation of the bainitic ferrite plate.

2.2.5 THE MARTENSITE REACTION

The martensite reaction in steels is a classic example of a displacive transformation. The characteristics are therefore:-

1) No diffusion of atoms occurs.

2) There is a lattice correspondence between the parent and product phases.

3) There is an invariant plane strain deformation associated with the transformation.

Two morphologies are usually recognised (Kelly and Nutting, (1960)) in steels, determined essentially by the carbon content of the system considered. Lath martensite (or low carbon martensite) generally forms

in packets of parallel laths with a high dislocation density. The habit plane usually ascribed to this martensite is (111)$_\gamma$. Twin martensite (or high carbon martensite) comprises of heavily twinned plates with a (225)$_\gamma$ or (259)$_\gamma$ habit plane. A more detailed review of the crystallography and observed habit planes in steels can be found elsewhere eg. Bhadeshia (1979).

2.2.6. THE DECOMPOSITION OF AUSTENITE IN ALLOY STEELS

This section will review the literature concerning the role of alloying elements on the various austenite decomposition reactions described previously. Particular emphasis will be placed on recent work which has contributed directly to a better understanding of the overall operative growth mechanism. This review can not therefore summarise the extensive literature regarding either the hardenability aspects of the various alloying elements or the resultant structure/property relationships, even though they have extremely important industrial significance. The reaction of greatest interest is again the proeutectoid ferrite reaction, with the other four reactions being considered only briefly.

Alloying elements in steels are generally referred to as either austenite stabilisers, eg. Ni, Mn, or ferrite stabilisers eg. Cr, Mo, depending on whether they expand or contract the austenite phase field. A further distinction can be made between those elements which are usually termed carbide formers, eg. Cr, and those which are not eg. Ni. It is the study of this former group - the carbide forming elements - which has provided further information regarding the growth mechanism of proeutectoid ferrite.

A useful starting point is to consider the categories reported by Honeycombe and Pickering (1972) in their review of the ferrite and bainite reactions in alloy steels.

1) Pearlite - type structures

2) Fibrous carbide-ferrite structures

3) Interphase precipitation

The first two categories have received relatively little attention, since the alloying levels required for both of these reactions are generally high, and the morphology of the lamellar product would seem to preclude any useful industrial application. The subject has been recently investigated by Ricks (1979) in Mo containing steels and Parsons (1981) in medium carbon, V containing steels.

It is the investigation of the final category, interphase precipitation, which has provided new and detailed information regarding the growth mechanism of proeutectoid ferrite. Initially, the use of niobium and vanadium in microalloyed steels provided an impetus for the study of the interphase precipitation reaction, but it has been now observed in carbon free alloys, eg Ricks (1979). The extensive work in this field by Honeycombe and co-workers has shown that this mechanism is operating in many systems eg. WC (Davenport, Berry and Honeycombe, (1968)) Mo_2C (Berry and Honeycombe (1970)).

In an extensive review, Honeycombe (1976) summarised four characteristics of interphase precipitation.

1) Sheets of precipitate form parallel to the interphase boundary and are therefore sensitive to any change in direction of the boundary.

2) The precipitate phase nucleates on the interphase boundary.

3) The ferrite/precipitate crystallography is generally that encountered in tempered martensite.

4). Typically only one variant of the orientation relationship is observed in a single ferrite grain.

The precipitate sheet spacing and precipitate size was observed to be a sensitive function of transformation temperature (eg. Batte and Honeycombe (1973)).

Campbell and Honeycombe (1974) provided definitive evidence for interphase precipitation in chromium steels, occuring in association with a ledge mechanism. Schematically, as shown in Fig.2.7, precipitation was shown to occur on the planar interphase boundary, with the ledge itself remaining free from precipitation. As previously discussed in section 2.2.1, this implies that a partially coherent interface exists between the austenite and ferrite and under these circumstances precipitation would be expected on the high energy ledge itself. However, this has been rationalised, since the ledges are too mobile for nucleation to occur on these sites. This mechanism has now been observed in other systems, as shown in Fig.2.8, where Ricks (1979) has noted precipitation of Mo_2C behind a stepped interphase boundary in Mo containing steels.

These observations have provided perhaps the most vivid evidence for the operation of a ledge mechanism between austenite and ferrite in the growth of proeutectoid ferrite.

Though the above reaction mechanism (generally termed coherent precipitation) has now been widely observed, at least two other mechanisms have been observed to account for arrays of discrete precipitates in ferrite. Heikkinen (1973) and recently Howell and Ricks (1981) have described the operation of a bowing mechanism where, initially, the interphase boundary is pinned by precipitates. Depletion ahead of the interface allows it to 'bulge' between the precipitates, bypassing them, and finally being pinned again when the interface became planar. On this basis, there is clearly a limiting sheet spacing below which it is unlikely that this mechanism can operate, and in the case of vanadium containing steels, Ricks (1979) concludes that the observed spacing is too small for the operation of this mechanism.

Observations by Dunlop et al (1978) of interphase precipitation of VC in the ferritic component of pearlite have led Parsons (1981) to

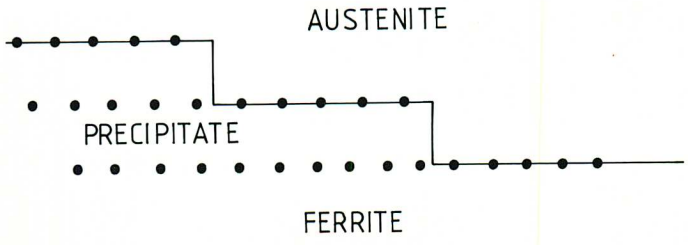

Fig.2.7 Schematic diagram, illustrating precipitation occurring in conjunction with a ledge mechanism.

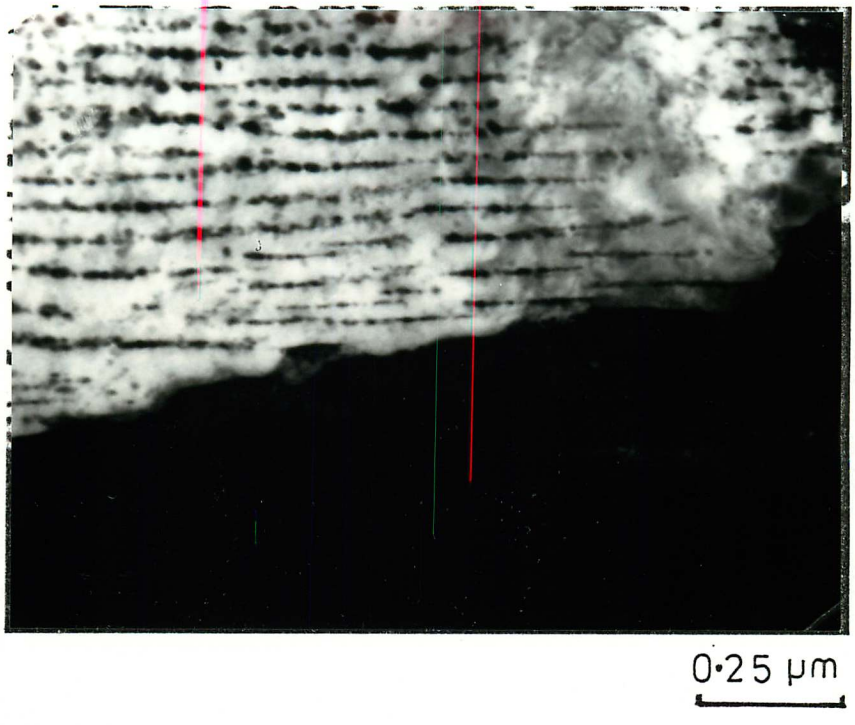

Fig.2.8. Example of interphase precipitation of Mo_2C behind a stepped interface in a Fe/C/Mo alloy. (Courtesy R.A. Ricks (1979).).

propose an incoherent step mechanism to explain the formation of this product. This incoherent step mechanism has also been employed by Ricks (1979) to explain observations of curved precipitate rows in iron-copper alloys.

2.3 EXPERIMENTAL OBSERVATION OF FERRITE MORPHOLOGIES IN H.S.L.A. STEEL WELD METALS

The ferrite morphologies described in this section were those observed in a quenched weld (M.M.A. 4) deposited using a Philips 56S basic low hydrogen electrode. Examination by optical microscopy at various stages of transformation indicated that all the morphologies reported in the Dubé classification scheme were present. The columnar austenite grain structure is evident in all the microstructures considered.

Fig.2.9 illustrates the morphology of ferrite grain boundary allotriomorphs. Typically, saturation of austenite boundary sites occurs rapidly in these materials, resulting in impingement between adjacent nucleation sites. In some cases, allotriomorphic ferrite develops as a continuous film along the austenite boundaries, as shown in Fig.2.10. In very few cases, intragranular idiomorphs were observed, as shown in Figs.2.11 and 2.12. In the former case, the ferrite idiomorph appears approximately rectangular in section and closely resembles those reported by Aaronson (1962) in the original classification scheme. A further point to note in this case is that they appear to be associated with inclusions. The idiomorph illustrated in Fig.2.12 appears faceted.

At low temperatures (and consequently in the case of continuous cooling, higher degrees of transformation), faceted morphologies were more frequently observed. This is indicated in Fig.2.13, where primary ferrite sawteeth are illustrated. More frequently however, secondary

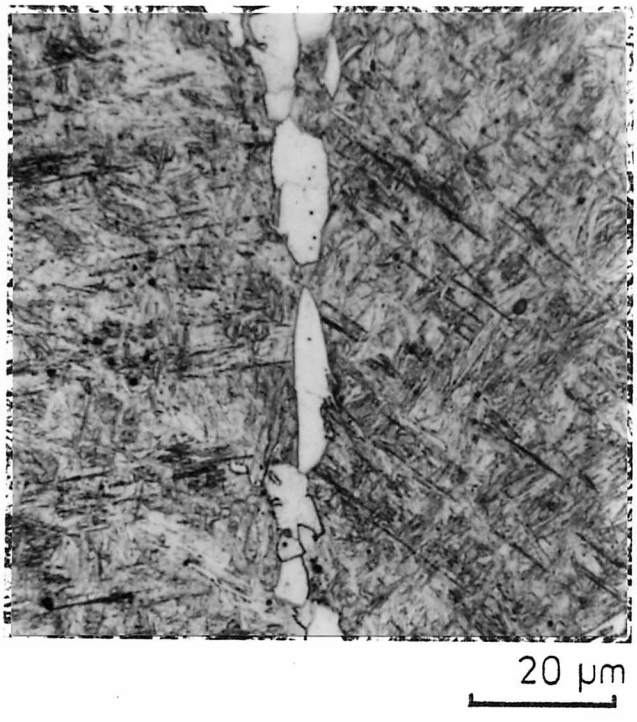

Fig.2.9 Typical appearance of a grain boundary allotriomorph.

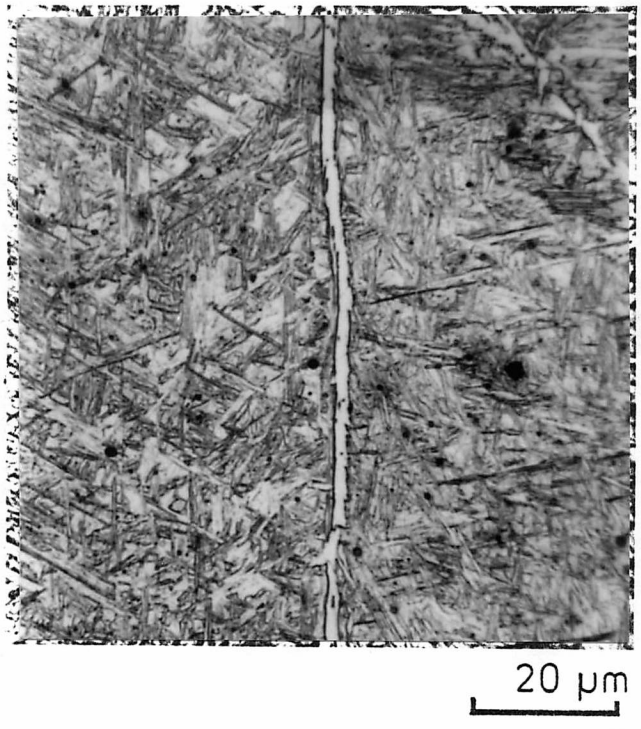

Fig.2.10 Ferrite allotriomph formed as a continuous film at a grain boundary.

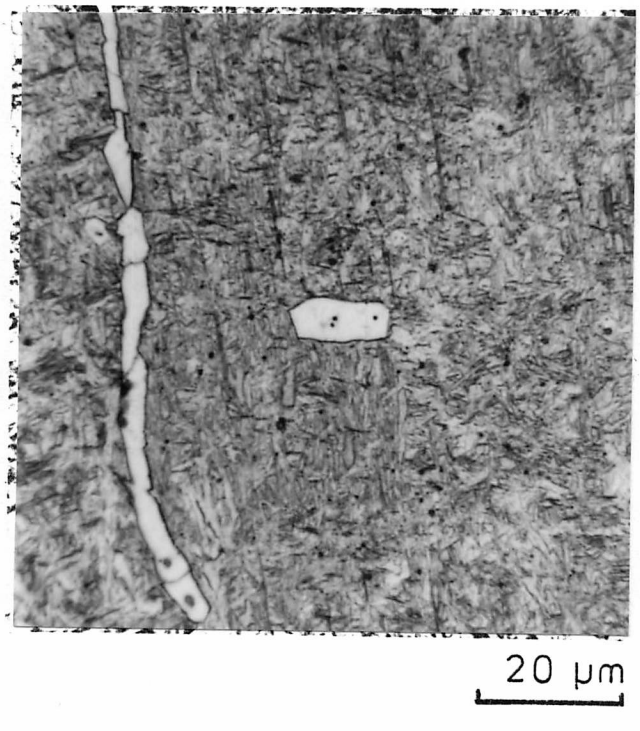

Fig.2.11 Rectangular intragranular idiomorph.

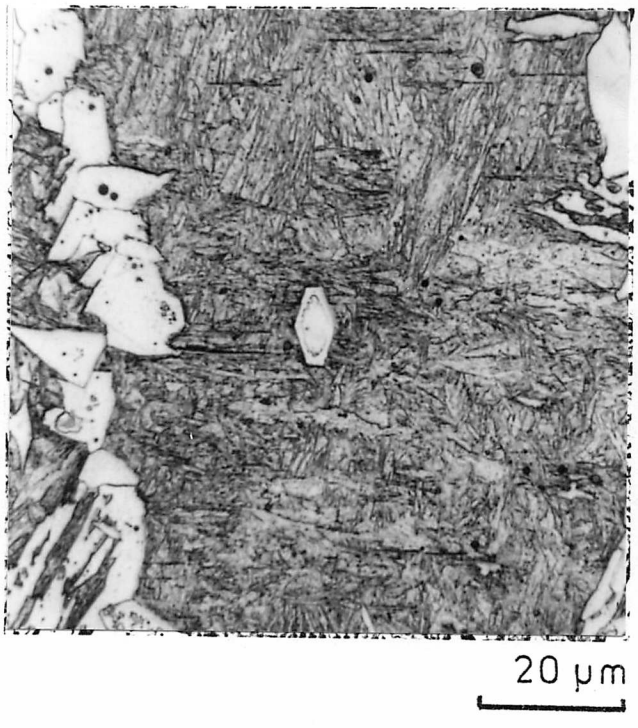

Fig.2.12 Faceted intragranular idiomorph.

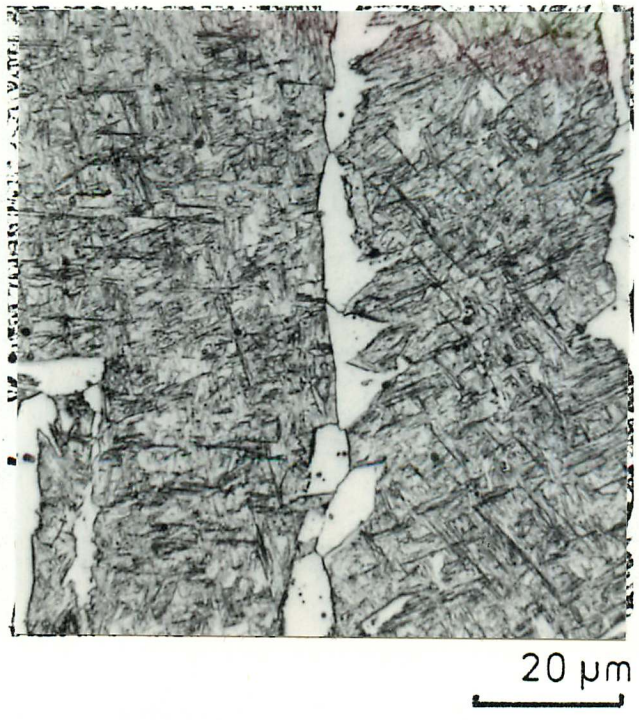

Fig.2.13 Primary Widmanstätten sawteeth.

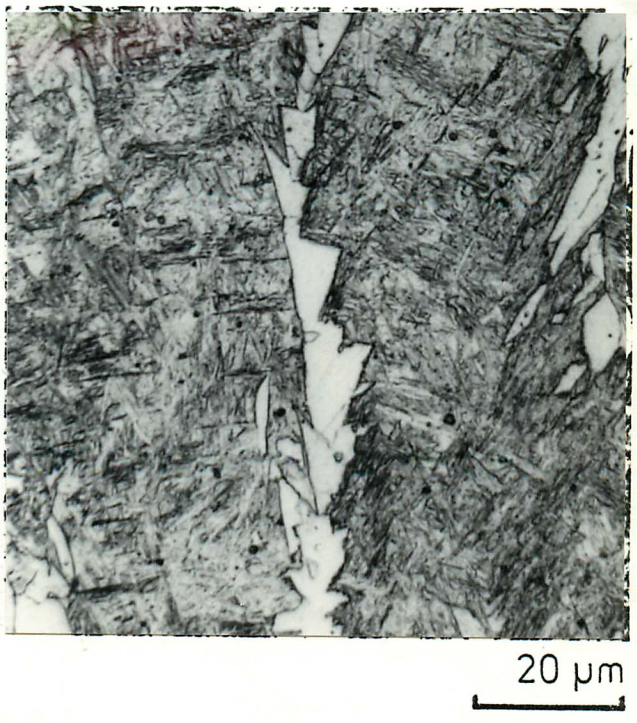

Fig.2.14 Secondary Widmanstätten sawteeth.

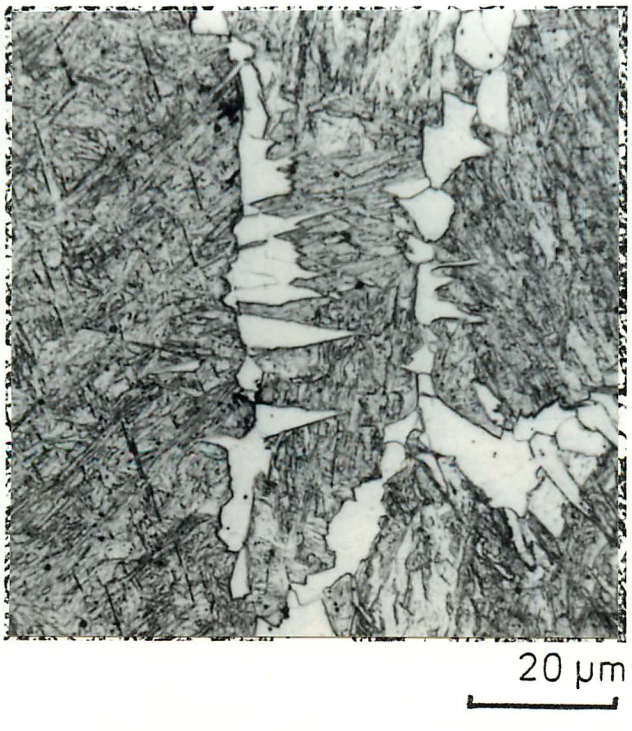

Fig.2.15 Primary Widmanstätten sideplate.

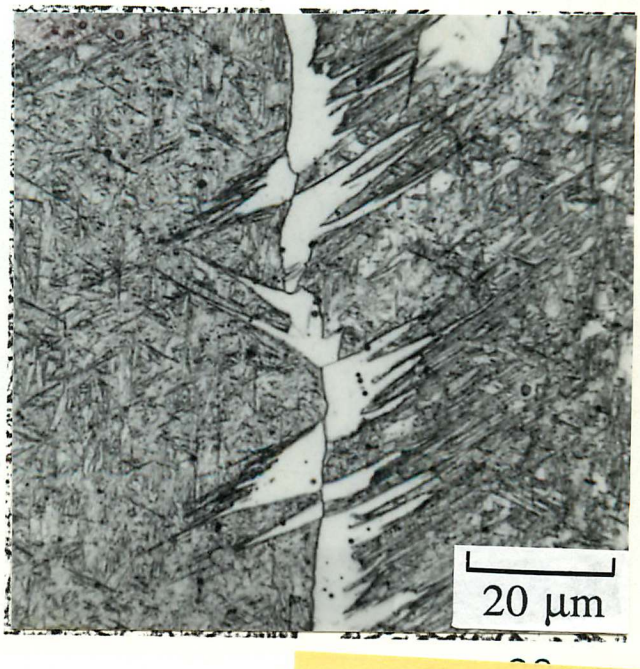

Fig.2.16 Seconda
sideplate.

negative
+ 3 prints
of same
size

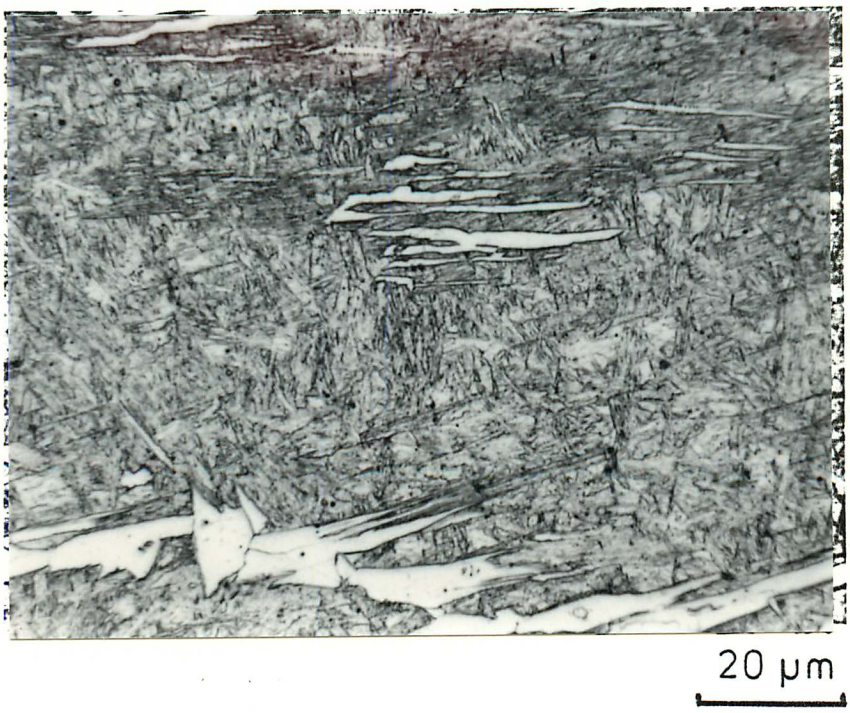

Fig.2.17 Example of the larger ferrite plates observed in the intragranular regions of weld MMA 4. Such plates would generally be termed acicular ferrite in the fully transformed microstructure of the final weld deposit.

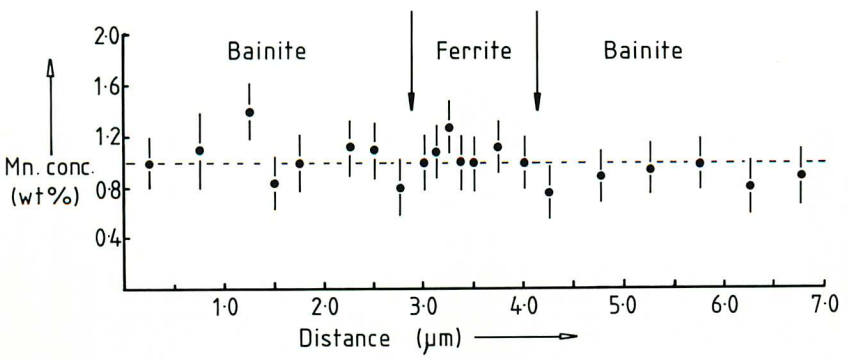

Fig.2.18 Typical S.T.E.M./E.D.X. trace across a grain boundary ferrite allotriomorph. No partitioning of manganese is observed between the austenite and ferrite.
(In this case the austenite has transformed to bainite during the quenching treatment).

ferrite sawteeth were observed developing from pre-existing grain boundary allotriomorphs, as shown in Fig.2.14. Extremely few examples of primary Widmanstaten ferrite sideplates were observed due to the preceding high temperature reactions. However, by serial sectioning, primary plates could be located, as illustrated in Fig.2.15. A further example, including secondary sideplates (Fig.2.16), indicates that in many cases the plates develop preferentially into only one grain. The most predominant microstructural consitutuent in this weld deposit is shown in Fig.2.17, which illustrates the development of what morphologically would be termed secondary Widmanstatten sideplates and intragranular Widmanstatten plates.

Since the weld system considered above contains a significant level of manganese, it is instructive to examine the possibility that partitioning occurs during the early stages of the ferrite reaction. Aaronson and Domain (1966) have reported partitioning of manganese during the high temperature ferrite reaction in a similar alloy system. Fig.2.18 shows a S.T.E.M./E.D.X. trace across a typical grain boundary allotriomorph extending into the austenite (now bainite) on either side. No partitioning of manganese is observed between the ferrite and austenite at the cooling rate considered.

2.4 SUMMARY

This chapter has reviewed the literature concerning the decomposition of austenite in ferrous materials. Particular emphasis has been placed on assessing the recent literature regarding the Widmanstatten ferrite and upper bainite reactions. It is apparent that in this area, there is still fundamental controversy regarding the operative growth mechanism.

With regard to the proeutectoid ferrite reaction, the experimental work described in this chapter has shown that the morphological variants reported in the Dubé classification scheme have been accurately reproduced in the H.S.L.A. steel weld examined. However, it must be pointed out that with respect to the Widmanstatten morphology, a more stringent definition is now envisaged [Bhadeshia (1981.1)], a point which will be discussed further in Chapter 5.

On the basis of the limited EDX analysis results presented, it seems likely that at the cooling rates considered in this investigation, (ie. the relatively short period of time at high temperatures), substitutional partitioning is unlikely to occur.

CHAPTER 3

EXPERIMENTAL PROCEDURE

3.1. INTRODUCTION

In this chapter the experimental procedure and the various welding techniques used in this investigation will be described. Typical macrostructures of the welds together with their chemical analysis will be given. Detailed information regarding individual fluxes or welding rods will not be included, as this can be found in standard manufacturers guides. The only welding technique which will be described in depth is that of Tungsten-Inert-Gas (T.I.G.) remelting, as the terminology and welding procedures for the other techniques (e.g. submerged arc welding) are well established. All the welding carried out in this investigation was performed at the Welding Institute.

3.2 WELDING TECHNIQUES AND PROCEDURES

3.2.1. PLATE (BASE) MATERIAL

The base steels used throughout this investigation are summarised in Table 3.1, together with their chemical analysis. In general, the submerged arc and electron beam welding described in the following investigations was carried out on plate B (25mm), and manual metal arc welding was carried out on plate C (12.5mm). Plate A and Plates D to G were only used for specific investigations i.e. Plate A for the study of preheat, and Plates D to G for the investigation into plate deoxidation practice, both described in Chapter 8.

Table 3.1: COMPOSITIONS OF BASE STEELS

CODE	PLATE DESCRIPTION	ELEMENT WEIGHT % C	S	P	Si	Mn	Ni	Cr	Mo	V	Cu	Nb	Ti	Al	N2 PPM	O2 PPM
A	C-Mn-Nb Al TREATED Si KILLED	0.16	0.022	0.018	0.42	1.43	0.06	0.07	0.01	0.01	0.06	0.038	0.01	0.02	70	51
B	C-Mn Al TREATED Si KILLED	0.14	0.006	0.008	0.24	1.24	0.01	0.01	0.01	0.01	0.01	0.005	0.01	0.04	53	30
C	C-Mn Al TREATED Si KILLED	0.15	0.025	0.011	0.32	1.02	0.02	0.04	0.01	0.01	0.02	0.005	0.01	0.048	66	30
D	C-Mn-Nb rimming	0.17	0.018	0.016	0.01	1.37	0.03	0.06	0.02	0.01	0.14	0.031	0.003	0.007	23	162
E	C-Mn-Nb Si KILLED	0.15	0.014	0.019	0.38	1.21	0.09	0.10	0.05	0.01	0.22	0.029	0.005	0.005	50	132
F	C-Mn-Nb Si KILLED Al TREATED (LOW Al)	0.19	0.023	0.036	0.37	1.43	0.08	0.10	0.02	0.01	0.18	0.035	0.007	0.052	50	30
G	C-Mn-Nb Si KILLED Al TREATED (HIGH Al)	0.16	0.017	0.012	0.40	1.30	0.03	0.02	0.01	0.01	0.01	0.038	0.004	0.09	53	32

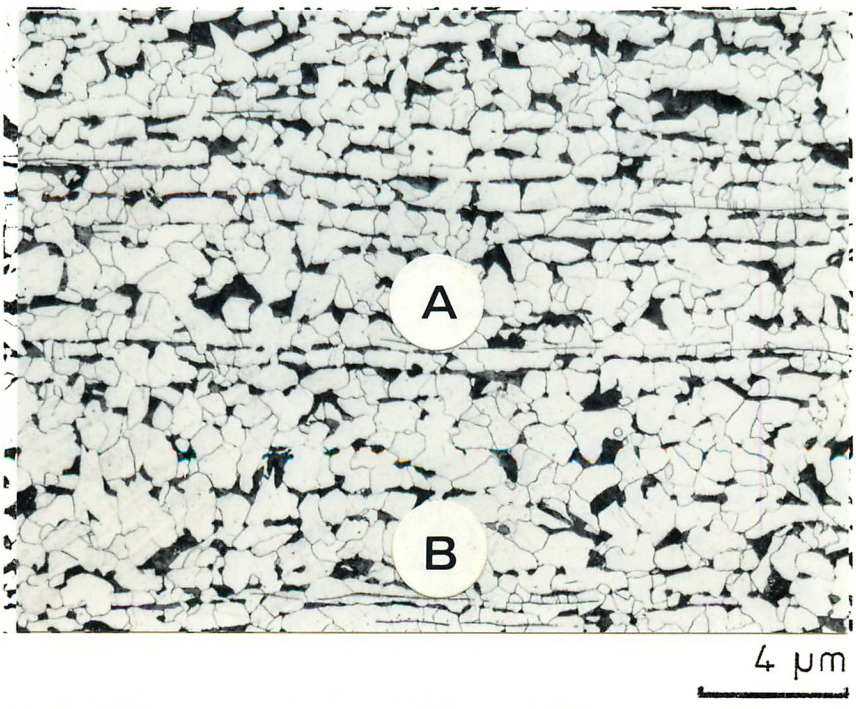

Fig.3.1 Typical microstructure of the base steels considered in this investigation (Plate B). A banded ferrite/pearlite constituent predominates. Several manganese sulphide stringer inclusions are also present eg at A and B.

A typical microstructure of these plates is shown in Fig. 3.1, which shows a banded ferrite/pearlite constituent and the presence of several manganese sulphide stringer inclusions. The compositions of these steels falls into two groups: C-Mn and C-Mn-Nb, and are typical of the compositions encountered in commercial line pipe and shipbuilding steels.

3.2.2. SUBMERGED ARC WELDING

(a) Two pass welds

Tandem submerged arc welding (DC + ve/AC) was carried out on 25mm plate. The joint preparation used is shown in Fig. 3.2. Each panel was 40cm in width and 50 cm in length, ensuring that thermal saturation of the weld deposit did not occur. The standard welding conditions used for the two pass welds are summarised in Table 3.2.

The two principal fluxes which were of interest in this investigation (OPI2ITT and BOC 80R) gave distinctive bead profiles to the weld deposits, which are shown in Figs. 3.3 (a) and (b). Both deposits resulted in 55% dilution with the parent plate. The composition of the four welds deposited in this manner (Welds SA, 1,2, 4 and 5) are given in Table 3.3.

(b) Single pass (bead in groove) welds

For comparative studies, such as the investigation into the effect of manganese in submerged arc weld metal, single pass (ie bead in groove) welds were prepared. This procedure gave closer control over the overall dilution, and the joint preparation employed is shown in Fig. 3.4.

The welding conditions used for the tandem submerged arc welding (DC + ve/AC) were identical to those used for the 2nd pass of the two pass welds described above and are given in Table 3.2. The chemical composition of these welds are also given in Table 3.2. A typical macrostructure of the bead-in-groove welds is shown in Fig. 3.5.

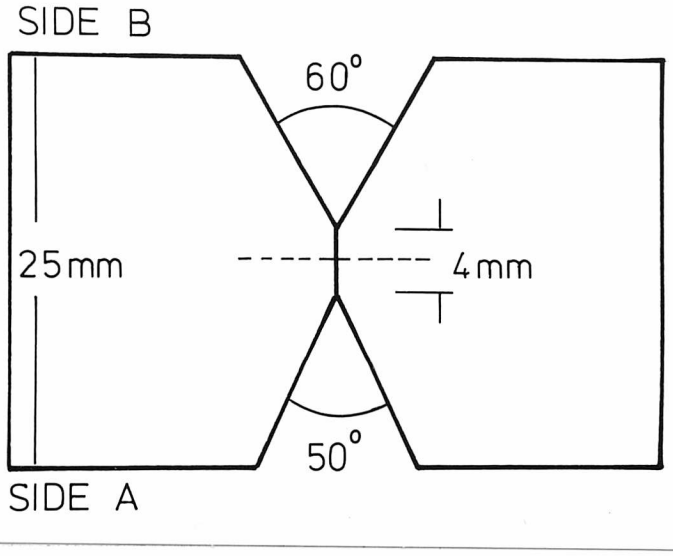

Fig.3.2 Joint preparation for two pass submerged arc welding

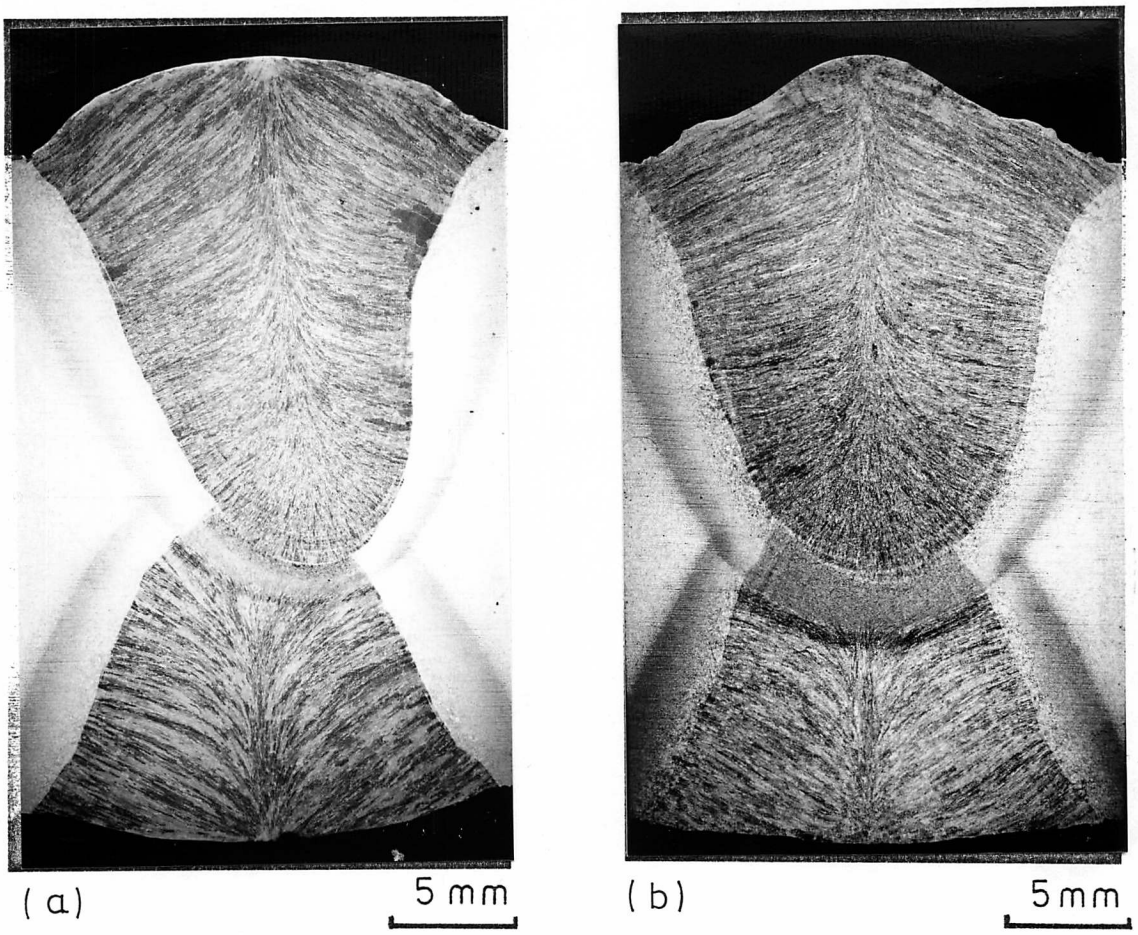

Fig.3.3 (a) and (b)
Macrostructure of submerged arc welds deposited using OP121TT (a) and BOC 80R (b) fluxes respectively.

Table 3.2 Welding conditions for two pass submerged arc deposits.

PROCESS	TANDEM SUBMERGED ARC DC+ ve / AC 25 mm INTER ELECTRODE SPACING : 30 mm ELECTRODE EXTENSION : 40° TRAIL
VOLTAGE	1st PASS 30 40 V 2nd PASS 30 40 V
CURRENT	1st PASS 750 800 A 2nd PASS 950 840 A
TRAVEL SPEED	1st PASS 800 mm/min 2nd PASS 760 mm / min
HEAT INPUT	1st PASS 4·1 kJ/mm 2nd PASS 4·9 kJ/mm
WIRE	4 mm DIAMETER COPPER COATED
PREHEAT	~20° C
INTERPASS	~20° C
FLUX	OERLIKON OP121TT DRIED AT 300° C FOR 30 mins. STORED AT 150° C
	BOC 80R STORED AT 150°C FOR 1 hr.

Table 3.3 Composition of submerged arc weld deposits.

S. A. CODE	DESCRIPTION	ELEMENT WEIGHT %													O_2 ppm	N ppm
		C	S	P	Si	Mn	Ni	Cr	Mo	V	Cu	Nb	Ti	Al		
1	S3 / Mo / 80	.12	.007	.007	.40	1.26	.04	.03	.24	<.01	.07	<.005	<.003	.018	675	89
2		.12	.008	.007	.41	1.26	.03	.03	.21	<.01	.07	<.005	<.003	.019	623	69
3		.11	.005	.006	.28	1.28	.02	.02	.20	<.01	.07	<.005	<.003	.018	656	65
4	S3 / Mo / 121	.14	.007	.010	.30	1.30	.04	.04	.25	<.01	.08.	<.005	<.003	.025	246	68
5		.13	.005	.010	.28	1.28	.04	.04	.25	<.01	.08	<.005	<.003	.021	239	70
6		.12	.005	.007	.24	1.30	.03	.03	.22	<.01	.08	<.005	<.003	.021	238	100
7	S1 / Mo / 121	.12	.006	.009	.17	1.04	.03	.03	.18	<.01	.13	<.005	<.003	.026	291	50
8	S1 / Mo / 80	.12	.011	.008	.24	1.05	.03	.03	.17	<.01	.11	<.005	<.003	.020	482	100
9	S4 / Mo / 121	.14	.006	.011	.26	1.50	.03	.03	.15	<.01	.07	<.005	<.003	.026	205	60
10	S4 / Mo / 80	.13	.010	.010	.33	1.43	.03	.03	.15	<.01	.06	<.005	<.003	.019	359	62
11	S1 / 121	.10	.008	.009	.15	.91	.01	.02	<.01	<.01	.04	<.005	<.003	.020	312	40
12	S1 / 80	.11	.011	.009	.28	.89	.02	.02	<.01	<.01	.04	<.005	<.003	.018	629	113
13	S4 / 121	.13	.011	.013	.18	1.43	.02	.03	<.01	<.01	.13	<.005	<.003	.018	237	48
14	S4 / 80	.12	.013	.012	.29	1.44	.02	.03	<.01	<.01	.12	.005	<.003	.016	528	55

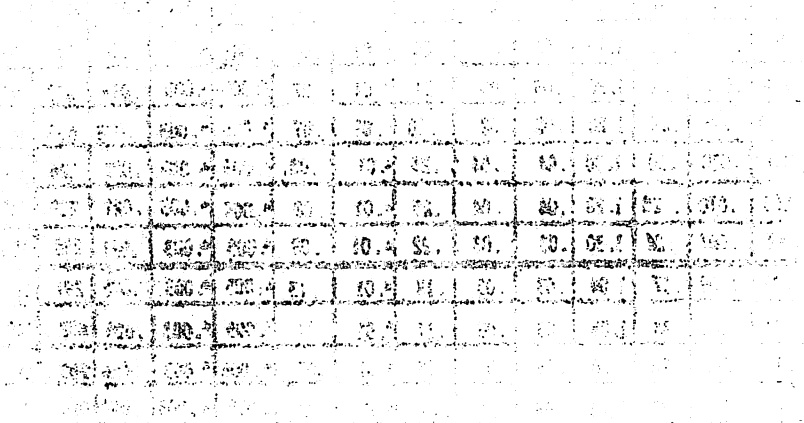

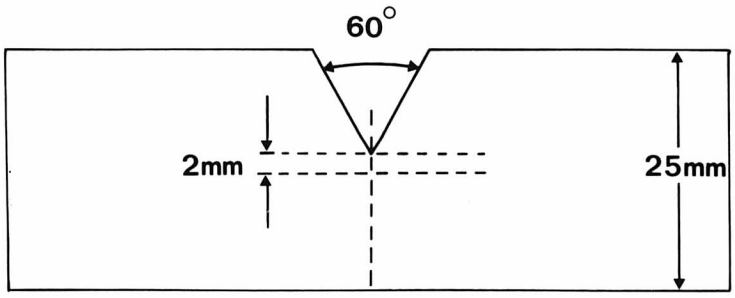

Fig.3.4 Joint preparation for one pass submerged arc welding.

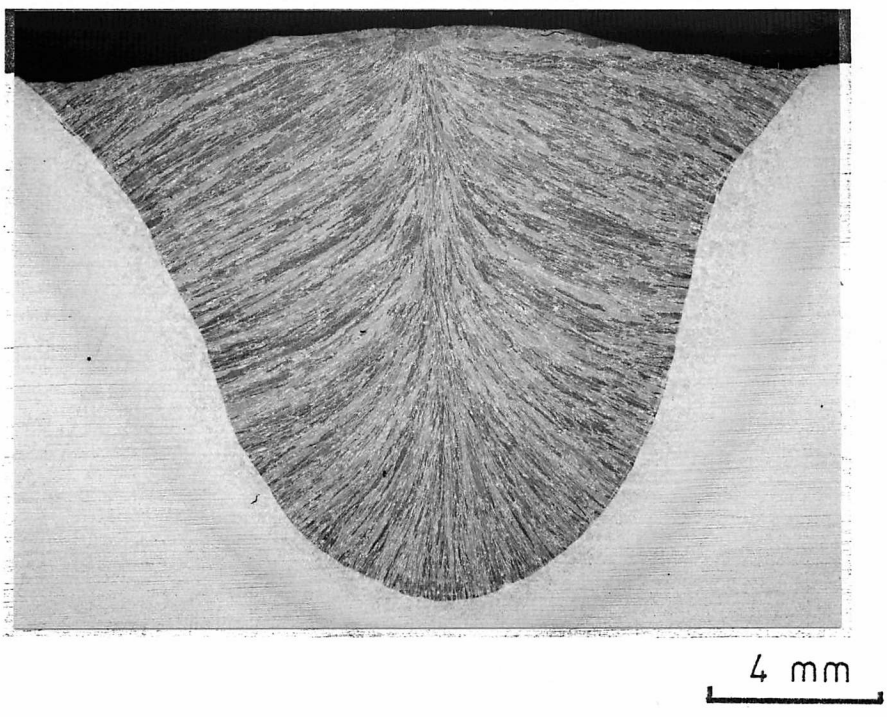

Fig.3.5 Macrostructure of one pass submerged arc weld deposits.

(c)Tungsten-inert-gas (T.I.G.) remelting and quenching of submerged arc welds

The procedure of T.I.G. remelting and quenching of submerged arc weld deposits was employed in this study as a means of following microstructural development in submerged arc welds. Previous work at the Welding Institute on direct quenching of submerged arc deposits had proved unsuccessful, due to the experimental difficulties involved. Subsequently, however, this has been achieved in this investigation and is described in the next section.

The complex nature of T.I.G. remelting and quenching requires that the experimental procedure be described in depth.

Two submerged arc welds are considered in this study - SA 2 and SA 5- which were standard two pass submerged arc welds as described in section (a). From each submerged arc weld two reduced plates were machined from the second pass as shown in Fig. 3.6. A support arm was welded onto the side of reduced panel A, which also served to support the standard thermocouple arrangement used to measure the weld cooling rate.

T.I.G. remelting was carried out along the centre of the original submerged arc weld as described in Fig. 3.7. The deposit and the thermocouple rig were quenched into iced brine as soon as the temperature reached $500^{o}C$. The welding conditions used for the remelting are given in Table 3.4 and the macrostructure of the deposit is shown in Fig. 3.8.

Two T.I.G. remelted panels were prepared in this manner from each of the two original submerged arc deposits - one for microstructural examination and the other for chemical analysis. In the latter case, the composition of the original submerged arc weld was analysed by spark emission at three separate positions along the length of the weld. After remelting, the surface was reground and again, spark emission analysis carried out in the same three

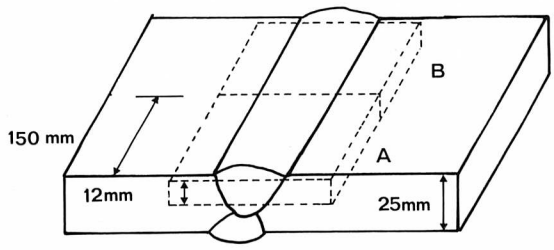

Fig.3.6 Machining diagram for T.I.G. preparation.

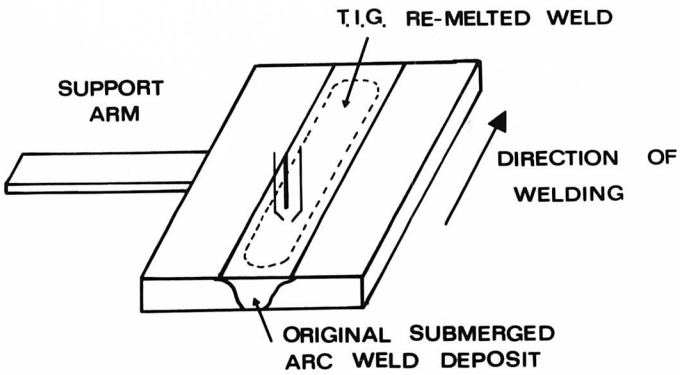

Fig.3.7 Schematic diagram showing T.I.G. remelting.

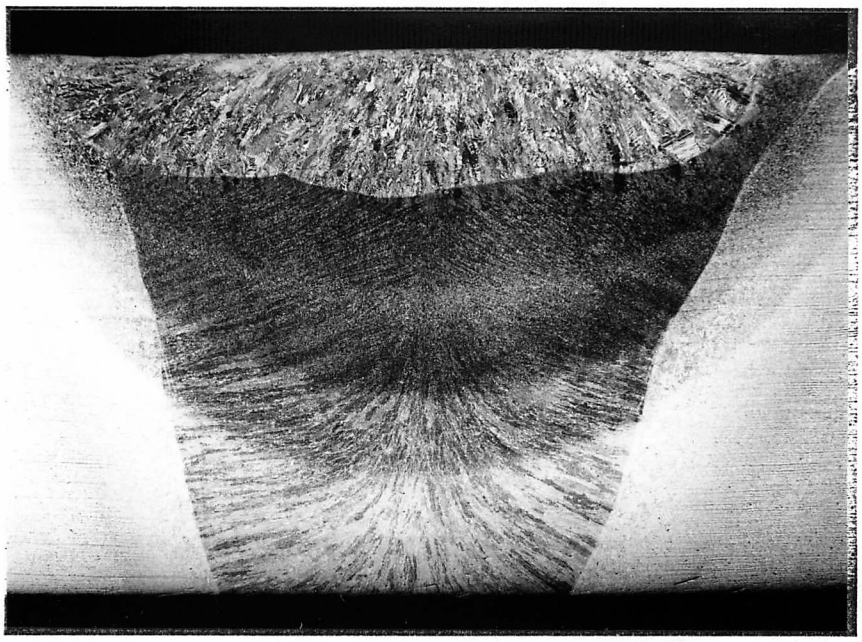

Fig.3.8 Macrostructure of T.I.G. remelted submerged arc weld deposit.

4 mm

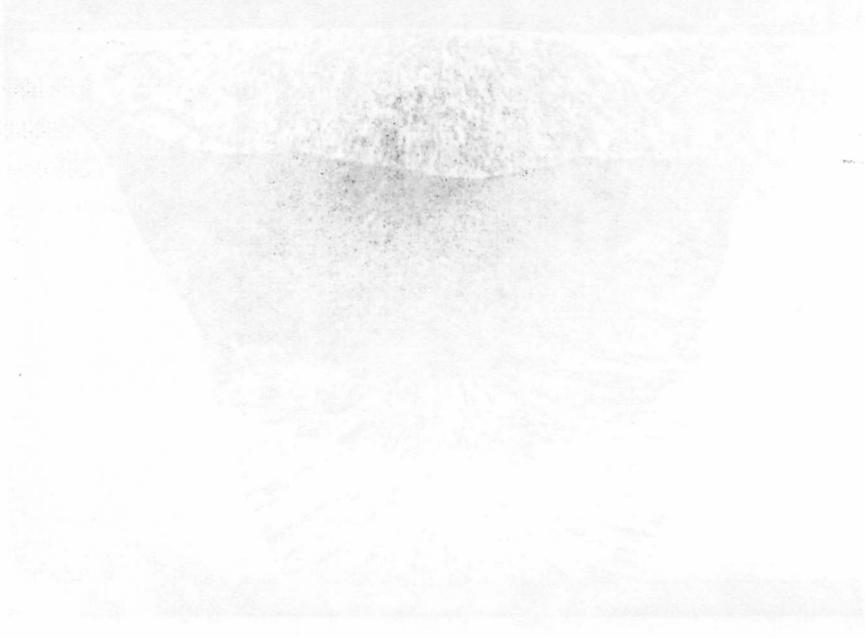

Table 3.4 Welding conditions for T.I.G. remetling of submerged arc deposits.

SHIELDING GAS	He - 10 L / min.
WORKING DISTANCE	2 mm
TORCH ANGLE	70°
TRAVEL SPEED	72 mm/min
CONDITIONS	350 A , 17 V
HEAT INPUT	0·5 kJ/mm

Table 3.5 Composition of weld deposits (SA 2,5) before and after T.I.G. remelting

T.I.G. WELDS		ELEMENT WEIGHT %													O_2	N_2
		C	S	P	Si	Mn	Ni	Cr	Mo	V	Cu	Nb	Ti	Al	ppm	ppm
SA 5	1	.12	.007	.008	.21	1.29	.03	.03	.21	<.01	.07	<.005	<.003	.013	295	73
	2	.12	.007	.008	.23	1.31	.03	.03	.21	<.01	.07	<.005	<.003	.011		
BEFORE	3	.13	.008	.010	.23	1.34	.04	.03	.22	<.01	.08	<.005	.004	.014	305	81
AVERAGE		·12			·22	1·31			·21						300	77
SA 2	1	.12	.010	.007	.33	1.30	.03	.03	.19	<.01	.07	<.005	<.003	.013	487	72
	2	.11	.008	.010	.36	1.32	.03	.03	.20	<.01	.07	<005	<003	.010		
BEFORE	3	.11	.011	.007	.35	1.31	.03	.03	.19	<.01	.07	<005	<003	.011	519	72
AVERAGE		·11			·35	1·31			·19						503	72
SA 5	1	.11	.007	.009	.23	1.24	.03	.03	.22	<.01	.07	<.005	<003	.014	109	64
	2	.11	.008	.010	.25	1.27	.04	.03	.23	<.01	.07	<.005	<003	.014		
AFTER	3	.12	.008	.010	.24	1.22	.04	.03	.22	<.01	.07	<.005	<003	.017	100	80
AVERAGE		·11			·24	1·24			·22						105	72
SA 2	1	.08	.010	.007	.34	1.16	.03	.03	.20	<.01	.06	<.005	<003	.015	219	64
	2	.08	.009	.007	.34	1.29	.03	.03	.19	<.01	.06	<.005	<003	.013		
AFTER	3	.08	.010	.008	.34	1.24	.03	.03	.19	<.01	.06	<005	<003	.014	199	64
AVERAGE		·08			·34	1·23			·19						209	64

positions. Oxygen and nitrogen values were obtained from the original submerged arc deposit and the T.I.G. remelted region in the usual manner. The results of this analysis are given in Table 3.5.

(d) Quenching of submerged arc welds

The experimental procedure adopted in this work is shown schematically in Fig. 3.9. Welding was carried out at a heat input of 1.5 kJ/mm on clean base plate C. The plate geometry and welding conditions are given in Table 3.6. By removing the weldment as the current was switched off, it was possible to release the welding wire by pulling it through the weld crater. The weldment, including the remaining flux, was then quenched into iced brine. Thermal analysis using this experimental approach proved extremely difficult, but the quenching time was estimated to be 4 seconds between 1200°C and 300°C. The actual cooling rate was similar to a weld with a 3 kJ/mm heat input.

An SD3 Mo welding wire and two commerical fluxes (BOC 80R, OP121TT) were employed. The resulting chemical compositions of the weld deposits are given in Table 3.7, which also includes the analysis of the welding wire.

(e) Mechanical properties of submerged arc weld deposits

All the mechanical testing reported in this investigation were carried out at the Welding Institute. Charpy impact and standard Hounsfield tensile specimens were machined from the second pass of as deposited welds, as shown in Fig. 3.10. Tensile testing was carried out at room temperature and Charpy impact values determined in the range -80°C to +80°C. It was beyond the scope of the current investigation to consider a complete study of the mechanical properties of weld metals involving C.O.D. testing and fracture analysis. In this study, Charpy impact properties were used only as a comparative guide to the overall fracture behaviour of a given weld deposit.

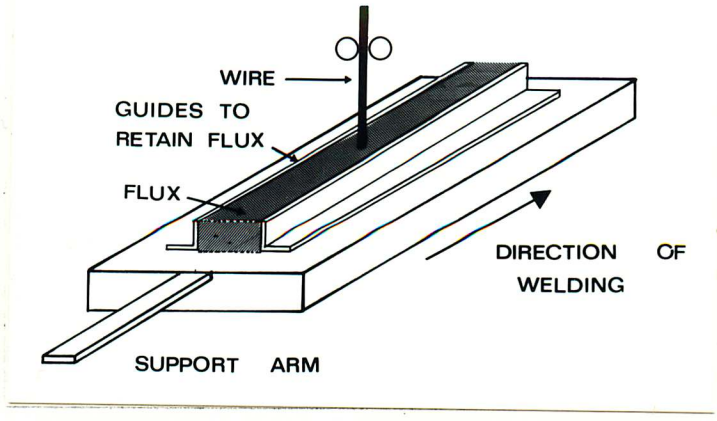

Fig.3.9 Schematic diagram showing the experimental procedure adopted for quenching submerged arc welds.

Table 3.6

Welding conditions for quenched submerged arc weld deposits.

BEAD ON PLATE	10 × 180 × 100 mm
CONDITIONS	30 v, 450 a
TRAVEL SPEED	540 mm/min
HEAT INPUT	1·5 kJ/mm
FLUX	BOC 80R, OP121TT

Table 3.7 Chemical composition for quenched submerged arc welds.

WELD	ELEMENT WEIGHT %													O_2	N_2
	C	S	P	Si	Mn	Ni	Cr	Mo	V	Cu	Nb	Ti	Al		
SAQ 1	.10	.026	.017	.43	1.22	.06	.06	.22	<.01	.11	<.005	<.003	.017	720	65
SAQ 2	.12	.012	.017	.33	1.14	.07	.07	.22	<.01	.12	<.005	.005	.028	285	71

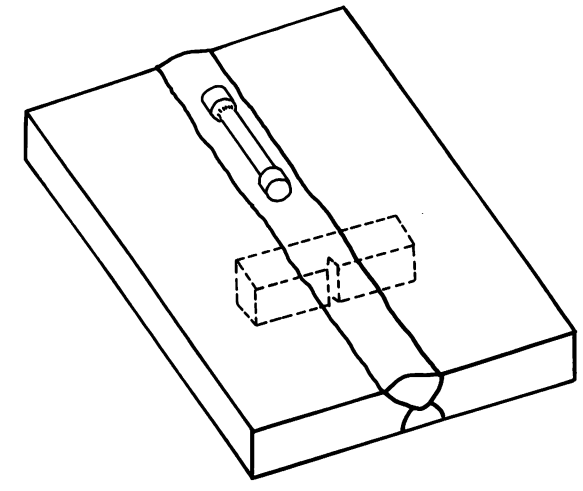

Fig.3.10 Machining diagram for mechanical property specimens.

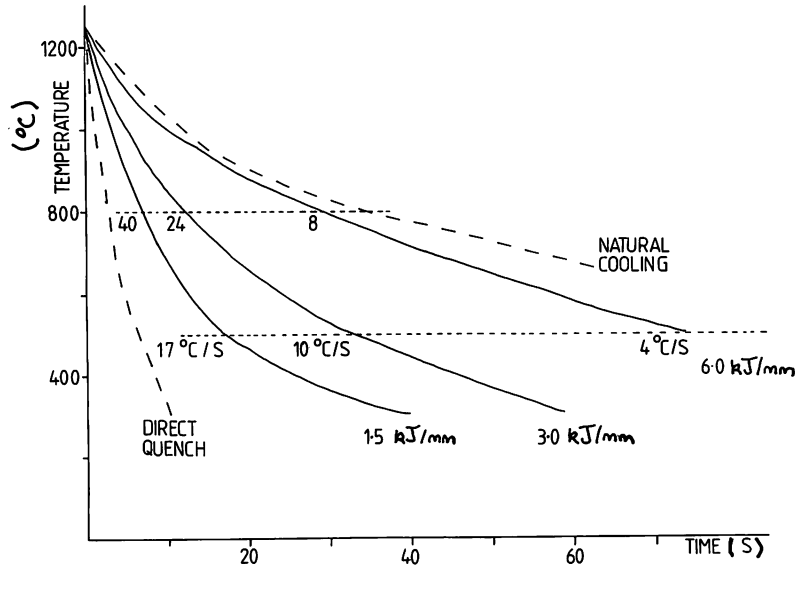

Fig.3.11 Thermal analysis, using W/W 26% Re harpoon thermocouples, of weld deposits at 1.5, 3.0, 6.0 kJ/mm. The cooling rate at 800°C and 500°C is also indicated. For comparison purposes, the dashed lines indicate natural cooling and quenching of solid (3mm) dilatometer specimens.

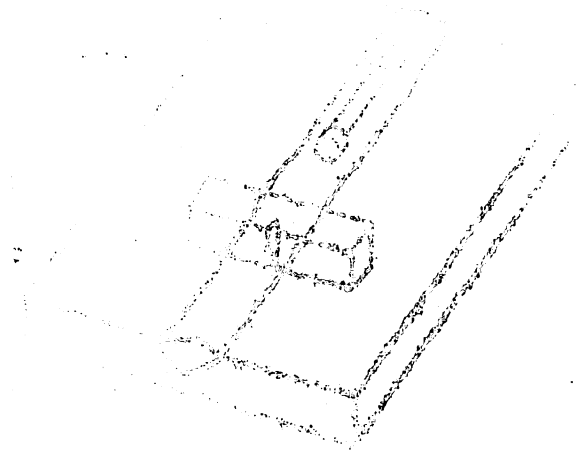

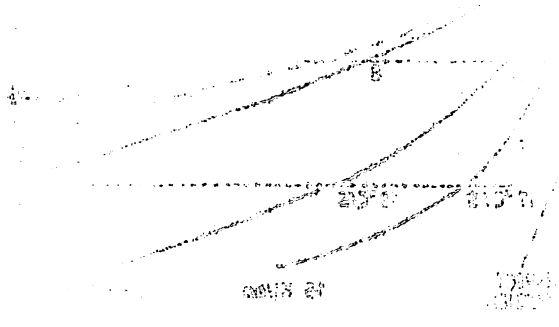

(f) Thermal analysis of weld deposits

Two methods of measuring the weld thermal cycle were employed in this study.

A W/W-26% Re harpoon thermocouple was used to give details of the high temperature (1500°C to 1000°C) region of the weld thermocycle. The resulting cycles for welds deposited at 1.5, 3.0 and 6.0 kJ/mm are shown in Fig. 3.11.

In general, information regarding the weld thermal cycle was obtained using a Pt/Pt -13% Rh harpoon thermocouple, which also gave a derivative trace of temperature with respect to time. Using this method, the low temperature (below 1000°C) region of the weld thermal cycle could be studied and an estimation of the transformation start and finish obtained.

The thermal cycles obtained using these methods under similar conditions (i.e. heat input, plate thickness, etc) showed excellent agreement between the cooling curves obtained as shown in Fig. 3.12.

(g) Specimen preparation from submerged arc weld deposits

Specimens 3 mm diameter by 15 mm in length for isothermal and continuous cooling treatments were machined from submerged arc weld deposits (SA1 and SA 4) as shown in Fig. 3.13). For austenite grain size determinations, 3mm square rods were machined from the same areas, one face being subsequently prepared as a 0.25 μm finish.

3.2.3. MANUAL METAL ARC WELDING

In this investigation, two types of manual metal arc electrode have been investigated. Using the designation adopted by the American Welding Society, they are referred to as E7016 and E7018 type. Both are basic low hydrogen electrodes, extensively used in the shipbuilding, construction and piping industries and represent the so-called high technology field for welding thick plate (40-100 mm). The essential difference in electrode type is that

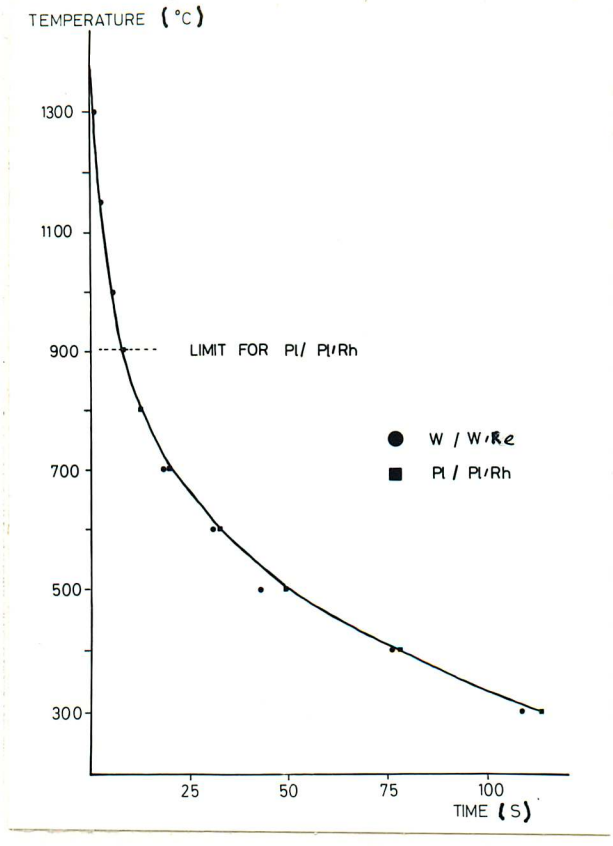

Fig.3.12 Comparison of the thermal cycles obtained using W/W-Re and Pl/Pl-Rh thermocouples at 4.2 kJ/mm.

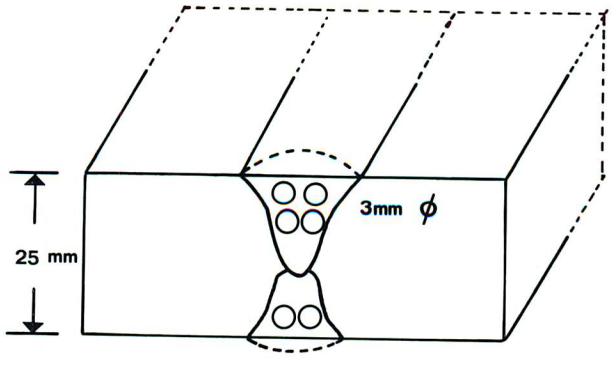

Fig.3.13 Specimen preparation from two pass tandem submerged arc welds.

the E7018 electrodes contain Fe powder additions to the coating, producing high deposition rates and metal recoveries of the order of 130-150%.

The aim of the investigation was to understand the factors affecting the development of microstructure in these two electrode types in as -deposited weld metal. In order to achieve this aim, a technique of partial transformation was employed, so that the sequence of microstructural development could be followed.

Bead-on-plate welds were prepared by depositing the manual metal arc electrode along the centre of clean steel plate. Details of the welding conditions and plate geometry are given in Table 3.8. The welded plate was either air cooled or ice-brine quenched immediately after the welding process was completed. The electrode designation and final composition of the weld deposits is given in Table 3.9.

3.2.4. ELECTRON BEAM WELDING

Electron beam welding was carried out in a vacuum of $\simeq 10^{-4}$ torr. The welding conditions are summarised in Table 3.10 and a typical macrostructure of the welds is given in Fig. 3.14. Previous experience at the Welding Institute has shown that little compositional changes occur during vacuum welding of this kind and the resulting oxygen level would be of the order of 40 ppm. The composition of the welds will reflect those of the base material (Plate B).

The narrow width of this type of weld requires that, for comparison purposes, Charpy impact specimens must be surface notched.

3.2.5. ELECTRO-SLAG WELDING

The electro-slag weld referred to in this study (E.S.1) was provided by the Welding Institute. It had been welded using an S3 wire ($\simeq$ 1.5% Mn) at a heat input of 57 kJ/mm under a basic flux. It thus represents a typical

Table 3.8 Welding conditions for manual metal arc welds.

BEAD ON PLATE	10 mm
CONDITIONS	23 v 215 a
TRAVEL SPEED	170 mm / min
HEAT INPUT	1·75 kJ/ mm
ELECTRODES	E 7018-7016

Table 3.9 Chemical composition of manual metal arc deposits.

CODE	DESCRIPTION	ELEMENT WEIGHT %													O_2	N_2
MMA	OF ELECTRODE	C	S	P	Si	Mn	Ni	Cr	Mo	V	Cu	Nb	Ti	Al	ppm	ppm
1	Tensitrode 55	.08	.015	.015	.38	1.40	.03	.03	.01	.02	.02	.005	.011	.006	244	92
2	Tensitrode 48.30	.08	.010	.009	.43	1.05	.02	.03	.01	.02	.02	.005	.018	.009	271	76
3	Tensitrode 55	.09	.012	.009	.51	1.42	.03	.04	.01	.01	.o2	.005	.010	.015	208	70
4	Phillips 56 S	.10	.008	.010	.29	1.13	.03	.03	.01	.01	.03	.005	.022	.008	270	100
5	Ferrex 7018 LT	.09	.014	.011	.42	1.23	.03	.03	.01	.01	.04	.005	.008	.010	405	80
6	Hytrode 7016	.10	.010	.013	.31	1.13	.03	.03	.o1	.01	.03	.005	.019	.011	307	72
7	EXP. 7018 E1	.09	.013	.013	.50	0.92	.02	.05	.01	.01	.03	.005	.015	.012	381	109
8	EXP. 7018 E3	.09	.011	.013	.48	1.19	.02	.04	.01	.01	.02	.005	.014	.009	337	114
9	EXP. 7018 E5	.09	.011	.013	.52	1.45	.02	.05	.01	.01	.03	.005	.008	.009	312	85
10	E 7016 1	.09	.009	.013	.26	1.35	.02	.03	.01	.01	.03	.005	.016	.011	339	87
11	E 7016 2	.10	.010	.012	.24	1.44	.02	.04	.01	.01	.04	.005	.017	.010	310	113
12	E 7016 3	.010	.010	.013	.24	1.61	.03	.03	.01	.01	.03	.005	.014	.011	303	74
13	7016 1 D	.12	.011	.015	.18	1.33	.05	.04	.02	.01	.09	.009	.017	<.005	266	49
14	7016 1 E	.12	.009	.018	.33	1.38	.07	.07	.03	.01	.14	.015	.017	<.005	229	103
15	7016 1 F	.11	.012	.024	.31	1.48	.05	.06	.02	.01	.11	.013	.018	.012	305	43
16	7016 1 G	.13	.012	.013	.37	1.43	.03	.02	.01	.01	.02	.017	.021	.024	328	52

Table 3.10 Welding conditions for selected electron beam welds.

WELD CODE	VOLTAGE Kv	CURRENT mA	TRAVEL SPEED mm/min	PLATE THICKNESS mm
EB 1	140	32	600	20
EB 2	140	22	600	15
EB 3	140	12	600	10
EB 4	140	20	600	10

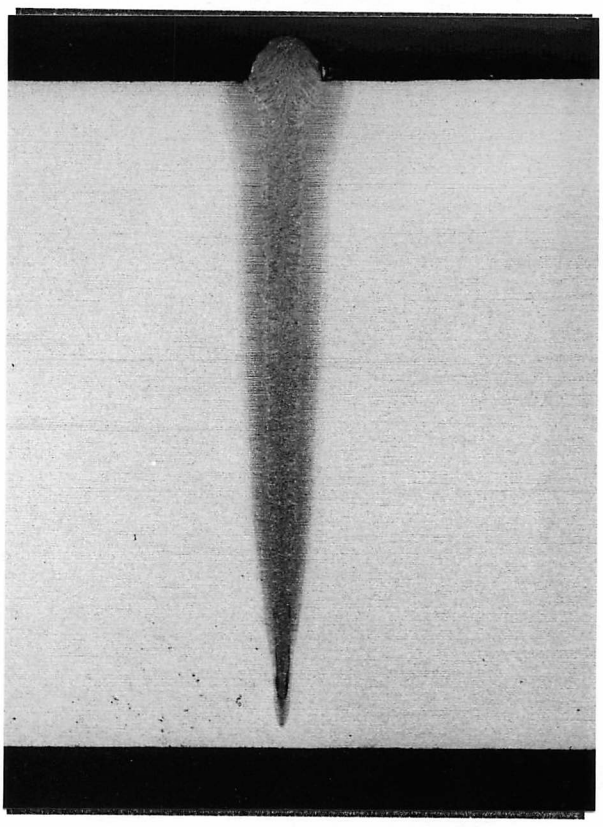

Fig. 3.14 Macrostructure of electron beam weld on 15mm base plate.

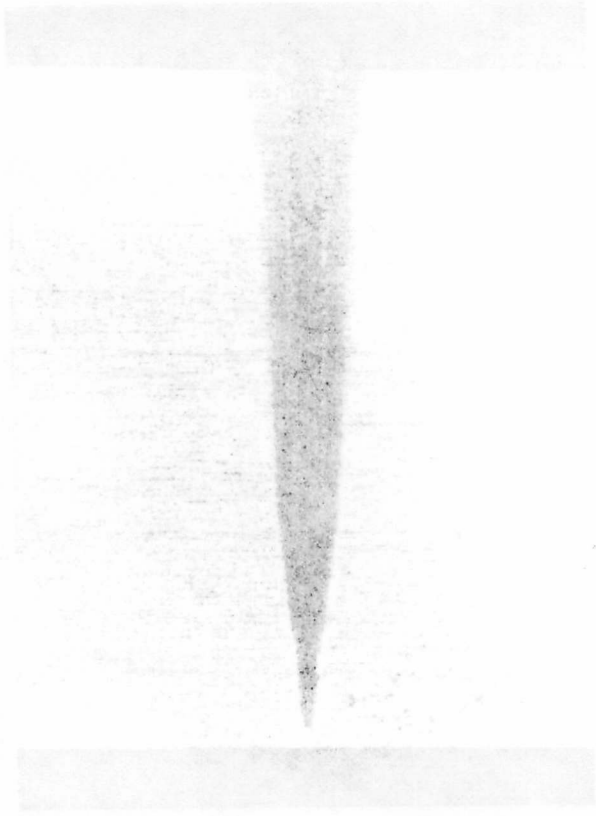

electro-slag deposit with good toughness.

3.3 EXPERIMENTAL TECHNIQUES

3.3.1. PREPARATION OF MODEL ALLOYS

In the following chapters, the role of small, if not trace amounts of second phase particles, are shown to have a pronounced effect on the development of ferritic microstructure. Hence, to clarify the role of the main alloying elements present, it was vital to use high purity base materials. The steels prepared in this investigation for dilatometric analysis were based on 20 pass zone refined iron with a purity of 99.9999%. The purity of the alloying elements (C, Mn, Si, Mo) was guaranteed better than 99.995% in all cases.

65 gm melts were prepared in an Edwards Argon Arc Furnace at a vacuum of 10^{-3} torr under a partial pressure of argon. This resulted in an oxygen level in the final ingot of 10ppm and a corresponding nitrogen level of 4ppm. The ingots were homogenised at 1250°C for 3 days in a sealed quartz tube under a partial pressure of argon. Spark analysis was carried out on each of the ingots and the nominal and actual compositions are given in Table 3.11. The ingots were then hot rolled and swaged to 5mm diameter rod. Specimens for dilatometry were machined from this diameter to completely ensure that no decarborised or oxidised material was sampled.

In order to facilitate an extensive isothermal study, a model steel (designated J) of similar composition to the weld metals investigated was prepared in an Edwards argon arc furnace. This was prepared from electrolytic iron and resulted in the following composition:-

0.13% C, 0.35%Si, 1.19%Mn, 0.25%Mo

with a final oxygen level of $\triangleq$ 50 ppm and nitrogen level of 20 ppm.

Table 3.11 Chemical composition of high purity steels A-D.
All other elements were below the limit of detection.

ALLOY	ELEMENT WEIGHT %							
	NOMINAL				ACTUAL			
	C	Si	Mn	Mo	C	Si	Mn	Mo
A	0·12	0·35	0·6	0·25	0·09	0·35	0·59	0·25
B	"	"	1·1	"	0·14	0·36	1·10	0·27
C	"	"	1·6	"	0·09	0·37	1·57	0·27
D	"	"	2·1	"	0·14	0·37	2·01	0·28

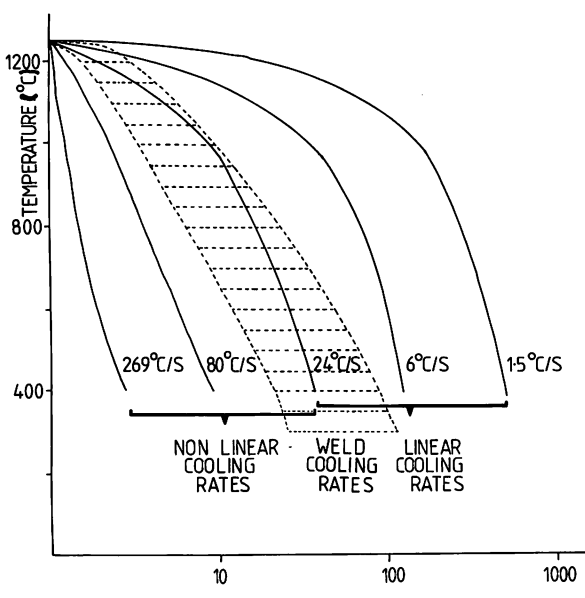

Fig.3.15 Summary of selected cooling cycles employed for the dilatometric analysis. 24°C/S represents the maximum cooling rate at which linear cooling rates could be maintained in the dilatometer. For comparison purposes, dashed lines correspond to weld cooling rates in the range 1.5 to 6.0 kJ/mm of heat input.

3.3.2. DILATOMETRY

All dilatometry was performed on a Theta Industries high speed dilatometer. Two specimen sizes were used, depending on the cooling rate required. For rapid cooling, eg all isothermal studies and continuous cooling rates > 7°C/sec, a hollow cylinder was used (1.5 mm in bore, 3mm in diameter and 15 mm in length). At slower cooling rates solid cylinders could be used (3 mm in diameter and 15 mm in length). To ensure no decarborisation occurred, all specimens were nickel plated, using standard plating solutions. Each specimen was used for only one test.

The essential details of the design and operation of the dilatometer have been described by Ricks (1979). This procedure was used for the isothermal investigations. Similarly, the methods and procedure for determining the Ac_1 + Ac_2 temperatures have been described by Lenel (1980).

For continuous cooling treatments a DATA TRAK PROGRAMME was used to follow a preplotted cooling curve on a rotating drum. This system allowed linear cooling rates from the austenitising temperature to be maintained without the use of the helium quenchant at cooling rates slower than 7°C/S. At cooling rates between 7°C/S and 24°C/S, gas quenchant was needed to maintain linear cooling rates. At faster rates than this, linear cooling could not be maintained, and direct quenching with helium at various flow rates was adopted. These cooling rates are summarised in Fig.3.15.

The thermal analysis carried out in the previous section (3.2) had established cooling curves for various heat inputs of submerged arc welds. These curves were re-plotted on the DATA TRAK PROGRAMME and, following a given austenitising treatment, it was possible to follow precisely the weld cooling cycle, again using the helium quenching at a low flow rate.

It is thus possible to define four types of cooling cycle:

(i) LINEAR COOLING

(ii) ACCELERATED LINEAR COOLING

(iii) PROGRAMMED COOLING (e.g. weld cooling cycles)

(iv) GAS QUENCHING

For cooling cycles (i) and (ii), the start and finish temperatures can be readily measured by an offset technique. In order to estimate the transformation start and finish temperature in cases (iii) and (iv), the dilation must be plotted directly against temperature before the appropriate temperatures can be measured.

No standard method of presenting C.C.T. data has been developed in the literature and, in this work, it was decided arbitrarily to record 5%, 50% and 95% transformation. These quantities could be assessed readily in the optical microscope which was used in subsequent investigations.

3.3.3. ISOTHERMAL HEAT TREATMENT PROCEDURES

Isothermal heat treatments of 3mm diameter rods were carried out in a molten tin bath, following an austenitising treatment of 1250°C for 10 minutes. For these short austenitising treatments the specimens were protected with Bercatect (a commercial ceramic compound) in an argon atmosphere, to ensure no significant decarborisation occurred. Isothermal treatments were interrupted by iced brine quenching in order that the development of microstructure could be followed.

3.3.4. MICROSTRUCTURAL EXAMINATION

(a) Optical metallography

Optical specimens were etched in 2% nital and photographed on either a Zeiss Universal Microscope using Ilford FP4 35 mm film or a Neophot microscope using cut Ilford orthofilm.

(b) Transmission electron microscopy

(1) CARBON EXTRACTION REPLICA PREPARATION

Direct carbon extraction replicas were prepared from lightly etched sections of the welds. The areas not under investigation were covered with lacomit, to ensure that inclusions did not float onto the replica from other parts of the specimen. Replicas were removed in 5% nital.

(2) THIN FOIL PREPARATION

Thin foil specimens were prepared for T.E.M. from 0.25 mm thick discs slit from the welds or heat-treated rods under conditions of flood lubrication. The discs were subsequently ground to 0.1mm thickness and thinned in a twin jet electropolishing unit using a 5% perchloric/95% acetic acid electrolyte at room temperature and 90V. In general, preferential chemical attack occurred at the inclusion/ferrite interface and no ideal polishing conditions could be defined.

Carbon extraction replicas and thin foil specimens were examined in either a Philips EM 400 or EM 300 electron microscope operating at 120 Kv and 100 Kv respectively.

3.3.5 OTHER TECHNIQUES

(a) Determination of austenite grain size

The austenite grain size of as-deposited weld metals was determined by a linear intercept method. Tracings were carried out directly from a ground glass screen of a Neophot miscroscope at a nominal magnification of x 200, to record the bands of proeutectoid ferrite which usually delineates these boundaries. The tracings were subsequently analysed using a Quantimet 720 image analysing computer. The method of thermal etching was used to determine austenite grain size for specimens subject to heat treatment. This involved preparation of one face of a 3mm square rod to a good 0.25μm finish,

sealing the specimen in a silica tube under a partial pressure of argon prior to the selected heat treatment. In most cases, as shown in Fig.3.16, this allowed direct assessment of grain size on the Quantimet 720 image analyser.

For the dilatometric investigation, thermal etching could not be employed, since the attainable vacuum in the specimen area was inadequate, resulting in slight oxidation of the polished surface. This problem was circumvented by adopting a heat-treatment cycle which coated the austenite boundaries with a layer of proeutectoid ferrite. For isothermal heat treatment cycles, this was conveniently achieved by an intermediate hold at 725 °C for thirty seconds, followed by a helium quench. For continuous cooling cycles, interrupting the cooling when 20% transformation had occurred produced a similar effect as shown in Fig.3.17. Grain size was again measured by tracing and the Quantimet 720 analyzer.

In all cases, the actual magnification used was calibrated using a ruled grating at the time of measuring.

(b) Measurement of inclusion size distribution

Widgery (1974) concluded that the most appropriate method available to size weld metal inclusions was that proposed by Ashby and Ebeling (1966). The basic assumption of this method is that all inclusions which touch the plane of polish are extracted onto a carbon extraction replica. This leads directly to two important results, which can be summarised as follows:-

$$N_v(X) = \frac{1}{X} N_a(x) \qquad (1)$$

$$Vv = \frac{2}{3} Aa \qquad (2)$$

where $N_v(x)$ = Number of inclusions of diameter x, per unit volume

X = Diameter of inclusions

$N_a(x)$ = Number of inclusions of diameter x per unit area

Vv = Volume fraction of inclusions

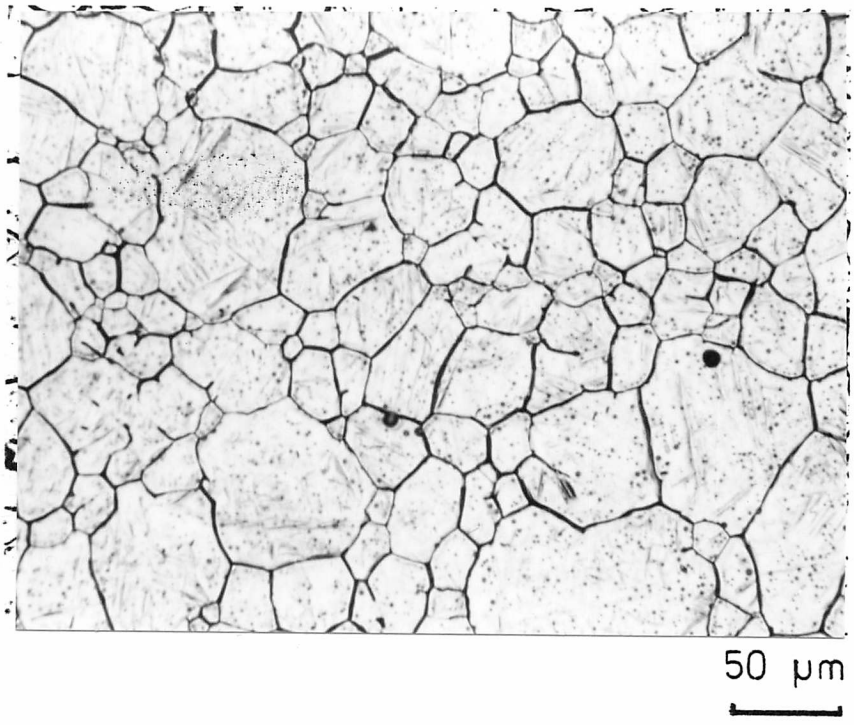

Fig.3.16 Thermally etched austenite grain boundaries in weld SA.1., following heat treatment at 1210°C for 1 hour.

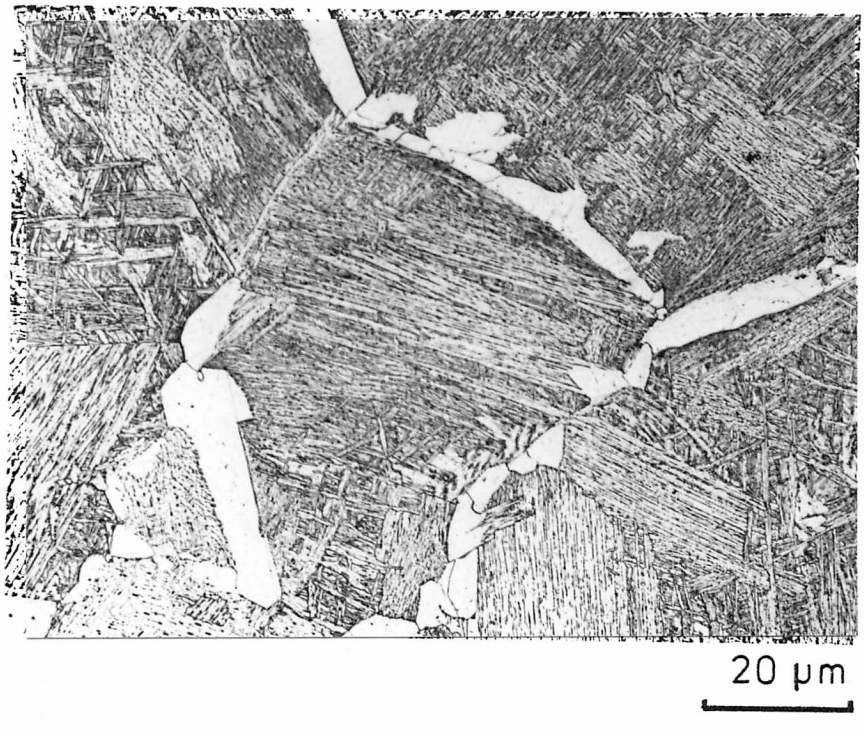

Fig.3.17 Microstructure produced following continuous cooling at 3°C/second, interrrupted by helium quenching. Proeutectoid ferrite has formed at prior austenite grain boundaries with the residual austenite transforming to upper bainite. (Alloy D, heat treatment of 1220°C for 10 minutes).

A'_a = Apparent area fraction of inclusions on a carbon extraction replica.

In this study, 40 fields of view were photographed at a nominal magnification of 4000 x for each of two weld deposits (welds SA1 and SA4). Tracings were made of the inclusions from enlarged prints and the size distribution and apparent area fraction measured directly using a Quantimet 720 image analyser. The actual magnification was calibrated using a ruled grating at the time of measuring.

This method also allowed direct derivation of two nearest-neighbour distances, denoted by Δ_2 and Δ_3, which are defined as the average distance between nearest-neighbour pairs of point particles in a plane and in a volume respectively. Underwood (1970) has detailed the derivation of these values which results in the following equations.

$$\Delta_3 = 0.554\ N_V^{-1/3}$$

$$\Delta_2 = 0.500\ N_a^{-1/2}$$

(c) Quantitative stereology

A Quantimet 720 image analyser fitted with a 2D auto detector monitored by a PDP 11 computer was used to measure and quantify several parameters in this project. Its use for the measurement of austenite grain size and inclusion size distribution is well established and has been briefly described in the previous two sections.

In an investigation into the effect of preheat on submerged arc weld metals, a technique was required to estimate the volume fraction of cementite in the final microstructure. Point counting at high magnification (x 1000), which has been used by several investigators, proved unreliable, since, in many cases, carbide areas were indistinguishable from ferrite grain boundaries. Initial experiments with carbon extraction replicas taken from

lightly etched specimens also proved problematic, since the extraction efficiency varied from area to area and from specimen to specimen. Finally, a deep etching method was employed, which ensures that extraction efficiency was high and relatively uniform throughout the carbon extraction replica. In order to facilitate a direct analysis of transmission electron micrographs, plates were overexposed by a fixed amount, resulting in a sharp black/white contrast between the extracted cementite and the remaining areas. In all, 40 fields of view were examined for each specimen. This technique thus allowed a comparative study between welds, since the absolute values of cementite volume fraction would clearly depend on the degree of etching.

(d) X-ray Determination of Retained Austenite

Transverse sections of welds SA 1 and SA 4 were analysed using a Philips horizontal diffractometer using Co K_α radiation. A typical diffractometer trace is shown in Fig. 3.18, corresponding to 1.5% retained austenite in weld SA4. The method described by Dickson (1969) was employed to quantify the results, as this accounts for any effect of texture in the material.

(e) Chemical Analysis

All bulk analysis referred to in this investigation was carried out at the Welding Institute by x-ray fluorescence. The limits of detection and the standard errors in the measurement of each element are given in Table 3.12. Oxygen and nitrogen were measured simultaneously by a vacuum fusion method.

For the comparative study of bulk composition and matrix composition described in Chapter 7, sparking was carried out on a transverse slice (1mm thick) from welds SA1 and SA4. Discs for electron microscopy were subsequently punched from the centre of the sparked region and prepared for E.D.X. analysis as previously described in section 3.4 Considering the

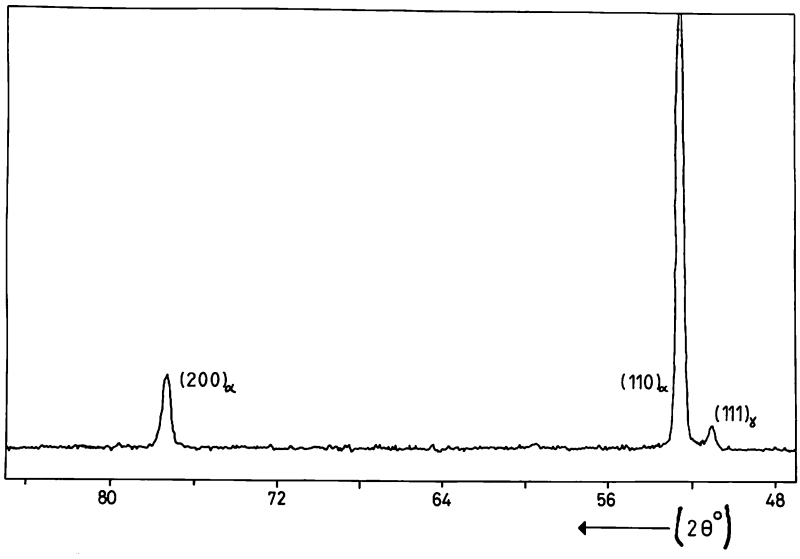

Fig.3.18 Diffractometer trace from weld SA 1 indicating the presence of 1.5% retained austenite.

Table 3.12

Limits of detection and standard errors in the measurement of elements currently employed by the Welding Institute.

X-RAY FLUORESCENCE

	ELEMENT WEIGHT %													
	C	S	P	Si	Mn	Ni	Cr	Mo	V	Cu	Nb	Ti	Al	B
LIMIT	•01	•005	•005	•01	•01	•01	•01	•01	•01	•01	•005	•003	•005	•0005
ERROR	•01	•003	•003	•01	•01	•01	•01	•01	•01	•01	•003	•003	003	•0003

VACUUM FUSION 2700°C

NITROGEN ± 2 % OXYGEN ± 3%

chemical analysis of the submerged arc and manual metal arc deposits as a whole, the values obtained for nickel and chromium were generally constant (0.04%). For all welds deposited on base plates free from microalloying elements (ie. plates B and C), the niobium and vanadium levels in the final weld were less than the limit of detection for those elements. In the case of titantium, the detection limit was lowered from 0.01% to 0.003% during the course of this work. For the manual metal arc deposits, titanium was always significantly above this lower level, whereas, in the submerged arc deposits of special interest (welds SA1 -SA4), it was consistently below the detection limit.

As a general comment, one of the main problems in designing experiments in weld materials is to keep the various compositional factors constant. For example, if two fluxes are selected to deposit different oxygen levels (as in the case of welds SA 1-6), it is usual for this to be accompanied by different manganese and silicon recoveries in the final weld. Fortunately, the two principal fluxes employed in this investigation, BOC 80R and OP121TT, have deposited manganese levels which were closely matching. The silicon levels were generally higher in high oxygen welds (SA1-3), but in the case of the welds used for the dilatometric investigation (SA 3 and SA6), the levels were similar. A further problem is encountered when a given element is systematically increased in a weld deposit. For example, Evans (1980) noted that as the manganese level was increased in manual metal arc welds, a corresponding increase in carbon levels was observed. However, in the investigation described in Chapter 8 into the effect of manganese, no variation of carbon content has been observed in the final weld analysis as manganese is systematically increased.

3.4 SUMMARY

This chapter has described the experimental procedure used throughout this investigation; individual welds will subsequently be referred to by the code given in the list of chemical analysis in Tables 3.3, 3.7 and 3.9.

CHAPTER 4

THE MICROSTRUCTURE OF H.S.L.A. STEEL WELD METALS

4.1 INTRODUCTION

This chapter will describe the microstructure and toughness of selected weld deposits using electron beam, submerged arc and electro-slag welding techniques. All the welds considered were deposited on commercial steel plate using consumables which have been employed in several recent investigations, eg Abson and Dolby (1978), and are all used extensively in commercial practice.

Central to the work described here is the microstructure of two submerged arc welds designated SA1 and SA4. The three welding techniques considered cover a range of cooling rates typical of industrial practice.

A detailed investigation into the fracture characteristics was not carried out in this work, as several studies, eg Levine and Hill (1977), Tweed and Knott (1981), have summarised the main parameters involved. Charpy impact and tensile properties will therefore be only used in a comparative sense to indicate major differences in mechanical properties between the welds.

The literature which deals with the microstructure and toughness of HSLA steel weld metals will also be reviewed. However, due to the large amount of data available, only the literature which is closely related to this work can be discussed. Further, the various microstructural classification schemes which have been proposed to quantify as-deposited weld metal microstructures will be discussed and summarised.

4.2 EXPERIMENTAL TECHNIQUES

The welds considered in this chapter comprise

1) Electron Beam weld EB3

2) Submerged arc weld SA1

3) " SA4

4) Electro Slag weld ES1

Full details of the welding parameters, chemical analysis and consumables used have already been detailed in Chapter 3. Summarising, they represent C/Mn/Si or C/Mn/Si/Mo welds deposited over a range of cooling rates.

4.3 LITERATURE REVIEW

The aim of this literature review is twofold. It discusses the various schemes that have been proposed to quantify weld metal microstructures and, secondly, it reviews the literature which deals with the relationship between microstructure and toughness in H.S.L.A. steel weld metals.

4.3.1. Classification Schemes for Ferrite Weld Metal Microstructures.

In recent years several schemes have been proposed to describe ferrite morphology in as-deposited steel weld metals. They are summarised in Table 4.1 and it should be noted that they are all based on optical microscopy and, in some cases, a point counting technique. Widgery (1974) classified four individual microstructural constituents.

(I) Proeutectoid ferrite

(II) Lamellar component

(III) Acicular ferrite

(IV) Other constituents

Table 4.1

Summary of the classification schemes proposed to describe ferritic weld metal microstructures.

AUTHORS	CLASSIFICATION SCHEME
WIDGERY (1974)	Individual constituents identified as : I) PROEUTECTOID FERRITE II) LAMELLAR COMPONENT III) ACICULAR FERRITE IV) OTHER COSTITUENTS
LEVINE AND HILL (1977)	Overall microstructure classified as : I)CATEGORY I those microstructures containing both grain boundary ferrite and acicular ferrite II)CATEGORY II those microstuctures containing "lath" structures originating from prior austenite grain boundaries
COCHRANE (1977)	Dubé classification I) ALLOTRIOMORPHIC FERRITE II) PRIMARY and SECONDARY FERRITE SIDEPLATES III) INTRAGRANULAR FERRITE SIDEPLATES
ABSON AND DOLBY (1980)	Individual constituents identified as: I) GRAIN BOUNDARY FERRITE II)POLYGONAL FERRITE III)ACICULAR FERRITE IV)FERRITE WITH ALIGNED M - A - C V) FERRITE- CARBIDE AGGREGATE

He showed that if microstructures were classified into these groups, the proportions of these constituents could be simply and consistently related to toughness properties.

In contrast, Levine and Hill (1977) chose to discuss the overall microstructure of a weld deposit by dividing them into two groups: Category I microstructures consisted of those weld deposits containing grain boundary ferrite and acicular ferrite: Category II microstructure comprised those containing predominantly a lath morphology originating from a prior austenite grain boundary.

Cochrane (1977) is the only investigator, in this context, to try to relate weld metal microstructures to those structures identified unambiguously in wrought steels. He used the original classification of ferrite morphologies by Dubé et al (1958) and considered :-

(I) Allotriomorphic ferrite

(II) Primary and secondary ferrite sideplates

(III) Intragranular ferrite sideplates

However, this work could not distinguish between primary and secondary sideplates, or uniquely identify the characteristic morphologies of the ferrite allotriomorphs (eg. ferrite sawteeth), as discussed by Aaronson (1962).

More recently, Abson and Dolby (1980) have proposed that a descriptive approach should be adopted, and that the following categories of microstructures should be considered:-

(I) Grain Boundary ferrite

(II) Polygonal ferrite

(III) Acicular ferrite

(IV) Ferrite with aligned M-A-C (martensite-austenite-carbide)

(V) Ferrite-carbide aggregate (including pearlite)

A further classification of the so-called 'microphases' using picral etching at higher magnification was recommended.

Several criticisms of this scheme, which the author was a party to, must be made. Firstly, despite the claims of Almqvist et al (1972) and Garland and Kirkwood (1975), NO accurate assessment of the 'microphase' regions (retained austenite, martensite, cementite) or their identification can be made by optical microscopy. A further relevant point is that since many of the familiar terms, eg proeutectoid ferrite, ferrite sideplates, are now omitted in the scheme, this must lead to further confusion in semantics and terminology, which already abounds in welding literature. It thus remains to be shown if this scheme, with all its sub-divisions of microstructure, can be used to describe ferrite weld metals accurately.

In addition to the work already discussed, welding literature is full of purely descriptive terms which have been applied to ferrite microstructure. Ito and Nakanishi (1976) use the term "fine lath-like structures" to describe the microstructure European authors commonly call acicular ferrite. Recently, Watson et al (1981) have used the term 'Mackerel Skin' to describe the appearance of ferrite sideplates, which in itself highlights the confusion regarding terminology in the welding literature.

In the past, the term bainite has always produced controversy wherever it has been applied to transformation product in steel. In this context, the study of weld metal microstructures have indeed contributed to this confusion by consistently trying to identify the constituent using optical microscopy. Previous identifications of this microstructural feature remain unclear. The structure pointed out by Cochrane in his review (1977) cannot be distinguished metallographically from the Widmanstatten side plates he also identifies. Similarly, the claim by Abson & Dolby

(1978) to have identified upper bainite with no directionality was not supported by T.E.M. and in this case was almost certainly grain boundary ferrite. (The identification of upper bainite in this chapter was only possible after the work carried out in Chapters 5,6,7).

At this point, it is important to summarise that there are two conflicting requirements in studying weld metal microstructure. There is a commercial need to describe the microstructure of as-deposited weld metal in order that the proportions of the various constituents can be linked with toughness. In this case, the need is that only optical microscopy must be used. Secondly, there is a desire to describe and study weld metal microstructure per se, which is the aim of this investigation . In the latter case, it is essential to use every available technique.

4.3.2. The Microstructure and Toughness of As-Deposited H.S.L.A. steel weld metals

(a) INTRODUCTION

In attempting a literature survey of this kind, it must be recognised that it would be impossible to be completely exhaustive. Japanese work alone in this field eg. Sakaki (1959); Ito & Nakanishi (1976), represents a broad base on which a review could be written. Thus, the most constructive method of assessing the large volume of data available is to consider the various reviews which have been written in recent years.

It is also instructive to list the problems that are associated with the task of correlating information on microstructure and toughness in HSLA steel weld metal. This can be conveniently divided into three groups:-

(I) Communication Variables

(II) Experimental Variables

(III) Metallurgical Variables

Dolby (1976) has highlighted the first two points by showing that depending upon which toughness parameters are selected (eg. 27J transition temperature or absorbed energy at a fixed temperature), different trends in behaviour can be recorded. In this context, some authors eg. Taylor (1981) report 'lower bound' impact properties when comparing Charpy impact data. This method must be considered a more accurate guide to the mechanical properties of a particular weld than those based on simple transition curves. Also in this category are the problems associated with the description and quantification of the various microstructural features, which have been discussed in the previous section.

Experimental variables include details such as the many configurations from which impact specimens can be removed from a given weld deposit. For example, specimens removed from the root regions of welds (where the parent plate dilution is very high) would be expected to have different mechanical properties from the surface regions (where the parent plate dilution is very low).

In this study, as far as possible, the communication and experimental variables have been kept constant. Microstructure of as-deposited welds has been classified according to the scheme suggested by Widgery (1974), and impact properties are reported as a standard Charpy transition curve.

Obviously, the effect of metallurgical variables are of greatest concern in this work, and their review occupies the greatest proportion of this text. There are a number of ways in which data relating to weld metal toughness can be reviewed, for example

(I) By the fracture mechanism operating eg. Dolby (1976)

(II) By the role of alloying element eg. Ito & Nakanishi (1976)

(III) By the role of microstructure eg. Widgery (1974)

With following work in mind, it was decided that initially, an overall review, based closely on the review by Dolby (1976), should be given before specific topics, eg. the role of manganese, were considered. Dolby's review centred on examining the factors controlling (or promoting) cleavage resistance in weld metals. He conveniently summarised these effects as illustrated in Fig. 4.1, which shows the role of the major alloying elements in promoting cleavage resistance in weld metals. It should also be noted that implicit in increasing the main alloying elements, eg. Ni or Mo, is that an increase in the fine interlocking acicular ferrite microstructure is also produced.

This model predicts three regimes of behaviour, depending on the heat input of the weld deposit as shown in Fig.4.2. At low heat inputs (where toughness is usually highest), the high toughness (at A) at low alloying element concentrations was attributed to the beneficial effects of the low yield strength. Toughness is not improved with increasing alloying element from this point (towards B) until a significant improvement in microstructure occurs (ie. a larger proportion of acicular ferrite is produced). The maximum value of toughness (at C) is generally obtained when 90% of the microstructure is comprised of the fined grained acicular ferrite microstructure. Over this value, toughness again falls off, since no further improvement in microstructure occurs and the alloying elements will serve only to increase the yield strength by solid solution hardening. The validity of this model can be demonstrated by referring to the work of Ito & Nakanishi (1976). Fig. 4.3 shows the effects they observed on toughness by increasing %Mo in submerged arc weld metal. The 3 regions (A,B,C) may be termed 'under alloyed' (A), 'correctly alloyed' (B) and 'over alloyed' (C), where in the latter case, an additional factor could be the promotion of martensite in the microphase regions.

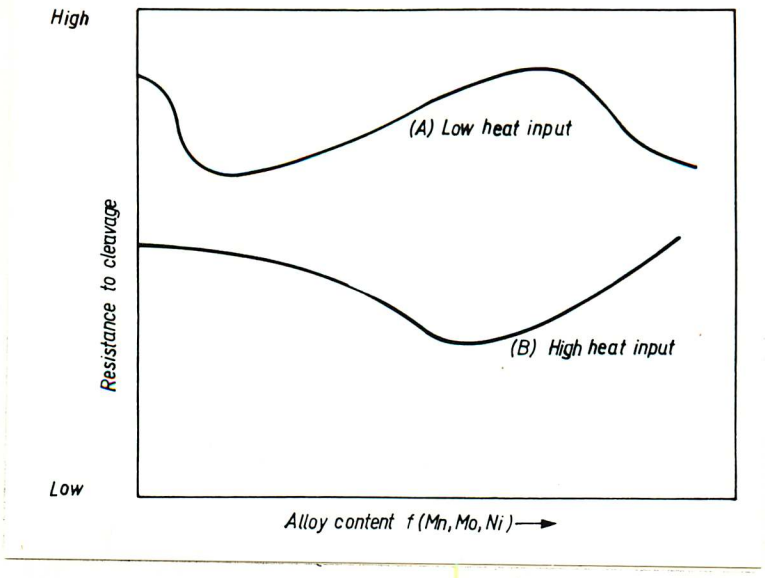

Fig.4.1 The role of alloying elements in promoting resistance to cleavage in weld materials, after Dolby (1976).

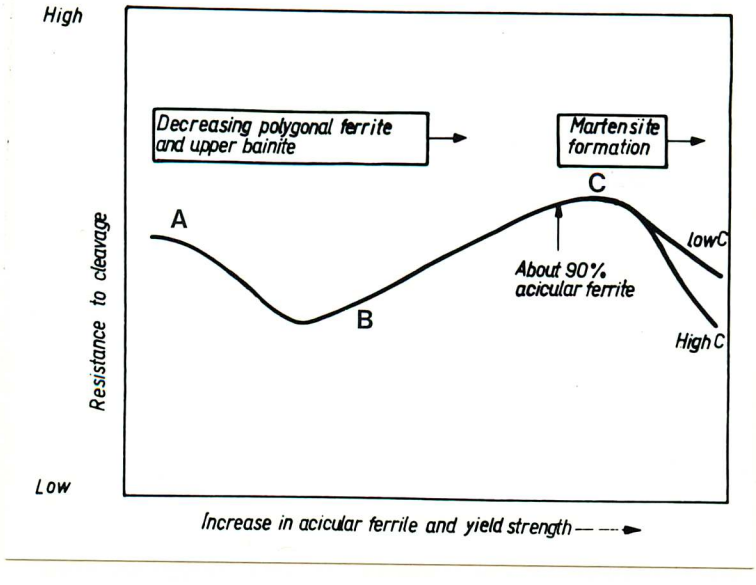

Fig.4.2 The role of microstructure in promoting resistance to cleavage in weld materials, after Dolby (1976).

N.B. the term 'upper bainite' used by Dolby is now recognised (eg Abson & Dolby (1978)) to refer to Widmanstätten ferrite sideplates.

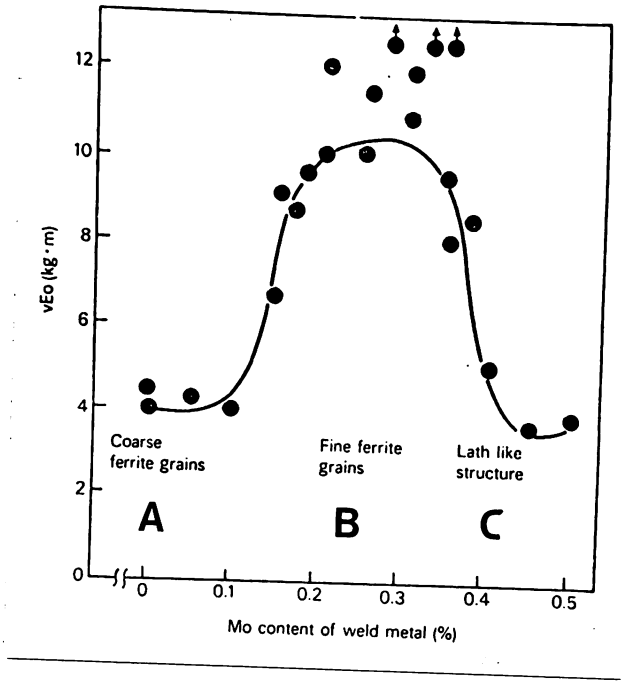

Fig.4.3 The effect of Molybdenum on the impact properties of submerged arc weld metal, after Ito and Nakanishi (1976). (the term vE_o(Kg.m) is an impact parameter).

Dolby also pointed out that at high heat inputs (slow cooling rates), a larger percentage of alloying element would be required to produce the same level of acicular ferrite in the microstructure. This is indicated by a shift to the right for the curve depicting the behaviour of high heat input welds in Fig. 4.1.

(B) THE INFLUENCE OF ALLOYING ELEMENTS ON THE MICROSTRUCTURE AND TOUGHNESS OF H.S.L.A. STEEL WELD METALS.

In this section, the roles of the major alloying elements, eg C, Mn, Si, Mo, Ni, and those elements present in small proportions, the microalloying elements eg. Nb, V, Ti, Al, will be discussed. In view of the overall effect of oxygen in both these types of weld metal, each group must be considered in two sections. Firstly, those elements active in both the deoxidation reactions and also affecting hardenability eg. Mn, Si, Ti and Al and, secondly, those essentially determining only the hardenability of the deposit eg. Ni, Mo and Nb, V.

The complex role of rare-earth additions will not be discussed here, as several reviews eg. North et al (1979), Funakoshi et al (1977) have covered this field. However, it must be pointed out that even the simple alloying elements considered in this review can have complex synergistic effects, which can further complicate the overall behaviour pattern.

(1) DEPOSITS FREE FROM MICROALLOYING ELEMENTS

The alloying elements in this group can influence toughness in three principal ways -:

1) They can modify the yield strength and toughness by changing the microstructure of the deposit.

2) They can modify the yield strength by solid solution hardening.

3) They can modify the oxygen level of the weld deposit by participating in the deoxidation reactions.

Obviously some elements, eg. Mn, Si, can participate in all three mechanisms simultaneously, whereas other elements, eg. Mo and Ni only affect the first two points.

The effect of carbon on the microstructure and toughness of HSLA steel weld metals has received many reviews, eg. Sakaki (1959); Ito & Nakanishi, (1976); Abson, (1978.2). There is general agreement that increasing carbon is detrimental to toughness. For example, Abson (1978) showed a decrease in Charpy transition temperature as the carbon content in submerged arc welds was increased from 0.1 to 0.19 % C. He attributed this to a reduction in grain boundary ferrite and an increased proportion of pools of retained microphases. Similarly, Masumoto and Ozaki (1974) and Masumoto (1976) showed clearly that increasing carbon changed the solidification mode in comparable weld metals and cast steels. This effect was itself thought to have a marked reduction in impact properties.

In simple C-Mn weld deposits, silicon has been shown to have an optimum level for toughness. For example, Tuliani and Farrar (1975) studied the variation of silicon in submerged arc weld metals in the region 0.09% to 0.40%. Above 0.2%, there was a marked increase in the proportion of acicular ferrite microstructure produced. Ito & Nakanishi (1976) detailed an optimum silicon level, depending on the manganese and oxygen levels in the weld deposit, of 0.3%. Abson (1978.2) studied the effects of increased silicon (between 0.23 and 0.56%) in C-Mn-Mo submerged arc weld metal. Over this range, he observed only a slight decrease in toughness, despite recording an apparent improvement in microstructure.

The role of silicon in manual metal arc deposits has recently been reviewed by Boniszewski (1979). He highlighted its complex role in both deoxidation, metal fluidity and effect on microstructure. In simple mild

steel weld metals, he showed an optimum level of 0.4% Si for maximum toughness, which also achieved a low level of oxygen in the weld deposit. In more complex weld metals, eg. 2.5 Ni and 2% Ni /1% Mo electrodes, high silicon levels were shown to be detrimental to toughness.

The role of manganese in promoting good microstructure and toughness in weld metals has been extensively documented. Sakaki (1959), Tuliani et al (1969), (1972) showed clearly that increasing manganese in submerged arc welding in the range 0.4 to 1.4% Mn improved toughness. Similar improvements in microstructure and toughness have been subsequently reported by Widgery (1974), Garland & Kirkwood (1975) and John et al (1976), to select but a few of the reviews on this subject. Ito & Nakanishi (1976) showed that the optimum manganese level was dependent on both the silicon and oxygen levels in the submerged arc welds considered. Recently, Farrar & Watson (1979) have suggested that manganese is indeed the controlling factor in the development of microstructure in submerged arc weld metals. This point will be further discussed in Chapters 6 and 7.

The beneficial effects of manganese have also been established in CO_2 shielded welds, eg Widgery (1974), and manual metal arc welds, eg Boniszewski (1979). Recently, Evans (1980) has shown that in type E7018 manual metal arc electrodes (those with iron powder additions), 1.4% manganese represents the optimum in toughness. In a similar study in electrodes where iron powder was excluded from the coating (type E7016 electrode), Taylor (1981) has shown that 1.7% manganese represents the optimum in toughness. This work also demonstrated that at this level of manganese, the simple C-Mn electrodes can replace the familiar 2.5 Ni electrode in offshore and pressure vessel applications.

Both Mo and Ni have been used extensively to produce strong, tough weld metal in both manual metal arc and submerged arc welding. For

example, Ito & Nakanishi (1976) showed the beneficial effects of Mo in submerged arc weld deposits. In combination with titanium and boron, they showed that the optimum level for toughness was 0.3% Mo. Similarly, Tuliani et al (1969) have shown that increasing Ni in submerged arc welding produces a finer acicular ferrite microstructure which has excellent cleavage resistance.

Summarising, this overall review of the microstructure and toughness of as-deposited weld metal has shown that the major compositional factors promoting toughness have already been established.

(2) DEPOSITS CONTAINING MICROALLOYING ELEMENTS

The use of microalloyed steels (particularly those containing vanadium and niobium) is now well established in both pipeline and general construction steels. The literature which deals with the welding of these steels is both extensive and conflicting.

Research in this field has naturally concentrated on determining the factors affecting toughness in both as-deposited weld metal and the re-heated regions of multi-pass welds. An overall criticism which must be made with respect to microstructural investigations in microalloyed weld metals is that, in general, only optical microscopy has been used in microstructural work. In this sense, a phrase which is frequently found in the literature 'this needs to be confirmed by electron microscopy' highlights the very limited nature of microstructural investigations in this area. Several authors, eg Signes et al., (1979), have speculated and even interpreted results on the basis of precipitation hardening due to these microalloying additions without any direct evidence to support the claims.

Recent reviews on toughness in this area, eg Dolby (1980), Dolby (1981), Abson and Hart (1980) have summarised and extensively reviewed the

data available. They have shown that the effect of the microalloying elements Nb and V depends strongly on the overall alloy composition. In general terms, over the range up to 0.07% Nb and between 0.06 and 0.11% V, they have only a small effect on cleavage resistance (eg. 15°C change in 27J transition temperature) when the overall composition and microstructure of the major alloying elements had been optimised. In reheated weld metal, they detected an increase in 0.1mm COD temperature due to an increase in hardness.

In the field of microstructure, the work of Bosansky et al.(1977) must be emphasised, as the recent reviews mentioned above have omitted to highlight the work. It showed clearly that two mechanisms of precipitation in weld metals are to be expected. Classic interphase precipitation of NbC in polygonal ferrite was detected (in as-deposited weld metal), and secondly, precipitation on dislocations and subgrain boundaries was observed after stress annealing treatments.

The precise role of both titanium and boron in the toughness and development of weld metal microstructure is both complex and unclear. Recently, Koshio (1981), Mori et al. (1981) have all shown that suitable additions of these elements can markedly improve the toughness of submerged arc weld metals. These two authors attribute this improvement to the effective nucleation of acicular ferrite on Ti oxides and the considerable reduction in the free nitrogen available in the weld deposit. In the same context, Funakoshi et al. (1977) have shown that ferrite can nucleate on BN precipitates in rare-earth treated weld deposits.

4.4 RESULTS

The general microstructure of the four as-deposited welds considered are shown in Figs. 4.4-4.7. They are most conveniently considered in order of decreasing cooling rate, starting with the electron beam weld EB 3. The optical microstructure comprises a mixture of upper bainite (at a) and martensite (at b). This can be more clearly seen in Figs. 4.8 and 4.9, which show (a) lath martensite, and (b) autotempered martensite, reflecting the very high cooling rate induced in the welding process. Some intragranular nucleation was observed, as indicated in Fig.4.10, which shows an MnS inclusion associated with intragranular ferrite (at a), which in turn has nucleated laths at (b) and (c).

To assess the toughness of such deposits, surface notching of Charpy specimens is required, and the resultant impact properties are given in Fig. 4.11. This indicates a transition temperature of the order of room temperature, which in terms of HSLA steel weld deposits represents poor toughness.

In contrast, the microstructure of the welds ES1 and SA4 (Figs. 4.5 and 4.7) show the development of what is commonly called an acicular ferrite microstructure. All these microstructures comprise grain boundary nucleated ferrite (eg. at a in Fig.4.5) and a fine intragranular product (eg. b in Fig.4.5). The differences in both ferrite and prior austenite grain size observed in these welds reflects the widely different cooling rates experienced.

A distinctive feature in the electro slag weld (ES1) is the large equiaxed prior austenite grain size and the nucleation of ferrite on twin boundaries, which is detailed in Fig. 4.12(a). Also, in this weld, pearlite can be resolved in the fine regions between the intragranular ferrite, and is shown in Fig. 4.12 (b).

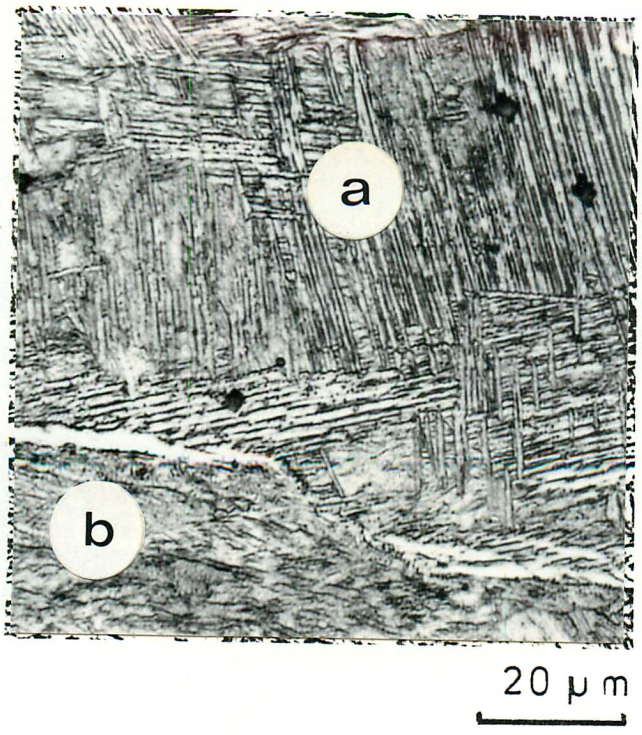

Fig.4.4 Typical microstructure of electron beam weld comprising fine upper bainite and martensite.

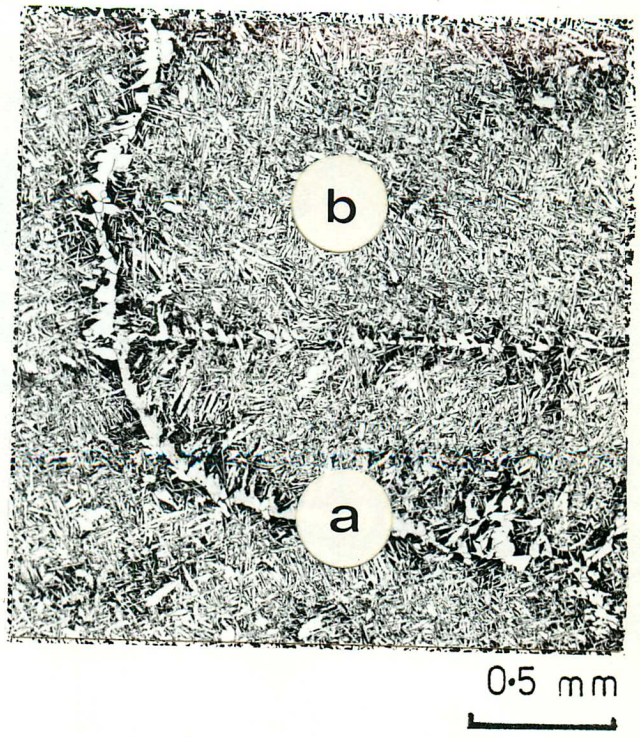

Fig.4.5 Typical microstructure of electro slag weld with a coarse austenite grain size.

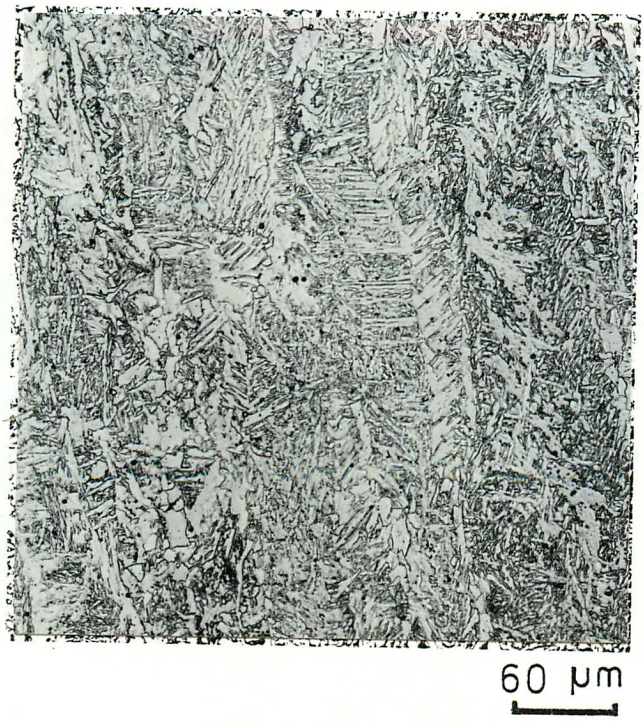

Fig.4.6 General microstructure of high oxygen submerged arc weld SA 1.

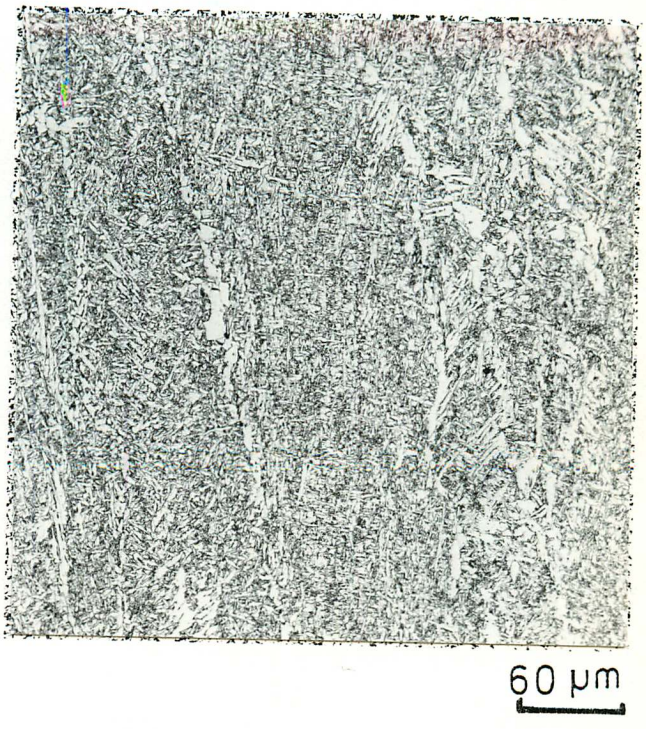

Fig.4.7 General microstructure of medium oxygen submerged arc weld SA 4.

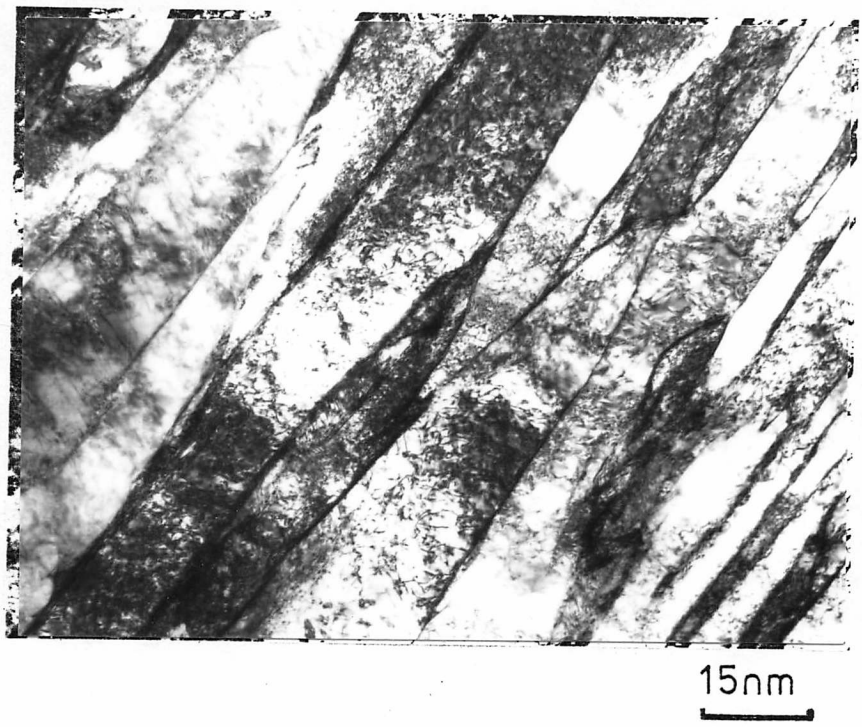

Fig.4.8 . Transmission electron micrograph of lath martensite in electron beam weld EB 3.

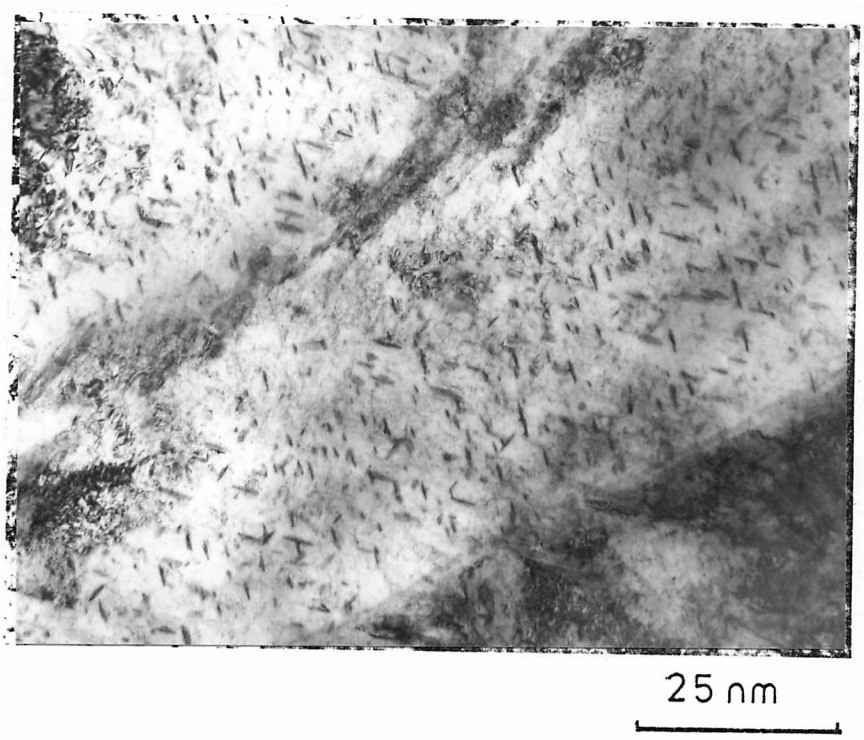

Fig.4.9. Transmission electron micrograph of auto tempered martensite in electron beam weld EB 3.

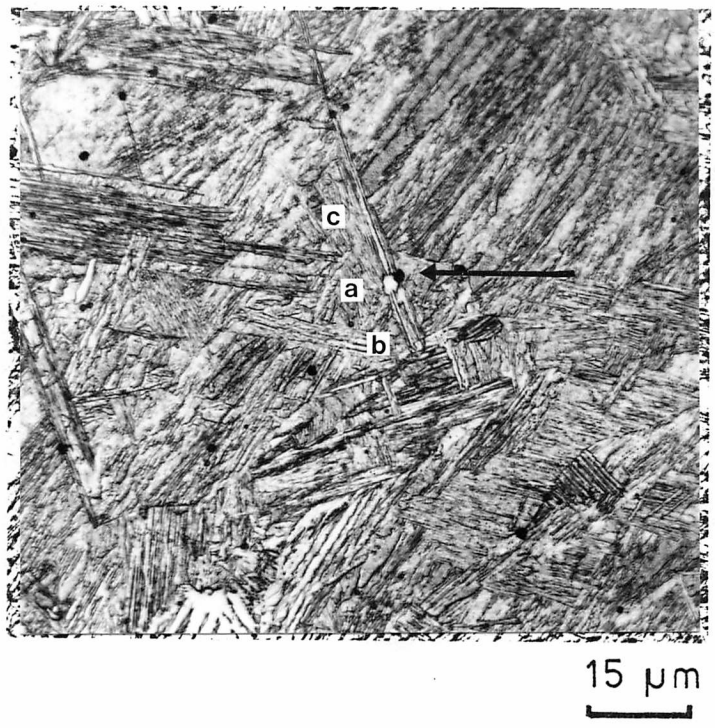

Fig.4.10 Nucleation of ferrite (as arrowed) on manganese sulphide inclusion in electron beam weld. Subsequent laths appear to have nucleated on the ferrite constitutuent.

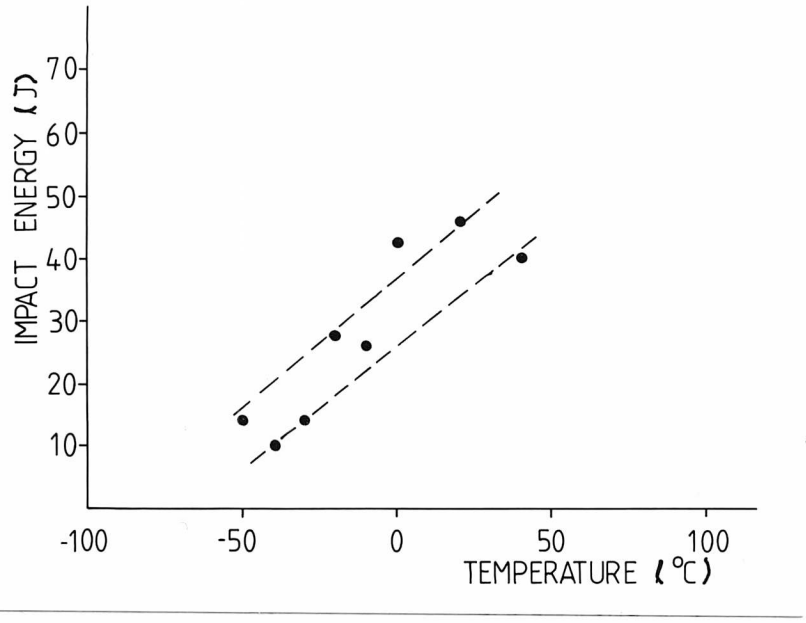

Fig. 4.11 Impact properties for typical electron beam weld EB 3.

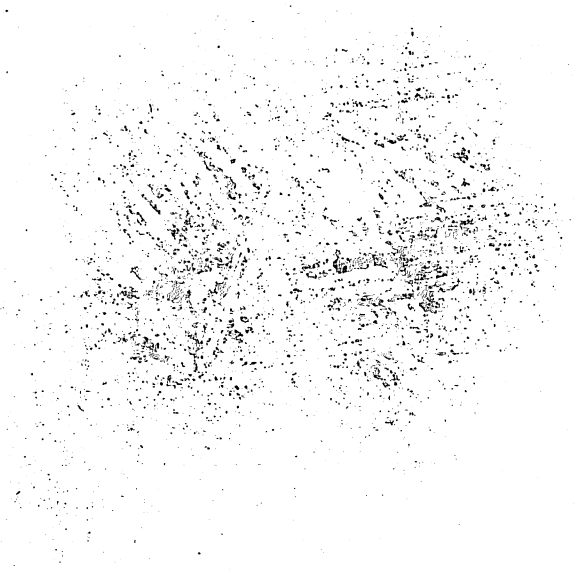

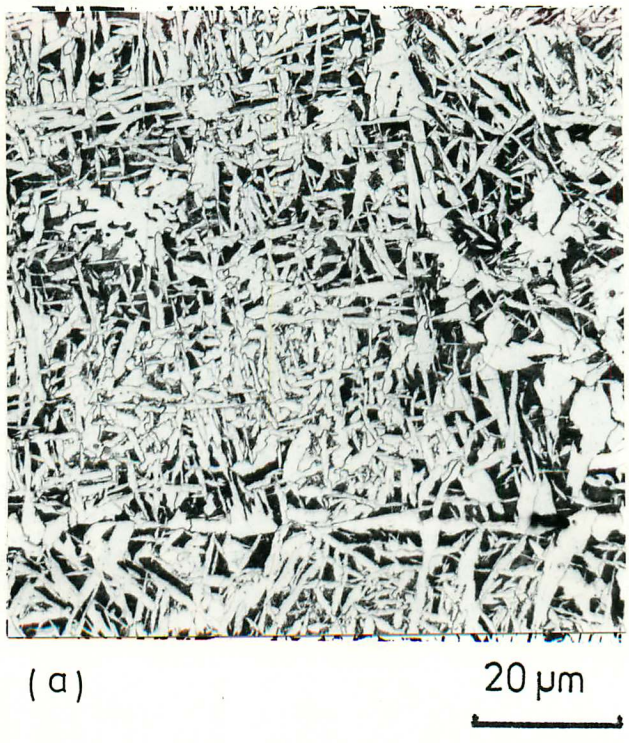

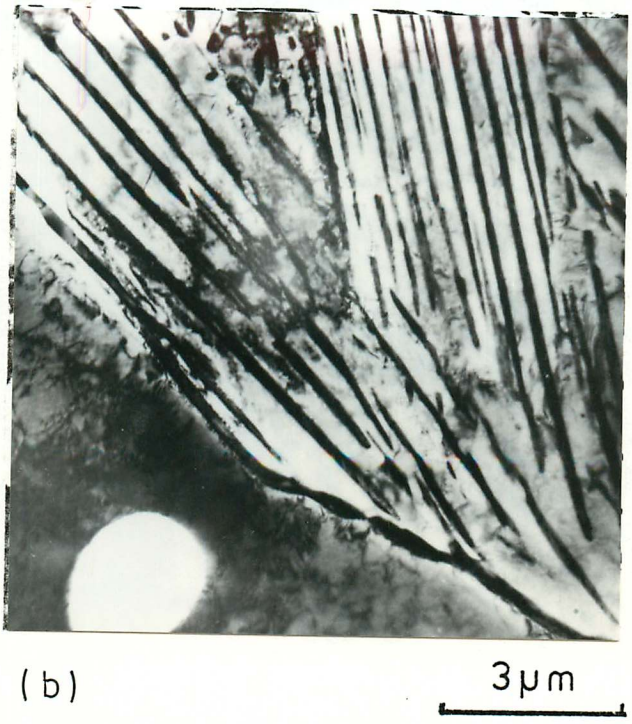

Fig.4. 12. Further microstructural observations of electro slag weld ES1.

(a) Nucleation of ferrite on twin boundaries.

(b) Pearlite in intralath regions.

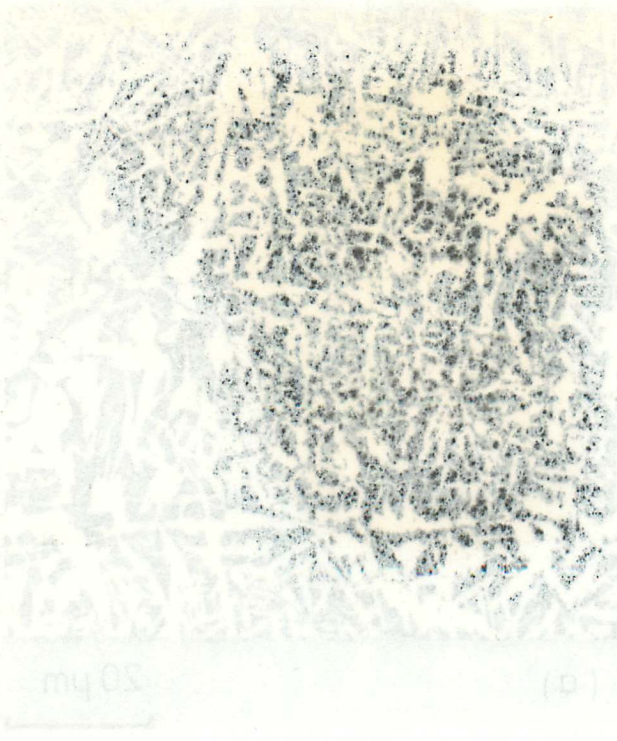

The microstructure and toughness of the two submerged arc welds SA1 and SA 4 will now be described. Figs 4.13 and 4.14 show the fine detail of these two microstructures. SA 1 comprises of predominantly grain boundary nucleated ferrite, whereas SA 4 has a large proportion of fine intragranularly nucleated ferrite. These micrographs also give some indication that inclusions are in some way affecting the development of microstructure. In SA 1 (Fig. 4.13), a large inclusion is present in the prior austenite grain boundary (arrowed), and in SA4, fine interlocking ferrite is associated with an inclusion at (A). It should be emphasised at this point that these welds have almost identical compositions with respect to the main alloying elements present (ie. C, Mn, Si, Mo), with the exception of oxygen, SA 1 having twice the level of the other deposit.

Two features which previous investigations in this field have failed to highlight are also illustrated in Figs. 4.13 and 4.14. Firstly, there is a large difference in prior austenite grain size between the two deposits, which was measured as 66 μm and 120 μm respectively. Further, the average ferrite grain size was much smaller in weld SA4 than SA1. There was no indication whether this difference in prior austenite grain size was the result of solidification effects.

The Charpy impact properties for these two welds are summarised in Fig.4.15. It is clear that the acicular ferrite microstructure (weld SA4) has much better toughness at all temperatures than the predominantly grain boundary nucleated ferrite microstructure of weld SA1. These results show clearly that both the resistance to cleavage fracture and to fracture by microvoid coalescence is higher in the acicular ferrite microstructure (weld SA4). Further, as Table 4.2 shows, the increase in toughness associated with the acicular ferrite microstructure occurs <u>despite the fact</u> that the yield strength increases.

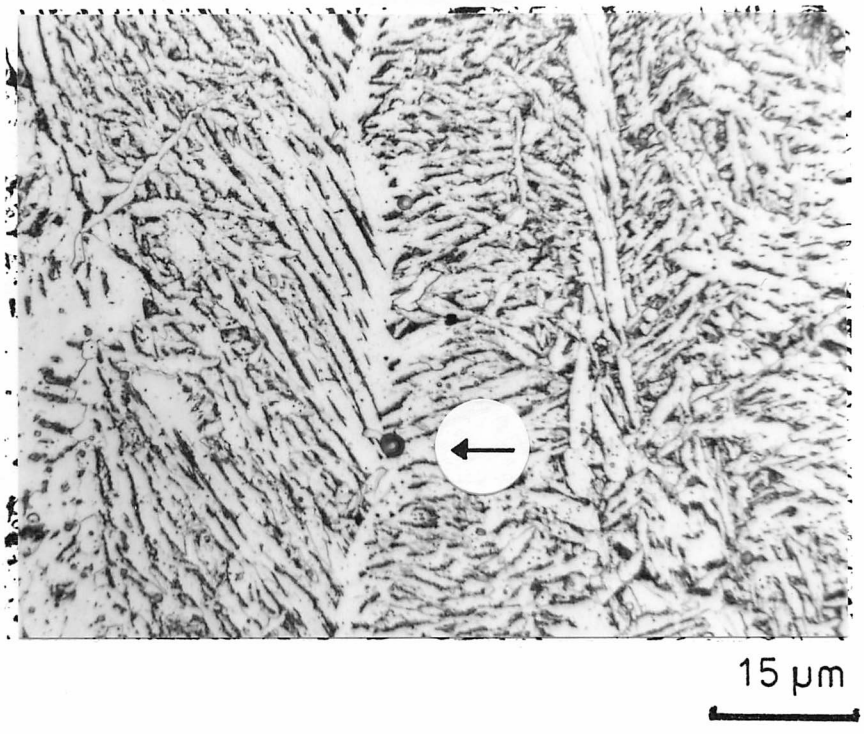

Fig.4.13 Oil emersion photomicrograph of high oxygen weld metal (SA 1), for discussion see text.

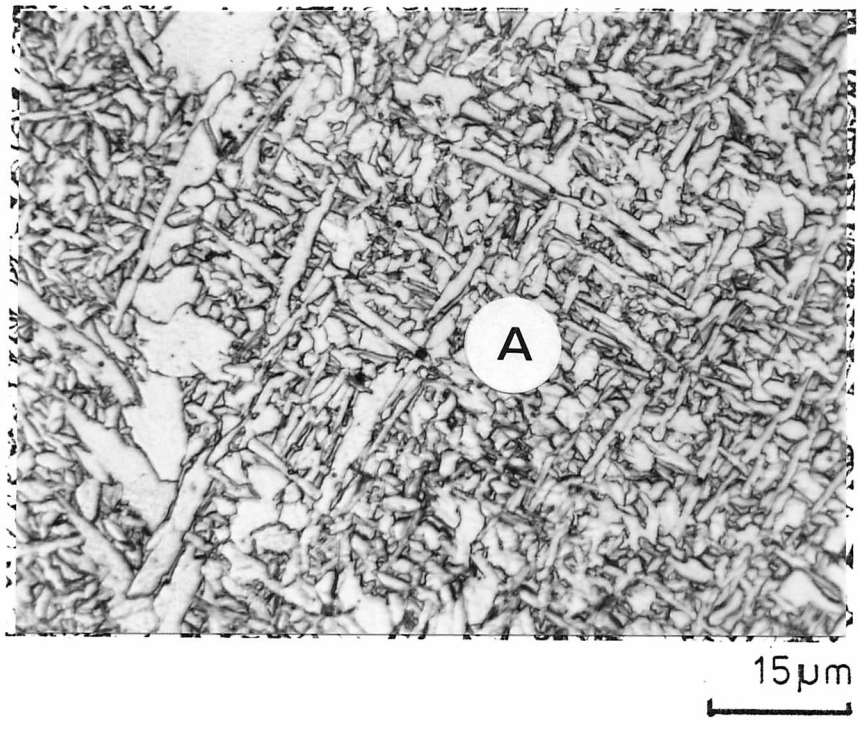

Fig.4.14. Oil emersion photomicrograph of medium oxygen weld metal (SA 4), for discussion see text.

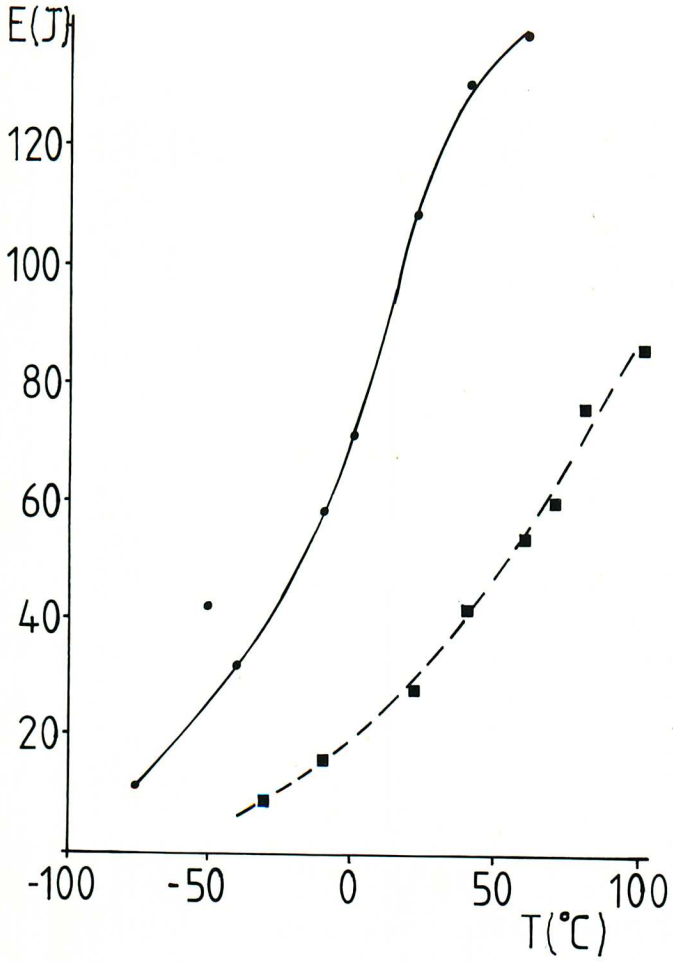

Fig. 4.15 Charpy impact properties for welds SA 1 (■) and SA 4 (●).

Table 4.2

Mechanical properties for welds SA1 and SA 4.

	LOWER YIELD STRESS N/mm²	ULTIMATE TENSILE STRENGTH N/mm²	ELONGATION %	REDUCTION IN AREA %
SA 4	539 548	642 647	29 28	55 65
SA 1	477 481	606 622	28 27	55 57

Table 4.3.

Quantitative metallography for welds SA 1 and SA 4.

	GRAIN BOUNDARY FERRITE %	SIDE PLATES %	ACICULAR FERRITE %	OTHER FEATURES %
SA4	10	9	72	9
SA 1	26	41	24	9

Though several criticisms of the techniques of point counting can be made, the results of such an analysis for welds SA 1 and SA 4 are given in Table 4.3. In this study, the catagories of ferrite microstructure considered were :

(i) GRAIN BOUNDARY FERRITE

(ii) FERRITE SIDE PLATES

(iii) ACICULAR FERRITE

(iv) OTHER FEATURES

which are the broad categories considered by Widgery (1974). These results are consistent with the overall relationship determined in many investigations, eg Widgery (1974), that the proportion of the acicular ferrite microstructure can be directly linked with toughness.

Transmission electron microscopy was used to fully characterise the microstructure of the weld deposits. The results presented here will deal specifically with the microstructure of the weld SA1 - a complete description of a typical acicular ferrite microstructure as observed in weld SA 4 will be given in Chapter 6. Fig 4.16(A),(a) shows a transmission electron micrograph of cementite situated between two grain boundary nucleated ferrite side plates. A cementite dark field and corresponding diffraction pattern are given in Figs. 4.16(A),(b),(c), respectively. Cementite formed the largest proportion of the so-called microphases in these welds. The presence of retained austenite was detected using x-ray diffraction (see Chapter 3 Fig. 3.18), but only rarely in thin foils, as shown in Fig.4.16(B),(a) with the corresponding dark field image and diffraction pattern in Figs. 4.16 (B), (b) and (c). High carbon, twinned martensite was observed, as shown in Fig.4.17, and in this case a small area of degenerate pearlite is also present.

The chemical analysis of these welds indicated that a large volume fraction of inclusions would be present in both the deposits. Carbon

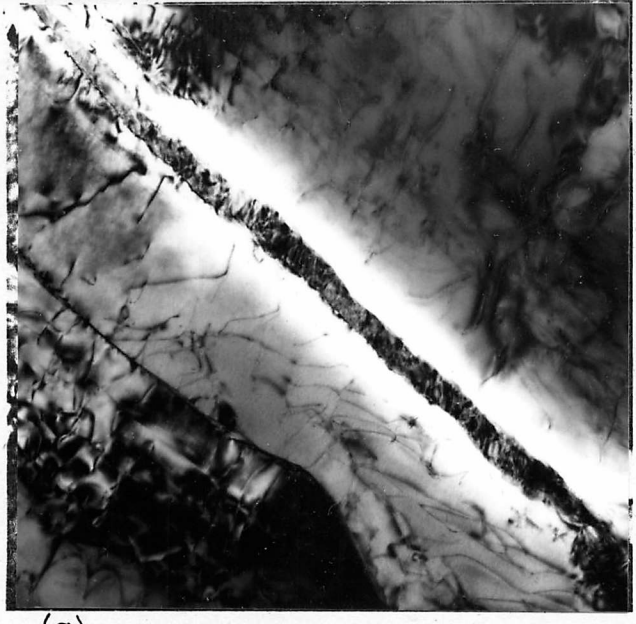

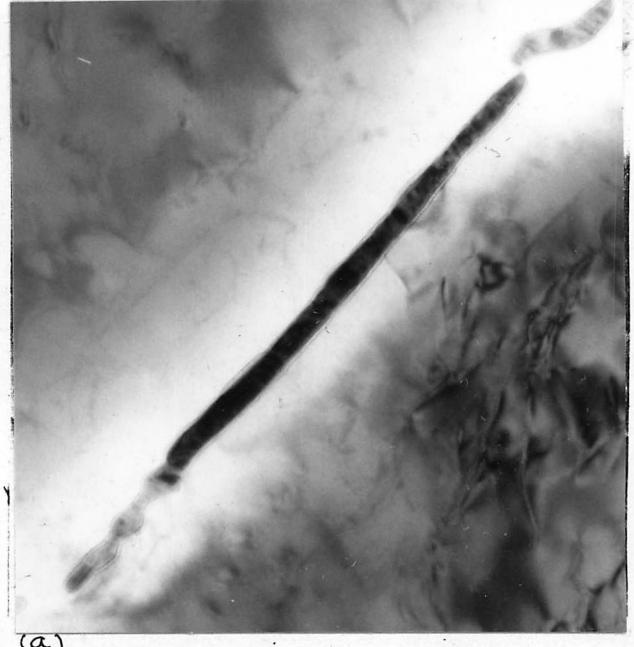

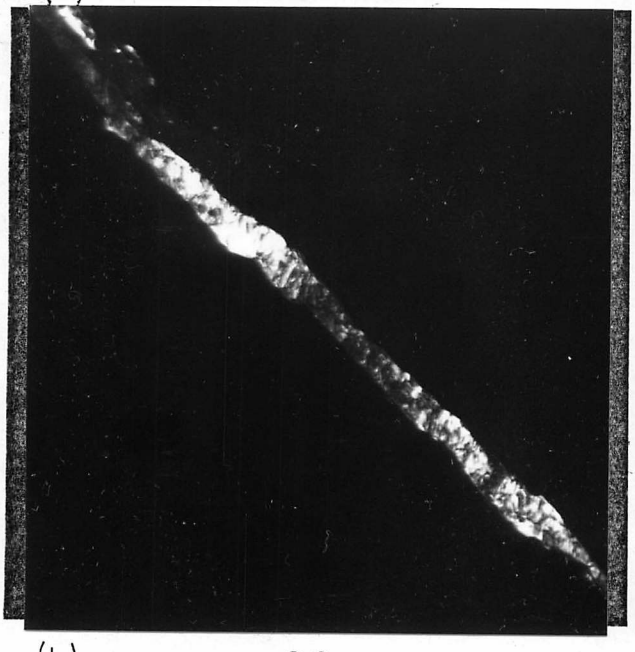

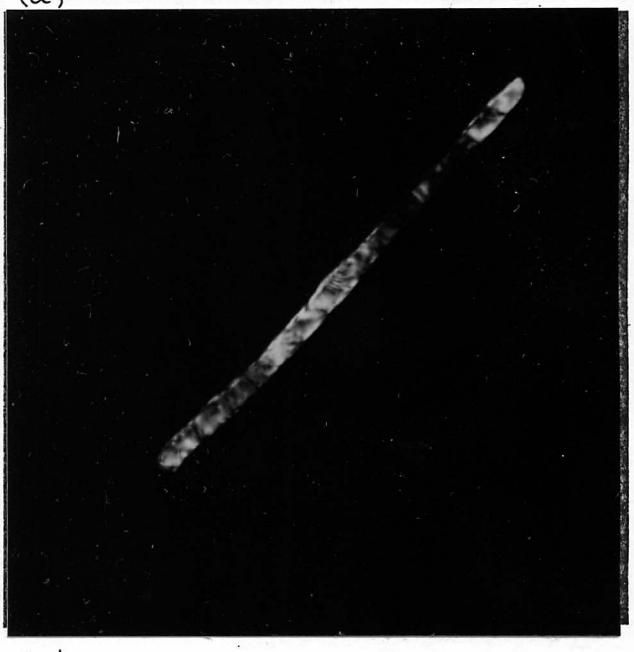

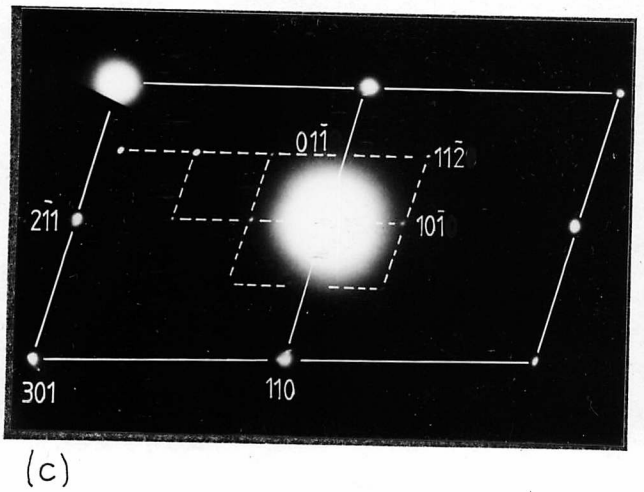

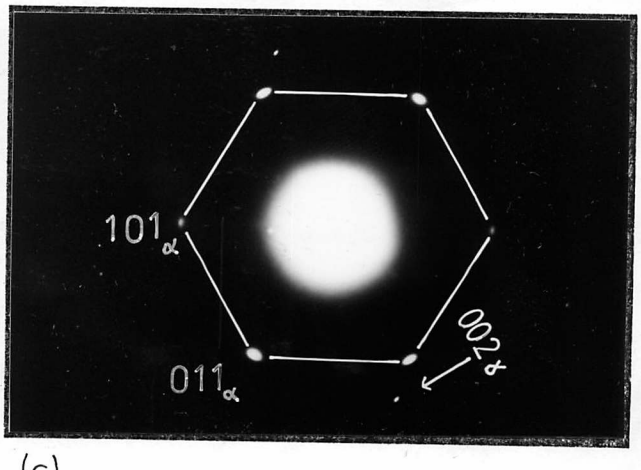

(A) (B)

Fig.4.16 Microphase region of weld SA 1 showing presence of cementite (A) and retained austenite (B).
(a) Brightfield.
(b) Dark field.
(c) Corresponding diffraction pattern + solution.

Fig. 4.17 Microphase region of weld SA 1, showing presence of twinned martensite and a small area of degenerate pearlite - at A.

extraction replicas from these two welds revealed a large number of inclusions as shown in Figs. 4.18(a) (b). A Quantimet image analysing computer was used to measure the size distribution and volume fraction of the inclusions present. These results are summarised in Figs. 4.19 (a) and (b), which show the number of inclusions per unit volume in each of the welds SA1 and SA4 respectively. The volume fraction of inclusions was calculated directly from the field area as 0.193 % (weld SA4) and 0.392% (Weld SA1), which is in good agreement with the calculated values based on the work of Bailey and Pargeter (1979), which predicts volume fractions of 0.184 and 0.377 respectively from the bulk compositions. The nature of these inclusions and their effects on matrix compositions will be discussed in Chapter 7. Table 4.4 summarises further details of the Quantimet analysis of inclusion parameters. The nearest neighbour spacings (Δ_3 and Δ_2) are similar to those reported by Widgery (1974).

Having established a distinct difference in inclusion size distribution between the two welds (ie. there are more and larger inclusions in weld SA1 than SA4), it is important to assess, at least qualitatively, how the inclusion size distribution itself is affecting toughness. By reaustenitising Charpy specimens from these welds to the same austenite grain size, followed by furnace cooling, it is possible to establish a constant ferrite microstructure. This is shown in Fig 4.20, where the microstructure comprises of an equiaxed ferrite/pearlite constituent.

The resultant Charpy impact properties are shown in Fig. 4.21, which suggests that the inclusion size distribution itself is affecting both the upper shelf impact behaviour (microvoid coalescence fracture mode) and the Ductile/Brittle impact behaviour (cleavage fracture mode). Whilst the former point is well established, eg Dolby (1976), the role of inclusions

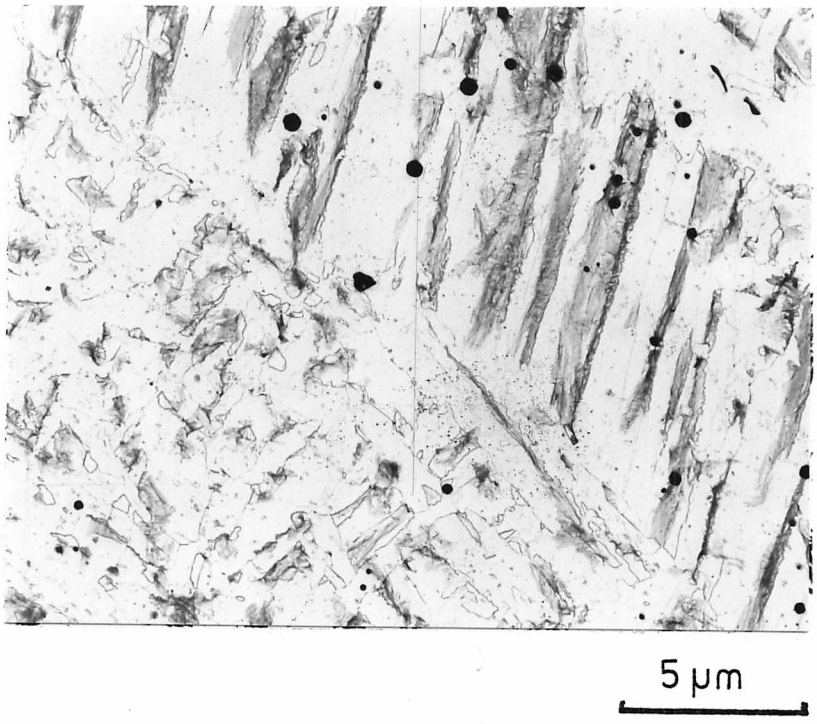

Fig. 4.18(a) Carbon extraction replica from weld SA 1

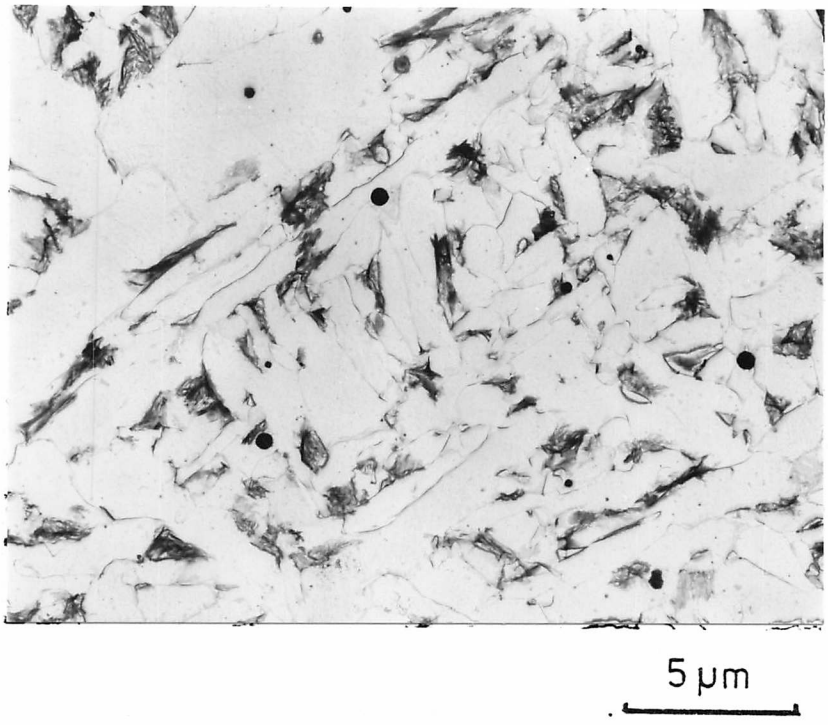

Fig. 4.18(b) Carbon extraction replica from weld SA 4

(N.B. In both cases, these carbon replicas were prepared from lightly etched specimens resulting in poor extraction of cementite.).

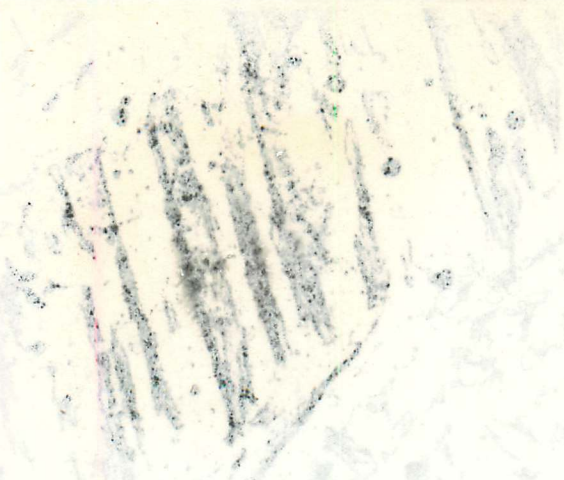

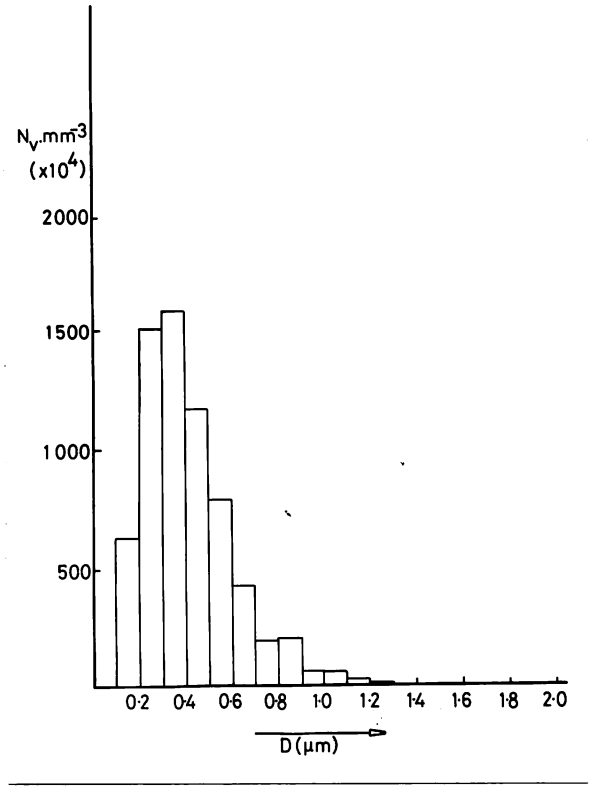

(a)

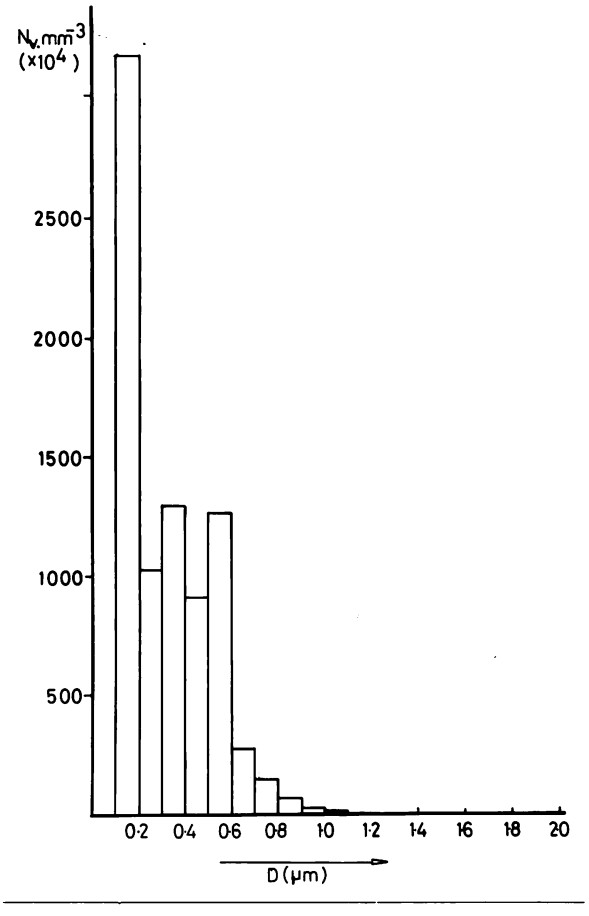

(b)

Figs. 4.19 (a) (b)

Inclusion size distribution for welds SA 1 (a) and SA 4 (b), indicating the number of inclusions per mm^3 of diameter D.

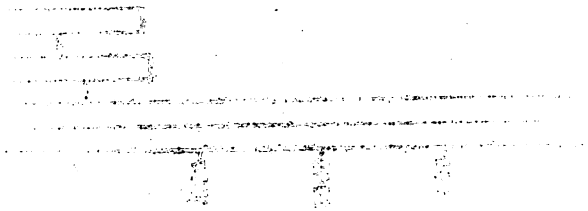

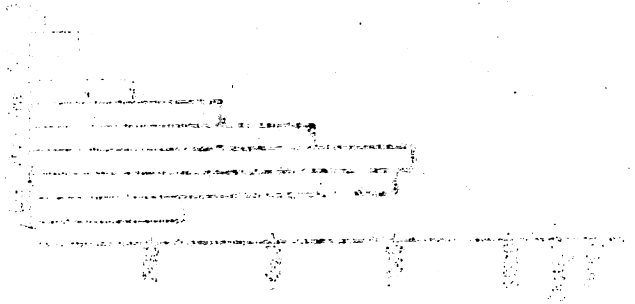

Table 4.4 Summary of inclusion parameters for welds SA 1 and 4.

	N_a /mm^2	N_V /mm^3	Δ_3 μm	Δ_2 μm	$\bar{X}$ μm	S mm^2/mm^3
SA 4	25,335	$1{\cdot}1\times10^8$	1·15	3·14	0·39	30·9
SA 1	32,726	$1{\cdot}6\times10^8$	1·02	2·76	0·46	47·5

N.B. The parameter S refers to the total surface area of inclusion/matrix interface. It is interesting to note that in both welds it exceeds the total austenite grain boundary area, which assuming hexagonal cyclinders were calculated as 11.7 and 35.3 mm^2/mm^3 for welds SA 4 and SA 1 respectively.

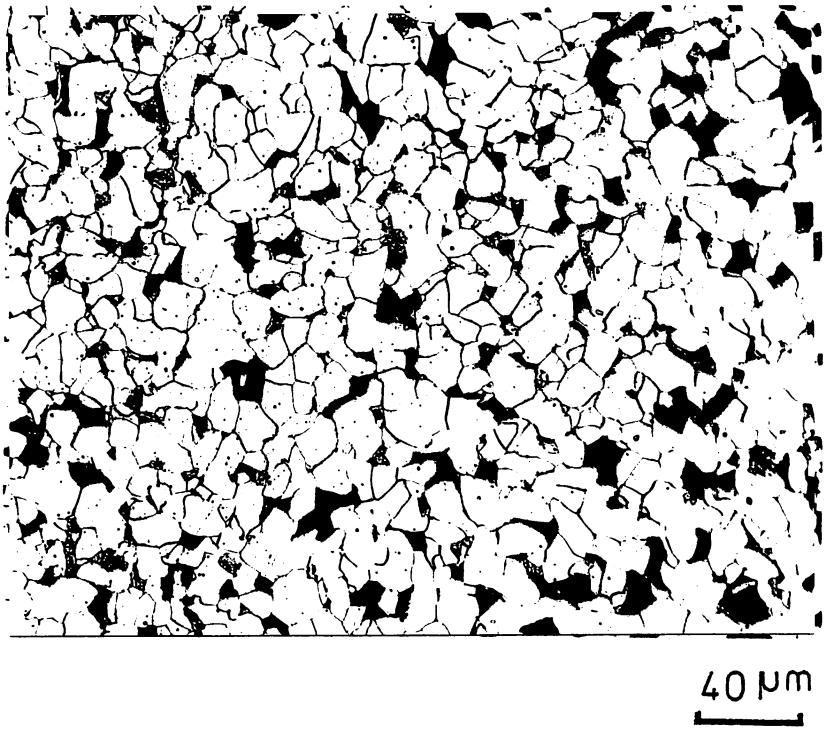

Fig. 4.20. Ferrite/pearlite microstructure produced by furnace cooling Charpy specimens from welds SA 1 and SA 4.

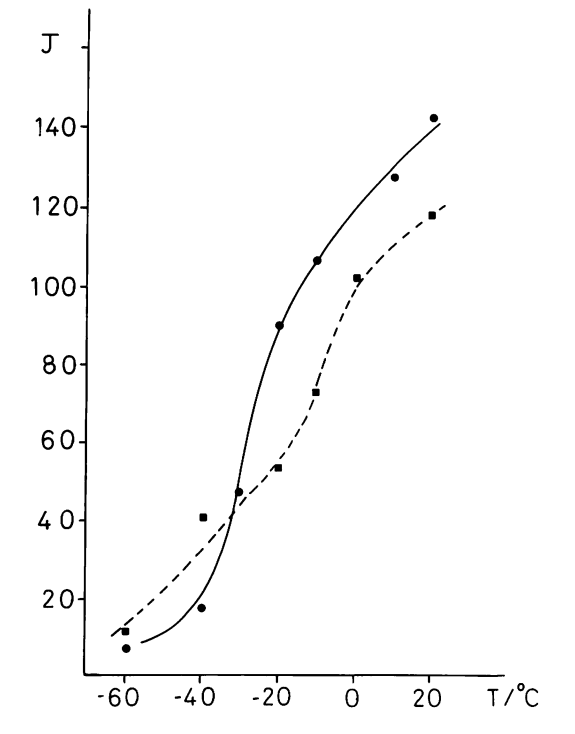

Fig. 4.21. Charpy impact properties for high oxygen (■) and medium oxygen (●) weld deposits with constant ferrite/pearlite microstructure.

in reducing cleavage resistance has only just been clearly demonstrated in weld metals, Tweed and Knott (1981).

4.5 DISCUSSION

This chapter has investigated a series of typical microstructures which might be encountered in the three welding procedures considered. They have served to demonstrate the overall effect of cooling rate on the microstructure of steel weld metals. A progression from a mixed upper bainite/martensite microstructure (observed in the electron beam weld) at fast cooling rates to a coarse mixture of grain boundary ferrite/-Widmanstatten ferrite/ pearlite microstructure (observed in the electro-slag weld) has been noted.

With respect to the submerged arc welds deposits (SA1) and (SA4), the techniques of point counting and simple Charpy transition curves have again shown that a high proportion of the acicular ferrite microstructure is desirable for good toughness. Additional information regarding the fracture characteristics of these two welds has also been obtained. The two distinct inclusion distributions observed in the welds (SA1) and (SA4) have themselves changed the resistance to cleavage fracture of the two deposits, as indicated by Fig. 4.21. Direct evidence to support this claim has been established in similar material by Tweed and Knott (1981).

The new information which has arisen from the microstructural investigation is that derived using the higher resolution techniques. Specifically, oil emersion photography has indicated three probable roles for inclusions in these particular weld deposits.

In the electron beam weld (EB1) a close association of intragranular ferrite and a manganese sulphide inclusion has been observed (Fig.4.9). This has occurred despite the fact that the grain boundary regions in the same austenite grain are associated with an upper bainite microstructure. This in itself strongly suggests that the inclusions are locally affecting

the austenite composition, as demonstrated by Salmon-Cox (1964) in cast steels.

In the high oxygen submerged arc weld (weld SA1), large inclusions have been observed in prior austenite grain boundaries, supporting the argument put forward for grain boundary pinning proposed by Cochrane (1978). Similarly, an apparent association of inclusions and intragranular ferrite, as proposed by Abson and Dolby (1978), has been observed in medium oxygen weld metal (weld SA4).

Electron microscopy has shown clearly the nature of the so-called microphase regions in the submerged arc deposit (SA1). Cementite and twinned martensite have been identified in this deposit.

4.6 CONCLUSIONS

The broad conclusions of the work described in this chapter can be summarised as follows:

1) The literature reviews included in this chapter have indicated a need for a systematic study of microstructure in steel weld metals. At present, the most appropriate scheme to describe the microstructure of as-deposited weld metals is considered to be that proposed by Widgery and Saunders (1975).

2) The experimental investigation has pointed directly to those areas which must be considered in following chapters. In considering the role of inclusions with respect to the development of microstructure, three main features must be investigated.

i) Their role as sites for intragranular nucleation of acicular ferrite

ii) Their role in determining matrix chemistry

iii) Their role in pinning austenite grain boundaries and the significance of this parameter on subsequent transformation.

CHAPTER 5

A RATIONALISATION OF PHASE TRANSFORMATIONS IN H.S.L.A. STEEL WELD METALS.

5.1 INTRODUCTION

This chapter will describe a detailed isothermal and continuous cooling study of two typical submerged arc weld deposits and a model steel of the same composition. The aim of the investigation was to identify the morphology and microstructural characteristics of the various components present at any given temperature. The experimental work is analysed in terms of a recent thermodynamic analysis due to Bhadeshia (1980.1) (1982.2), which sought to rationalise displacive phase transformations in steels.

Particular attention has been placed on the investigation of the early stages of the ferrite and bainite reactions since, at any given temperature, these observations are most relevant to the situation of continuous cooling. Carbide precipitation reactions are shown to be secondary to the overall reaction mechanism for both the Widmanstatten ferrite and bainite reactions, and consequently are not reported in detail. One unfortunate limitation of the microstructural examination was that, due to the very fast isothermal reaction observed throughout the temperature range of interest, surface relief experiments could not be carried out.

5.2 THERMODYNAMIC ANALYSIS

The thermodynamic calculations presented in subsequent sections were carried out using computer programs described in detail in Bhadeshia (1981.4) The general background and basis to this work can best be considered in two sections as follows. Bhadeshia's notation for free energy is used throughout this chapter

5.2.1. RATIONALISATION OF SHEAR TRANSFORMATIONS IN STEELS.

For many years, several authors eg Pickering (1967) have sought to incorporate Widmanstatten ferrite and upper bainite into a single framework which could describe the mechanism of formation of these constituents. For example, on the basis of metallographic studies of alloy steels, Honeycombe and Pickering (1972) concluded that both Widmanstatten ferrite and upper bainite formed by a mechanism involving shear. However, only recently has a complete thermodynamic analysis of this proposal been established. This rationalisation of shear transformations by Bhadeshia (1981.1) can best be discussed with reference to Fig.5.1, which presents the free energy-temperature curves for a Ni/Si steel. The three curves designated ΔF_N, $\Delta F^{\gamma \rightarrow \alpha_s}$ and $\Delta F^{\gamma \rightarrow \gamma_1 + \alpha}$ refer to :-

ΔF_N - The driving force, calculated on the basis that carbon partitions during nucleation, required to obtain a detectable nucleation rate.

$\Delta F^{\gamma \rightarrow \alpha_s}$ - Free energy change accompanying the formation of ferrite of the same composition as austenite.

$\Delta F^{\gamma \rightarrow \gamma_1 + \alpha}$ - Free energy change accompanying the formation of ferrite which at all times contains an equilibrium carbon content.

The ΔF_N curve represents quite a unique method of understanding the nucleation behaviour of Widmanstatten ferrite and bainite. Its basis is to calculate the driving force required to obtain a detectable

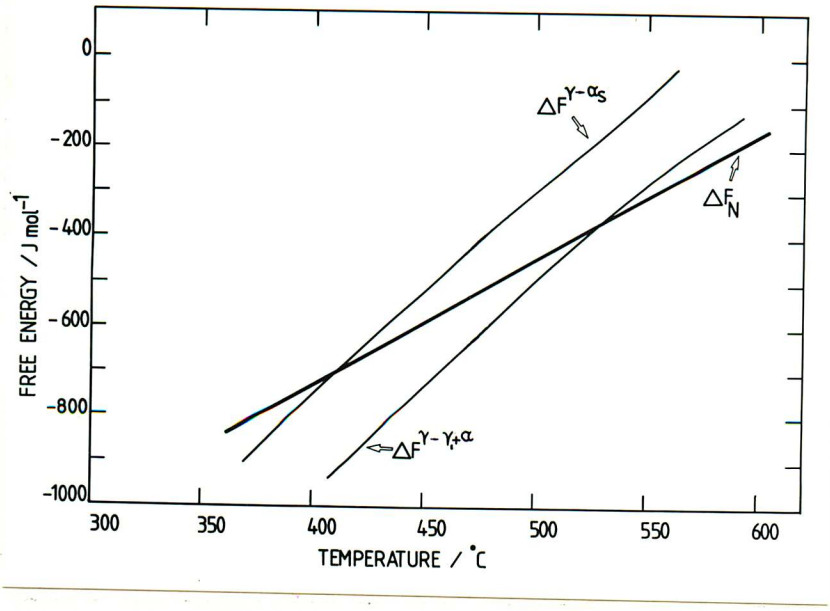

Fig.5.1 Free energy vs temperature curves for a Fe-Ni-Si-C steel, after Bhadeshia (1981.1). The ΔF_N curve represents the free energy change necessary in order to obtain a detectable nucleation rate for displacive transformations. The $\Delta F^{\gamma \rightarrow \alpha_s}$ and $\Delta F^{\gamma \rightarrow \gamma_i + \alpha}$ curves refer to the free energy change accompanying the formation of a BCC phase of the same composition and of equilibrium composition respectively.

nucleation rate, in a series of low alloy steels, at which a B.C.C. phase first forms with a shape change. The term B.C.C. phase is used here, since it can refer to either Widmanstatten ferrite or upper bainite. Initially, to establish this curve, two possibilities were considered - ferrite forming with a full parent austenite composition and ferrite forming with only the equilibrium carbon content. This latter case was shown to be the only operative possibility at the nucleation stage, since if a full supersaturation was considered, a positive free energy change was obtained for a few of the steels considered, a situation which is clearly impossible. The concept of a partial supersaturation was shown to be unstable with respect to fluctuations in the interface composition. The form of this universal curve was only consistent with isothermal martensite nucleation theory and not with classical nucleation theory which predicts a ΔF_N^{-4} dependence.

Although the nucleation stage involves the equilibrium partitioning of carbon, it seems reasonable that the subsequent growth of this B.C.C. phase depends critically on the free energy available for the transformation. Thus two possibilities are to be considered - growth with equilibrium carbon partitioning (represented by $\Delta F^{\gamma \rightarrow \gamma_1 + \alpha}$) and growth with full carbon supersaturation (represented by $\Delta F^{\gamma \rightarrow \alpha_s}$), corresponding to Widmanstatten ferrite and bainite respectively. By determining the W_s and B_s temperatures, Bhadeshia was able to establish the magnitude of $\Delta F^{\gamma \rightarrow \gamma_1 + \alpha}_{(\text{at the } W_s)}$ and $\Delta F^{\gamma \rightarrow \alpha_s}_{(\text{at the } B_s)}$ as 50 J/mol and 400 J/mol. These are subsequently referred to as F_1 and F_2 respectively.

On this basis, the general condition for the B.C.C. phase to grow as Widmanstatten ferrite would be when

$$\left| \Delta F^{\gamma \rightarrow \gamma_1 + \alpha} \right| > F_1$$

Similarly, the B.C.C. phase would grow as bainite when

$$\left| \Delta F^{\gamma \rightarrow \alpha_s} \right| > F_2$$

In both cases, clearly the original condition

$$\left| \Delta F^{\gamma \rightarrow \gamma_1 + \alpha} \right| > \Delta F_N$$

would have to have been satisfied, otherwise nucleation of the B.C.C. phase would not have occurred in the first place.

By definition, at those temperatures where ΔF_N exceeds the value of $\Delta F^{\gamma \rightarrow \gamma_i + \alpha}$, nucleation and growth involving a shear process is thermodynamically impossible; thus transformation can only occur by an entirely diffusional process. To complete the rationalisation of shear transformations, the free energy change required for nucleation of martensite was taken after the analysis of M_s temperatures of plain carbon steels, Bhadeshia (1981.3).

The results of such an analysis for the composition 0.13%C, 0.35%Si, 1.27% Mn and 0.25% Mo is summarised in Fig. 5.2. The calculated curves for $\Delta F^{\gamma \rightarrow \alpha_s}$ and $\Delta F^{\gamma \rightarrow \gamma_1 + \alpha}$ have clearly exceeded the ΔF_N curve throughout the temperature range of interest (ie nucleation is possible). The temperature corresponding to the Widmanstatten start temperature (W_s), the bainite start temperature (B_s) and the martensite start temperature (M_s) were calculated as 700°C, 570°C and 475°C respectively.

To further characterise microstructural development under isothermal heat treatment conditions, it is possible (after Zener (1946)) to define a T_o temperature where stress-free austenite and ferrite of identical composition are in a metastable equilibrium. The calculation of this line as a function of temperature and carbon content is now well

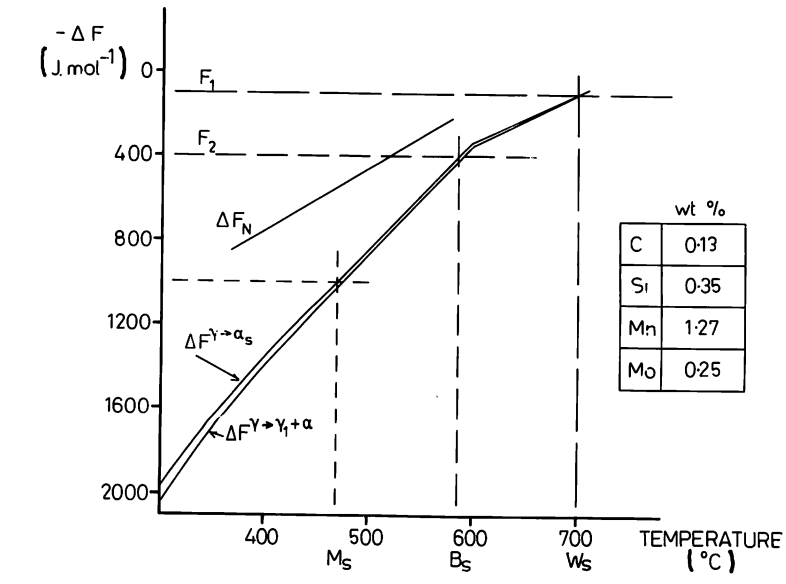

Fig.5.2 Free energy vs temperature curves for C-Mn-Mo weld metal as discussed in text.

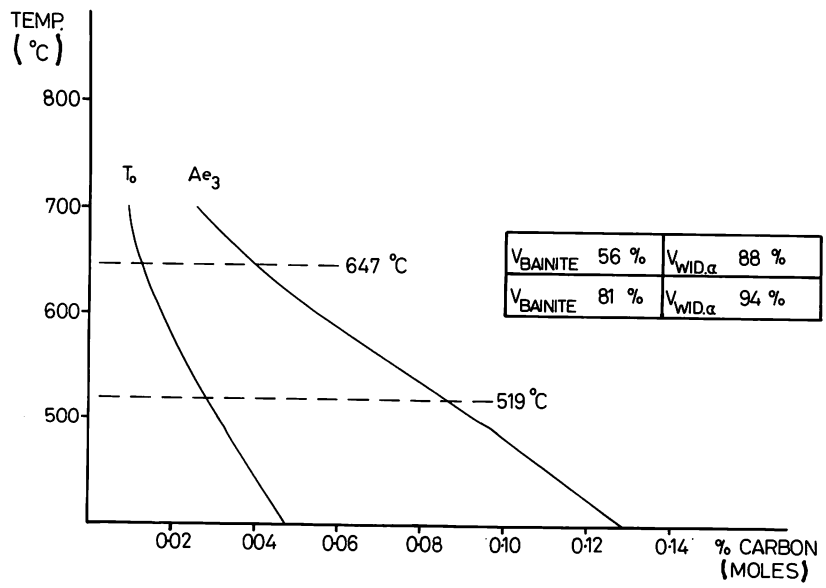

Fig.5.3 Calculation of To and Ae_3 curves for C-Mn-Mo weld metal referring to no partitioning and no substitutional partitioning respectively.

established, as is the calculation of the Ae_3 line, which describes the equilibrium when carbon partitioning is allowed to occur. In both cases, no partitioning of substitutional alloying elements is allowed. The calculations for the composition of interest in this investigation were carried out using the analysis of Bhadeshia (1979), and are summarised in Fig.5.3. The effect of the strain energy and interfacial energy contributions (referred to as the stored energy contribution) is to reduce the extent of the transformation in both cases. This is indicated by a slight shift to the left for both curves. This analysis allows the extent of the isothermal reaction to be established assuming either a bainite or Widmanstatten reaction, since the transformation should stop when the carbon content of the residual austenite reaches either the T_o or Ae_3 tie line respectively. This assumes, of course, that carbide precipitation has <u>not</u> reduced the carbon content of the residual austenite, since this would allow further transformation as the carbon level would be reduced below the T_o level.

With the subsequent experimental work in mind, two temperatures were selected for extensive investigation, 520°C and 650°C, these being at the centre of the calculated Widmanstatten ferrite and bainite temperature ranges. The estimated volume fractions of bainite and Widmanstatten ferrite at these temperatures (in the absence of carbide precipitation) are also shown in Fig.5.3.

5.2.2 ISOTHERMAL TRANSFORMATION DIAGRAMS

In a new analysis, Bhadeshia (1981.4) has recently presented a thermodynamic model, allowing the calculation of the reaction start times for Time-Temperature-Transformation diagrams. He proposes that such diagrams can be considered to comprise two overlapping 'C' curves. These describe the high temperature ferrite and pearlite transformations

(the diffusional 'C' curve) and the low temperature Widmanstatten ferrite and upper bainite reactions (the displacive 'C' curve). The interaction of these two curves is shown to account for the 'bay' which is frequently observed in low alloy steels about the so called B_s temperature.

The essence of this method is to fit experimental values to Russell's (1968) general equation:-

$$t_s = f\left[\frac{T}{(\Delta G)^X . D}\right]$$

where t_s = time taken to establish a steady state nucleation rate

T = Absolute temperature

D = Appropriate diffusion coefficient

G = Appropriate free energy change

X = dependent on the nature of the nucleus

for both the displacive and diffusional products. This method therefore precludes any preconceived ideas regarding the shape, the coherency or the size of the initial nucleus. The calculations generate two 'C' curves as a function of time and temperature. In the case of the lower 'C' curve the diagram is truncated at the W_s, since this represents a natural upper limit for the Widmanstatten ferrite and bainite reactions as previously discussed. Bhadeshia has emphasised that while this method gives good agreement with experimental results, the formalisation must, as yet, be considered empirical.

The resultant T.T.T. diagram for the alloy system considered in this investigation is shown in Fig.5.4. Clearly, an extremely fast isothermal reaction is predicted for both the displacive and diffusional 'C' curves.

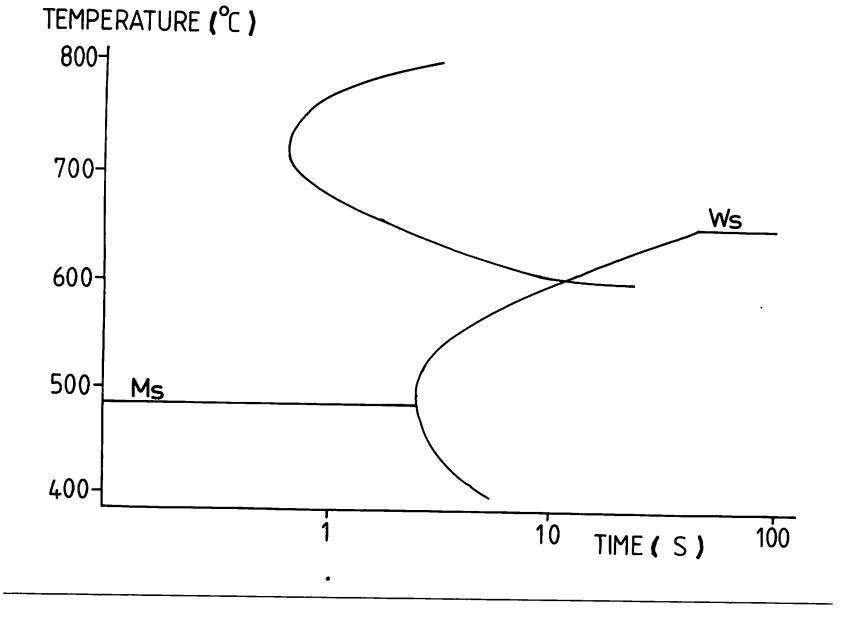

Fig.5.4 Calculated T.T.T. curve for the nominal composition 0.13%C, 0.35% Si, 1.27 % Mn, 0.25 % Mo. The upper 'C' curve describes diffusional transformation (ferrite and pearlite) whereas the lower 'C' curve refers to displacive transformation (Widmanstatten ferrite and upper bainite).

5.2.3. APPLICATION OF THERMODYNAMICS TO THE ANALYSIS OF TRANSFORMATIONS OCCURRING ON CONTINUOUS COOLING.

It is instructive to list the problems associated with any attempt to apply a thermodynamic analysis to transformations occurring on continuous cooling. These are in addition to the problems already considered in the isothermal analysis described by Bhadeshia.

1) There is no extensive (if any) data source which relates those temperatures, compositions and cooling rates below which a B.C.C. phase forms from austenite with a shape change.

2) Since by definition, a range of temperatures are encountered at any given cooling rate, the driving force for transformation varies with time and temperature.

3) At the cooling rates of interest, it is likely that a range of transformation mechanisms can operate at various stages during the cooling cycle.

Further problems are again encountered when considering transformations in weld materials, of which the most limiting are as follows:-

1) No possibility exists of examining surface relief effects.

2) As yet, there is no possibility of accounting for the possible effects of austenite grain size or the question of the actual nucleation site - both of which are thought to have powerful effects in weld materials.

Ideally, any continuous cooling transformation (CCT) diagram may be considered to be one of eleven primary possibilities with respect to the measured reaction start and finish temperatures. These are represented in Fig.5.5, relative to the isothermal parameters previously discussed.

The most obvious possibility is that transformation does not occur at all on cooling to room temperature, as indicated by case A. The

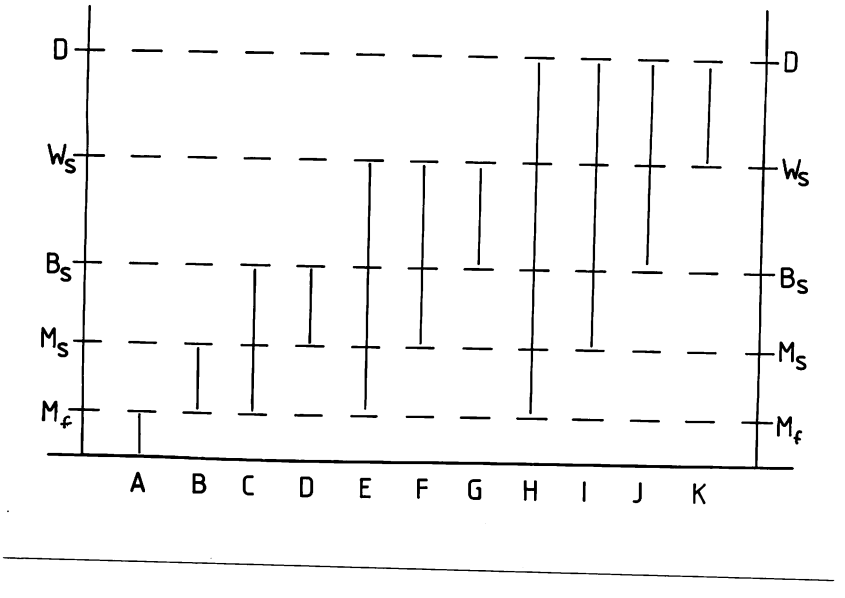

Fig.5.5 Schematic representation of the possible transformation ranges of reaction product occurring on continuous cooling. For discussion see text.

second relatively simple possibility is the case when transformation occurs entirely at high temperature by diffusional processes (case K). For each of the nine other possibilities, mixed transformation mechanisms are likely, since the observed transformation range spans one or more of the isothermal phase fields. In this case, a series of secondary possibilities exist, depending on the stability of any remaining (residual) austenite. This will itself depend critically on the alloy composition, cooling rate and the precise effect of any prior transformation.

The situation which must be analysed in weld materials is case H where, in general, the observed transformation range encompasses a wide range of transformation mechanisms.

5.5. EXPERIMENTAL RESULTS

5.3.1. ISOTHERMAL INVESTIGATION

Two weld metal types and a model steel (Alloy J) were investigated in this study - all having closely matching compositions, with the exception of the oxygen content. This varied from 600 ppm (welds SA 1,3) and 300 ppm (weld SA 4,6) to <50 ppm in the model steel.

For the weld materials, two austenitising treatments were investigated. In order to produce the same austenite grain sizes in each weld, 1300°C for 10 minutes (weld SA 3) and 1300°C for 6 minutes (weld SA 6) were employed to give an average grain size of 85 μm. To reflect the difference in austenite grain size observed in the as-deposited weld materials, 1310°C for 10 minutes conveniently produced grain sizes of 65μm and 115 μm in welds SA 3, 6 respectively. Subsequent investigation showed that in both welds, any austenite grain size in the range 40 to 115 μm produced the same reaction characteristics, since the overall kinetics of this alloy system seemed

to dominate in the temperature range of interest (ie. < 700°C). The reaction kinetics also limited the isothermal investigation to temperatures above 430°C, since below this value, transformation commenced during the quench to the isothermal temperature (ie the C.C.T. characteristics had become important).

The experimentally determined Time-Temperature-Transformation diagrams for the two welds are shown in Figs. 5.6(a) and 5.6(b). In both cases, the reaction start times occur in less than one second in the temperature range 700°C to 500°C. A bay is observed in the reaction finish curve between 625°C and 675°C, where dilatometrically it is difficult to establish the precise reaction finish time.

To characterise the various microstructural components present, heat treatment of 3mm rods was carried out in a tin bath in the temperature range 700°C to 500°C, following austenitising treatment of 1250°C for 15 minutes. In both welds considered, the same general characteristics were established with respect to the development of microstructure. The results will therefore be reported in terms of the various microstructural components observed, rather than the individual weld deposits (welds SA1 and SA4).

(a) THE BAINITE REACTION

Transformation below 550°C in both welds produced a characteristics plate-like or 'feathery' microstructure, designated upper bainite. For example, Fig.5.7 (a) and 5.7 (b) show the microstructure resulting from heat treatment at 550°C and 500°C for 5 seconds in weld SA 1. In general, the product appeared grain boundary nucleated though the degree of transformation precluded any positive identification of intragranular nucleation. Individual laths have in many cases grown completely across the austenite grains (eg. in A in Fig. 5.7(a)), though impingement seems to restrict the size in many cases (eg. in B in Fig.5.7 (a)). Clear

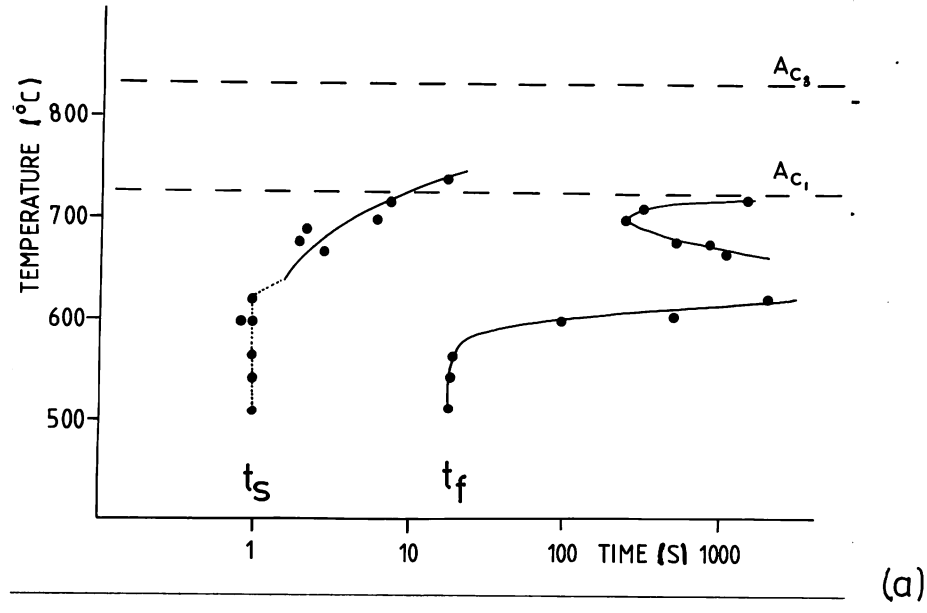

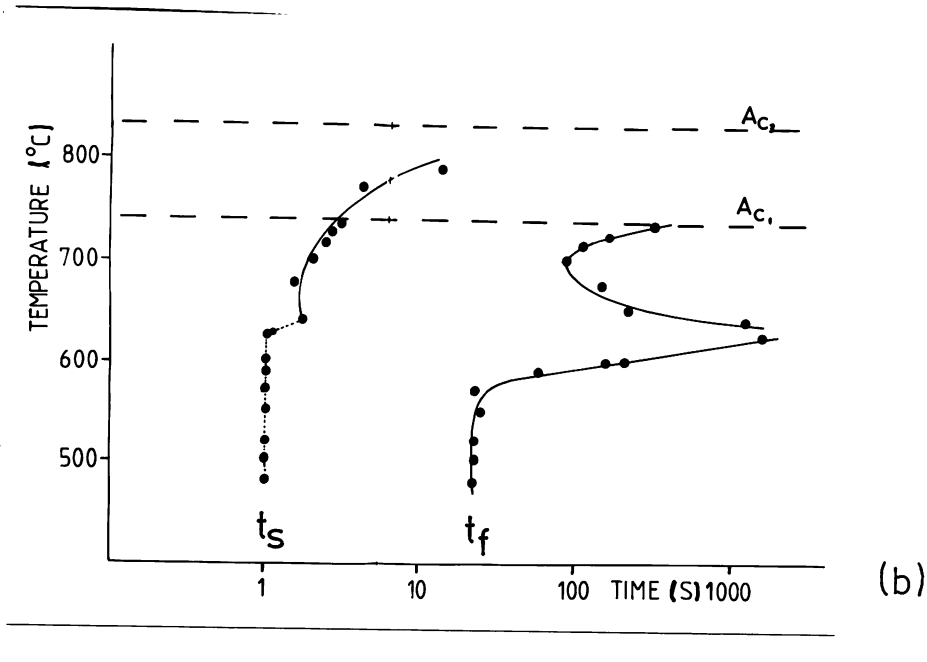

Fig.5.6 Dilatometrically determined T.T.T. diagrams for welds SA 3 (Fig.5.6(a)) and SA 6 (Fig. 5.6(b)).

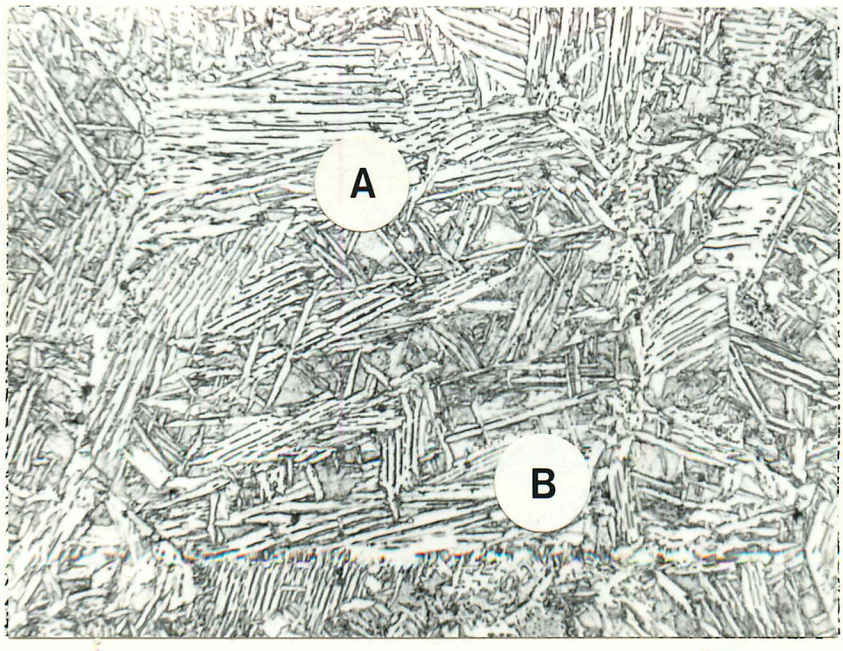

(a) 20μm

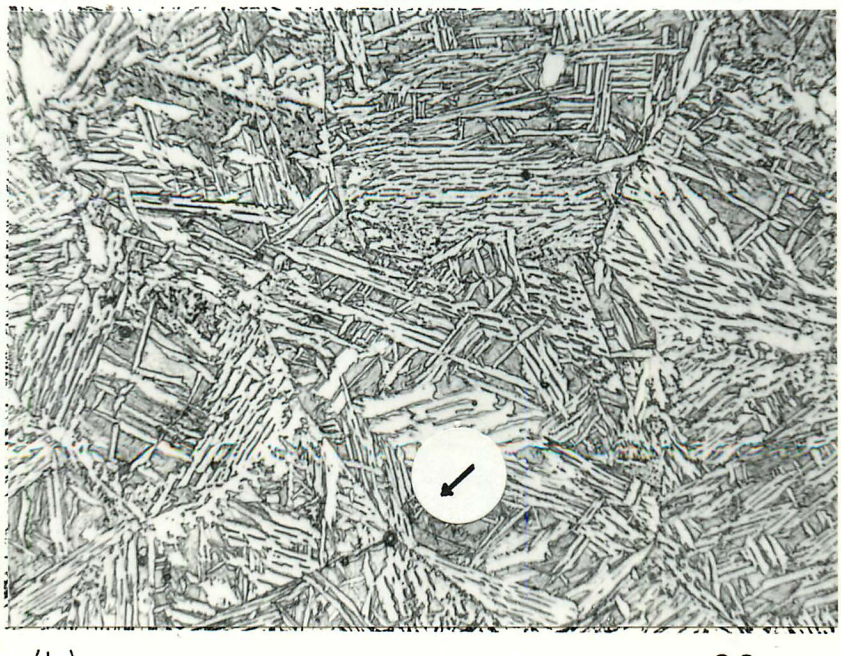

(b) 20μm

Fig.5.7 Optical micrographs of upper bainite microstructure following isothermal heat treatment of specimens from weld SA1.
(a) 550°C for 5 seconds.
(b) 500°C for 5 seconds.

evidence for inclusion pinning of austenite grain boundaries is evident in Fig. 5.7(b), where a large inclusion is present at an austenite grain boundary triple point. There is no obvious indication that inclusions are playing a major role in the development of this constituent.

Transmission electron microscopy of the upper bainite microstructure at this stage of development yielded several important results. Fig.5.8(a) shows that individual colonies of upper bainite are comprised of individual units of bainitic ferrite separated by well defined boundaries. Over the temperature range of interest, the width of these bainitic ferrite plates remained constant at 0.2μm with the length varying from 10 μm to in some cases 80-100 μm. Closer inspection reveals that individual laths have a high dislocation density and were separated by fine intralath films of a highly dislocated constitutent, as shown in Fig.5.8(b). In all cases in this temperature range at this stage of development, the constituent was identified as retained austenite. This is illustrated in Figs. 5.9 (a)(b)(c)(d), which show a typical brightfield, austenite centred dark field and diffraction pattern from a bainite colony observed at 550°C in weld SA 4. The orientation relationship between the austenite and bainitic ferrite was the Nishiyama - Wasserman orientation relationship.

Carbide precipitation occurred after 20 seconds in this temperature range, as shown in Fig.5.10, which refers to transformation at 550°C in weld SA 4.

(b) THE FERRITE REACTION

Transformation to ferrite occurred over a wide range of temperatures in these materials. For example, the ferrite morphology observed after transformation at 600°C for ten seconds in weld SA 4 is shown in Fig.5.11. At this temperature, the microstructure consists almost entirely of Widmanstatten plates. In many cases, these had grown

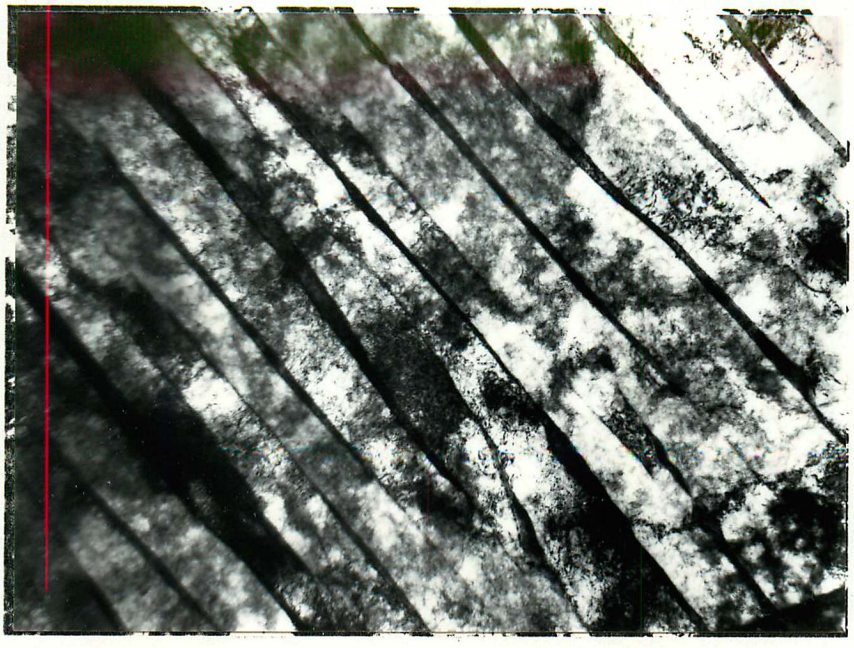

Fig.5.8(a) Transmission electron micrograph of upper bainite microstructure observed following isothermal heat treatment of specimens from weld SA 4 (550°C for 5 seconds). The constituent appears predominantly grainboundary nucleated.

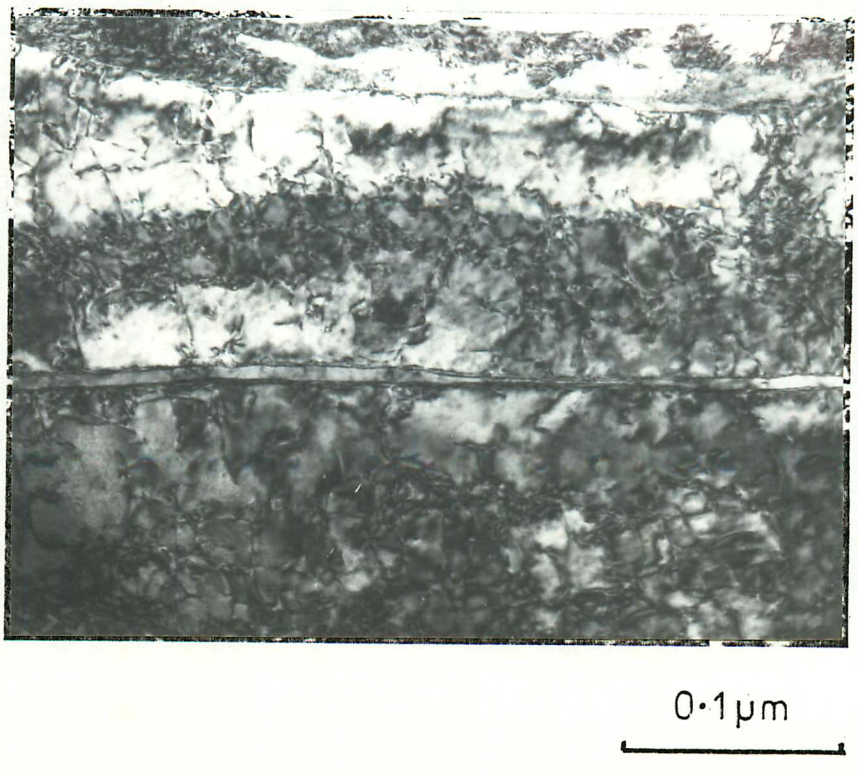

Fig.5.8(b) Transmission electron micrograph of upper bainite microstructure (as above) showing individual laths of bainitic ferrite separated by fine intralath films of austenite.

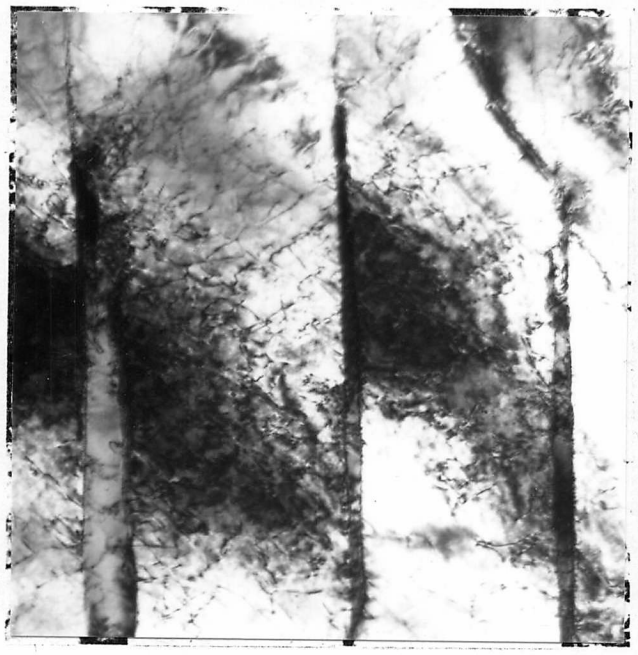

(a)

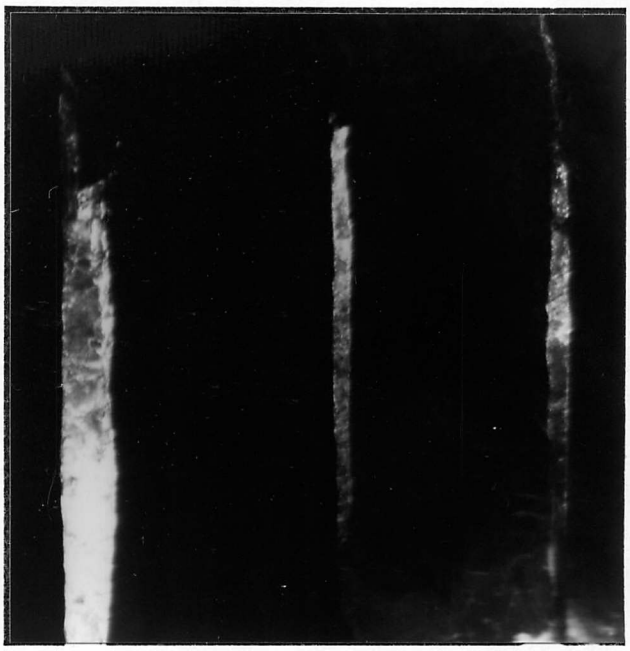

(b)

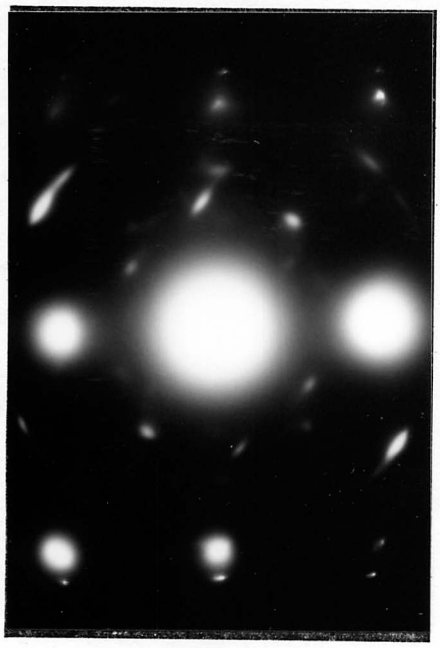

(c)

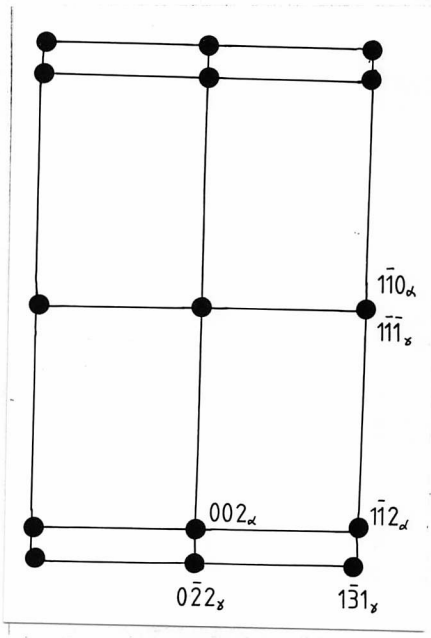

(d)

Fig.5.9 Transmission electron micrographs of the early stages of development of the upper bainite microstructure.
(a) Bright field micrograph.
(b) Austenite centred dark field.
(c) Corresponding diffraction pattern.
(d) Solution to (c).

0·2μm

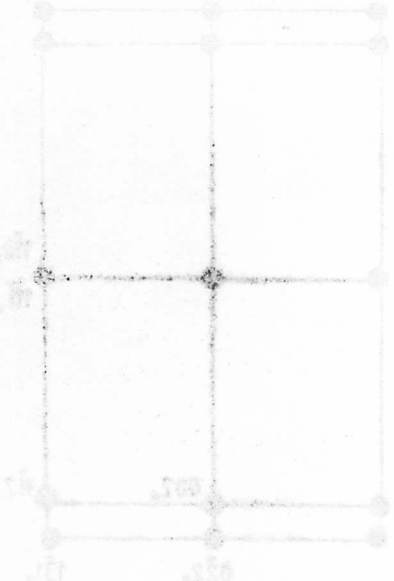

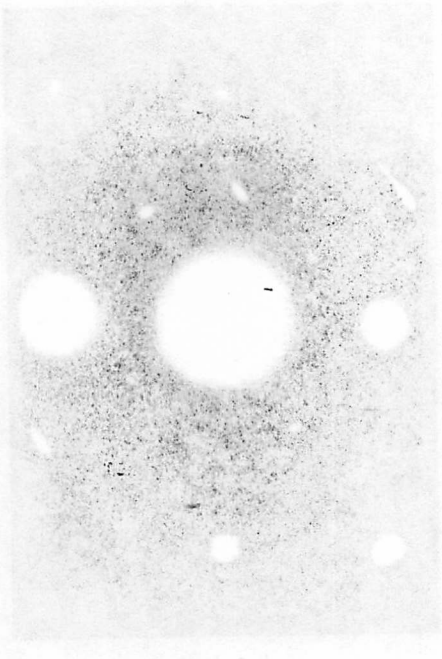

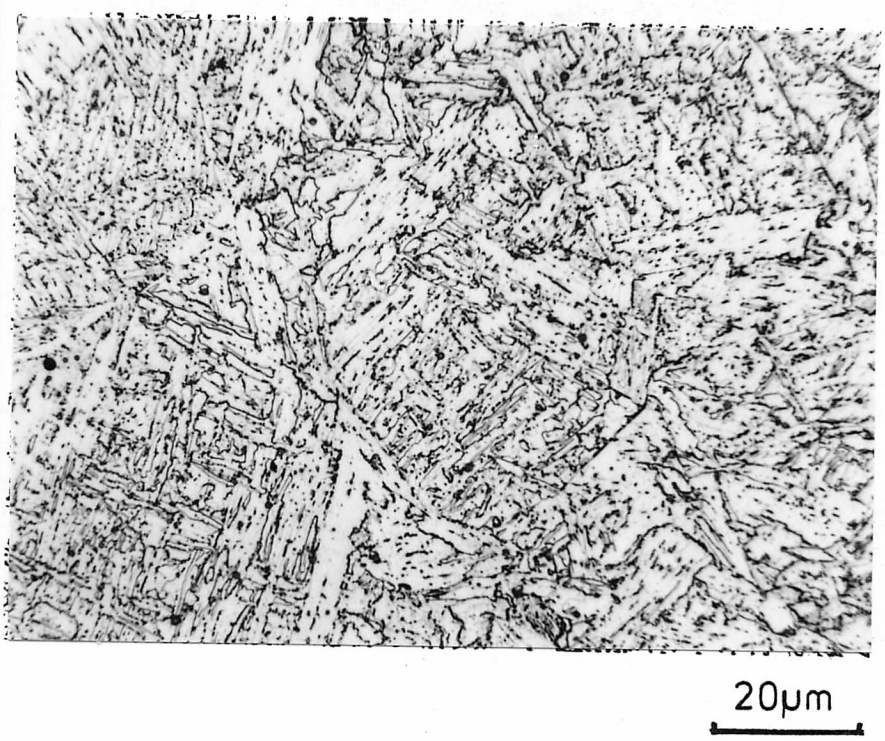

Fig.5.10 Optical micrograph of upper bainite microstructure following isothermal transformation at 550°C for 20 seconds. The colonies are extensively impinged and prior austenite grain boundaries are barely resolvable. (Weld SA 4)

completely across austenite grains (eg. at a), whereas in other areas, the plates were possibly associated with weld metal inclusions in the intragranular regions (eg. at b). Occasionally, Widmanstatten sawteeth were also observed at this temperature (eg. at c). After longer transformation times (eg. 10 minutes at 600°C) in weld SA 4, the microstructure appears interlocking, due to the extensive impingement. This microstructure is shown in Fig.5.12.

Transmission electron microscopy of the ferrite microstructure at the early stages of development revealed that many of the plates had subgrain boundaries along the centre, as shown in Fig.5.13(a). However, in several cases, eg. Fig. 5.13(b), no such boundary was observed. The precise crystallography of these plates could not be established, since interlath retained austenite was not observed in the adjacent martensite.

As the isothermal transformation temperature was increased, the frequency of observation of classic Widmanstatten ferrite plates decreased. Fig.5.14(a) shows the morphology of the ferrite microstructure after transformation at 650°C for 10 seconds in weld SA 4. The predominant components comprise allotriomorphic ferrite, as shown at (a), and secondary Widmanstatten plates, eg at (b). At high transformation temperatures, eg. 700°C, Widmanstatten plates were rarely observed. At early transformation times (eg. 1 minute), the experimental observations can be summarised for weld SA 1 in fig.5.14 (b). A single Widmanstatten plate can be observed at (a), a Widmanstatten sawtooth at (b), together with several examples of faceted ferrite growth eg at (c). At longer times at these high temperatures, slight disagreement with the dilatometric analysis was observed. The transformation finish recorded dilatometrically was 2 minutes at 700°C, whereas transformation in the tin bath was not complete after 10

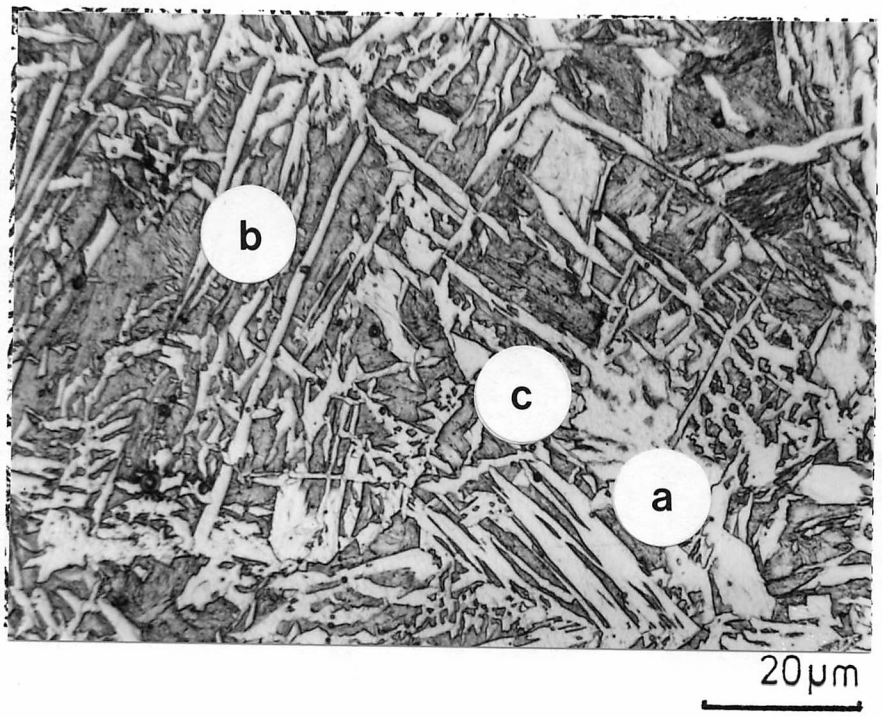

Fig.5.11 Optical micrograph of Widmanstätten ferrite microstructure during early stages of development.
(Weld SA4, 600°C - 10 seconds)

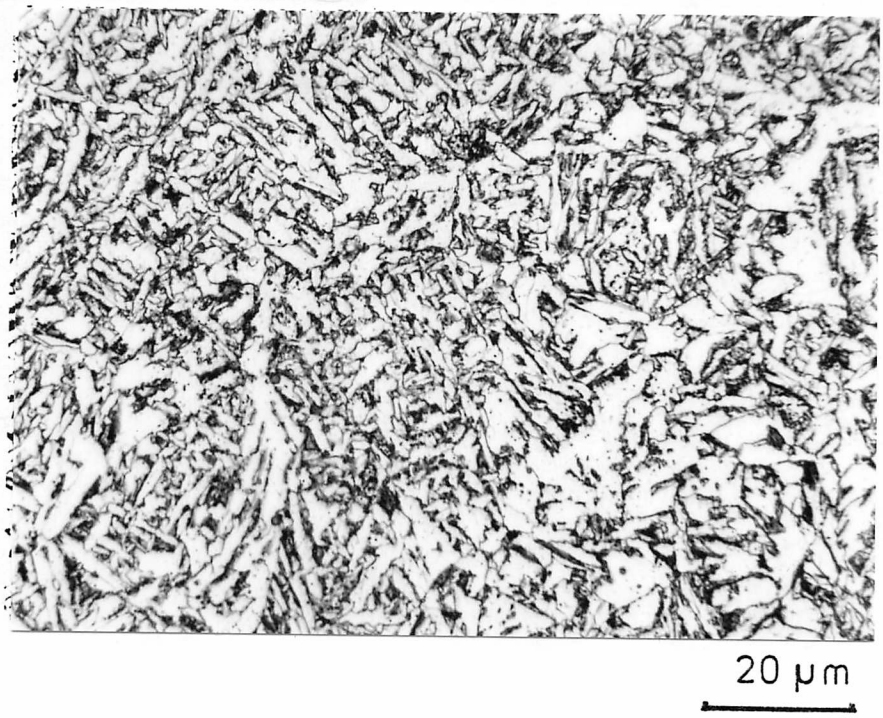

Fig.5.12 Optical micrograph of Widmanstätten ferrite microstructure after extensive impingement.
(Weld SA 4, 600°C - 10 minutes)

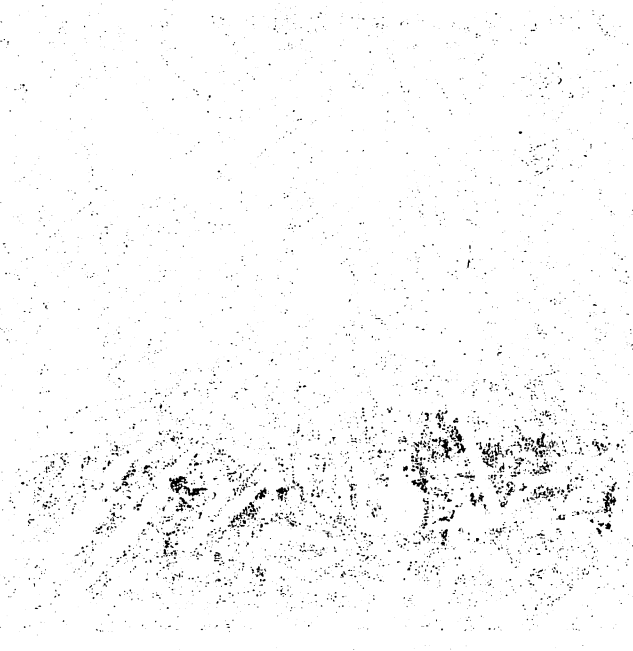

(a)

1 μm

(b)

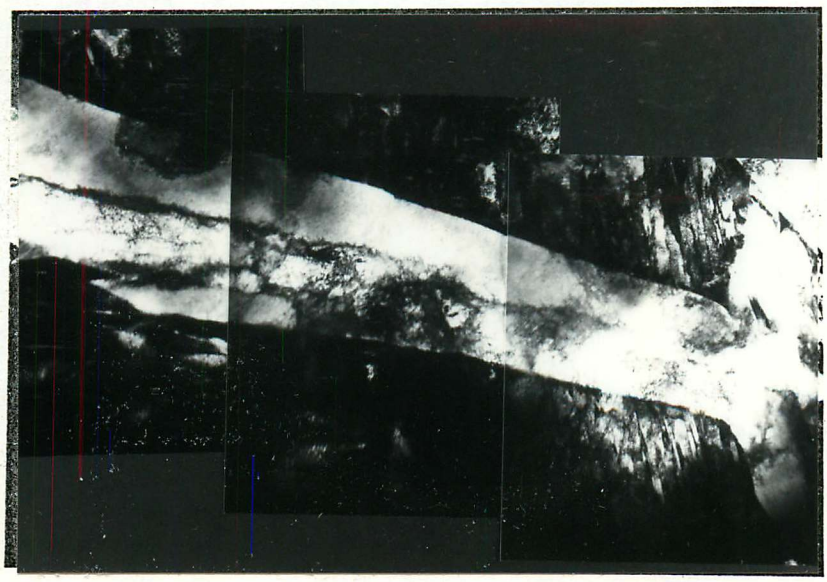

1 μm

Fig.5.13 Transmission electron micrograph of Widmanstätten plates following isothermal heat treatment. (Weld 594 , 600°C - 10 seconds)
(For discussion see text)

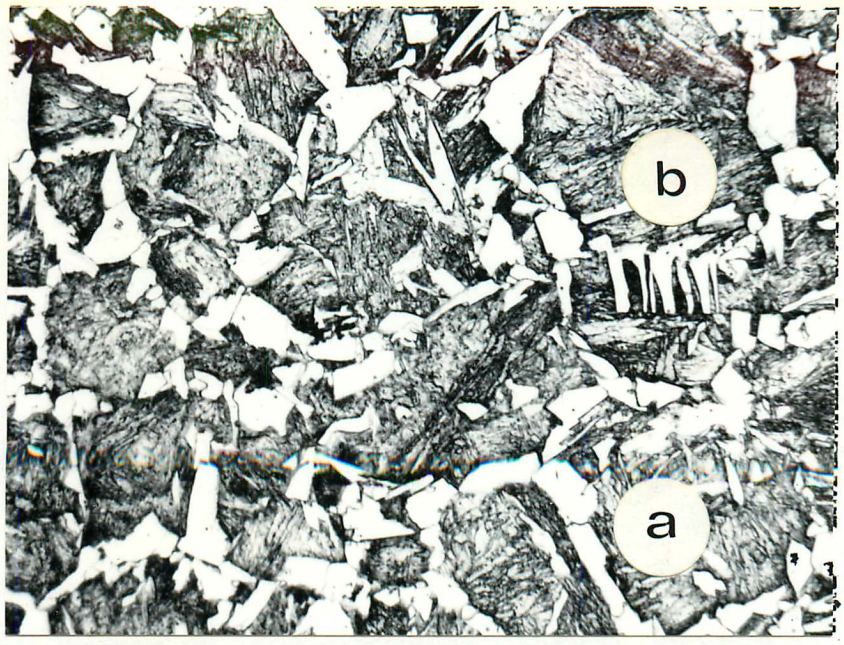

(a)

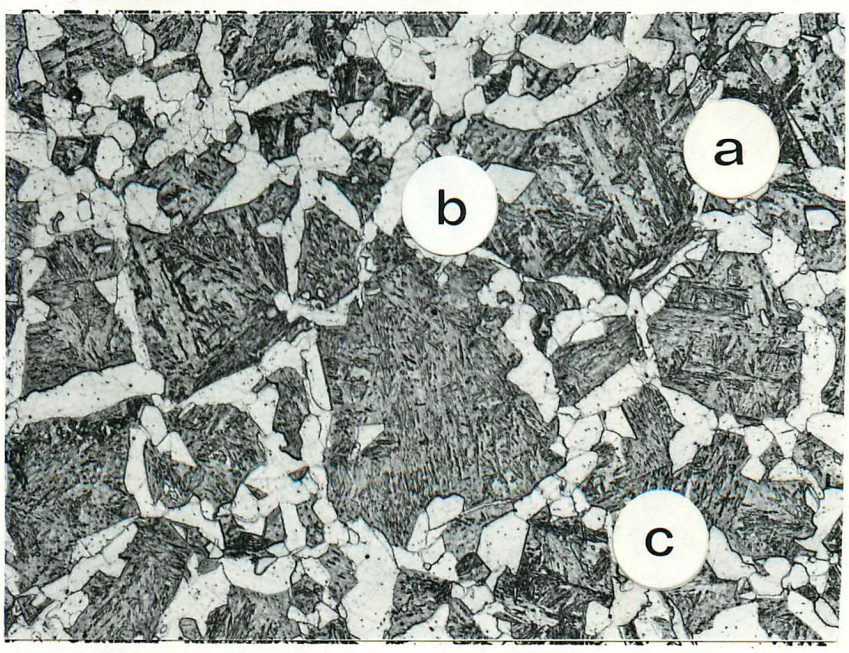

(b)

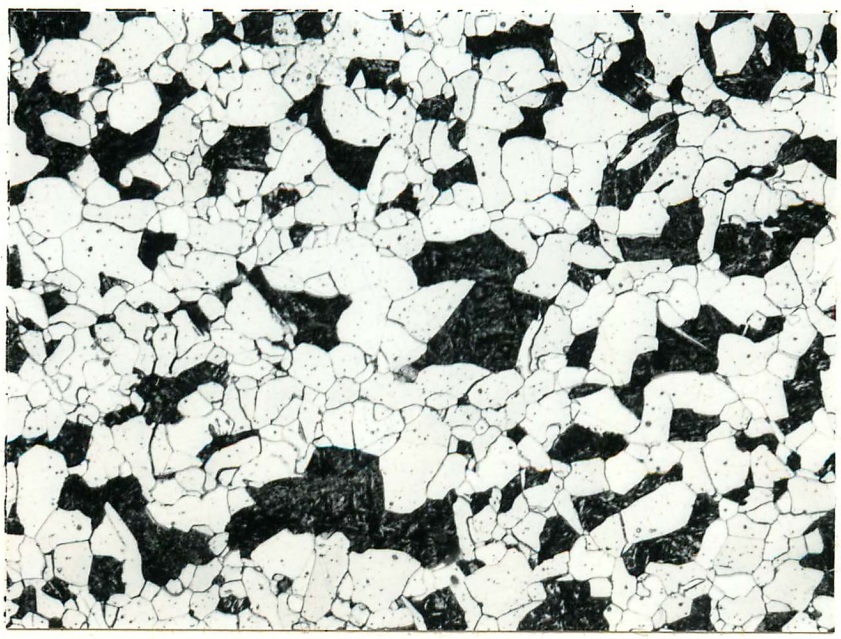

(c)

Fig.5.14 Optical micrographs of the high temperature reaction products observed under isothermal treatment in weld SA (For further discussion see text)

(a) Weld SA4 650°C 10 seconds
(b) Weld SA1 700°C 1 minute
(c) Weld SA1 700°C 10 minutes

20 µm

minutes, as shown in Fig. 5.14 (c), where the residual austenite has transformed to martensite.

(c) FURTHER ISOTHERMAL STUDIES OF THE UPPER BAINITE AND FERRITE REACTIONS IN A HIGH PURITY ALLOY

This further investigation was carried out to establish additional information regarding the nucleation characteristics of upper bainite and Widmanstatten ferrite. In addition, quantitative metallography was used to derive information regarding the extent of the isothermal Widmanstatten ferrite reaction. The advantage of using a model steel of the same composition as the weld metals previously investigated was principally that it removed any restrictions regarding austenite grain size. By using very large austenite grain sizes (circa 500μm), impingement effects were minimised. However, the overall reaction kinetics at the two selected temperatures (520°C and 650°C) were still such that the reactions began immediately.

The microstructures observed after transformations at 520°C and 650°C for 5 seconds in Alloy J are shown in Figs. 5.15 (a), (b) and (c), (d) respectively. The Widmanstatten ferrite morphology has been described adequately in the previous section and Chapter 2. For both the Widmanstatten morphology and the upper bainite microstructure, growth had usually only occurred into one grain, eg. Fig 5.15 (a) and (c), consistent with the classical hypothesis (Smith, 1953), though in some cases, eg. Fig. 5.15 (b), growth was observed into both austenite grains. Despite the high purity of the base steel (oxygen level 50 ppm, sulphur below the limit of detection), inclusion nucleation of intragranular ferrite was observed in one instance, as shown in Fig. 5.15(d) at the higher reaction temperature.

In the case of the upper bainite microstructure, it was impossible to assess accurately the extent of the bainitic ferrite reaction before carbide precipitation took place. However, at the latest stage of the

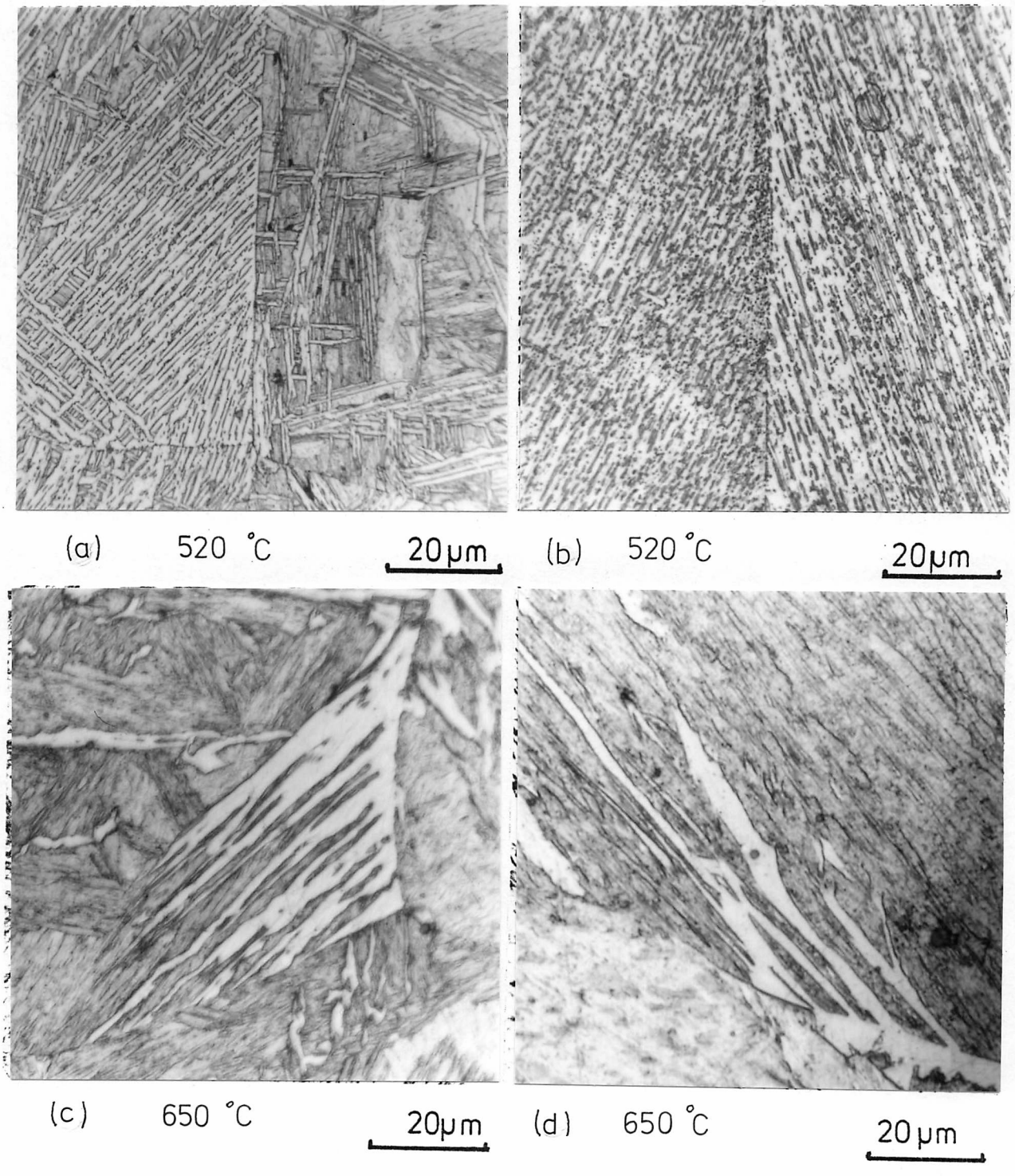

Fig.5.15 Further microstructural observations of upper bainite microstructure (Figs. 5.15 (a) (b)) and Widmanstätten ferrite microstructures (Figs. 5.15 (c), (d)). Alloy J, heat treatment at 520°C and 650°C for 5 seconds respectively.

[ALLOY J - 0·13 % C, 0·35 % Si, 1·19 % Mn, 0·25 Mo.]

reaction, when only retained austenite was detected (10 seconds at 520°C), transmission electron microscopy indicated that the width of the bainitic ferrite/ retained austenite components was approximately 4:1, indicating a volume fraction of bainitic ferrite of 80%. In this microstructure, there were no large residual austenite areas as described by Bhadeshia and Edmonds (1979).

The higher reaction temperature corresponded closely to the bay observed in the reaction finish curve for the two welds examined in the previous section. Quantitative metallography was used to estimate the volume fraction of ferrite at various stages of transformation; the results are summarised in Fig.5.16, where it is evident that even after prolonged holding the reaction is not complete - consistent with the bay reported dilatometrically. After forty eight hours the volume fraction of ferrite corresponded to 89 ± 3%.

5.3.2. CONTINUOUS COOLING INVESTIGATION

High speed dilatometry was used to study the continuous cooling kinetics of the weld deposits (SA 3 and SA 6) containing different oxygen levels. Initially, the re-austenitisation characteristics of the two welds were established and are summarised in Fig.5.17. To reflect the difference in austenite grain size of the as-deposited structures, 10 minutes at 1310°C was selected as a solution treatment temperature. This produced austenite grain sizes of 65 μm and 115 μm respectively in welds SA 3 and SA 6. The dilatometric study of these two welds is summarised in Fig.5.18, where the two continuous cooling diagrams (C.C.T.) for welds SA 3 and SA 6 are superimposed. The 5%, 50% and 95% transformation lines are represented, and typical weld metal cooling rates over the range 1.5 kJ/mm to 6.0 kJ/mm are indicated by the shaded area.

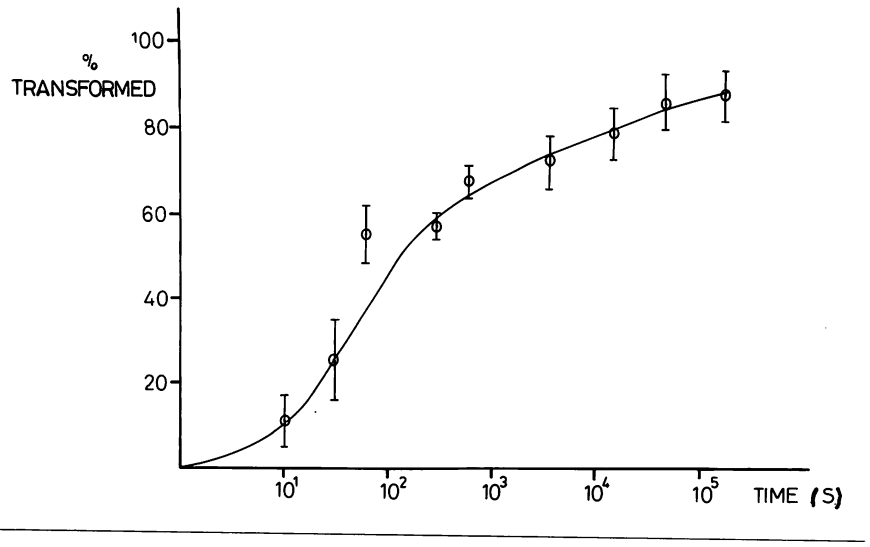

Fig.5.16 Isothermal transformation kinetics of Widmanstätten ferrite at 650° C in Alloy J. After long holding times the degree of transformation exceeds 56% Vol - that predicted by the To analysis of Bhadeshia if the product were upper bainite.

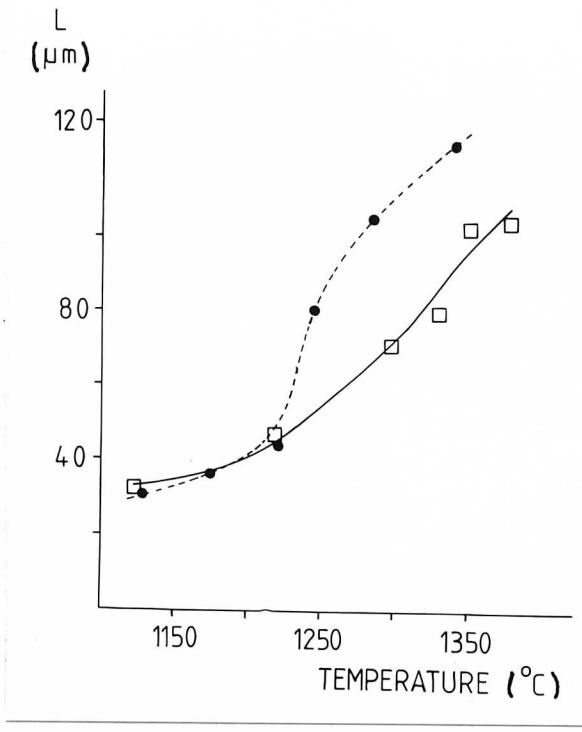

Fig.5.17 Reaustenisation characteristics of welds SA 3 and SA 6. Higher oxygen deposits (□) offer more effective barriers to grain growth than medium oxygen levels (●).

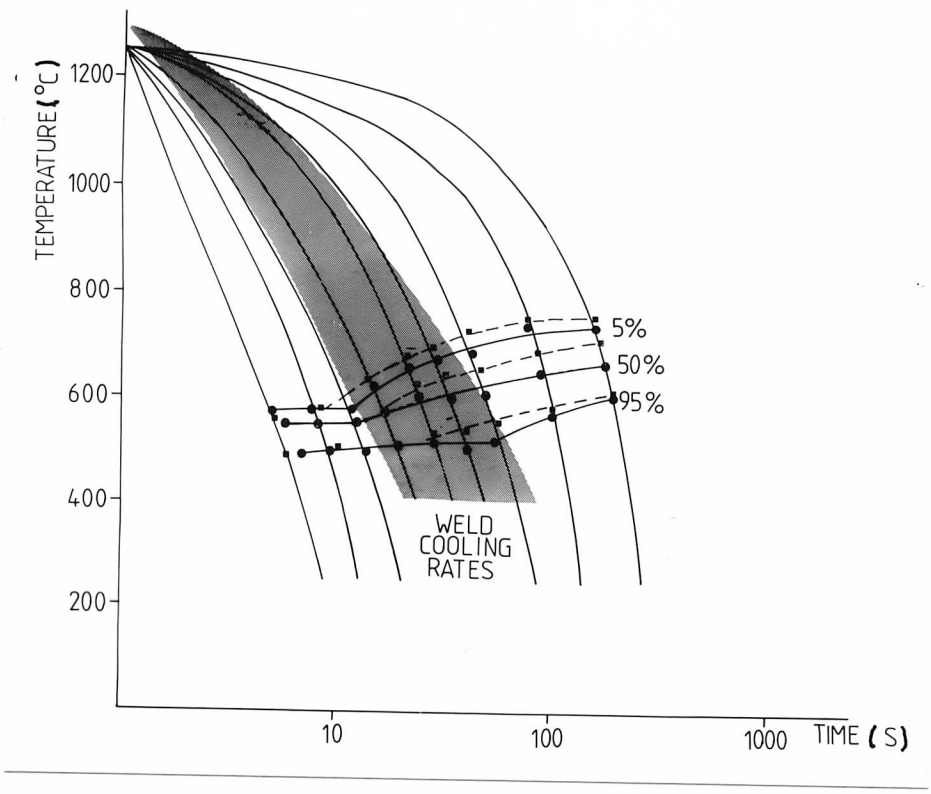

Fig.5.18 Continuous cooling diagrams for welds with different oxygen levels. Higher oxygen deposits (SA 3) transform at significantly higher temperatures than those containing medium oxygen levels (SA 6). The shaded region shows typical weld cooling rates.

----■-- WELD SA 3

——●—— WELD SA 6

It can be seen that the high oxygen weld metal (SA 3) transforms at significantly higher temperatures at typical weld metal cooling rates than the medium oxygen weld metals (SA 6). At faster cooling rates (eg those cooling rates greater than $\approx 40°C/sec$), there is no difference in the transformation start temperature observed. This trend is consistent with previous work reported by Cochrane and Kirkwood (1978), and more recently by Harrison and Farrar (1981) at one selected cooling rate. However, it must be emphasised that, as in the original weld deposit, there is a very significant difference in initial austenite grain size. When specimens from welds SA 3 and SA 6 were heat-treated to identical grain sizes, there was NO detectable difference in the observed start temperature between the two welds at typical weld metal cooling rates, contrary to the claim of Cochrane and Kirkwood (1978).

Direct comparison with the calculated thermodynamic parameters previously established for these welds, eg B_s, M_s temperatures, indicates that at the cooling rates of interest, the transformation range observed experimentally occurs both above and below the calculated isothermal bainite start temperature. This is contrary to the comment by Abson and Dolby (1978), who claimed (but did not report) that transformation was complete above the M_s and B_s temperatures in typical weld materials.

In order to analyse this complex situation, the variation of volume % transformed with time and temperature was experimentally determined at selected cooling rates for weld SA 6. This data, derived dilatometrically, is summarised in Table 5.1 and is the average of four separate determinations at the same cooling rate. On the assumption that the carbon content of the reaction product never exceeds 0.03%C, the composition of the residual austenite can be calculated as follows, assuming no carbide precipitation occurs:

$$X_\gamma = \bar{X} + \frac{V_\alpha (\bar{X} - X_\alpha)}{1 - V_\alpha}$$

Table 5.1 Typical example of the data analysed to establish the 'effective' B_s and M_s curves in Fig. 5.19. The first two columns report the experimental parameters which are the average of four separate determinations. The carbon content (Wt%) of the residual austenite is reported in column three which forms the basis of the calculated B_s and M_s temperatures reported in columns five and six. The W_s is reported as the centre of the observed range since the actual start temperature is known to be sensitive to parameters such as austenite grain size which cannot be accounted for in the current analysis.

TEMPERATURE °C	VOLUME % TRANSFORMED	COMPOSITION OF RESIDUAL AUSTENITE	CALCULATED W_s °C	CALCULATED B_s °C	CALCULATED M_s °C
642	5·5	0·1358	660	573	451
618	16·6	0·1499	"	570	447
578	49·2	0·2261	"	545	412
561	63·0	0·3003	"	521	379
550	76·1	0·4466	"	468	302
525	90·1	1·003	"	248	−106

where $\bar{X}$ = average alloy composition

X_γ = composition of residual austenite

X_α = composition of reaction product

V_α = Volume fraction of reaction product

V_γ = Volume fraction of residual austenite

(ie. $V_\gamma = 1 - V_\alpha$)

Since the carbon content of the residual austenite changes with the extent of transformation, an effective or operative bainite and martensite start temperature can be calculated at any stage of transformation. The result of such calculations are documented in Table 5.1 and plotted with respect to the average cooling rate in Fig.5.19. The locus of the B_s and M_s lines are such that they never exceed the actual cooling curve at any temperatures at the cooling rates considered. Thus the observed reaction products commonly observed in H.S.L.A. steel weld metals can, for the first time, be accurately described as ferrite and Widmanstatten ferrite.

It is interesting to note the changes which occur in the calculated T.T.T. curves, representing the transformation behaviour of the residual austenite as the carbon content of the residual austenite is increased. Such calculations for a slightly slower cooling rate (20°C/sec, ie ≡ 6 kJ/mm) are summarised in Fig. 5.20. The three curves represent carbon contents of 0.13%C, 0.5%C and 1.0%C at the same level of substitutional alloying elements. The curves are progressively suppressed, with the 'bay' regions becoming more pronounced. Further, the incubation time becomes extremely long for both the diffusional ferrite reactions and the bainite reactions at high carbon concentrations. In this case, the calculated M_s is of the order of room temperature after 95% transformation.

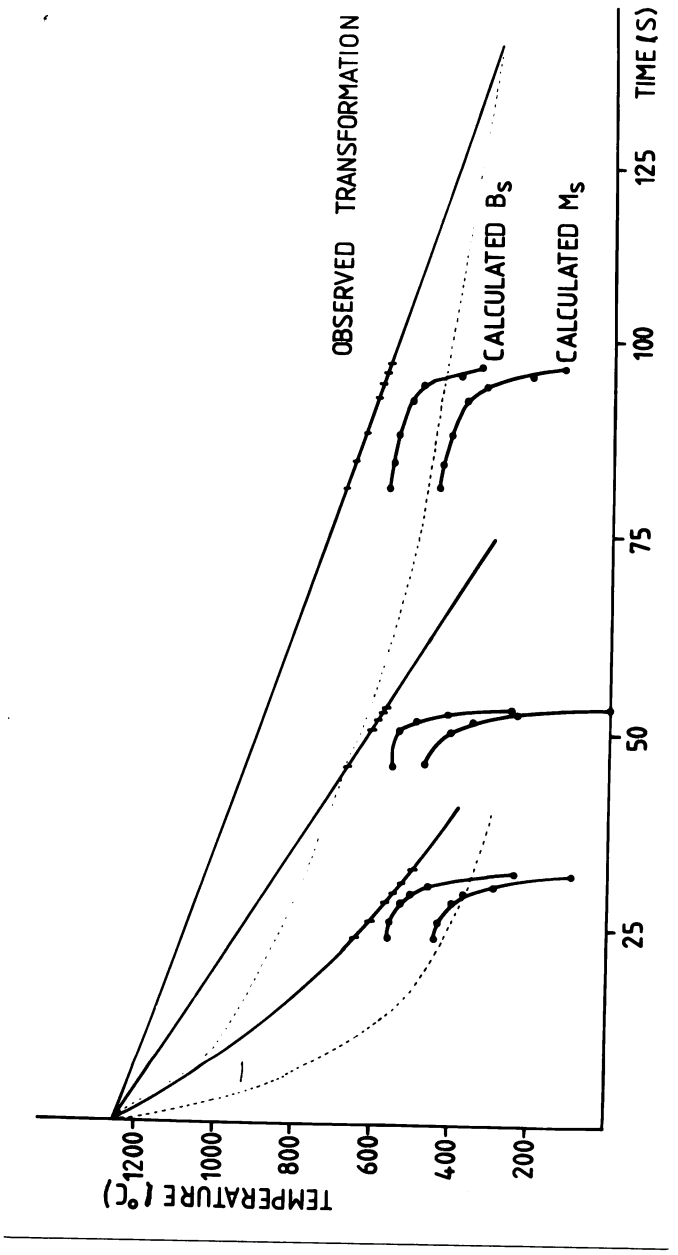

Fig.5.19 A rationalisation of phase transformations in weld metals. In the alloy considered, transformation proceeds entirely above an effective bainite start temperature as shown for three selected cooling rates. The dashed lines indicated weld cooling rates in the range 1.5 to 6.0 kJ/mm.

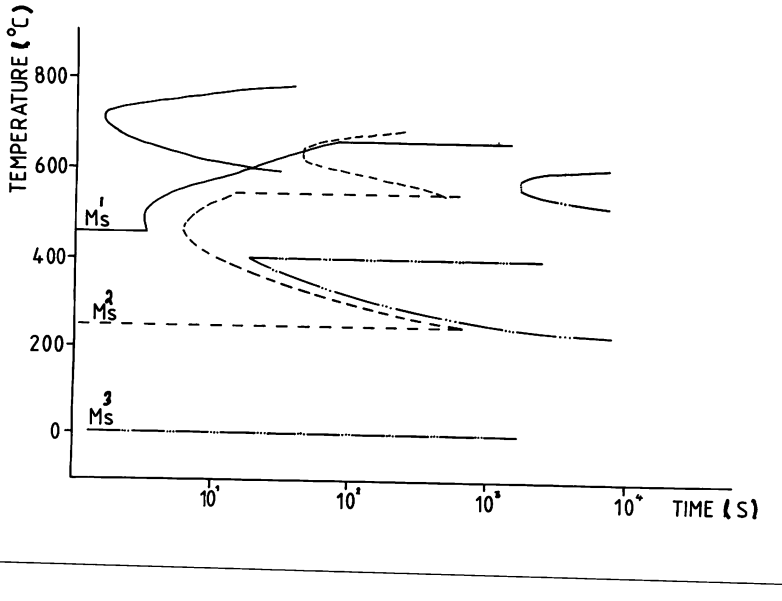

Fig.5.20 Effect of increasing carbon content on the calculated T.T.T.curve for the nominal composition 1.27% Mn, 0.35% Si, 0.25% Mo. The solid curve (-) represents the starting composition. As the carbon enrichment increases (---) the curves are depressed and separated. At high degress of enrichment (1% C by wt.) the curves become completely separated (-..-..-) with the M_s approaching ambient temperatures.

5.4.DISCUSSION

The results described in this chapter have identified both the morphology and the transformation temperature ranges for the upper bainite and Widmanstatten ferrite reactions. In both the isothermal investigation and the continuous cooling study, the calculated thermodynamic temperatures, eg B_s, have been found to be in good agreement with those observed experimentally. The degree of isothermal transformation observed at 650°C in the model steel (Alloy J) was in reasonable agreement with the calculated value based on the work of Bhadeshia. This value is clearly greater than that allowed if the product was upper bainite (ie formed with a full supersaturation).

The morphology of upper bainite observed (both isothermally and under continuous cooling heat treatments) does not resemble that previously reported on the basis of optical microscopy by either Abson and Dolby (1978) or Cochrane (1977). For example, the 'bainite' reported by Abson and Dolby (1978) is shown in Fig.5.21. Their claim that this transformation product enveloped the 'acicular ferrite' microstructure must be viewed with extreme caution, as the microstructure more closely resembles grain boundary ferrite, as noted by Garland (1978). A further point to note is that on the basis of the new morphological scheme proposed by Abson and Dolby (1980) to describe weld metal microstructures, the reaction product identified here as upper bainite would be termed 'ferrite with aligned M-A-C' (martensite-austenite-carbide). Indeed, the actual microstructure used in that scheme (Fig.1.3) closely resembles the microstructure termed upper bainite in this investigation.

While the results have shown that the microstructures reported at typical weld metal cooling rates comprise grain boundary and Widmanstatten ferrite, it should be noted that the analysis cannot

Fig.5.21 Microstructure observed by Abson and Dolby (1978) in C-Mn-Mo submerged arc weld metal. The central feature was described as bainite without directionality.

account for the effect of nucleation site (eg grain boundary or inclusions) or the role of austenite grain size. These parameters will be investigated in subsequent chapters, but on the basis of the limited observation in this work, inclusion nucleation has been observed for the Widmanstatten ferrite reaction and not apparently for the upper bainite reactions. It is still unclear whether this observation reflects the difference in kinetics observed between the two products or a fundamental difference in the nucleation mechanism.

The new concept of an 'effective' or 'operative' bainite start (or martensite start) temperature which varies as a complex function of time, temperature and composition seems a reasonable proposal on the basis of the experimental results analysed. In principle, this procedure can be applied to any cooling rate if accurate experimental data is available and represents an exciting prospect for further research. At present this seems to be the most effective method of analysing continuous cooling data, as an analysis of the problem from first principles is a long way off, since the locus of the effective B_s and M_s temperatures is a complex function of driving force, diffusion coefficients and compositions, all of which vary with time. This method of analysis has also been able to explain the presence of martensite in the final as-deposited microstructure (see Chapter 4), since the predicted M_s temperature is close to room temperature at the highest carbon enrichment measured.

5.5 CONCLUSIONS

1) The results detailed in this chapter have provided further evidence to support the overall concept of two distinct 'C' curves, representing diffusional and displacive transformation under conditions of isothermal heat treatment.

2) The classic morphologies of upper bainite and Widmanstatten ferrite have been established and the observed transformation ranges under conditions of isothermal heat treatment are in good agreement with the calculated thermodynamic parameters proposed by Bhadeshia (1981.1)

3) The microstructure observed at typical weld metal cooling rates previously termed acicular ferrite has been shown to form entirely above an effective bainite start temperature calculated on the basis of the thermodynamic parameters previously discussed.

CHAPTER 6

THE NATURE OF ACICULAR FERRITE IN H.S.L.A. STEEL WELD METALS

6.1 INTRODUCTION

In this chapter the nature of the fine interlocking acicular ferrite microstructure in H.S.L.A. steel weld metals is investigated. The literature concerned specifically with the development of this microstructure will be reviewed and the various models proposed to account for its formation discussed.

The experimental work deals specifically with the development of an acicular ferrite microstructure in two manual metal arc welds (MMA 1,3); however, the same characteristics were established in all the manual metal arc deposits and submerged arc welds considered in this investigation.

6.2 LITERATURE REVIEW

This section will review the literature which deals with the nature and development of the microstructural component commonly called acicular ferrite. The extensive work which deals with the relationship of this constituent to mechanical properties has been discussed in Chapter 4.

Widgery (1974), Watson (1980) and Harrison et al.,(1981) have all noted the confusion in the literature regarding the terminology used to describe this reaction product. As Watson (1980) has noted, this has resulted in the terms Widmanstatten ferrite, fine ferrite, bainitic ferrite, massive ferrite, upper bainite, lower bainite, granular bainite, lath martensite and massive martensite all being used to describe the same product, which in this text is termed acicular ferrite.

The work of Ito and Nakanishi in 1976 represents an important milestone in the welding literature. As well as including an excellent and comprehensive study of the effects of the major alloying elements in submerged arc weld metals, they detailed a unique relationship linking the oxygen content of the weld deposit to its microstructure and toughness. This has become known as 'the oxygen effect'. They observed a peak in toughness at approximately 200ppm of oxygen, corresponding to the development of an acicular ferrite (called fine ferrite by Ito and Nakanishi) microstructure. Both above and below this optimum oxygen level, undesirable microstructural components are prevalent. Though they gave very little microstructural explanation for this effect, they did propose that oxygen was in some way affecting the hardenability of the weld deposit.

The experimental work of Ito and Nakanashi formed the basis on which several theories have subsequently developed to account for the so - called "oxygen effect" . Three main theories have developed to account for the formation of the fine interlocking acicular ferrite microstructure, and these theories are described below.

Abson and Dolby, in their in review in 1978, proposed three regions of behaviour, depending on the oxygen content of the weld deposit. These are summarised in Figs 6.1 (a) (b) (c) and refer to

(a) Low oxygen weld metal (0.01%)

(b) Medium oxygen weld metal (0.03 - 0.04%)

(c) High oxygen weld metal (0.06 %)

Using these schematic C.C.T. diagrams (Figure 6.1), they proposed that the oxygen content was affecting the hardenability of the higher ferrite transformation products in a complex manner. In both high and low oxygen regimes, ferrite sideplates were found to be the predominant microstructure, this being indicated by a shift in the 'ferrite sideplate phase field'

(a) LOW OXYGEN

0.01 % O_2

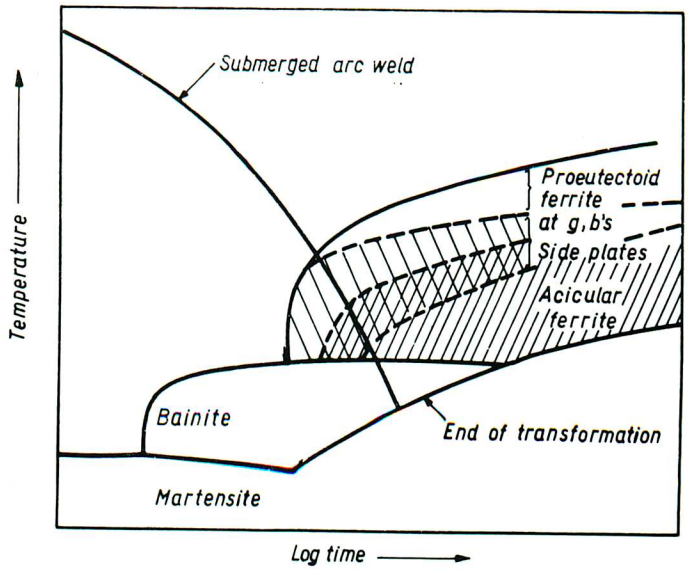

(b) MEDIUM OXYGEN

0.03 -0.04% O_2

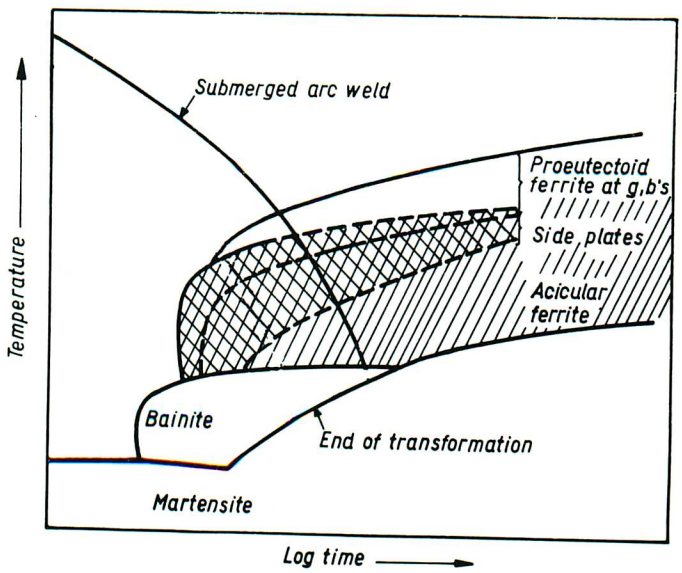

(c) HIGH OXYGEN

0.06% O_2

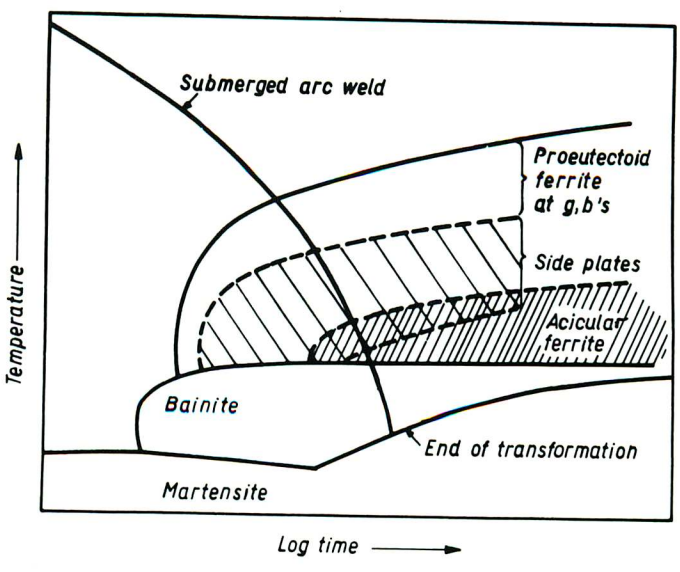

Fig.6.1 Schematic C.C.T. diagrams proposed by Abson and Dolby (1978) - for discussion see text.

being moved to shorter times. In addition, they invoked the idea of inclusion nucleation of the acicular ferrite phase in the medium oxygen regime. In the other regimes, high and low oxygen, the inclusions were termed to be 'ineffective' and 'insufficient', but no explanation could be offered to explain why the acicular ferrite microstructure developed only over a limited range of oxygen contents. They further postulated that the inclusion type and size distribution could be important factors in controlling the final transformation microstructure.

Further work by Abson et al (1978) confirmed the overall behaviour of the three oxygen regimes. However, in this investigation, neither the inclusion type or the relevant inclusion size distribution had been established. Watson (1980) has pointed out that this investigation did not succeed in separating the effects of oxygen, cooling rate and possible variations in prior austenite grain size, which all have a complex role to play in controlling the development of the final microstructure.

Kirkwood (1978) and subsequently Cochrane and Kirkwood (1978) studied the so-called 'oxygen effect' in both shielded arc and submerged arc weld deposits. The work of Kirkwood (1978) confirmed the work of Ito and Nakanishi (1976), in that high oxygen deposits were associated with poor microstructure and toughness and also showed that nitrogen was not a contributing factor. Cochrane and Kirkwood (1978) showed, using high speed dilatometry, that during the γ to α transformation, high oxygen weld metals transformed at significantly higher temperatures than those weld deposits containing lower oxygen levels. They further proposed that this was due to preferential nucleation of ferrite side plates on large inclusions in the prior austenite grain boundaries. They introduced a schematic model to account for this and concluded that the inclusion size distribution and the surface energy of the inclusion /matrix interface were important factors.

of the final microstructure.

In this case. They deconsetrated

Two main criticisms may be made of these claims. Firstly, the importance of the smaller austenite grain size (which they observed in the high oxygen welds) in determing the austenite to ferrite transformation temperature itself was overlooked. Secondly, the claim that during their dilatometric investigation a constant γ grain size had been achieved must be viewed with suspicion. Reaustenitising high and medium oxygen weld metals for the same time and temperature is unlikely to produce the same austenite grain size. Indeed, the effective pinning of grain boundaries by large inclusions is central to their main argument.

The discussion session following the conference where these two theories were proposed provided insight into the development of microstructure. Cochrane (1978), in a written contribution, documented further evidence to support the claim that it was the preferential nucleation of ferrite on inclusions in austenite boundaries which was responsible for the higher transformation temperature observed in high oxygen weld metal. He further claimed that the development of the acicular ferrite microstructure could be adequately covered by the theories of homogeneous nucleation and refuted the claim that there was a one to one correspondence between the number of inclusions and the number of ferrite laths, claiming there were insufficient inclusions.

It was at this stage that the current investigation commenced in an attempt to resolve the question posed by Abson and Dolby in their reappraisal of weld metal microstructures (1978):

> 'Why does acicular ferrite arise in weld metals only over a restricted range of oxygen contents' ?

In addition, there remained several other questions to be resolved in that the nature of acicular ferrite microstructure itself had not been clearly established. In the previous investigations discussed, the authors

had speculated that the inclusion type could be an important factor in terms of inclusion nucleation of the ferrite component. However, no identification of the inclusions present in the welds examined had been carried out in any of these studies.

The third proposal regarding the development of an acicular ferrite microstructure was presented by Watson (1980), who criticised the work of both Abson (1978) and Cochrane (1978), claiming that they had not satisfactorily accounted for the small variations in alloying elements in their experimental work. Further, he pointed to the fact that no direct evidence to support their claims had been presented. He concluded that acicular ferrite was a form of granular bainite as described by Habraken and Economopoulos (1967). In this manner, the microstructure is considered to develop because a dehomogenisation occurs before the B_s is reached leading to carbon enriched areas. Thus the nucleation of 'ferrite' then occurs in the same manner as the formation of martensite in carbon free alloys. He further proposed that this can account for the high dislocation density observed in the acicular ferrite component and the nature of the so called microphase regions.

More recent work of this school (Farrar and Watson, (1979)) proposes that the main factor controlling the development of an acicular ferrite microstructure is the manganese level in the weld deposit. Specifically, they claim that a threshold value of 1.1% Mn exists in the weld metal matrix, below which an acicular ferrite microstructure will not develop.

However, the results of recent thermodynamic analysis (eg Bhadeshia (1979)), would strongly refute this as a possible mechanism for a bainite reaction. Further, the acicular ferrite microstructure does not resemble the reaction products described by Habraken and Ecomomopoulos (1967).

Summarising, the three theories which have been proposed to account for the development of an acicular ferrite microstructure are,

1) Abson & Dolby (1978) - Inclusion nucleation of acicular ferrite.

2) Cochrane (1978) - Homogeneous nucleation of acicular ferrite.

3) Watson (1980) - Formation of acicular ferrite by a mechanism similar to that of granular bainite -% Mn being a controlling factor.

6.3 NUCLEATION THEORY

6.3.1. Introduction.

In this section, classical nucleation theory will be used to consider the effects of spherical inclusions on the nucleation of ferrite. The notation for free energy in this chapter follows that of Johnson et al (1975).

6.3.2. Solid State Nucleation

The nucleation barrier which must be overcome before a stable nucleus of ferrite may be formed, for the homogeneous nucleation of ferrite in austenite may be written as -

$$\Delta G^{*}_{h/unf} = \frac{16\pi \sigma^{3}_{\gamma/\alpha}}{3\ \Delta G_V^{2}}$$

where :- $\Delta G^{*}_{h/unf}$ = nucleation barrier for homogenous nucleation of an unfaceted nucleus.

$\sigma_{\gamma/\alpha}$ = Surface energy of the austenite/ferrite interphase boundary.

ΔG_V = Volume free energy change associated with the formation of ferrite from austenite.

The formation of a critical nucleus involves the random addition of atoms to an already energetically unfavourable situation, hence it is clear that the nucleus shape with the lowest surface to volume ratio will reach the critical size preferentially and become stable. Johnson et al (1975) investigated the effects of both faceting the nucleus and incorporating it into grain boundaries of the parent phase, on the magnitude of ΔG^*. These results were normalised with respect to $\Delta G^*_{h/unf}$ and then compared to determine the probable shape of a critical nucleus. In the following section, the same geometrical approach will be used to calculate the ΔG^* for the formation of a stable ferrite nucleus on a spherical inclusion.

6.3.3. Derivation of ΔG^* for nucleation of ferrite on spherical inclusions.

In this derivation, inclusions will be considered as hard, inert non-deformable substrates on which nucleation can take place. Fig. 6.2 shows a schematic illustration of a ferrite nuclei formed on a spherical inclusion. The inclusion will be assumed to be inert with no epitaxial growth occurring between the inclusion and the ferrite nucleus (this will be considered in Chapter 8). The boundary between the ferrite nucleus and the inclusion will be taken as disordered, and of similar energy to a disordered austenite/ferrite boundary. Simple consideration of the surface energy balance at the austenite ferrite inclusion triple point indicates that under the conditions outlined above, the angle formed by the austenite ferrite interface and the inclusion surface will be a right angle.

The volume of the nucleus shape shown in Fig.6.2 will be given by

$$V^1 = V_s - (V_{c1} + V_{c2})$$

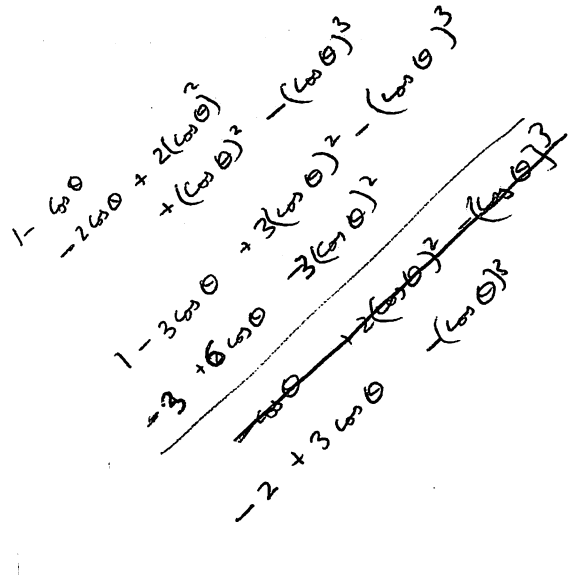

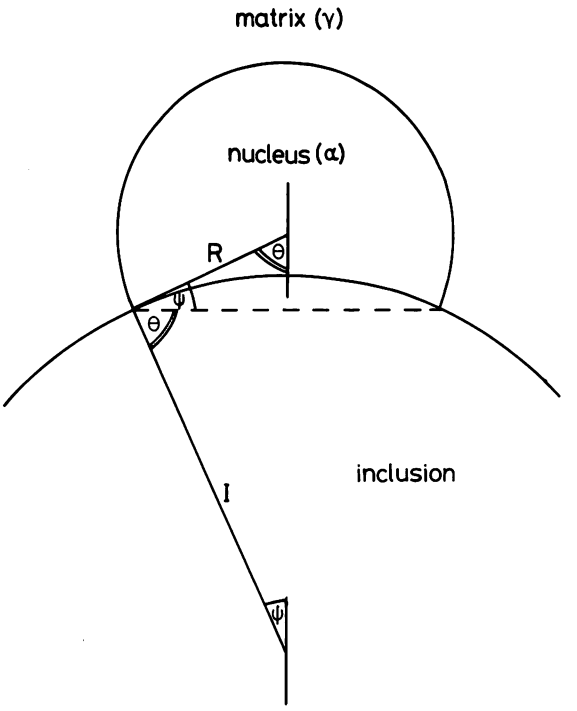

Fig.6.2 Schematic diagram showing the model used to analyse the nucleation of ferrite on weld metal inclusions.

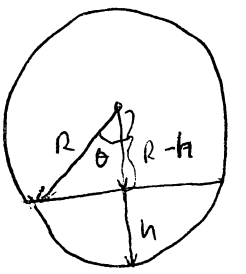

$$\cos\theta = \frac{R-h}{R} = 1 - \frac{h}{R}$$

$$\frac{h}{R} = 1 - \cos\theta$$

$$V_{\text{Shape}} = \frac{1}{3}\pi h^2 (3R - h)$$

$$= \frac{1}{3}\pi 3R^3 (1-\cos\theta)^2 - \frac{1}{3}\pi R^3 (1-\cos\theta)^3$$

$$= \pi R^3 \left[1 - 2\cos\theta + (\cos\theta)^2 \right.$$

where

V_s = Volume of sphere of radius R, where R is the radius of the nucleus

V_{c1} = Volume of spherical segment due to sectioning of the nucleus

V_{c2} = Volume of spherical segment due to intrusion into nucleus

Using appropriate formulae this gives

$$V^1 = \frac{4}{3}\pi R^3 - \left[\frac{1}{3}\pi R^3 \; f(\theta) + I^3 \; f(\Psi)\right]$$

$\frac{1}{3}\pi I^3 f(\Psi)$

where I = inclusion radius

R = nucleus radius

Ψ, θ as shown in Figure 6.2.

$$f(\Psi,\theta) = 2 - 3\cos(\Psi,\theta) + \cos^3(\Psi,\theta)$$

(see Johnson et al (1975))

The surface area of the nucleus is given by

$$A^1 = A_s - A_{c1} + A_{c2}$$

where

A_s = surface area of sphere of radius R

A_{c1} = surface area of nucleus lost due to sectioning.

A_{c2} = surface area of nucleus in contact with inclusion.

Thus the actual surface area increase created in forming the nucleus is

$$S^1 = A^1 - A_{c3}$$

where

A_{c3} = area of boundary between austenite and inclusion lost in forming the nucleus.

Since it is assumed $\sigma_{\gamma/INC} = \sigma_{\alpha/INC}$

where $\sigma_{\gamma/INC}$ = Surface energy between austenite and inclusion.

$\sigma_{\alpha/INC}$ = Surface energy between ferrite and inclusion

it follows that

$$S^{(1)} = A_s - A_{c1}$$

Again, using appropriate formulae this gives $S^{(1)}=4\pi R^2 - 2\pi R^2(1-\cos\theta)$

These formulae enable the free energy change associated with the formation of the nucleus to be calculated

$$\Delta G_{inc/unf} = V^1 \Delta G_v + S^1 \sigma_{\gamma/\alpha} \qquad (1)$$

where the subscript inc and unf refer to 'inclusion' and 'unfaceted' respectively.

Figure 6.3 shows a plot of $\Delta G_{inc/unf}$ as a function of nucleus radius calculated using typical values of I, ΔG_v and $\sigma_{\gamma/\alpha}$ (see Figure caption). It is clear that as the radius increases, $\Delta G_{inc/unf}$ first increases, reaches a maximum and finally decreases. The maximum positive value of $\Delta G_{inc/unf}$ is the barrier to nucleation, $\Delta G^*_{inc/unf}$.

The nucleation barrier (ΔG^*) may be obtained by differentiating equation (1) with respect to R, equating to zero and substituting this value of R in equation (1).

Figure 6.4 shows the variation of $\Delta G^*_{inc/unf}$ as a function of inclusion radius (I) (the values have been normalised to $\Delta G^*_{h/unf}$. The shape of this curve is such that at small inclusion radii, the nucleation barrier is similar to that for homogeneous nucleation. As I increases, the inclusions become more effective sites for nucleation and the value of $\Delta G^*_{inc/unf}$ decreases. It must be noted, however, that this value never reaches that associated with grain boundary nucleation, which is shown in Figure 6.4 for comparison purposes.

A similar analysis may also be performed for the derivation of the nucleation barrier for a faceted nucleus on an inclusion shown schematically in Figure 6.5. Facets will generally occur when an orientation relationship develops between the austenite and ferrite and

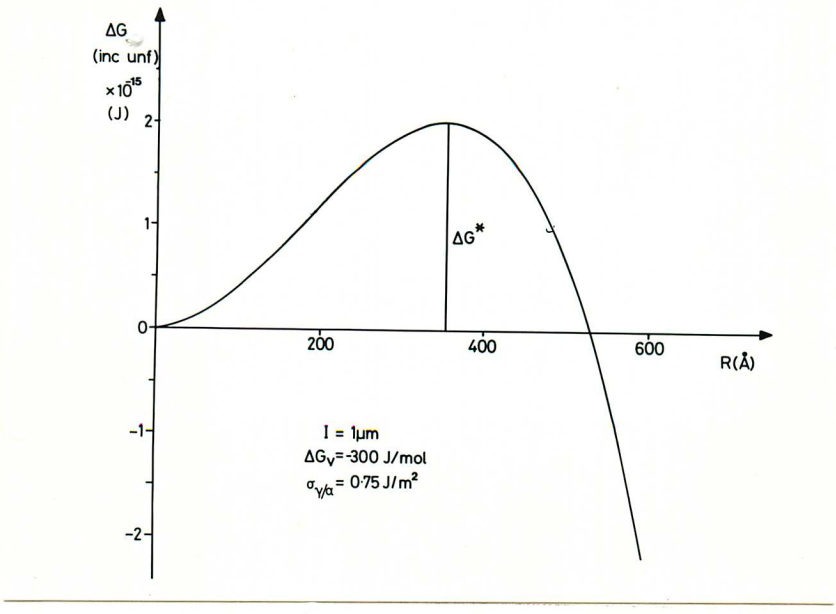

Fig.6.3. Plot of free energy barrier change for nucleation for an unfaceted nucleus on an inclusion (ΔG inc.unf.) as a function of nucleus radius.

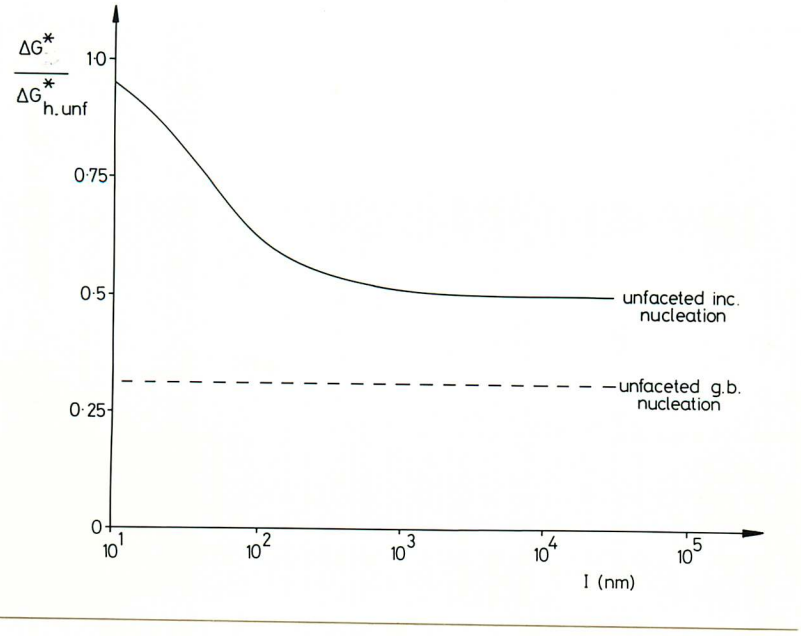

Fig.6.4 Plot of the normalised energy barrier to nucleation for an unfaceted nucleus on an inclusion (ΔG^* inc. unf) as a function of inclusion radius.

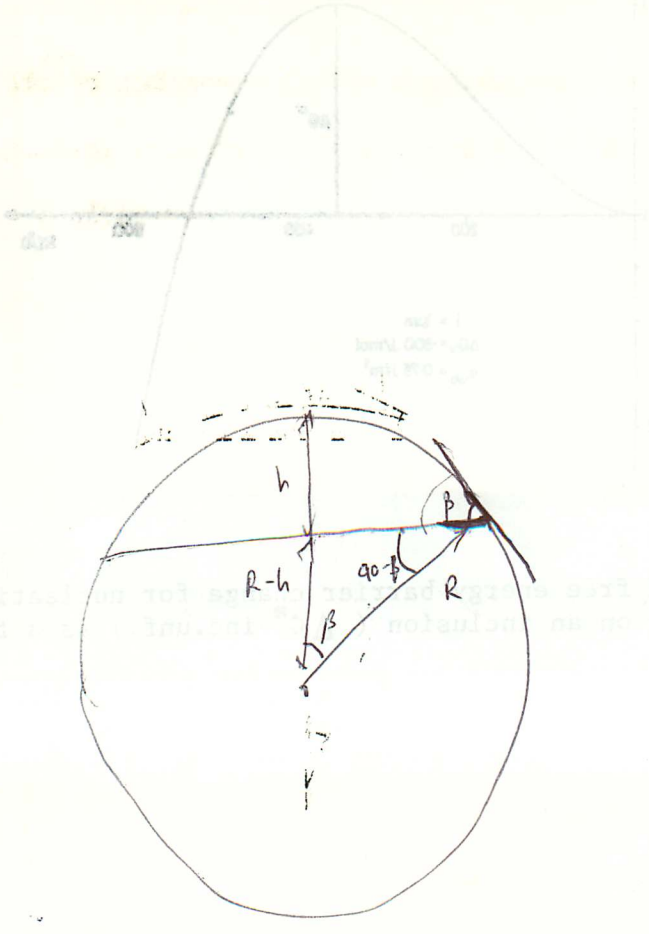
h
β
R-h
90-β
R

will reduce the energy barrier to nucleation. For the case of a faceted nucleus on a spherical inclusion the following relationships are used to obtain $\Delta G^*_{inc/f}$.

$$V^2 = V_s - (V_{c1} + V_{c2} + V_{c3})$$

where V_{c3} = Volume of nucleus lost by the formation of the facet.

The volume V_{c3} will be defined by the ratio of surface energies of the facet and the disordered γ/α boundaries. If this ratio is known, then

$$V_{c3} = \frac{4}{3}\pi R^3 \, (f(\beta))$$

where $f(\beta) = 2 - 3\cos\beta + \cos^2\beta$

and $\cos\beta = \dfrac{\sigma_{\gamma/\alpha}}{\sigma_{F\ \gamma/\alpha}}$

where $\sigma_{F\ \gamma/\alpha}$ = Surface energy of facet

The increase in surface area associated with the formation of a faceted nucleus on an inclusion is given by

$$S^2 = A_s - A_{c1} - A_{c4} + A_f$$

where A_{c4} = area of sphere lost by forming a facet

A_f = area of facet

using standard formulae this gives

$$S^2 = \pi R^2 \left[4 - 2(1-\cos\theta) - 2(1-\cos\beta) + (1-\cos\beta)^2 \right]$$

Thus the values of ΔG associated with the formation of a faceted nucleus on an inclusion may be written as

$$\Delta G_{inc/f} = V^2 . \Delta G_V + (S^2 - A_f)\sigma_{\gamma/\alpha} + A_f \sigma_{F\ \gamma/\alpha}$$

This function has the same form as that shown in Fig.6.3. The value of $\Delta G^*_{inc/f}$, again normalised to $\Delta G^*_{h/unf}$ is shown in Fig.6.6 as a function of inclusion radius I. The addition of a facet to the nucleus considerably lowers the value of ΔG^* but never reaches that of grain boundary nucleation.

The results of this analysis may be summarised as follows:-

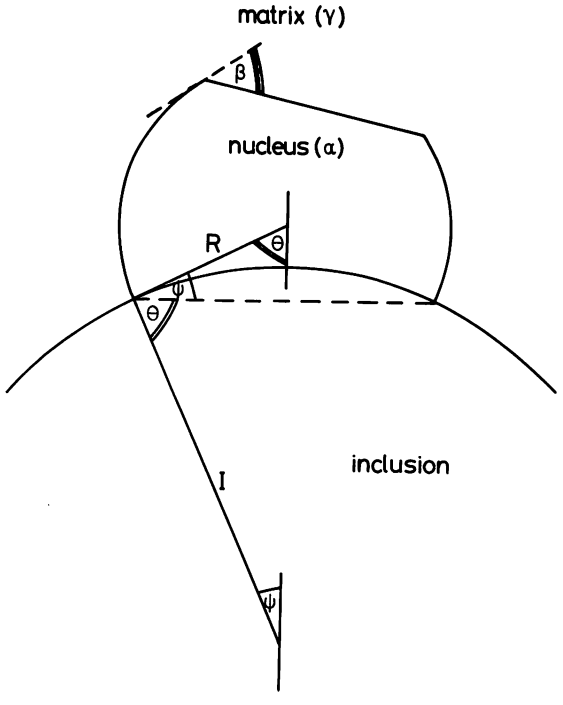

Fig.6.5 Schematic diagram showing the model used to analyse the nucleation of ferrite on weld metal inclusions. In this case a faceted nucleus is considered.

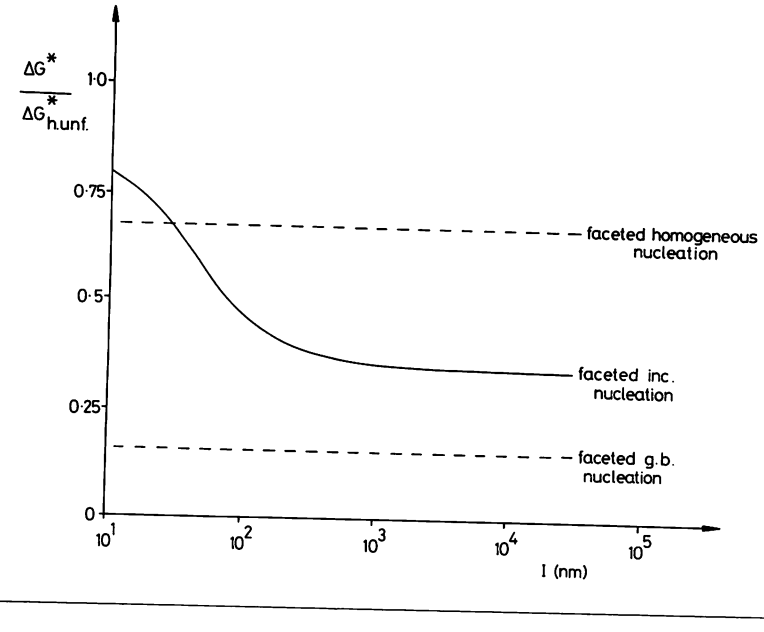

Fig.6.6 Plot of the normalised energy barrier to nucleation for a faceted ferrite nucleus on an inclusion (ΔG^* inc/f.). For comparison purposes the relative energy barriers to nucleation on austenite grain boundaries are also indicated (ΔG^* g.b/f.).

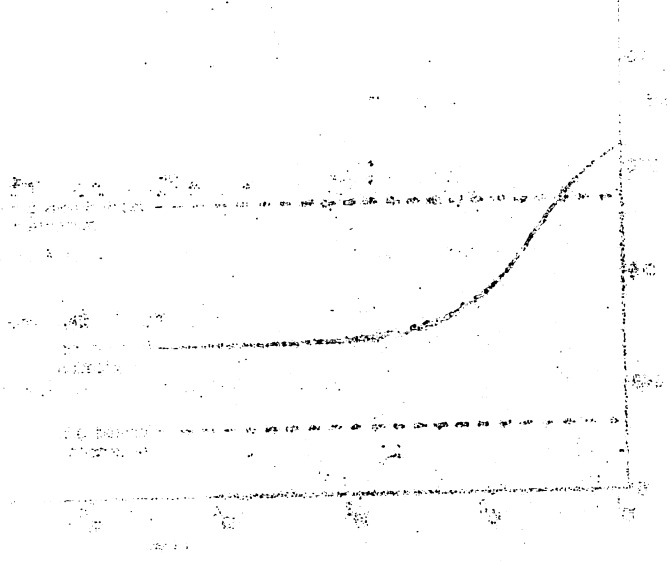

1) Irrespective of the radius of the inclusion, the nucleation barrier associated with inclusion nucleation is always less than that for homogeneous nucleation, but greater than that for the formation of an equivalent grain boundary nucleus

2) The formation of a facet on the ferrite nucleus will reduce the energy barrier for inclusion nucleation in the same manner as that for grain boundary and homogeneous nucleation described by Johnson et al (1975).

6.3.4. SYMPATHETIC NUCLEATION

The previous section has established the main geometrical factors governing inclusion nucleation of intragranular ferrite. It is also instructive to speculate that if inclusion nucleation of ferrite does occur, a new interface has been created in the intragranular regions. It seems likely that this austenite/ferrite interface could also become an active nucleation site for the further ferrite transformation in the manner identified by Aaronson (1956) and subsequently (1962).

He defined a process of SYMPATHETIC NUCLEATION as "the nucleation of a precipitate crystal at the interphase boundary of a previously formed crystal of the same phase". The criteria which must be established to uniquely identify the operation of this mechanism in a given system are as follows.

1) The grain considered must not be in contact with a grain boundary in the parent phase.

2) The spatial distribution of the sympathetically nucleated feature must be such as to preclude the possibility that the plane of section has concealed a grain boundary in the parent phase.

3) The boundary which separates the sympathetically nucleated plate and the parent substrate must not have risen by a process of polygonisation within a single crystal.

While noting that sympathetic nucleation occurred most frequently with Widmanstatten morphology in both non-ferrous (eg. Ti - 7%Cr) and ferrous systems, he outlined briefly the criteria for sympathetic nucleation of Widmanstatten ferrite. Summarising, the most likely situation leading to this configuration would be if the sympathetically nucleated ferrite formed at a high energy facet on the austenite/ferrite boundary, creating a low energy ferrite/ferrite boundary.

6.4 EXPERIMENTAL PROCEDURE

This chapter deals with two manual metal arc weld deposits, MMA 1 and MMA 3, which were deposited using a Tensitrode 55 basic low hydrogen electrode at a heat input of 1.5 kJ/mm. Weld MMA 1 was allowed to cool naturally to room temperature, whereas weld MMA 3 was quenched into iced-brine immediately welding was complete, in order that the sequence of microstructural development could be followed.

6.5 RESULTS

6.5.1. The nature of acicular ferrite

The fully transformed microstructure of weld MMA 1 is shown in Figure 6.7. Proeutectoid ferrite has formed on the prior austenite grain boundaries (arrowed in Figure 6.7), whilst the interior of the austenite grains comprise the fine interlocking constituent which has been termed acicular ferrite.

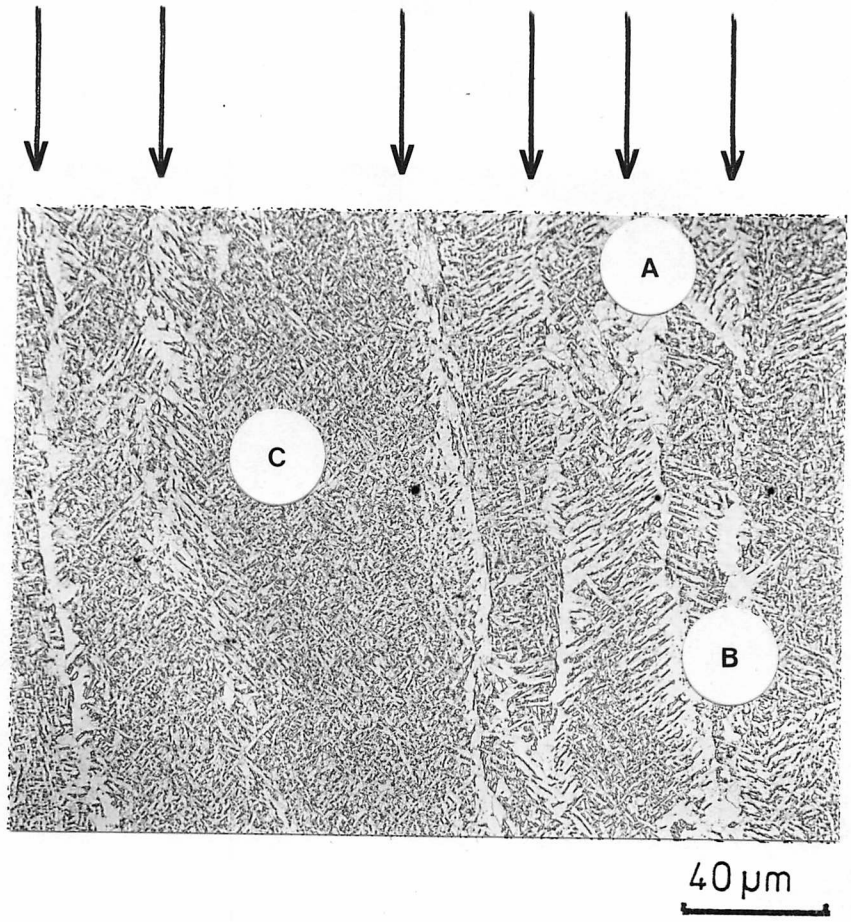

Fig.6.7 Optical micrograph of weld MMA 1. Typically the microstructure comprises of three constituents - equiaxed proeutectoid ferrite (eg. at A), grain boundary nucleated Widmanstätten sideplate (eg at B) and predominantly the acicular ferrite constitutent (eg. at C).

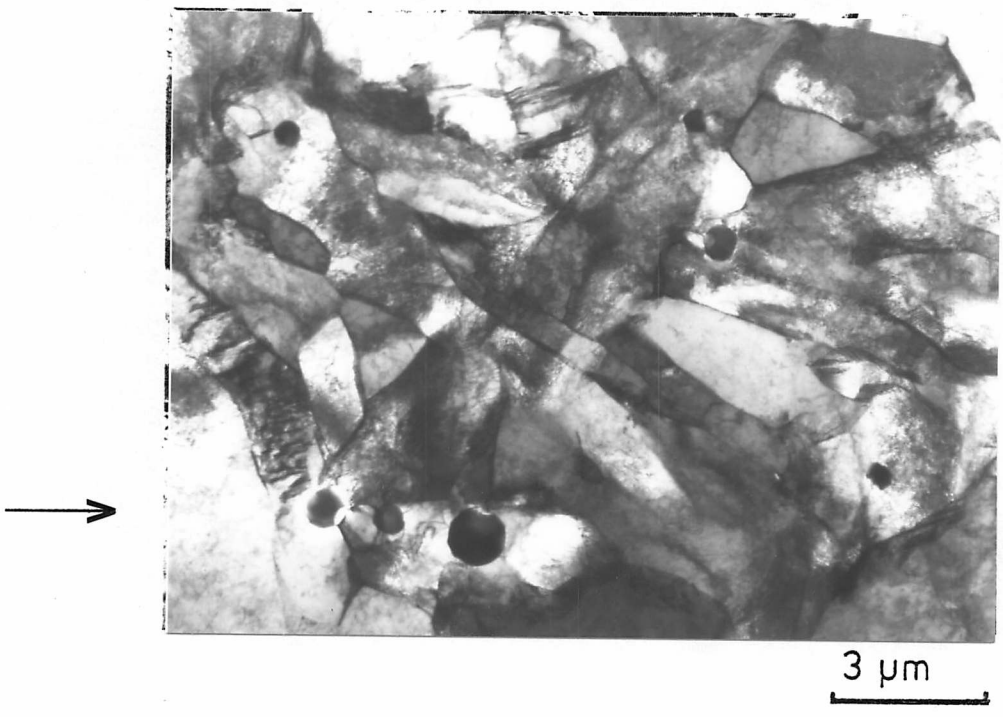

Fig. 6.8 Transmission electron micrograph of the intragranular region of weld MMA 1. The microstructure comprises the fine acicular ferrite constituent.

Transmission electron microscopy of thin foil specimens indicated that the acicular ferrite constituent comprised fine ferrite plates, as shown in Fig.6.8 (a prior austenite grain boundary is arrowed where coarse grain boundary allotriomorphs can also be seen). Fig. 6.9 shows that individual laths contained a relatively high dislocation density and some recovery of the dislocation sub-structure has occurred (eg. at A in Figure 6.9). No evidence of carbide precipitation was observed either within the laths themselves, or at the lath boundaries. Evidence for carbon enrichment of the untransformed austenite was provided by the observations of ferrite/carbide aggregate regions as indicated in Fig. 6.10. These areas closely resemble the morphology of degenerate pearlite found in a number of isothermally transformed steels eg Ohmori and Honeycombe (1971).

6.5.2 The nucleation of acicular ferrite

Fig. 6.11 shows the partially transformed (MMA 3) microstructure produced by ice-brine quenching. Again, proeutectoid ferrite has formed on the austenite grain boundaries (arrowed), whilst the interior of the austenite grains are now seen to contain isolated intragranular ferrite plates (eg. at A) in a martensitic matrix, which was formed during the quench. Carbon extraction replicas from this region show clearly there is an apparent association between the intragranular ferrite and weld inclusions. Figs. 6.12 and 6.13 show examples where intragranular ferrite plates are associated with one (Fig.6.12) and two (Fig.6.13) weld metal inclusions. The nature of similar inclusions will be discussed extensively in Chapter 7, but the general characteristics are summarised in Figs. 6.14 (a) and (b), which show typical spectra obtained from the centre and periphery of the inclusions, indicating they are mixed oxides of Al, Mn, Si, Ti with an outer coating rich in sulphur.

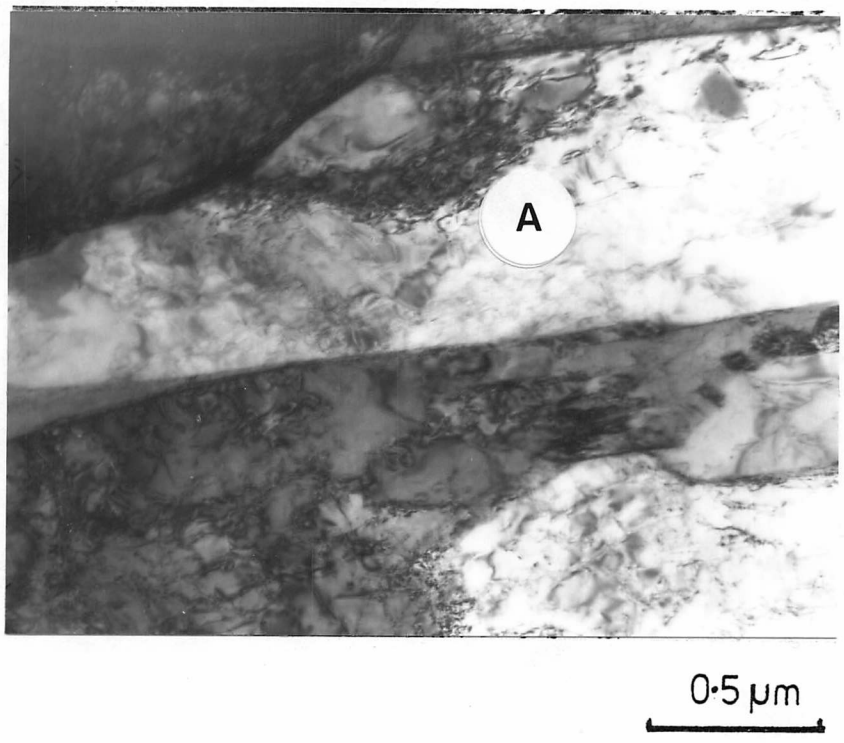

Fig.6.9 Transmission electron micrograph illustrating the relatively high dislocation density of the ferrite constituent in weld MMA 1.

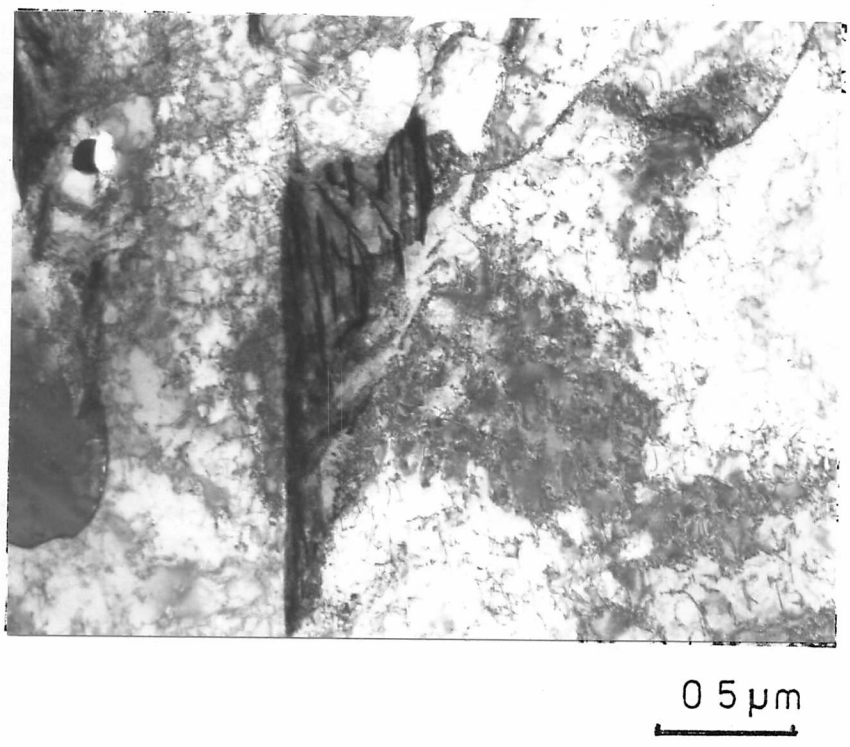

Fig.6.10 Transmission electron micrograph showing the morphology of ferrite/carbide aggregate in weld MMA 1.

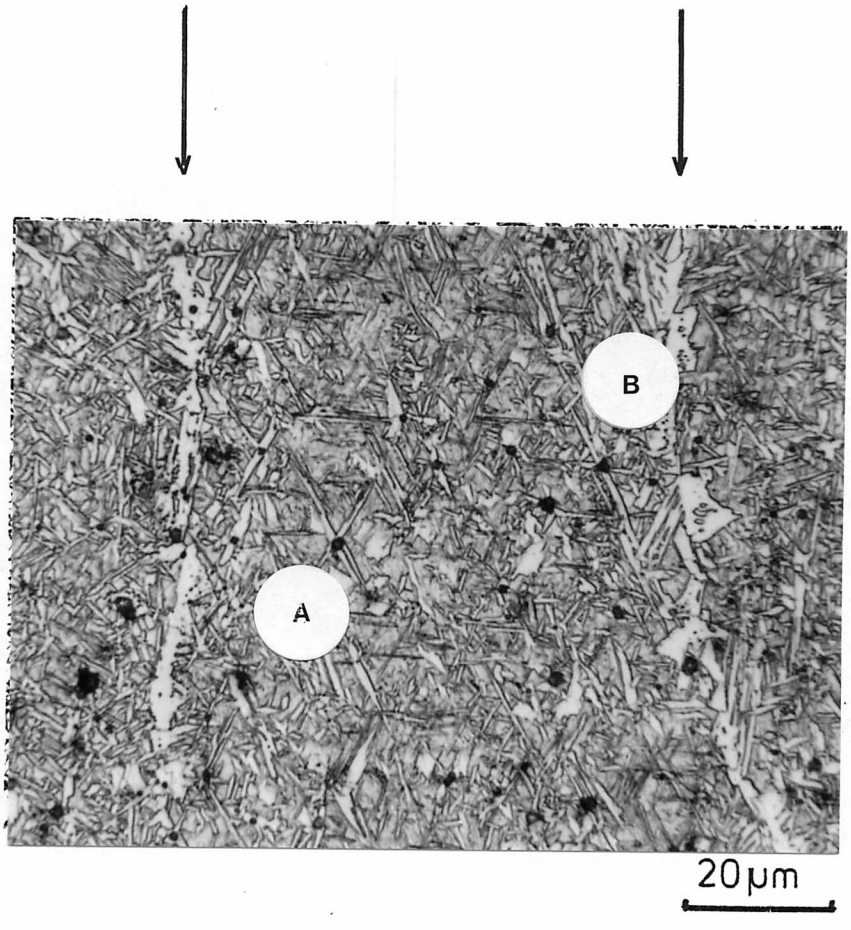

Fig.6.11 Light optical micrograph of the partially transformed weld metal. Proeutectoid ferrite has formed on the austenite grain boundaries (arrowed). Nucleation of intragranular Widmanstätten ferrite has also occurred (e.g. at A) and a close association between this ferrite and the weld metal inclusions is often observed (e.g. at B). Within one austenite grain there appeared no obvious relationship between nucleation sites and the solidification structure (as revealed by solute sensitive etches) or to the direction of maximum heat extraction.

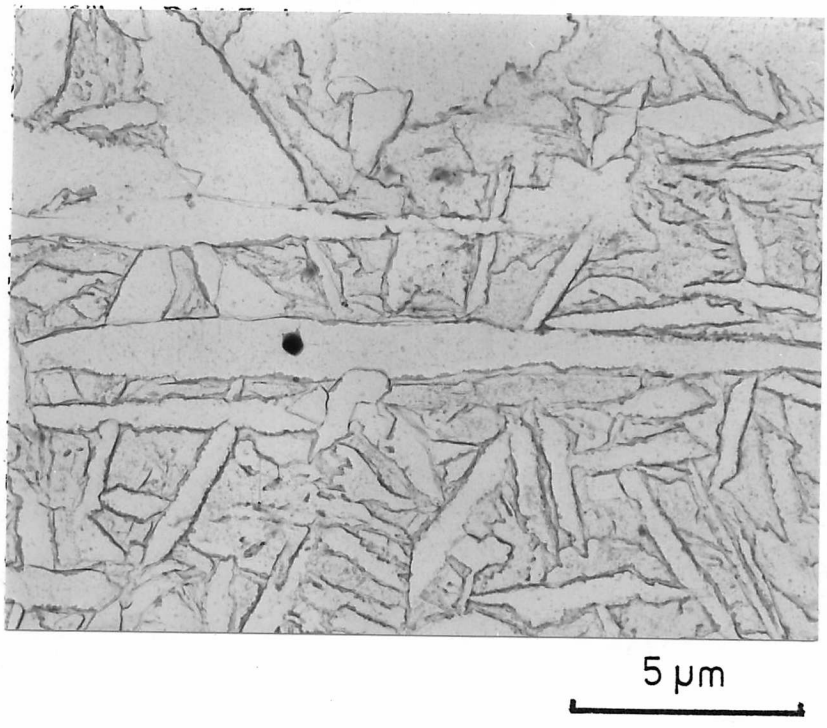

Fig.6.12 Transmission electron micrograph illustrating the association between weld metal inclusions and Widmanstätten plates.

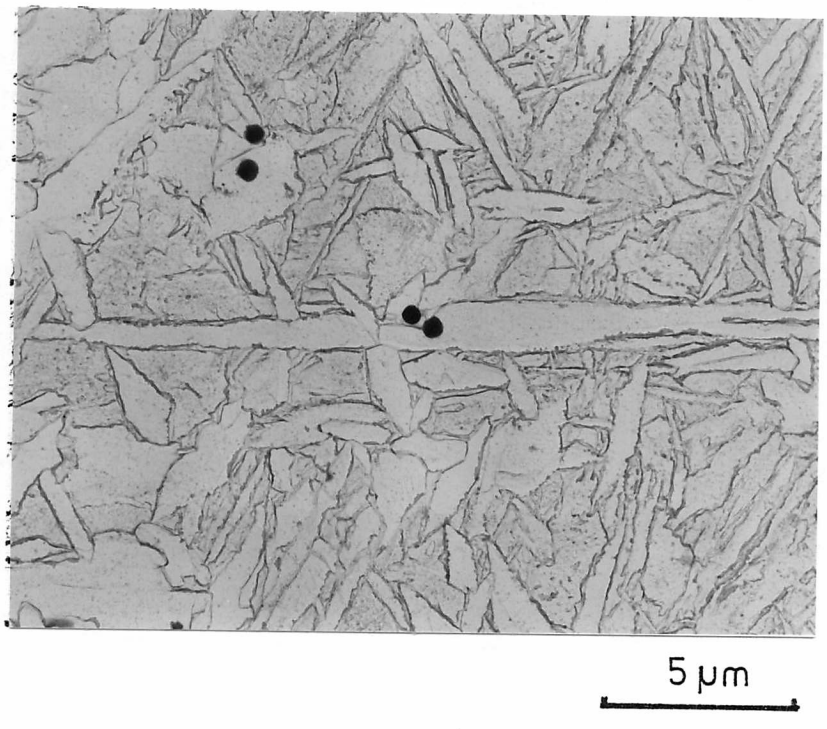

Fig.6.13 Transmission electron micrograph illustrating the association between two weld metal inclusions and Widmanstätten plates.

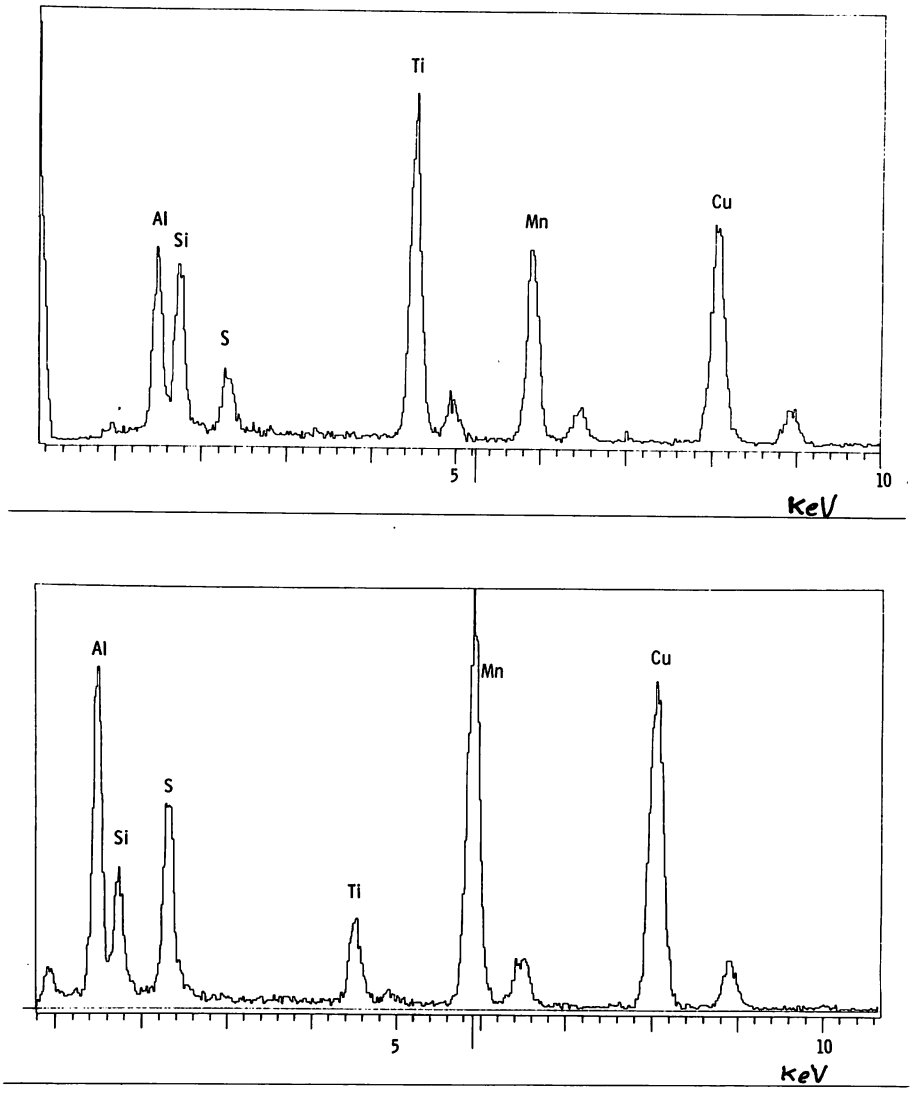

Fig.6.14 Typical X-ray spectra from a single inclusion using a 10 nm probe.
(a) Spectra from the centre of the inclusion. The major peaks present are Al, Si, S, Ti and Mn. The Cu peak arises from the support grid and is not characteristic of the inclusion.
(b) Spectra from the edge of the same inclusion. Although the same peaks are still present, their relative magnitudes have changed. From these and other similar spectra, it is suggested that the periphery of the inclusion is rich in sulphide.

Examination of the partially transformed regions revealed the presence of both retained austenite (Fig.6.15) and twinned martensite (Figure 6.16), which suggest during the growth of acicular ferrite, significant carbon enrichment of the untransformed austenite occurs. The morphology of these intragranular plates strongly resemble intragranular Widmanstatten plates reported by Aaronson (1962), who noted that such plates were also frequently inclusion nucleated. They are not characteristic of intragranular bainite plates which Aaronson also reported, which had typically a sheaf structure.

The association between the intragranularly nucleated Widmanstatten plates and weld metal inclusions was confirmed using transmission electron microscopy of thin foil specimens. Figs. 6.17 and 6.18 show clearly that Widmanstatten ferrite plates have nucleated on both one and two inclusions.

In many instances, however, it was found that multiple ferrite nucleation occurred at an inclusion, as shown in Fig.6.17, where a single inclusion has nucleated plates a, b, c, whilst in Figure 6.18, four Widmanstatten plates (a-d) are seen to radiate from two closely spaced inclusions. This latter image closely resembles the 'Widmanstatten Star' reported by Aaronson and Wells (1956). In some cases, the nucleation of ferrite close to inclusions had occurred not on the inclusion/austenite interface, but on existing ferrite laths. This is shown in Figs 6.19 (a) and (b) which show a bright field (a) and dark field (b) image of such a plate.

Since these inclusions have been shown to be manganese and silicon rich, it might be expected that the adjacent austenite might be lower than that well removed from the inclusions. This in turn could lead to a change in the driving force for ferrite nucleation at the inclusion. Application of S.T.E.M./E.D.S. techniques show that no detectable variation in either Mn or Si levels are present. The results of a typical analysis are shown

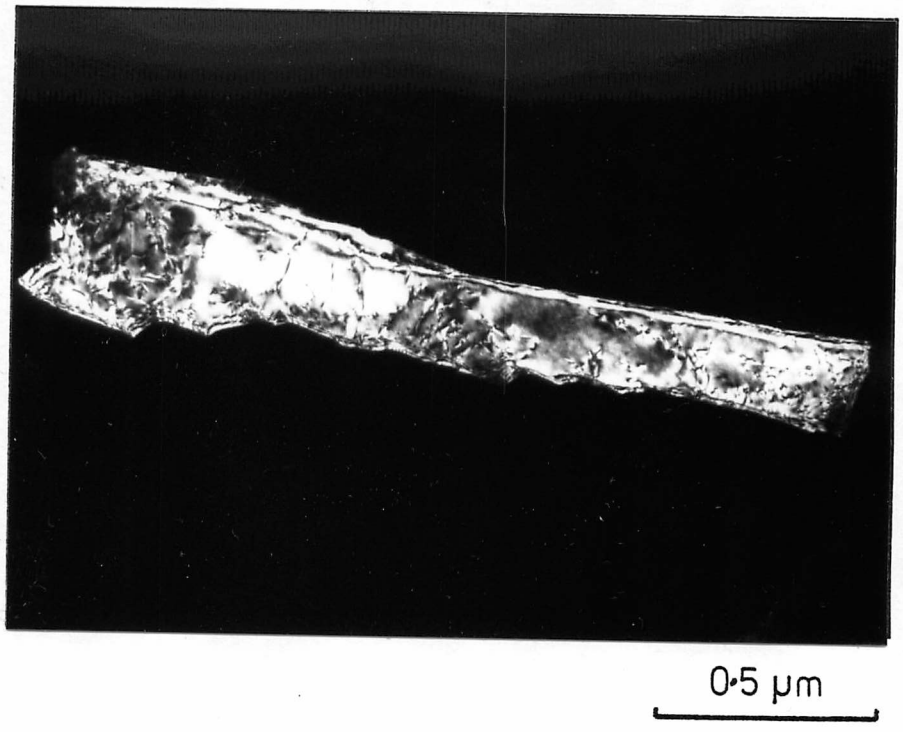

Fig.6.15 Transmission electron micrograph showing the presence of retained austenite in weld MMA 3. The centred dark field image shows clearly that in many cases the austenite/ferrite interface appears stepped.

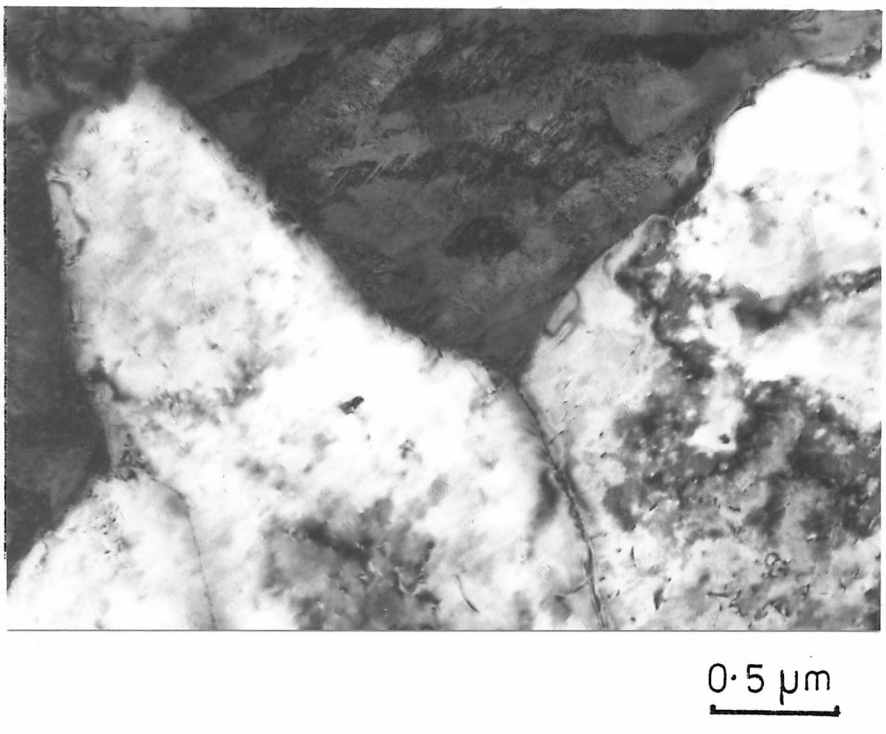

Fig.6.16 Transmission electron micrograph illustrating the presence of twinned martensite in weld MMA 3.

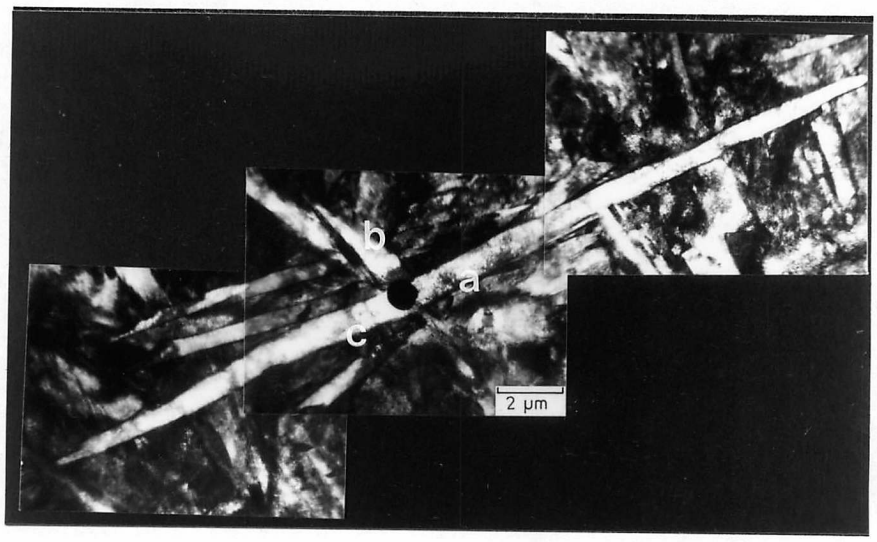

Fig. 6.17 Composite electron micrograph illustrating inclusion nucleation of Widmanstätten ferrite. For discussion see text.

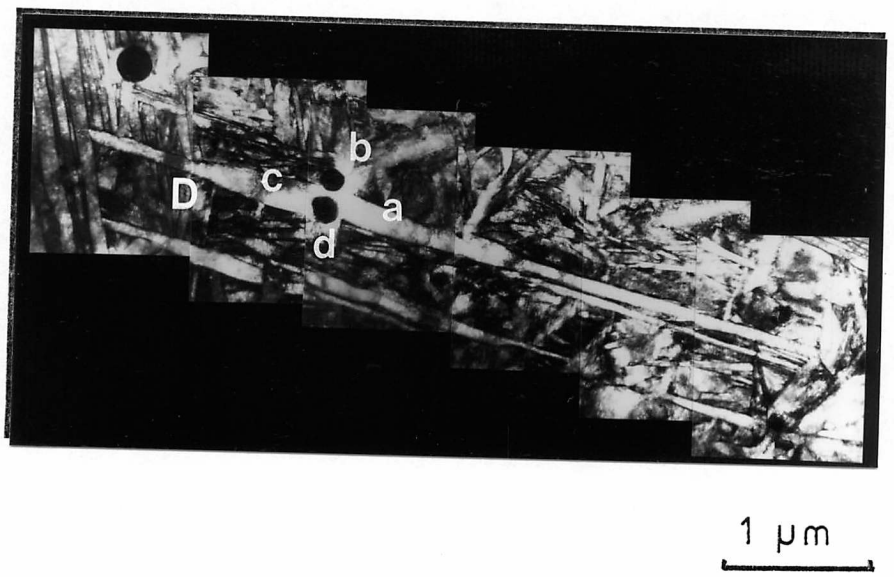

Fig.6.18 Composite electron micrograph illustrating association between two weld metal inclusions and Widmanstätten ferrite. For discussion see text.

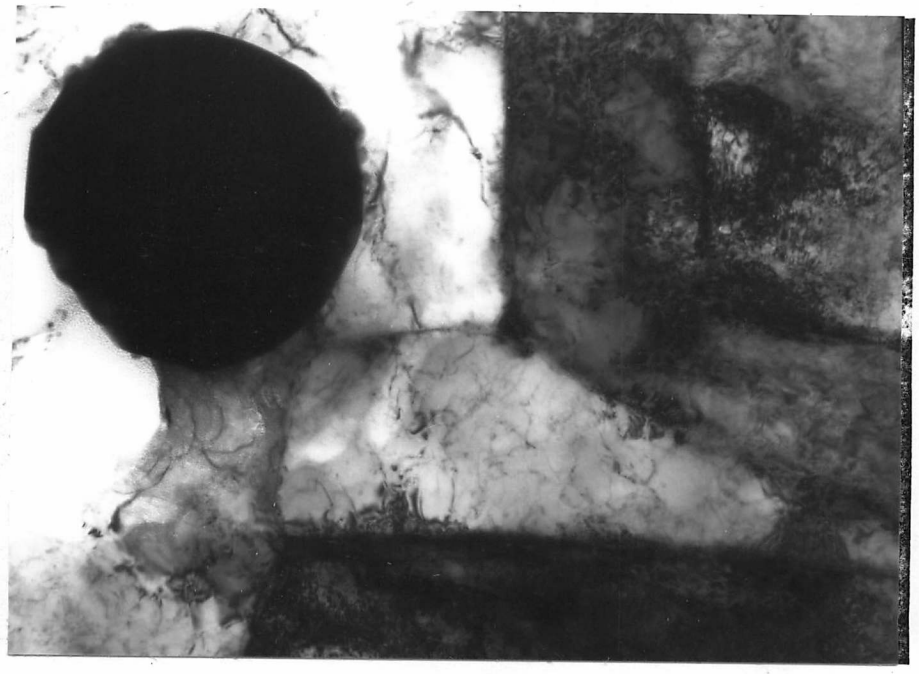

(a)

0·25μm

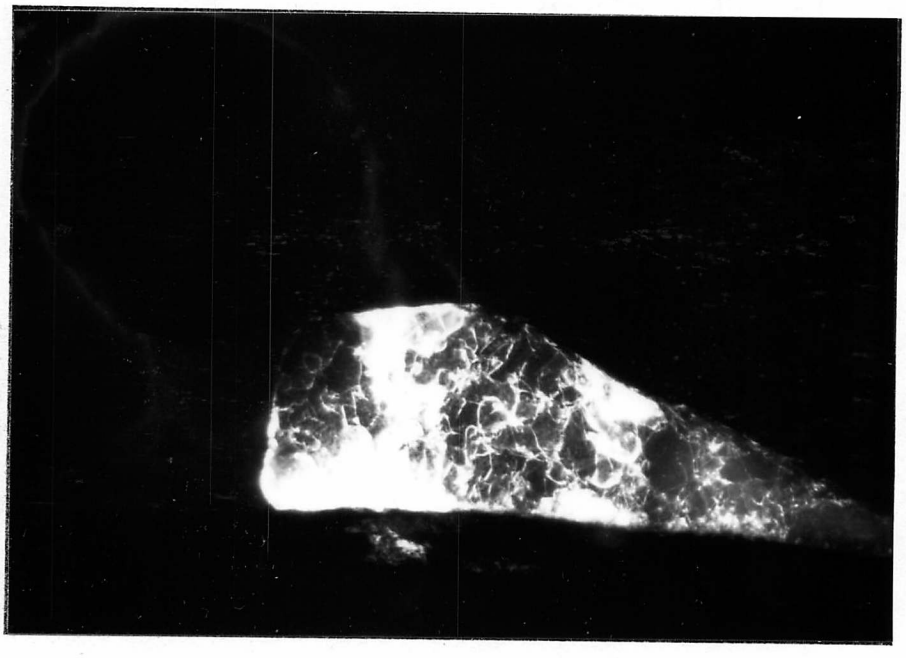

(b)

0·25μm

Fig.6.19 Transmission electron micrographs illustrating nucleation of Widmanstätten ferrite in close association with a weld metal inclusion. In this case the plate appears to have nucleated on an existing ferrite lath - which itself was probably inclusion nucleated.

(a) Bright field image.

(b) Dark field image.

in Fig. 6.20, which details the manganese and silicon profiles up to the inclusion illustrated in Fig 6.17.

In addition to the nucleation of intragranular ferrite on inclusions, it was found that ferrite plates developed from pre-existing inclusion nucleated Widmanstatten ferrite (ie. Ferrite could be sympathetically nucleated), as discussed by Aaronson and Wells (1956). Examination of Fig.6.18 in the region D reveals a number of sympathetically nucleated ferrite laths, as shown in Fig.6.21. Further examples of sympathetically nucleated plates are shown in Figs. 6.12 and 6.13.

The determination of the crystallography of the intragranular ferrite plate was far from straightforward, as this required the retention of austenite at room temperature. The use of inter-lath retained austenite in martensite laths in determining ferrite orientation relationship is now well established eg. Thomas (1973). However, in the welds examined in this investigation, no inter-lath austenite was found in the martensite, due probably to the relatively slow quench rate and the high proportion of auto-tempered martensite present. Films of retained austenite were detected in very few cases between ferrite plates, as shown in Fig. 6.22 (a) and (b), which are bright and austenite centred darkfields using an (002) reflection. The corresponding diffraction pattern is shown in Fig. 6.22 (c), which show that the intragranular plates have a Kurdjumov - Sachs (1930) orientation with the parent austenite.

Though much controversy surrounds the mechanism of growth of Widmanstatten ferrite (see Chapter 2) it is interesting to note that features compatible with its growth by both a shear and a diffusional mechanism were observed. Stepped growth interfaces were frequently observed between the acicular ferrite and the austenite or martensite regions, as shown in Figure 6.15. Similar evidence has previously been

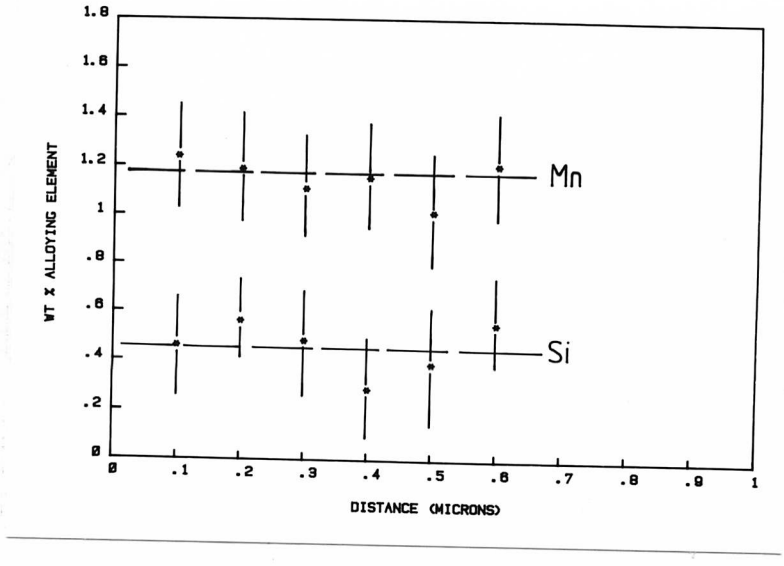

Fig.6.20 Manganese and silicon concentration profiles away from the inclusion detailed in Fig.6.17. No depletion of either Mn or Si is observed in the immediate area of the inclusion.

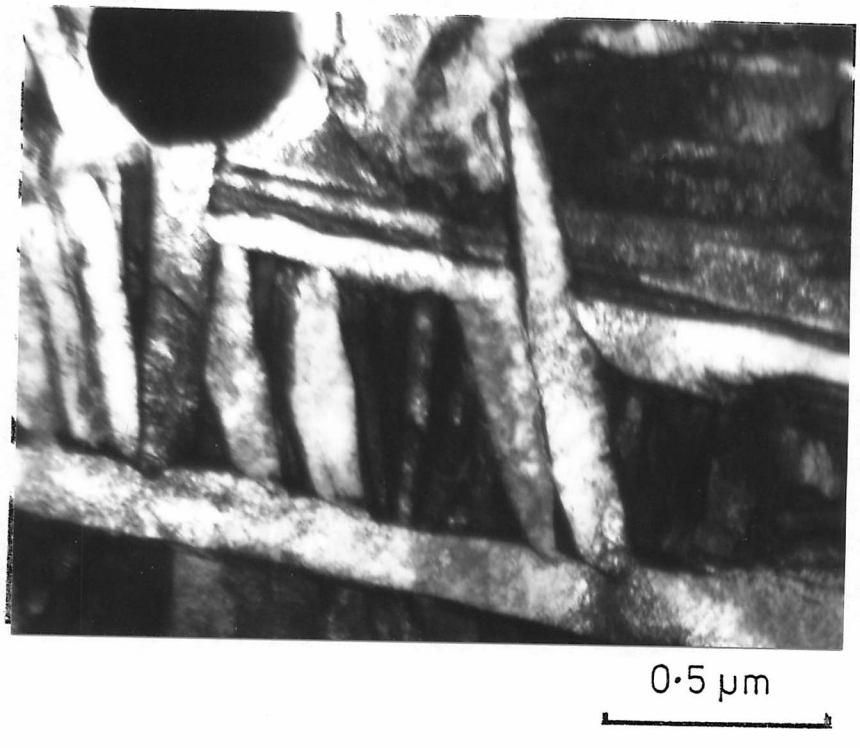

Fig.6.21 Transmission electron micrograph illustrating sympathetic nucleation of Widmanstätten ferrite. The lower ferrite plate refers to the region D from Fig.6.18.

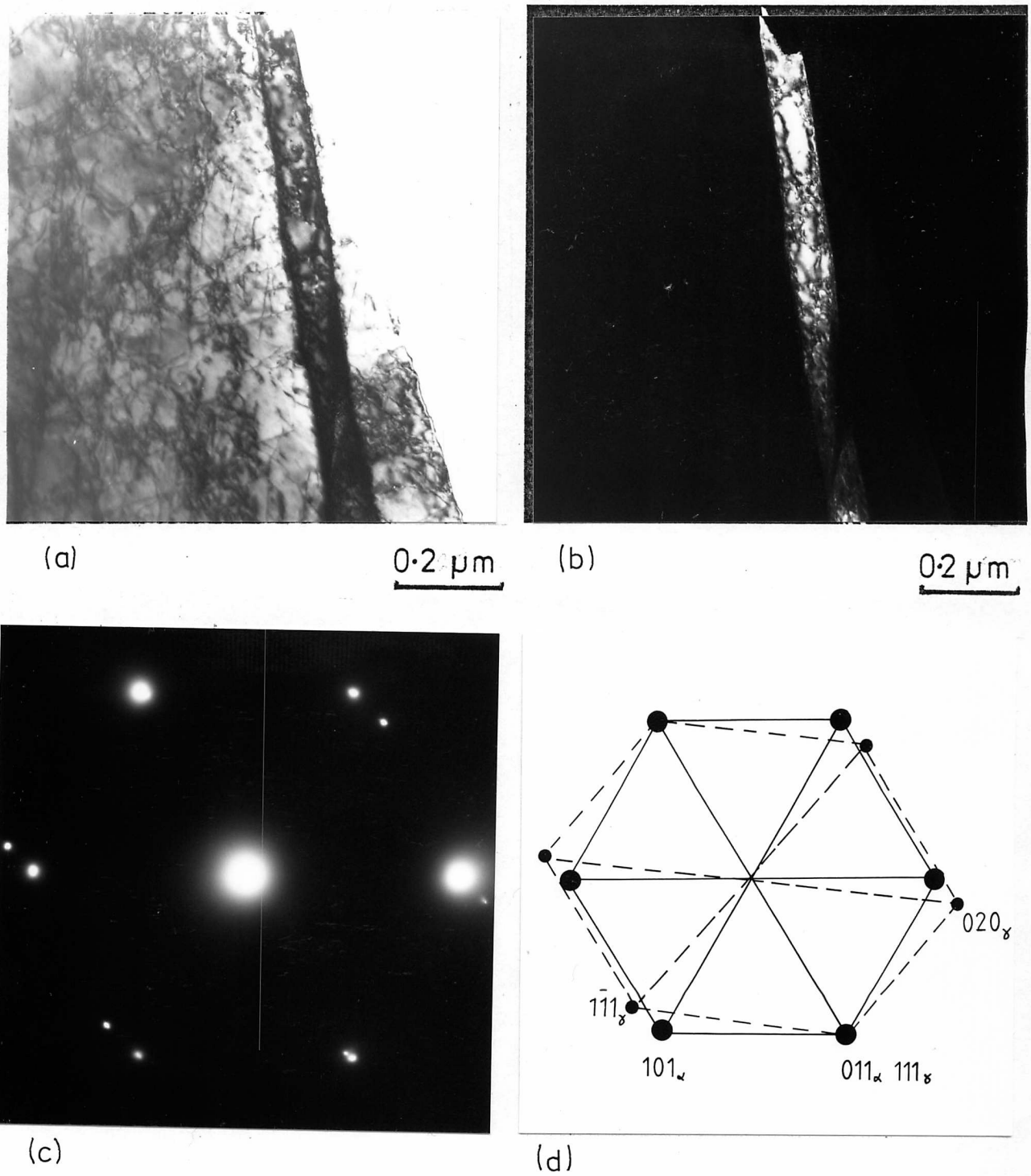

Fig.6.22 Transmission electron micrograph of Widmanstatten ferrite plates in weld SA 3.

(a) Bright field image
(b) Intralath film of retained austenite.
002 centred dark field.
(c) Corresponding diffraction pattern.
(d) Solution to (c)

interpreted, eg Kinsman et al (1975), as indicative of a ledge mechanism operating during the growth stage. Less frequently, the intragranular plates were observed to have a sub-grain boundary down the centre of of the plates (eg. Figure 6.18), which is a morphological feature which Bhadeshia (1981.1) has observed when the Widmanstatten plates are considered to form by a process involving shear.

6.6 DISCUSSION

The thermodynamic analysis and dilatometric work detailed in the previous chapter, together with the morphological evidence presented in the previous section, have shown that the acicular ferrite constituent of weld metal microstructure is comprised of intragranularly nucleated Widmanstatten ferrite. The primary nucleation sites are refractory inclusions. The fine interlocking microstructure which is characteristic of acicular ferrite may then be related to the subsequent multiple sympathetic nucleation events.

In general, inclusions may promote the intragranular nucleation of ferrite in three ways:

1) by affecting the local chemistry of the austenite, such that the driving force for the transformation may be increased.

2) by acting as a substrate such that the destruction of part of the austenite-inclusion interface, by the formation of a ferrite nucleus, reduces the overall energy barrier to the nucleation.

3) by the product phase nucleus (ie. ferrite) adopting rational orientation relationships with respect to both the inclusion and the austenite, such that low energy interfaces may form between the nucleus and both the austenite and inclusion.

The [illegible] geological [illegible]

[illegible] the formation of [illegible]

[illegible] cases of [illegible] lusions are less favour[illegible]

[illegible] with [illegible] boundaries. Despite [illegible]

[illegible] [illegible] years inve[illegible]

The composition of weld metal inclusions and their effect on matrix composition will be discussed in detail in Chapter 7. However, Figures 6.14 (a) and (b) show typical X-ray spectra from a weld metal inclusions. The major peaks present are Al,Si, S,Ti, Mn, which suggest that the inclusion must probably comprise mixed Al, Mn silicates and Al, Ti oxides and sulphides. Hence it might be expected that both the Mn and Si levels in the adjacent austenite would be lower than that well removed from the inclusions. This in turn could lead to a change in the driving force for ferrite nucleation at the inclusion. However, the application of a S.T.E.M. / E.D.S. technique has shown that no detectable variation in either Mn or Si levels are present. This is illustrated in Figs. 6.20, which shows the Mn and Si concentration profiles up to the inclusion in Fig.6.17.

The application of classical nucleation theory described in the previous section to the formation of ferrite on inclusions has shown that, in all cases, inclusions are less favourable sites for nucleation than austenite grain boundaries. Despite this, inclusion nucleation has been observed in the current investigation. Since the inclusions are not altering the chemical composition, inclusion nucleation of ferrite only occurs after the more favourable grain boundary nucleation sites have become saturated. This hypothesis is substantiated by the observation that austenite grain boundaries have rapidly become covered with proeutectoid ferrite, as indicated by Fig. 6.11.

The third manner in which inclusions may promote the intragranular nucleation of ferrite, ie. by adopting a rational orientation relationship with the inclusion, will be discussed in depth in Chapter 8. In this chapter, the assumption that the inclusion/ferrite interface is disordered seems realistic, since no simple inclusion type has been identified.

[illegible] damaged DNA p[illegible]

[illegible] [illegible] lattice defect or a

finally, probably the most outstand[illegible]

or [illegible] reproducibility of [illegible]

[illegible]

Further, since a range of compositions are generally observed, a constant crystal structure appears unlikely.

The observation of sympathetic nucleation has been clearly established in these materials. The conditions which must be established according to Aaronson (1962) have been satisfied, as can be judged in Fig.6.11 by comparing the size of the constituent at A with respect to the austenite grain size. Indeed, the usual conditions encountered in weld materials are ideal for the operation of a mechanism of sympathetic nucleation, since large austenite grain sizes, fast cooling rates (and therefore large undercooling) and high carbon enrichment are usually encountered. Further, the operation of inclusions as intragranular nucleation sites for the ferrite reaction provides an ideal substrate for sympathetic nucleation of ferrite. This is consistent with Aaronson's observation that only the initial plate in most assemblages of plates arise by 'conventional nucleation' (ie. at a lattice defect or an inclusion).

Finally, probably the most outstanding characteristic noted by Aaronson was 'the reproducibility of morphological configurations assembled primarily by sympathetic nucleation'. Perhaps the development of an acicular ferrite microstructure in weld materials provides the most potent example of the operation of this mechanism.

6.7 CONCLUSIONS

The results detailed in this chapter have shown that :-

1) Acicular ferrite is comprised of intragranularly nucleated Widmanstatten ferrite, as suggested by Abson and Dolby (1978), and not granular bainite, as proposed by Watson (1980).

2) Intragranular nucleation of ferrite occurs at lower transformation temperatures than that characteristic of austenite grain boundary nucleation and only after site saturation has occurred at these boundaries.

3) Weld metal inclusions are the primary nucleation sites for intragranular nucleation of Widmanstatten ferrite on which sympathetic nucleation of ferrite subsequently occurs. This leads to the fine interlocking nature of acicular ferrite.

4) The major effect of weld metal inclusions in the nucleation of ferrite is through their ability to reduce the energy barrier to nucleation by acting as an inert substrate.

5) No depletion of manganese or silicon concentrations have been detected in the austenite, either in the matrix or adjacent to the weld metal inclusions observed in this study.

CHAPTER 7

THE APPLICATION OF X-RAY MICROANALYSIS TO THE STUDY OF H.S.L.A. STEEL WELD METALS

7.1 INTRODUCTION

The results detailed in the previous chapter have shown clearly that weld metal inclusions have acted as the primary sites for the nucleation of the acicular ferrite microstructure. In that context, they were considered as an inert ceramic substrate which was shown to reduce the overall barrier to nucleation for the ferrite reaction. However, it is also possible that the driving force for ferrite nucleation may be changed if the inclusions also affect the matrix chemistry of the weld metal.

Such an effect has been observed in cast steel by Salmon-Cox (1964). Using electron probe x-ray microscopy, this work showed that under certain conditions, inclusions could indeed locally deplete the adjacent austenite matrix of manganese. This is illustrated in Fig 7.1, which shows the depletion associated with an Fe/Mn sulphide inclusion observed in a cast steel. Similarly, Farrar and Watson (1979) have suggested that certain submerged arc weld metals could differ in matrix composition, due to similar effects.

In this chapter, the composition of both inclusions and the adjacent austenite matrix have been examined using a STEM/EDS technique in two submerged arc weld deposits. In addition, electron energy loss spectrometry was used qualitatively to distinguish between oxygen and nitrogen in certain inclusions.

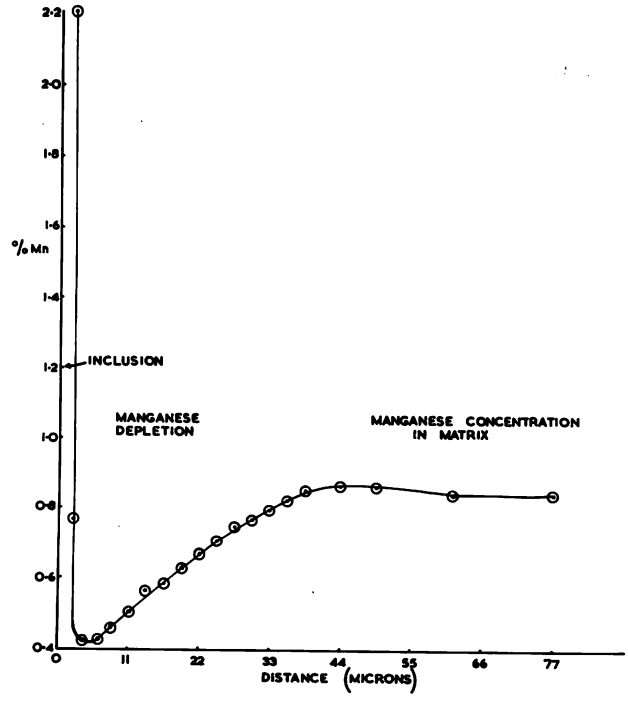

Fig.7.1 Depletion of manganese, observed by Salmon-Cox (1964), associated with a Fe /Mn sulphide inclusion in cast steel.

Recent work at the Welding Institute, Pargeter (1981), on weld metal inclusions in submerged arc deposits, had been undertaken using Particle Analysing Scanning Electron Microscopy (PASEM). This work had suggested that in any given submerged arc weld deposit, several inclusion types were present eg. MnS, $AlSiO_3$, MnO. This has direct implications for microstructural development, in that it would be possible for a single inclusion type to be responsible for the intragranular nucleation of ferrite. One aim of this investigation was therefore to correlate the qualitative information derived from PASEM analysis with that obtained from a study of inclusions on carbon extraction replicas using a STEM/EDS technique.

It is beyond the scope of this chapter to discuss the complex deoxidation/reduction reactions which occur in submerged arc welding. These have been recently studied by Davis & Coe (1977) in an investigation of commerical fluxes at the Welding Institute.

7.2 ENERGY DISPERSIVE ANALYSIS OF X-RAYS

The basis of microanalysis is to use a focussed electron probe to bombard a specimen, causing the emission of characteristic x-rays. The energies of these x-rays indicate which elements are present and the intensities the relative proportions of those elements. The analytical methods used to interpret this information can be conveniently divided into four techniques, which have been considered in this work.

7.2.1. Scanning electron microprobe analysis

The quantitative analysis of bulk specimens is now a well established technique. Details of the standard Z.A.F. (atomic number, absorption and fluorescence) corrections can be found in standard texts

e.g. Andersen (1973). An ISI-100 scanning electron microscope with E.D.S. facilities was used to examine typical inclusions in prepolished specimens. Using the same operating conditions used in the PASEM analysis, spectra were obtained from both the flat and tilted (45° towards the x-ray dectector) positions.

7.2.2. Analysis in Thin Foils

In contrast to bulk analysis, quantitative analysis of thin foils has only developed in recent years. Several reviews, eg. Hren, Goldstein & Joy (1979), have shown that this technique can now be used on a fully quantitative basis and the results regarded with a high degree of accuracy. The microanalysis (of thin films) described in this chapter was carried out on a Philips EM 400 TEM / STEM with a Link 860 microanalysis system, using standard thin foil correction programmes to compensate for x-ray detection efficiency and absorption.

7.2.3 Analysis of Individual Particles

Accurate quantitative analysis of individual particles on a substrate (in this work, the study of inclusions on a carbon extraction replica) requires a complex series of corrections. In addition to the usual absorption and fluorescence corrections, the effect of sample size and shape must be taken into account. Armstrong (1978) developed a quantitative analysis program for such particles, which showed that all of these factors could be quantified, given a homogeneous particle of a regular shape.

However, the weld metal inclusions investigated in this study are generally mixtures of oxides and sulphides formed over a wide range of temperatures and are probably therefore inhomogeneous. Since there is no quantitative method available for the microanalysis of such inclusions, the work described in section 7.3.1 records only the apparent composition. The microanalysis carried out in this section was performed on a Philips 400 TEM/STEM operating at 120 kV, using the standard EDAX EM programme. The apparent compositions were obtained by manual peak-stripping, to overcome the problems of overlapping peaks, after peak smoothing and background subtraction had been performed.

7.2.4. Particle Analytical Scanning Electron Microscopy (PASEM)

The technique of PASEM as applied specifically to weld metals has been summarised in a recent study (Pargeter (1981)) at the Welding Institute. Essentially, the technique consists of a scanning electron microscope with EDX analysis facilities driven by a Quantimet image analysing computer. On a flat, prepolished surface the machine automatically locates, sizes and analyses the elements present in each inclusion, using a preset threshold criteria for detection. Using the data for a large number of inclusions, it is possible to develop a series of histograms for each inclusion type.

7.3 RESULTS

7.3.1. Inclusion Chemistry

Two submerged arc weld metals have been considered in this investigation. The different oxygen levels in the deposits were produced using an acidic fused flux (SA 1) and a basic agglomerated flux (SA 4). The microstructure, toughness and inclusion size distribution of these welds has been described in Chapter 3.

7.3.1.(a) PASEM Analysis of Inclusions

PASEM analysis was carried out on the two welds (SA 1 and SA 4) at the Swedish Institute of Metals. For completeness, the main details of the standard print out received from the Institute is given in Tables 7.1 and 7.2. The results of this analysis are summarised in Figs. 7.2(a) and (b), which show the size distributions of the major inclusion types found in the two welds. In both welds, inclusions containing (Al, Si + Mn) were found to be most common, accounting for 40% of the inclusions in SA 1 and 35% in SA 4. Inclusions containing only (Si + Mn) and only (Mn) were also detected in large quantities in SA 1. In contrast, the elements detected in inclusions in weld SA 4 can be grouped as follows:- (Al) - 16%, (Al,Mn) - 12% and (Al,S) - 12%.

An alternative way to review the data contained in Figs. 7.2(a) and 7.2(b) is shown in Table 7.3, which shows the proportion of inclusions containing one particular element. It should be noted that most of the inclusions (92%) in SA 1 were found to contain Mn. In contrast, the element detected in inclusions most frequently (87%) in SA 4 was found to be Al.

These results strongly suggest that there are many inclusion types present in both welds eg. $MnSiO_3$, MnO, Al_2O_3 and that these different types are present in large numbers.

7.3.1.(b) STEM/EDS Analysis of Inclusions

Transmission electron microscopy of thin films indicated that two inclusion morphologies were observed in both welds, as shown in Fig.7.3. Spherical globular inclusions, which were usually electron opaque, (eg. at A) accounted for 95% of the total number of inclusions observed, with the remainder comprising smaller, angular inclusions (eg. at B). Carbon extraction replicas were prepared from the same area of the weld

Table 7.1 Summary of the data derived from the PASEM analysis of inclusions in weld SA 1. (Circles indicate the presence of particular elements).

TYPE	ELEMENTS FOUND IN INCLUSIONS								NUMBER OF PARTICLES	% OF TOTAL	NUMBER / mm² - SIZE (μm)					
	Mg	Al	Si	S	Ca	Ti	Cr	Mn			0·25–0·50	0·50–0·75	0·75–1·00	1·00–1·25	1·25–1·50	1·50–1·75
1									12	2·9	218	72	-	-	-	-
2								●	57	13·8	678	557	145	-	-	-
3		●	●	●				●	26	6·3	73	315	145	73	24	-
4		●	●					●	181	43·7	581	2493	726	315	73	97
5		●						●	11	2·7	194	73	-	-	-	-
6			●					●	68	16·4	896	629	121	-	-	-
7			●						10	2·4	241	-	-	-	-	-
8			●	●					1	0·2	24	-	-	-	-	-
9		●							4	1·0	97	-	-	-	-	-
10			●	●				●	13	3·1	97	145	48	-	-	-
11				●				●	15	3·6	145	121	97	-	-	-
12		●		●				●	2	0·5	24	-	24	-	-	-
13		●	●						5	1·2	97	24	-	-	-	-
14				●					2	0·5	73	48	-	-	-	-
15	VARIOUS								7	1·6	-	-	-	-	-	-

Table 7.2. Summary of the data derived from the PASEM analysis of inclusions in weld SA 4.

TYPE	ELEMENTS FOUND IN INCLUSIONS								NUMBER OF PARTICLES	% OF TOTAL	NUMBER /mm² - SIZE (μm)					
	Mg	Al	Si	S	Ca	Ti	Cr	Mn			0·25–0·50	0·50–0·75	0·75–1·00	1·00–1·25	1·25–1·50	1·50–1·75
1									4	1·7	97	-	-	-	-	-
2		●	●						29	12·4	629	48	24	-	-	-
3				●				●	9	3·9	73	97	24	24	-	-
4			●						2	0·9	48	-	-	-	-	-
5		●		●				●	8	3·4	48	48	48	24	24	-
6								●	2	0·9	24	24	-	-	-	-
7		●						●	30	12·9	412	266	48	-	-	-
8		●	●					●	67	28·7	654	920	48	-	-	-
9		●	●	●				●	12	5·1	73	97	73	-	-	-
10		●							38	16·3	750	169	-	-	-	-
11		●		●					5	2·1	121	-	-	-	-	-
12		●		●			●	●	1	0·4	24	-	-	-	-	-
13			●	●				●	4	1·7	48	24	-	24	-	-
14			●					●	1	0·4	-	24	-	-	-	-
15	VARIOUS								21	9·0	-	-	-	-	-	-

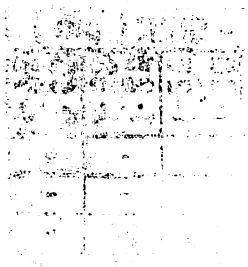

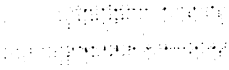

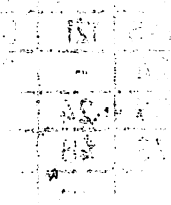

(a)

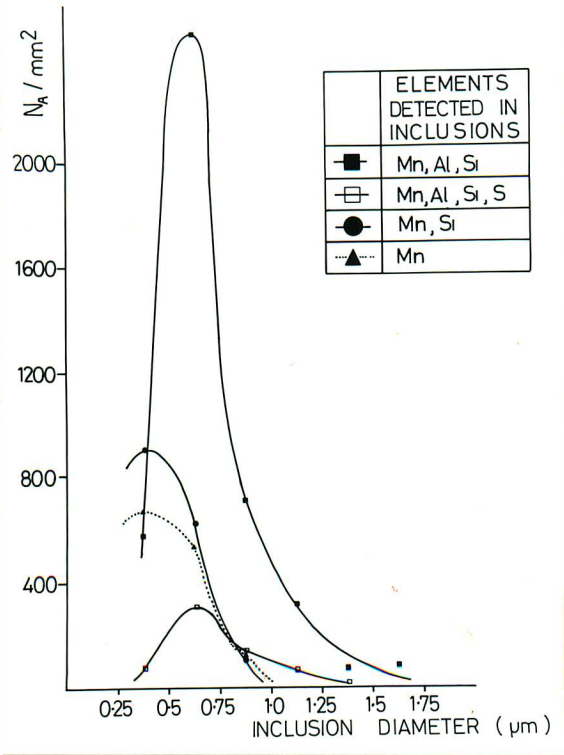

(b)

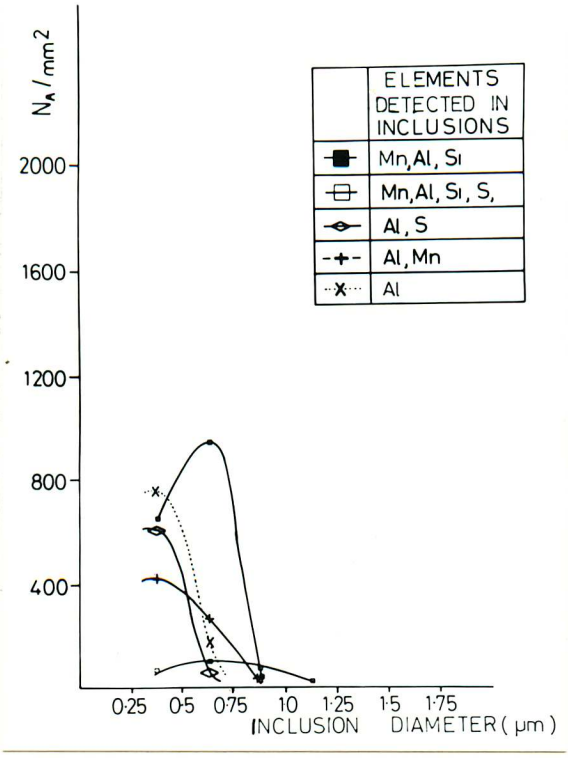

Fig.7.2 Summary of the main inclusion types detected in the PASEM analysis of welds SA 1 (a) and SA 4 (b).

Table 7.3. Alternative summary of the PASEM data for welds SA 1 and SA 4 indicating the percentage of inclusions containing one particular element.

INCLUSIONS CONTAINING %	WELD S.A. 1	WELD S.A. 4
Al	56	87
Mn	92	63
Si	76	56
S	15	50
Ti	05	3

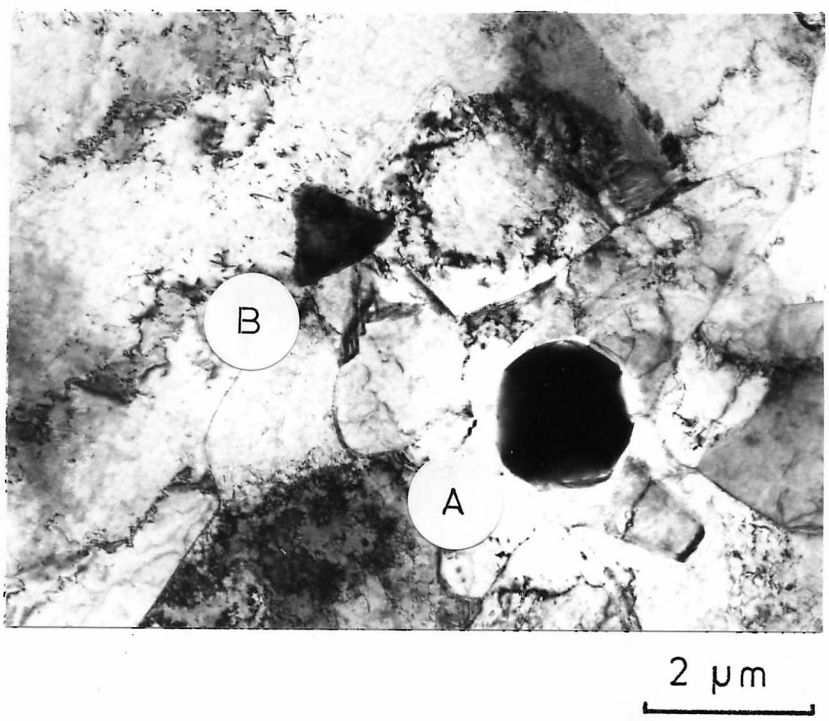

Fig.7.3 Transmission electron micrograph of inclusions in weld SA 4. Two morphologies are observed, spherical inclusions (eg. at A) comprising 95% of the total number and angular inclusions (eg at B).

deposits which had been used for the PASEM investigation. They were examined in a Philips 400 TEM/STEM operating at 120 kV.

Figs. 7.4(a) and 7.4(b) are typical EDX spectra obtained from singular spherical inclusions in SA 1 and SA 4 welds respectively. The spectra are characteristic of all the spherical inclusions observed in these welds. The spectra are very similar in terms of the elements present (the copper peak in both cases originates from the support grid and is not characteristic of the inclusion), the major difference being the presence of the small Ti peak in the spectrum of SA 4. Electron energy loss spectroscopy indicated the presence of oxygen in the inclusions, as shown in Fig.7.4 (c). The presence of Al, Si, Mn in large amounts indicates that the inclusions are mixed in character and most probably consist of $MnSiO_3$, $Al_2(SiO_3)_3$. The sulphur peak in both spectra implies probably that some MnS is also present.

Although the spectra obtained in SA 1 and SA 4 indicate that there is little difference in the elements detected in the inclusions, differences in the actual concentrations of Al, Si and Mn are observed. For example, Table 7.4 indicates that the inclusions in SA 1 contain more Mn than Al, while the opposite is true for SA 4. These differences may be qualitatively explained in terms of the compositions of the fluxes used in the welding process, which is given in Table 7.5. The high Si/Al ratio of the inclusions in weld SA 1 is associated with the acidic flux used, which contained 36% SiO_2 and 12% Al_2O_3. Similarly the low Si/Al ratio of the inclusions in weld SA 4 reflects the use of a basic flux containing 11% SiO_2 and 17% Al_2O_3. The flux compositions, however, give no clear indication why titanium has been transferred to the inclusions in SA 4 and not in SA 1.

Secondary electron imaging of the inclusions in both welds often revealed that they were coated by an outer layer of material, which was

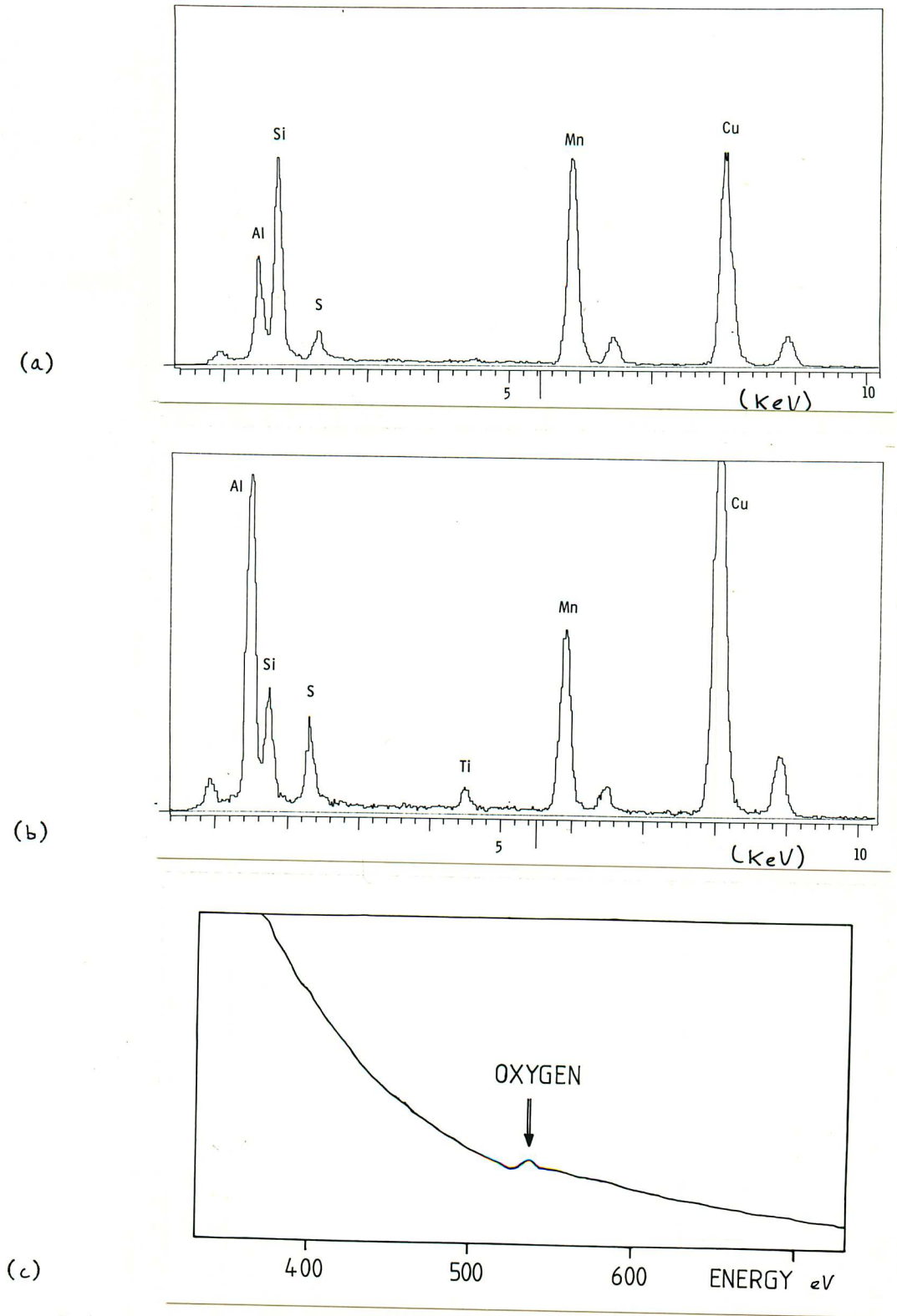

Fig.7.4 Typical spectra from inclusions in submerged arc welds SA 1 and SA 4; in both instances Cu peaks are characteristic of the support grid.
(a) weld SA 1 major elements detected are Al Si, S and Mn
(b) weld SA 4 - in addition to Al, Si, S and Mn a small Ti peak is also observed.
(c) Electron energy loss spectra from an inclusion in weld SA 4 indicating the presence of oxygen.

Table 7.4 Inclusion analysis from welds SA 1 and SA 4.

	WELD SA 1	WELD SA 4
Al	17	47
Mn	53	33
Si	26	11
S	4	5
Ti	<0·3	3

* The compositions (Wt%) only indicate the apparent concentration of the elements present.

Table 7.5 Approximate composition of the submerged arc welding fluxes, used for welds SA 1 (BOC 80R) and SA 4 (OP121TT). These compositions were derived by analysis of fluxes at the Welding Institute, courtesy D.J. Abson (1980).

FLUX	SiO_2	TiO_2	Al_2O_3	FeO	MnO	CaO	MgO	K_2O	Na_2O	CaF_2	BASICITY INDEX
BOC 80R	36	0·5	12	0·6	5	38	1·0	0·1	5·0	14	1·2
OP 121 TT	11	0·7	17	2	1	4	41	0·4	–	27	3·7

dissimilar in appearance to the bulk of the inclusions. Figs. 7.5(a) and 7.5(b) show examples of inclusions in SA 1, where a coating is clearly observed (Fig.7.5(a)) and apparently missing (Fig.7.5(b)). In order to establish the nature of this coating, microanalysis was carried out across such inclusions. The results of this analysis for inclusions in the SA 4 deposit are summarised in Fig.7.6(a) and a further example in Fig.7.6(b) and show the apparent variation of Al, Mn, Si, S and Ti across a typical inclusion. It must be stressed that this is only an apparent concentration, since no quantitative method of analysis is available.

No clear or consistent trend can be established for the major elements present ie. Al, Si,Mn. However, in both cases, a very large sulphur concentration is observed at the periphery of these inclusions. In both inclusions, the S level is seen to be much higher on one side of the inclusion (especially in Fig.7.6(b)). This may be explained by the orientation of the inclusion with respect to the x-ray detector. The highest sulphur level is associated with the side of the inclusion which is closer to the x-ray detector. Under these conditions, the effects associated with absorption and secondary fluoresence by the bulk of the inclusion will be minimised.

It therefore seems likely that the inclusions in both welds are composed of a central core of mixed (Al, Mn) oxides and (Al, Mn) silicates, which in some cases are coated with a layer of sulphide. This is also consistent with considerations of the melting point of the constituents of the inclusions. Thus the mixed oxides and silicates which tend to have high solidification temperatures would form relatively early in the thermal history of the weld deposit and subsequently act as nucleii for the formation of sulphides (eg MnS) at lower temperatures.

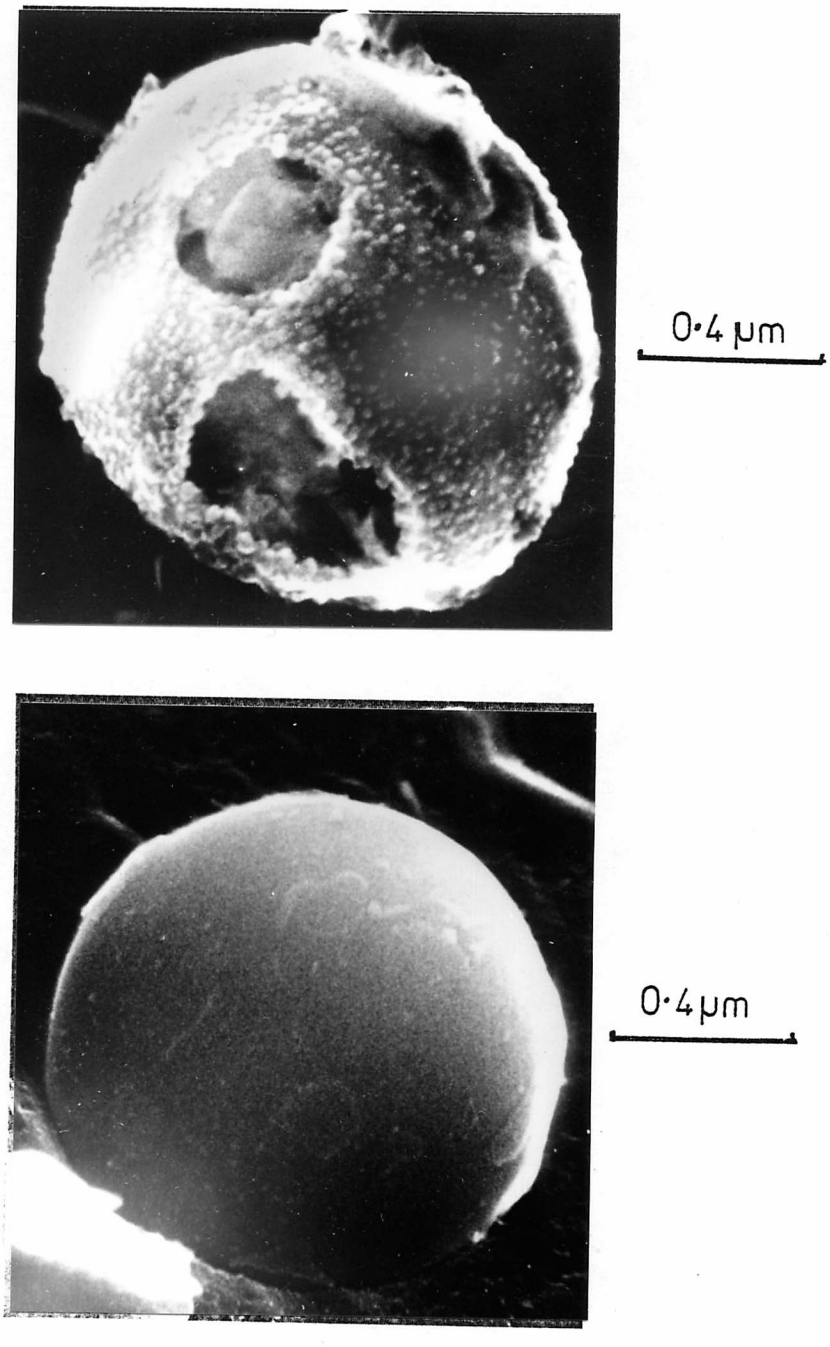

Fig. 7.5. Secondary electron images of large inclusions in weld SA 1.
(a) example of an inclusion where an outer coating of material is apparent
(b) example of an inclusion where no such coating is observed.

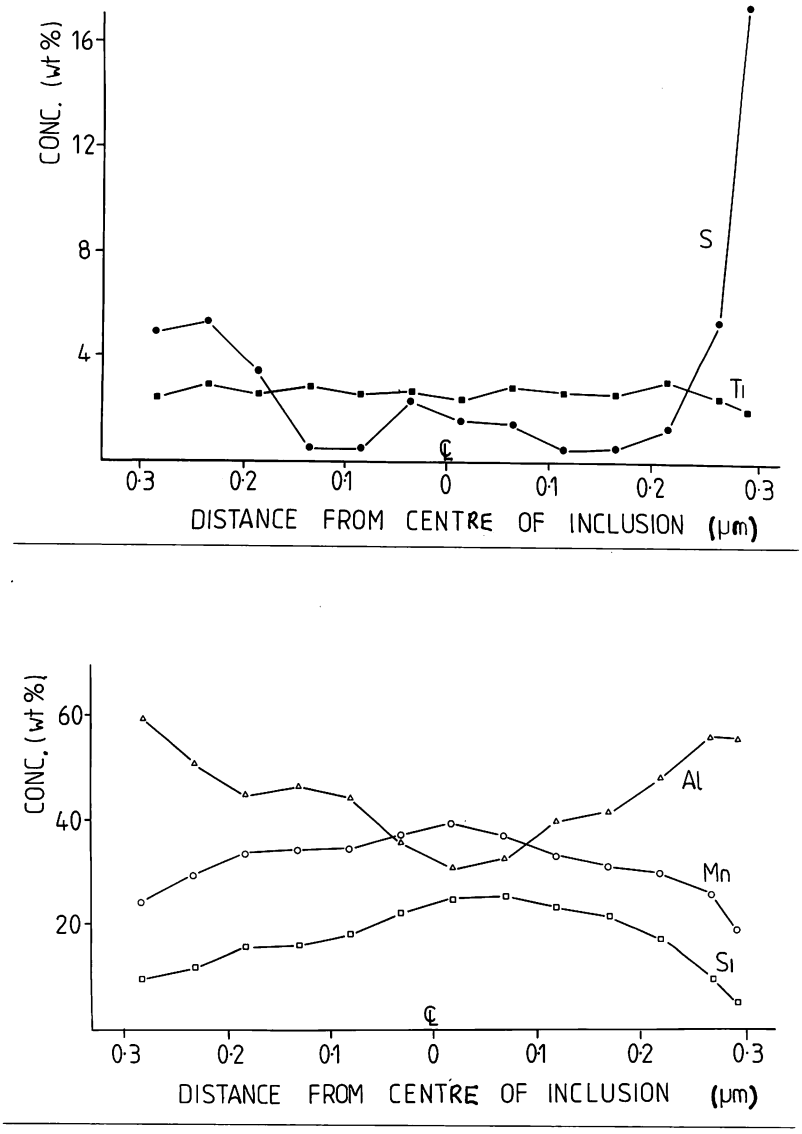

Fig.7.6(a) S.T.E.M./E.D.S. trace across a typical inclusion in weld SA 4. Microanalysis was carried out using a 100 Å spot size at an operating voltage of 120kV.

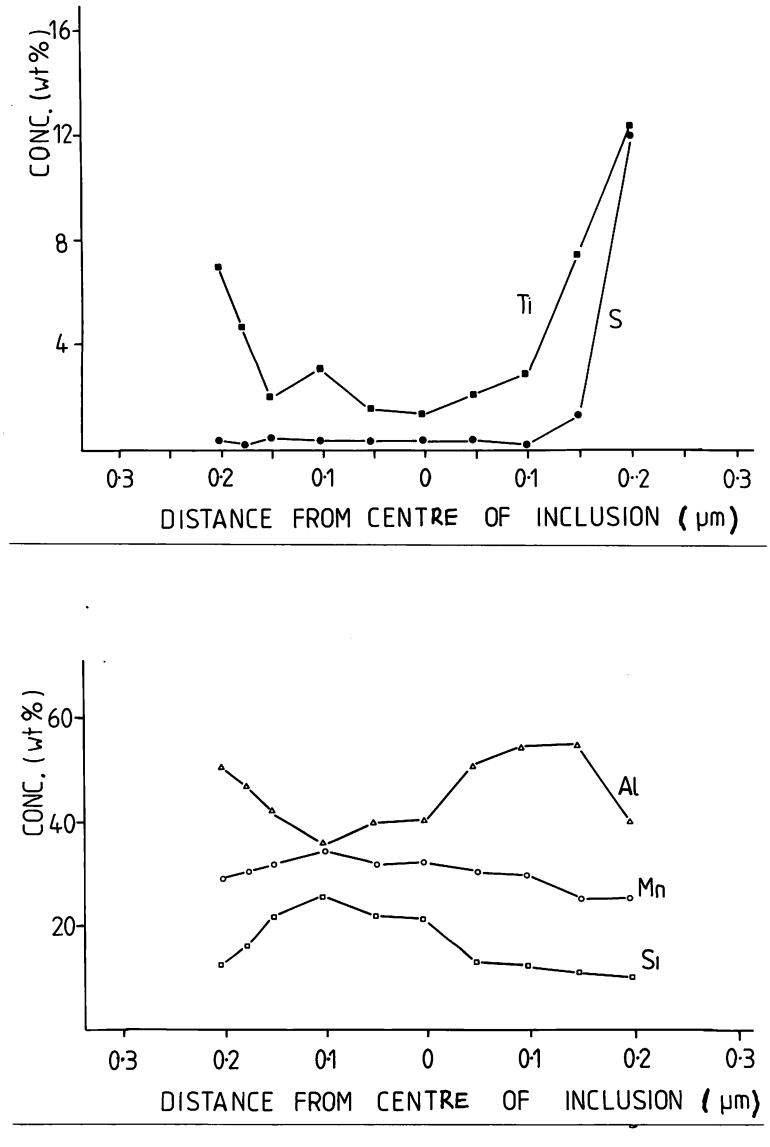

Fig.7.6(b) S.T.E.M./E.D.S. trace across a typical inclusion in weld SA 4 . Microanalysis was carried using a 100Å spot size at an operating voltage of 120kV.

The variation of titanium across the two inclusions considered differed markedly. In Fig. 7.6 (b) the apparent concentration of titanium remained almost constant across the inclusion. However, as shown in Fig.7.6(a), in some cases, titanium was seen in high concentrations at the periphery. This apparent variation could not be related to any metallographic features on the inclusions.

The other types of inclusions observed in both SA 1 and SA 4 welds were found in only small proportions (< 5% of the total number of inclusions). Fig.7.7(a) shows the morphology and typical EDS spectra of an angular inclusion from weld SA 4. The presence of Al, Mn and S indicate a mixed sulphide or oxide, however, this could not be uniquely identified by electron diffraction. In the same weld deposit, angular inclusions were also found that only contained manganese, as shown in Fig.7.7(b).

The morphology of other inclusions is weld SA 1 was less distinct. Fig. 7.8(a) shows the appearance of inclusions found to contain Al, S, Si , and Ca. However, again, these inclusions could not be identified by electron diffraction. Fig.7.8(b) shows the appearance of a typical manganese sulphide inclusion found in SA 1. These inclusions were generally spherical, with a contraction cavity (eg. at X) present in many cases.

7.3.2. Matrix Chemistry

Farrar and Watson (1979) have suggested that the exact matrix manganese content (rather than the bulk manganese composition) is the most important factor in controlling the formation of the acicular ferrite microstructure. In order to test this hypothesis, the average matrix compositions have been determined for both the acidic and basic weld deposits. In both cases, the average bulk analysis was given by spark fluorescence.

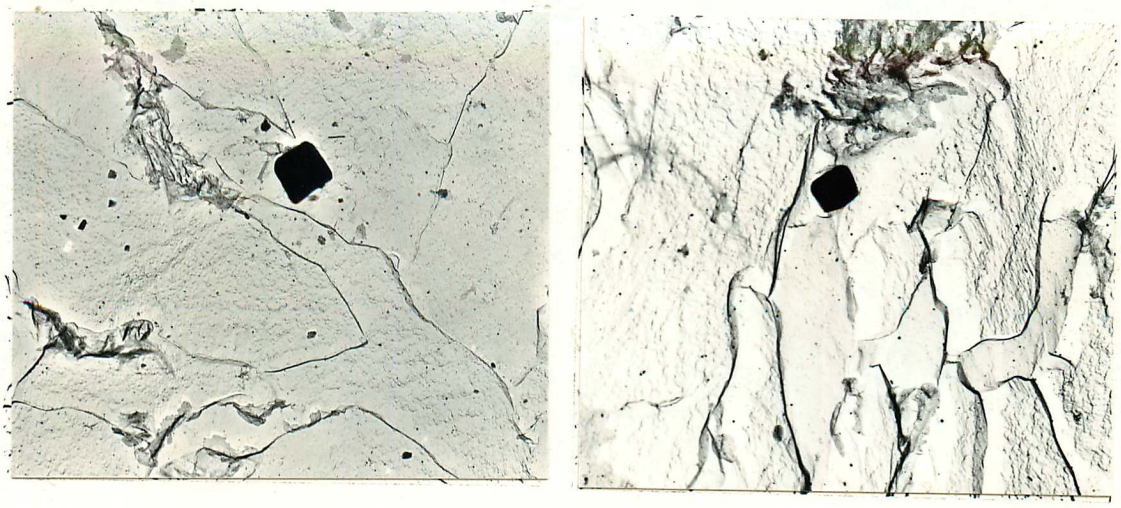

Fig.7.7 Morphology of angular inclusions in submerged arc deposit SA 4.

(a) Corresponding EDS spectra.

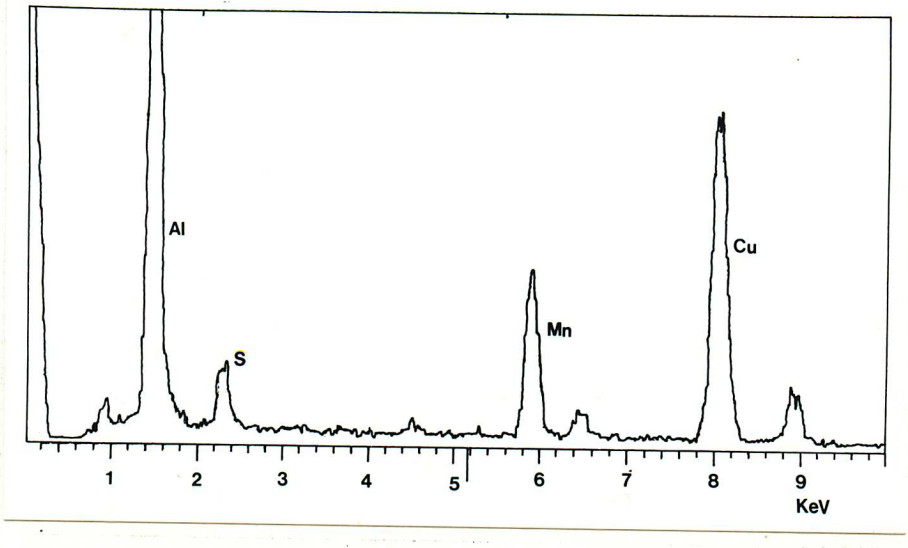

(b) Corresponding EDS spectra.

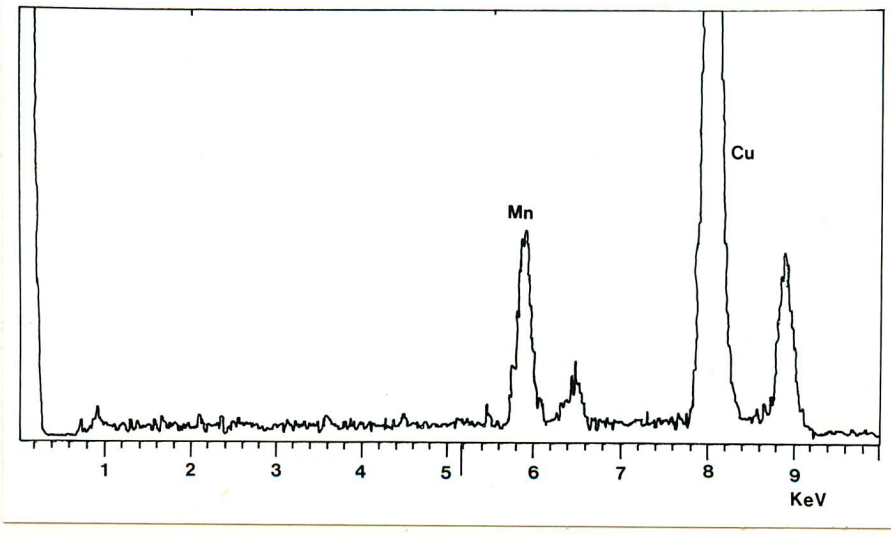

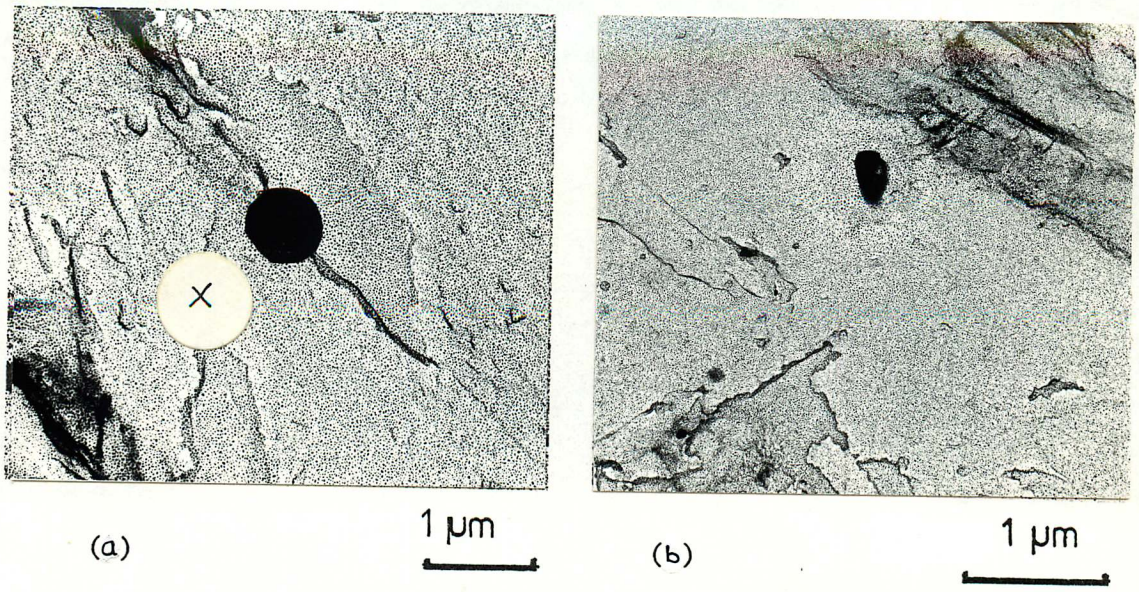

Fig.7.8 Morphology of inclusions in weld SA 1. The speckled appearance of the replica is due to gold shadowing, which accounts for the presence of Au in the EDS spectra.

(a) Corresponding EDS spectra.

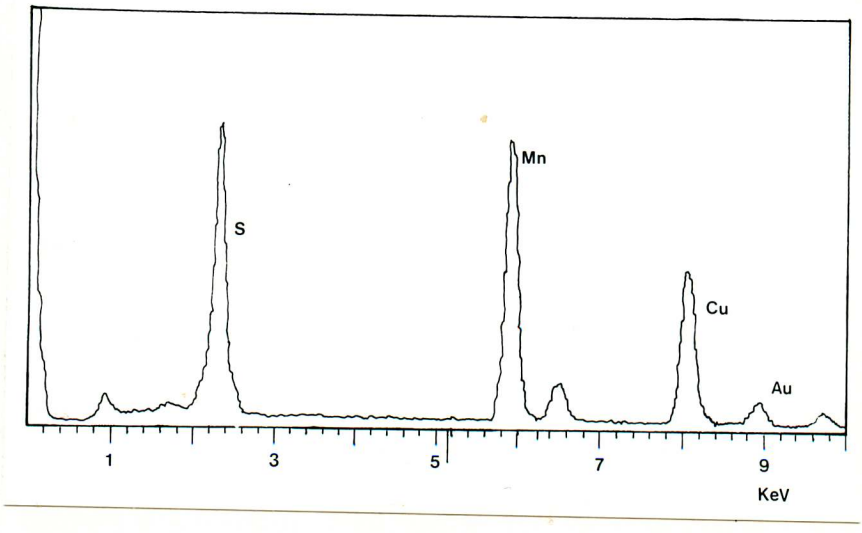

(b) Corresponding EDS spectra.

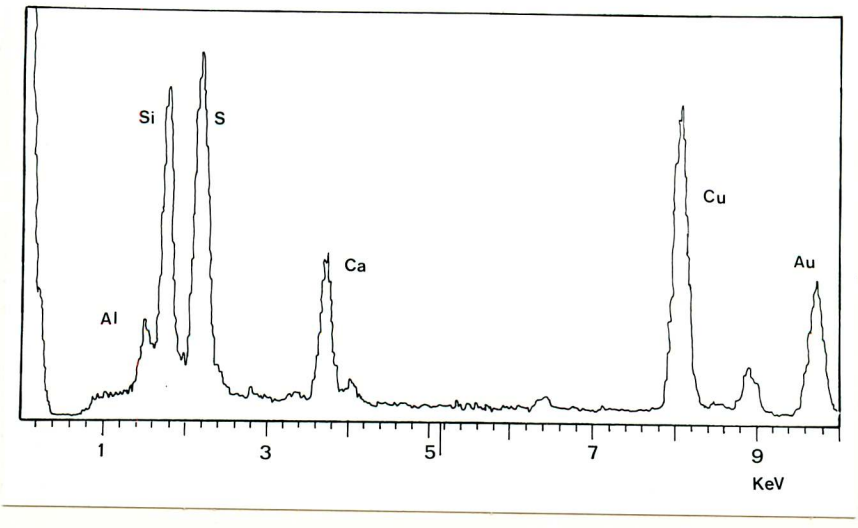

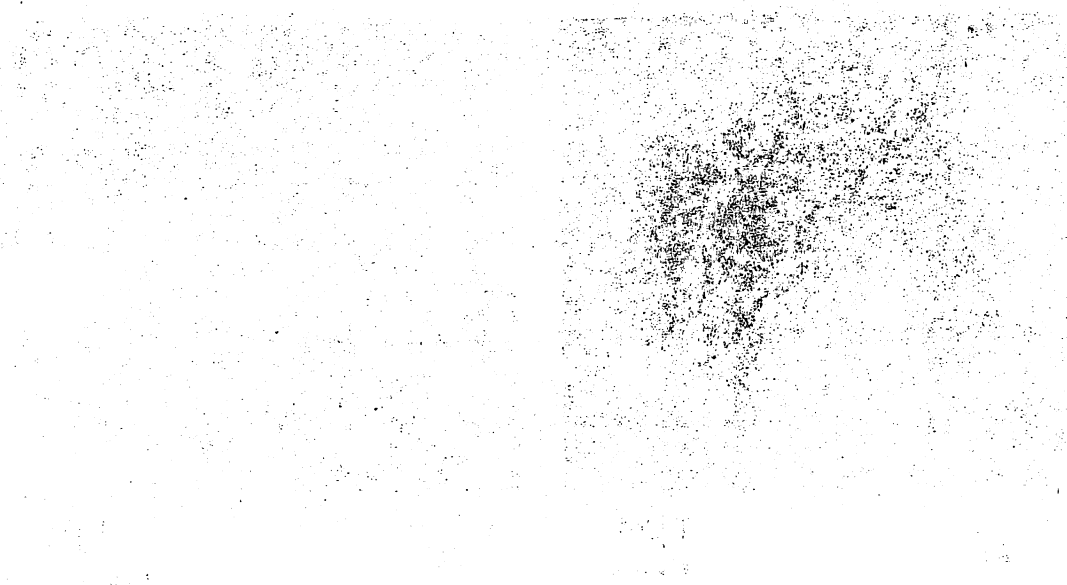

The results of the STEM / EDS analysis of the weld metal matrix compositions for SA 1 and SA 4 are given in Table 7.6, which also shows the relevant bulk analysis. The figures quoted are the means of a large number of individual analyses and the errors quoted are the standard deviations in the means. It is clear from these results that there is no detectable difference in the manganese levels between SA 1 and SA 4 and that these results correspond very closely to the bulk composition quoted. Similarly, calculations based on the work of Bailey and Pargeter (1979) with known bulk analysis and inclusion volume fractions have shown that at the oxygen levels of interest (ie between 0.03 and 0.06 wt %), little detectable change with respect to manganese should be found.

The possibility still exists that the inclusions in both welds can alter the composition of the adjacent matrix. The manganese and silicon profiles away from a typical inclusion in weld SA 1 are shown in Fig. 7.9. No decrease in either Mn or Si concentration are observed in the immediate vicinity of the inclusion. A further example of the distribution of manganese and silicon in the vicinity of an inclusion in weld SA 4 is given in Fig. 7.10. Again, no depletion of either Mn or Si were observed.

7.4 DISCUSSION

Non-metallic inclusions in both cast and wrought steel have been widely studied for many years. Several reviews eg Baker & Charles (1972); Kiessling and Lange (1978), have focussed attention on the occurrence, the identification and the effect on the mechanical properties of inclusions on the steels involved. In contrast, no such complete studies have been given to inclusions in weld-metals, particularly with respect to identifying the inclusions present. Thus, one aim of the current investigation was to correlate the information

Table 7.6 Comparison of bulk and matrix composition for submerged arc welds.

	BULK COMPOSITION OF WELD METALS (MEASURED BY X-RAY FLUORESCENCE wt%)		MATRIX COMPOSITION OF WELD METALS (MEASURED BY E.D.S. ANALSIS wt %)	
ELEMENT	SA 1	SA 4	SA 1	SA 4
C	0·13	0·14	—	—
Mn	1·31	1·32	1·3 ± 0·1	1·3 ± 0·1
Si	0·33	0·29	0·5±0·2	0·3±0·1
O	0·6	0·3	—	—

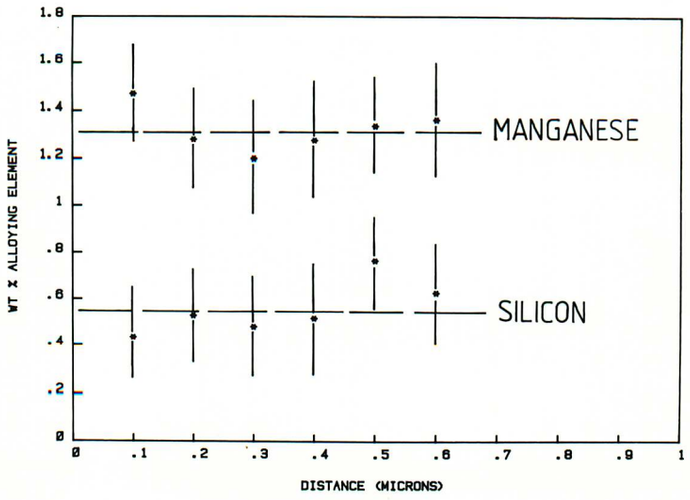

Fig.7.9 Manganese and silicon profiles away from inclusion in SA 1.

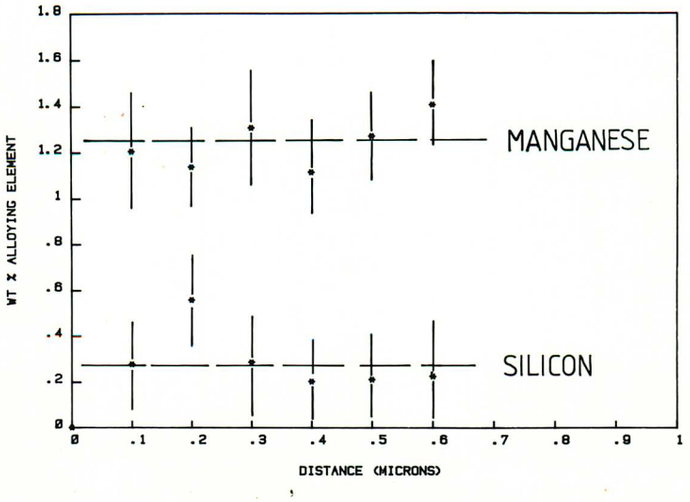

Fig.7.10 Manganese and silicon profiles away from inclusion in SA 4.

considered. In one case, the inclusion is located so as to be just detectable on the prepolished surface and under these conditions the maximum volume of the inclusion is sampled. Secondly, the inclusion is considered to be sectioned at its maximum diameter.

On this basis, it is possible to approximately estimate the ratio between the volume of the inclusion sampled to the total volume of

obtained on weld metal inclusions with that previously established for similar inclusions in cast and wrought steel.

7.4.1. PASEM Analysis

Before considering a detailed account of the inclusion chemistry, it is essential to account for the obvious discrepancies in the results obtained via the PASEM analysis. The information detailed in Figs. 7.1 and 7.2, which summarises the PASEM work suggests that the inclusions present in the two welds examined differ markedly in terms of the major elements present, ie Al,Si,Mn. However, the examination of these inclusions on carbon extraction replicas has shown that this is not the case and that Al,Si Mn are always present in inclusions in both welds, but that the relative proportion of those elements is different.

In order to explain the information derived from the PASEM analysis, it is useful to consider the volume of material from which x-rays are produced using this technique. Knowing the operating voltage, the probe size and the density of the target material, this can be calculated e.g. Andersen, (1973), and is shown schematically in Fig. 7.11. It should be emphasised that this represents the most conservative estimate of the volume containing the emitted x-rays and as stated by Andersen, this could be larger, due to enhanced beam penetration in the low density inclusions. In this Figure, two possible inclusion geometries are considered. In one case, the inclusion is located so as to be just detectable on the prepolished surface and under these conditions the maximum volume of the inclusion is sampled. Secondly, the inclusion is considered to be sectioned at its maximum diameter.

On this basis, it is possible to approximately estimate the ratio between the volume of the inclusion sampled to the total volume of material analysed, for a given inclusion diameter. The results of such an analysis indicate that for 0.3 to 0.5 μm diameter inclusions (the

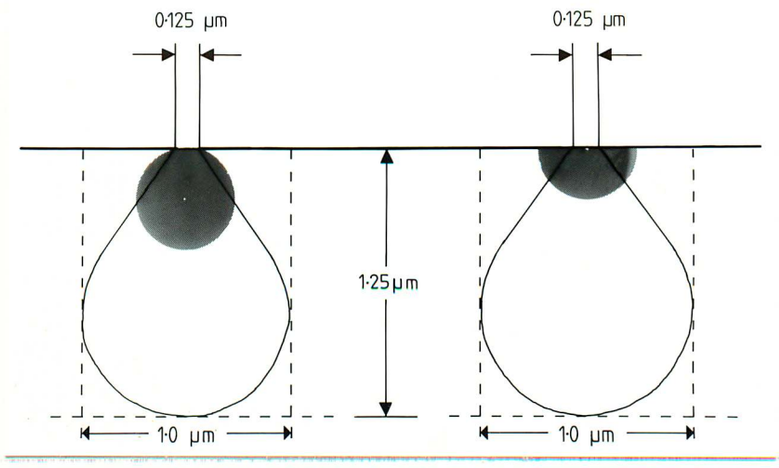

Fig.7.11 Schematic illustration of the relative volumes occupied by inclusions and the pear shaped x-ray envelope for a zero tilt position.

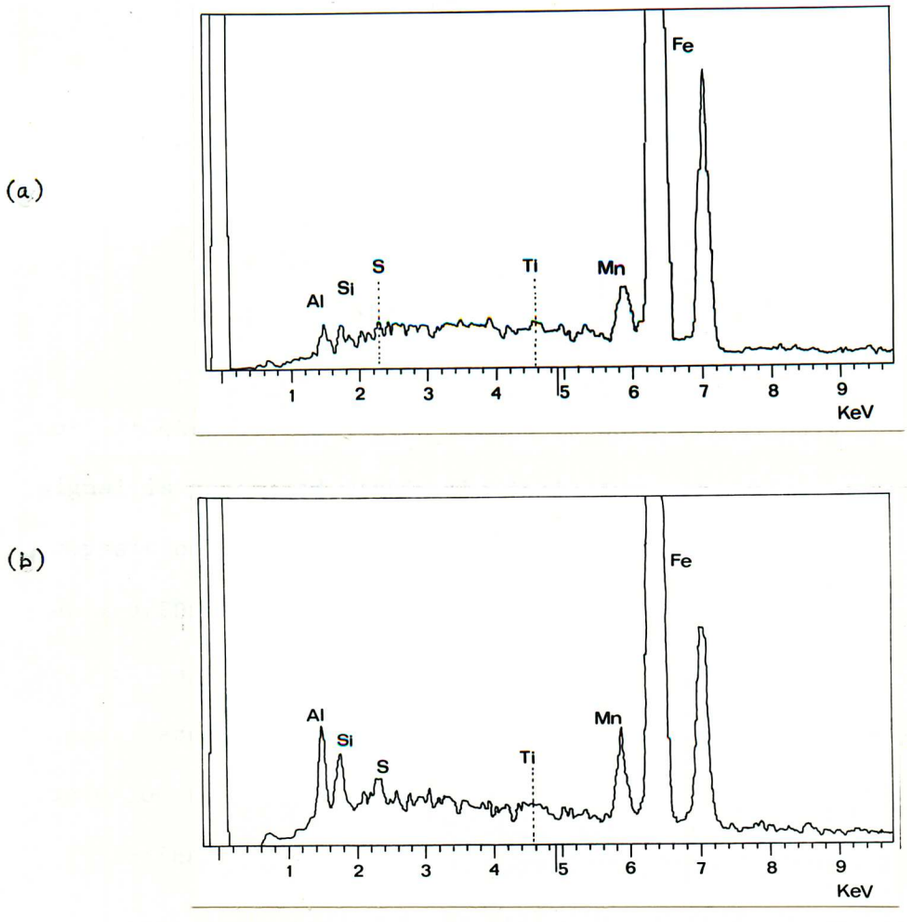

Fig.7.12 Typical spectra obtained from a large inclusion in a prepolished surface from weld SA 1.
(a) Specimen in the zero tilt position with respect to the detector.
(b) Specimen tilted 45° toward the detector.

their concentrations across the inclusions (as has been found in inclusions from weld SA 4) could easily preclude their identification in the PASEM analysis.

The same principle can be applied to understand the variation observed in the major elements present ie. Al, Si, Mn. Aluminium is only readily detected in the inclusions in the PASEM analysis of weld SA

most frequently found size groups in both welds), only 10% of the X-ray signal is generated within the inclusion. Further, if the average composition of the inclusions (as determined by the carbon extraction replica/EDS technique) are now considered, only 1/10 th of the relative proportion of an element detected in an inclusion will be present in the signal received in the PASEM analysis, eg. if a 0.5 μm diameter inclusion actively contains 30% Al (by wt), the PASEM signal will at best indicate only 3% Al(by wt).

This approach can immediately account for the sulphur and titanium peaks being consistently detected in the STEM/EDS technique, but absent in most cases in the PASEM work. Since the average concentration of sulphur and titanium in the inclusions (in weld SA4) is 3%, the effective concentration in the PASEM analysis is 0.3%, which is very close to the ultimate detection limit in microanalysis. Further, any actual variation in these elements in the inclusions or variation in their concentrations across the inclusions (as has been found in inclusions from weld SA 4) could easily preclude their identification in the PASEM analysis.

The same principle can be applied to understand the variation observed in the major elements present ie. Al, Si, Mn. Aluminium is only readily detected in the inclusions in the PASEM analysis of weld SA 4 because it is actually found in high concentrations ($\simeq$ 46%) in the inclusions in that weld. Similarly, manganese is detected in large numbers of inclusions in weld SA1 in the PASEM analysis because, again, it is found in high concentrations in the inclusions. Further, it is particularly noticeable that where silicon and manganese are not found in the PASEM analysis, this corresponds with the smallest size grouping (0.25μm to 0.50μm), where the ratio of the inclusion volume to that of the total volume containing the emitted x-rays is very large.

This interpretation has thus accounted for the PASEM data without considering the effects of absorption. (x-ray fluoresence is not of major concern in this case). Absorption is known to be particularly important in the case of light elements such as Al, Si, S, and Ti and can thus only further reduce the overall signal, indeed, the particular geometry adopted in the PASEM analysis (ie. that of zero tilt with respect to the x-ray detector) is to actually maximise the absorption effects. Using as near as possible the operating conditions used for the PASEM analysis, this can be demonstrated in Fig. 7-12(a), which shows the specta obtained from a 0.7μm inclusion from a prepolished specimen from weld SA 4 taken at zero degrees of tilt. The sulphur and titanium peaks can barely be distinguished, even after the 40 seconds counting time. By tilting the specimen 45 degrees towards the x-ray detector (as in the normal practise in x-ray analysis), the signal can be markedly improved, as shown in Fig.7.12(b). The Al, Si and S peaks are now clearly distinguished.

7.4.2. Inclusion Chemistry

The results detailed in section 7.3.1 (b) have shown that there is no difference with respect to the major elements present, between the inclusions found in welds SA1 and SA4. It is clear that in both cases, the inclusions are mixed in character and not the simpler type claimed by Farrar and Watson (1979).

As a starting point, it is interesting to note that the general guide concerning the Mn/Si ratio in inclusions suggested by Kiessling and Lange (1978) applies in the case of welds SA1 and SA4. That is to say that the Mn/Si ratio of the bulk analysis of these welds (3 for weld SA1 and 4 for weld SA 4) reflects the Mn/Si ratio observed in the inclusions (2 for the inclusions in weld SA1 and 3 for those in weld SA 4). This Mn/Si ratio in the bulk composition has also been used by

Widgery (1974), where it was shown to be directly linked to the inclusion volume fraction. The results detailed in that study are in close agreement with this work, in that the weld with the higher Mn/Si ratio (weld SA 4) had the lower volume fraction of inclusions. It is beyond the scope of the current investigation to comment further on the complex deoxidation processes involved, but a further discussion of the resulting inclusion chemistry will be considered.

Since three major elements (ie. Al, Si, Mn) are present in the inclusions, it is necessary to refer to the MnO- SiO_2 - Al_2O_3 ternary system. This system has been investigated in depth by Kiessling and Lange (1978) and their analytical results are summarised in Fig.7.13. It must be emphasised that this is not an isothermal section through the ternary system, but a record of the composition ranges of the various inclusions found in steels in this system.

The results detailed in Table 7.4 can be used to locate the approximate position of the inclusions in this study on Fig.7.13. This is indicated by the large stars and show that the inclusions in the acidic deposit are close to the stoichiometric composition ($3MnO-Al_2O_3-3SiO_2$), but also within the composition range for glassy inclusions in the MnO- SiO_2 -Al_2O_3 system. In contrast, the composition indicated for the inclusions in the basic flux show that it is well outside the glassy region observed in this system. The high Al_2O_3 content indicates that it is probably duplex comprising of an Al_2O_3 nucleus surrounded by a mixed $Al_2O_3/SiO_2/MnO$ phase, as reported in wrought steels of very similar composition (ie 0.11%C, 0.25% Si, 1.10%Mn, 0.026%Al).

7.4.3. Matrix Chemistry

The work of Farrar and Watson (1979) dealing with the effect of oxygen and manganese on weld metal microstructure will be further

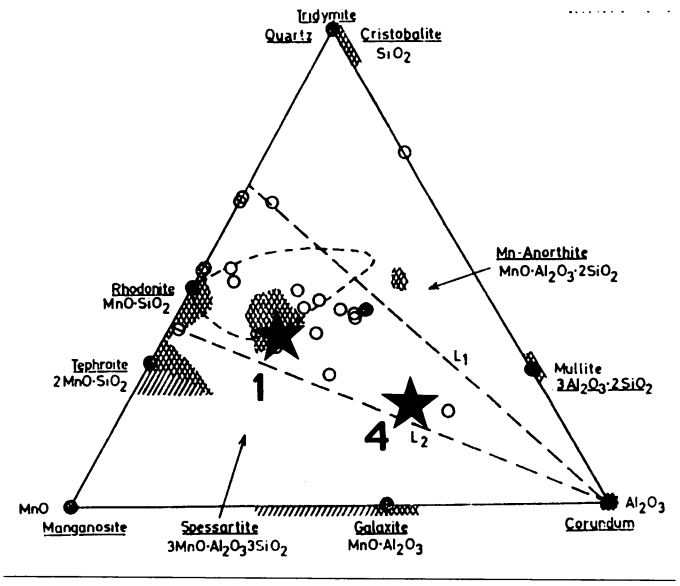

Fig.7.13 Summary of the analytical results obtained by Kiessling and Lange (1978) for inclusions in the $SiO_2/Al_2O_3/MnO$ system. The open circles indicate the composition of inclusions observed in practise together with stoichiometric compositions (full circles) and the observed homogeneity ranges. The central region (enclosed by dashed lines) indicates the glassy region of the system which encompasses the composition of inclusions observed in weld SA 1. In contrast, those inclusions in weld SA 4 are well removed from this region.

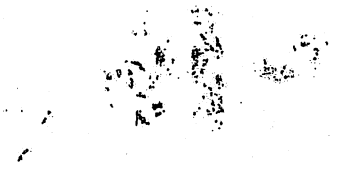

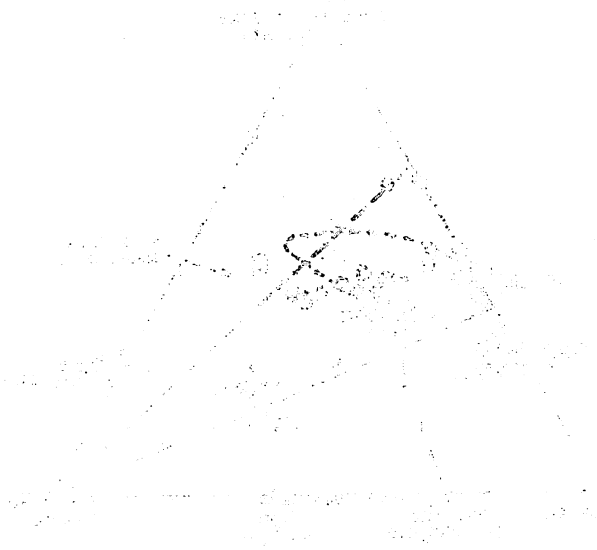

considered in the following chapter. However, it is clear from the work described in the previous sections that the inclusions present in typical acidic and basic weld deposits are unlikely to be single, simple, inclusion types. Further, it has been shown that they do not substantially affect the manganese content of the matrix austenite, either locally or as a whole. Calculation using the formulae for inclusion volume fraction have further supported these observations.

7.5 SUMMARY

The results detailed in this chapter have shown

(i) The vast majority of inclusions in the two submerged arc welds considered comprise mixed aluminium/manganese, oxides/ silicates, which can be coated by a thin layer of sulphide.

(ii) The inclusions in the basic deposit (SA4), in addition to the above, contain a significant TiO_2 content.

(iii) A significant difference in the proportion of the elements found in the inclusions has been detected, which suggest that inclusions in the acidic deposit (SA1) could be glassy, whereas those in the basic deposit (SA 4) are probably crystalline.

(iv) The inclusions have little effect on the overall composition of the matrix in these welds.

(v) The nucleation of intragranular Widmanstatten ferrite on inclusions, as described in Chapter 6, has not been promoted by local solute depletion around the inclusions.

(vi) In its present form, PASEM analysis of inclusions on weld materials CANNOT yield accurate or useful information.

CHAPTER 8

FACTORS AFFECTING THE DEVELOPMENT OF MICROSTRUCTURE IN H.S.L.A. WELD METALS.

8.1. INTRODUCTION

This chapter is concerned with several factors which have been identified as important parameters in the development of microstructure. The aim is to incorporate the experimental observations into an overall picture with reference to the previous three chapters. Particular attention will be focussed on those factors which affect, either directly or indirectly, the nucleation frequency of ferrite on weld metal inclusions.

8.2. THE SIGNIFICANCE OF AUSTENITE GRAIN SIZE AND INCLUSION SIZE DISTRIBUTION

This section will use the technique of T.I.G. remelting and quenching to investigate changes in the oxygen levels of two submerged arc weld deposits, SA2 and SA5. In parallel, direct quenching of submerged arc deposits SAQ1 and SAQ2 will be used to further characterize microstructural development in these materials. Finally, the possible effects of the inclusion size distribution will be discussed with reference to recent work at the Welding Institute, Pargeter (1981)

8.2.1. EXPERIMENTAL RESULTS

The procedure of T.I.G. remelting of submerged arc weld metal produces two areas of interest - a remelted region (where the oxygen level is reduced) and a reheated region (where the oxygen level remains unchanged).

Figs. 8.1(a) and (b) show the microstructure of the remelted region of welds SA2 and SA5. The reduction in oxygen level in weld SA2 seems to have promoted the development of the acicular ferrite constituent, whereas in weld SA5 a grain boundary nucleated ferrite sideplate microstructure predominates. Examination of the reheated regions of these deposits (which have had a very similar thermal cycle to the remelted region) reveals quite the reverse pattern of behaviour described above. The reheated region of weld SA2 retains the characteristic ferrite sideplate microstructure, as shown in Fig. 8.1(c). Similarly, the reheated region of weld SA5 again transforms to a typical acicular ferrite microstructure, as shown in Fig. 8.1(d). Contrasting the austenite grain size of these reheated areas again shows a significant difference, as previously observed in the as-deposited microstructure - see Chapter 4.

Examination of the partially transformed regions of welds SAQ1, SAQ2, indicates clearly the sequence of transformation. In high oxygen weld metals, it has been suggested that ferrite sideplates are nucleated on inclusions situated in the austenite grain boundaries (Cochrane and Kirkwood, (1978)). However, after extensive examination of both thin foils and carbon extraction replicas from such regions, no 1:1 correspondence between ferrite sideplates and inclusions was observed. A typical region from weld SAQ1 is shown in Fig.8.2. Where a typical acicular ferrite microstructure was developed (eg. weld SAQ2, the reheated area of weld SA 5 and the remelted region of weld SA2), the characteristic inclusion nucleation and sympathetic nucleation of ferrite were observed, as shown in Fig.8.3.

8.2.2. DISCUSSION AND CONCLUSION

The T.I.G. remelting and quenching experiment described in this investigation is closely based on the work reported by Abson et al (1978). Indeed, the welding conditions and procedures were themselves

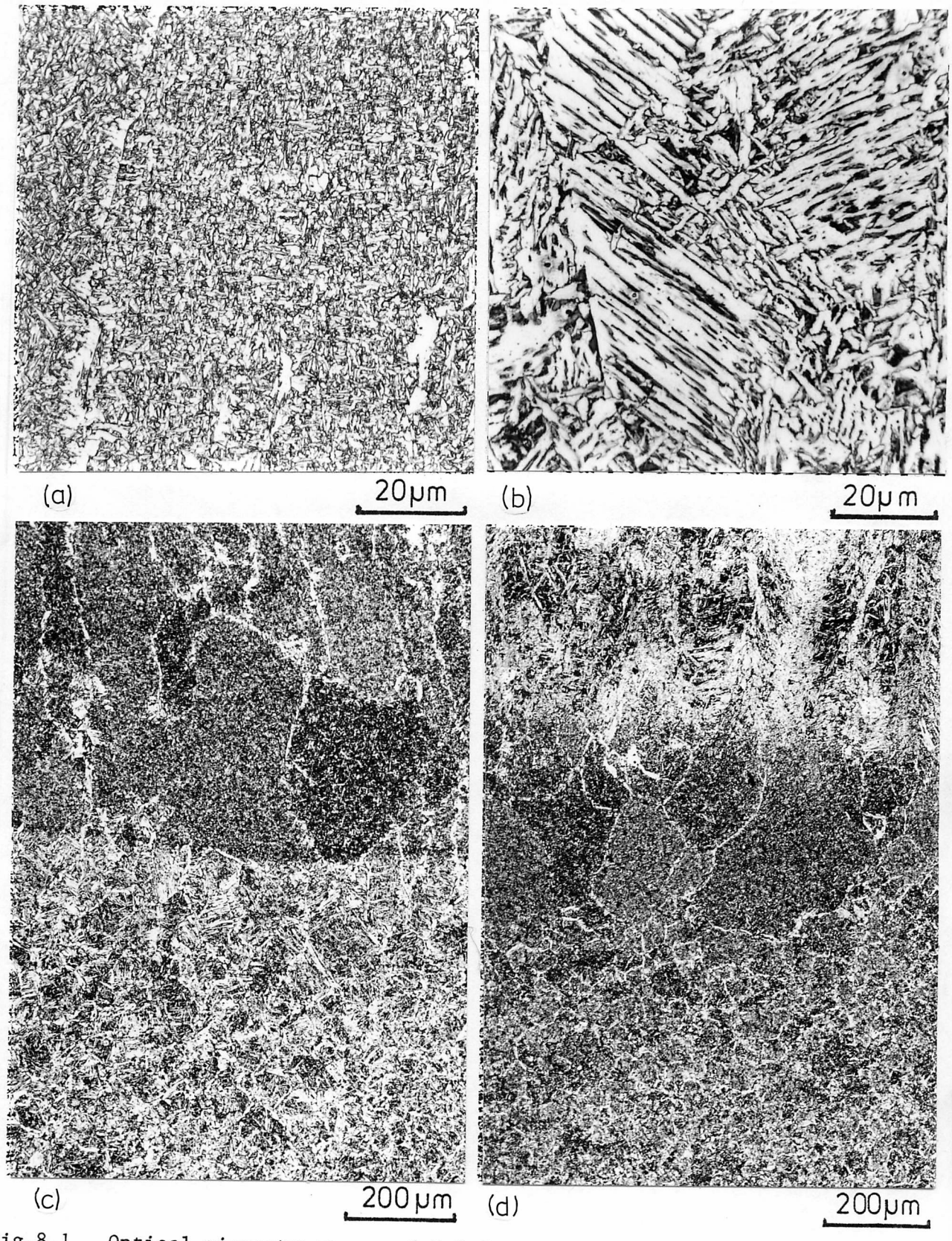

Fig.8.1 Optical microstructures of T.I.G. remelted submerged arc welds. Remelting produces a distinct change in the final microstructure whereas the reheated regions closely resemble the original as-deposited microstructure.

(a) Remelted region of weld SA2
(b) Remelted region of weld SA5
(c) Reheated region of weld SA2
(d) Reheated region of weld SA5

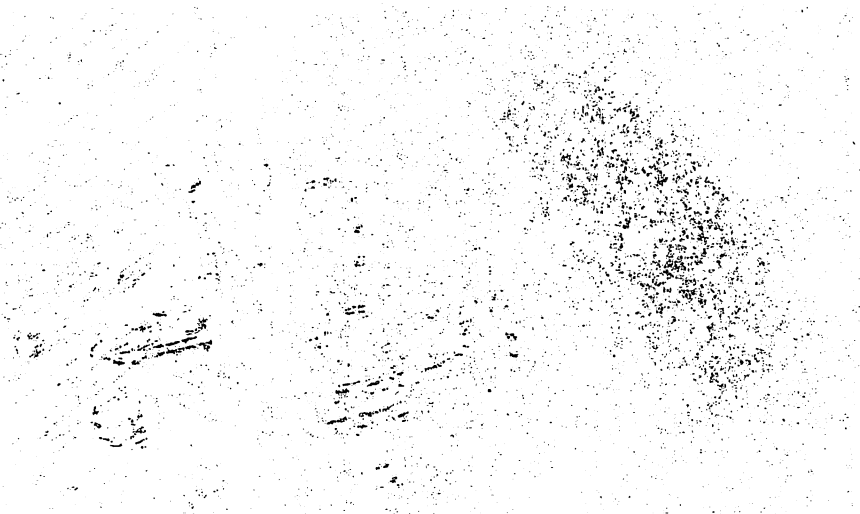

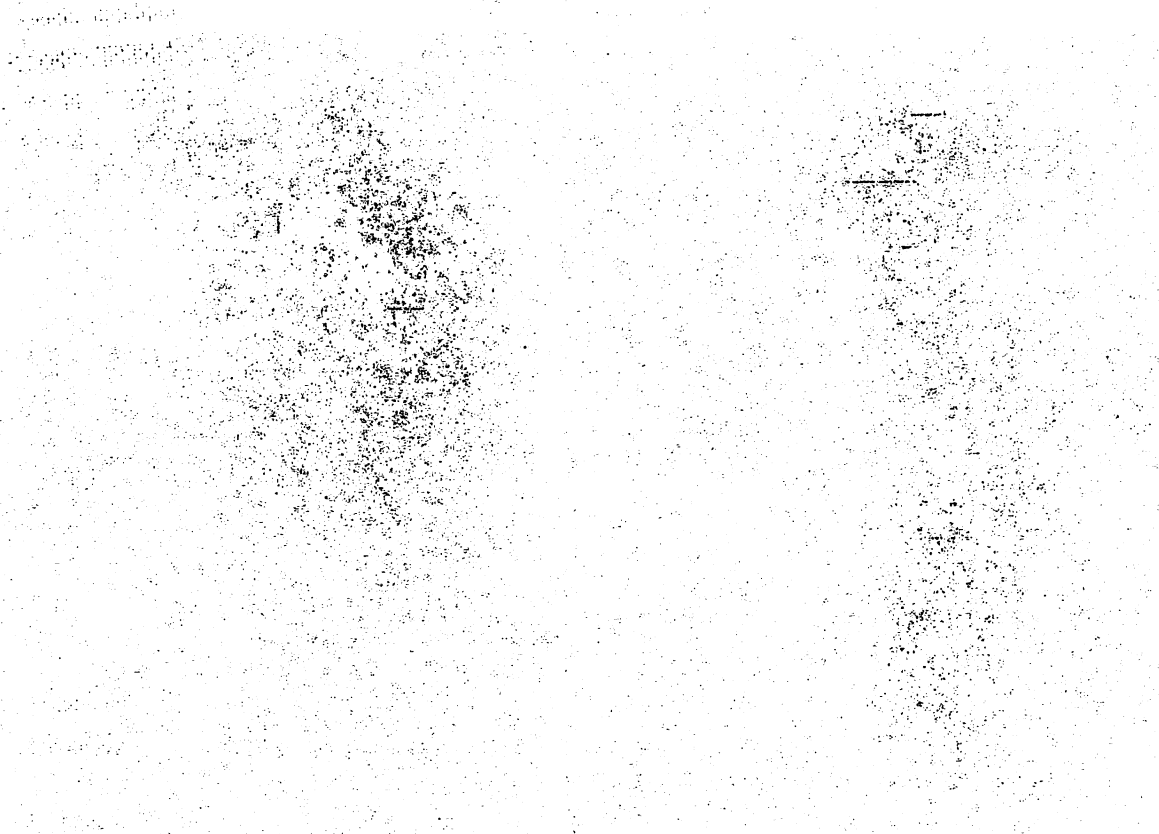

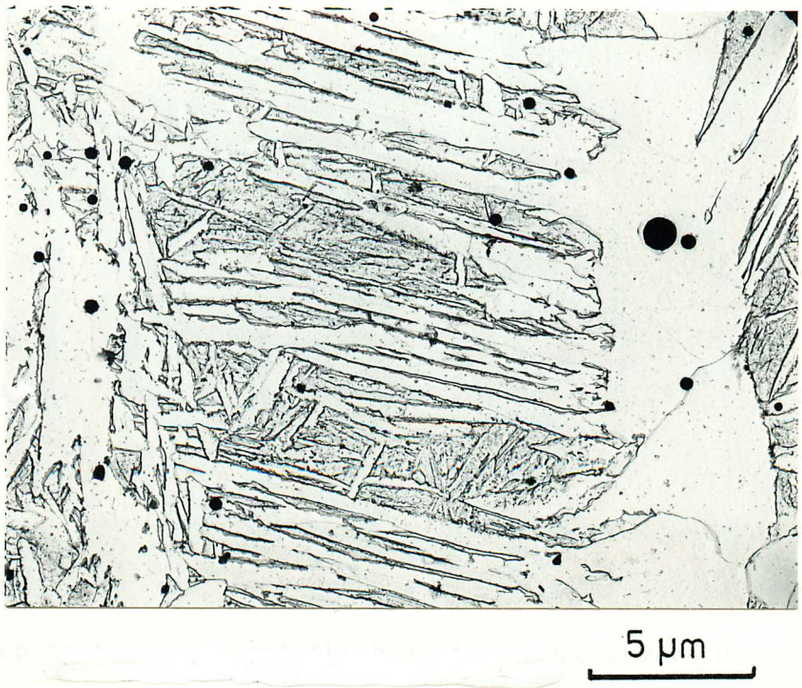

Fig.8.2 Transmission electron micrograph of a typical austenite grain boundary region of quenched weld SAQ1 . There is no obvious indication that inclusions in the austenite grain boundary have acted as nucleation sites for Widmanstätten ferrite sideplates. (carbon extraction replica)

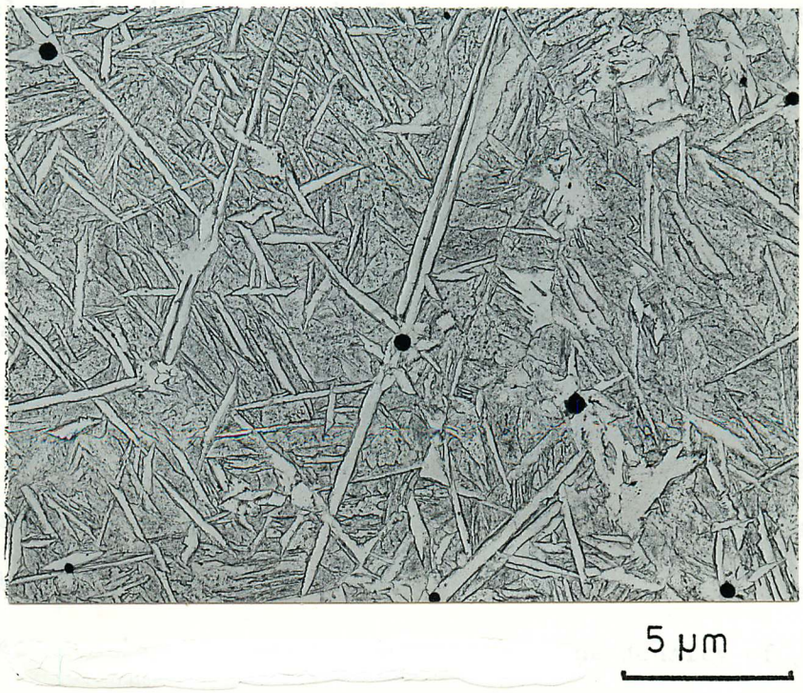

Fig.8.3 Transmission electron micrograph illustrating both inclusion and sympathetic nucleation of Widmanstätten ferrite. (reheated region of T.I.G. weld SA 5). (Carbon extraction replica)

In the case of low oxygen weld metals (i.e. the TIG remelted region of SA5), grain boundary ferrite reactions are again predominent. This

(see Chapter 4), as would be expected from theoretical grain coarsening arguments.

devised from subsequent work at the Welding Institute. Table 3.5 shows that the oxygen level has been changed without any major change in the alloying elements present. Further, the cooling rate induced was not sufficient to promote lower temperature reaction products as occurred in the Welding Institute study (Thermal analysis of the remelted regions in both welds indicated that the cooling rate was similar to that of 1.5kJ/mm, despite the fact that the heat input was lower, 0.5 kJ/mm, probably due to the small test plate used).

In the present study, it has been shown that whatever the oxygen content of the weld deposit, the austenite has decomposed to grain boundary nucleated and intragranularly nucleated ferrite. The balance between the relative activity in these sites depends critically on two interrelated factors - the inclusion content and the austenite grain size. As previously discussed, the acicular ferrite microstructure occurs predominantly in the medium oxygen range, where initially austenite grain boundary nucleation of ferrite occurs, with the subsequent reaction following intragranularly.

In high oxygen welds, although the inclusion content is high, for the same reason, the austenite grain size is small, due to inclusion pinning of those boundaries. This small austenite grain size has a powerful effect on the decomposition reaction. The density of grain boundary nucleation sites is larger, resulting in the higher transformation temperatures and shorter times observed dilatometrically. Further, and perhaps of most significance, this enhanced grain boundary reaction will tend to increase the carbon content of the residual austenite in the grain interiors. This acts to suppress the operation of intragranular nucleation sites and consequently reduces the proportion of the intragranular ferrite microstructure.

In the case of low oxygen weld metals (i.e. the TIG remelted region of SA5), grain boundary ferrite reactions are again predominent. This

can be easily resolved, since it is clear that the primary nucleation sites have been removed. Since homogenous nucleation is very unfavourable (see Chapter 6) and sympathetic nucleation of ferrite only occurs after the operation of the inclusion nucleation sites, it is unlikely that the intragranular reaction can proceed to a major extent.

Summarising, in this system, the three oxygen regimes can be rationalised in terms of the competitive nature of the grain boundary and intragranular ferrite reactions. In essence, microstructure is controlled by the inclusion content and the austenite grain size, which are themselves interrelated. Grain boundary reactions predominate in the high oxygen regime because of the small austenite grain size, whereas at low oxygen levels these reactions predominate because of the lack of primary intragranular nucleation sites.

Conscious of several discussions with colleagues at the Welding Institute, it remains to be tested if these observations are applicable to a range of commercial consumables.

Oxygen level alone cannot define, in a given system, if inclusion pinning of grain boundaries will be predominant in the final microstructure. For example, the same oxygen level could be achieved with two quite distinct size distribution of inclusions. In this system, it appears to be the very large inclusions (in the range 0.8μm to 2μm) which are responsible for pinning austenite grain boundaries (see Chapter 4), as would be expected from theoretical grain coarsening arguments.

It was beyond the resources of the current investigation to consider a wide range of oxygen levels; however, Pargeter (1981) has reported extensive studies of submerged arc welds using particle analysing scanning electron microscopy. This work details information regarding the oxygen level, the inclusion type and size distribution in a series of two pass and multipass submerged arc welds. Though the

microanalytical results have been shown to be invalid (see Chapter 7), Pargeter showed in a comparative study that the technique does accurately size the inclusions. To facilitate a direct comparison with the current investigation, the large number of welds considered by Pargeter must be rationalised. If the composition range is limited to 0.1% to 0.14% carbon, 0.9% to 1.2% manganese, and 0.15% to 0.25% silicon, the data reduces to five welds (designated 7200/27 7200/35, 7200/37, 7200/41, 7319/3) for the two pass submerged arc deposits.

The oxygen levels of the above deposits range from 0.064% O_2 (weld 7200/27) to 0.022% O_2 (weld 7200/41) The microstructure and inclusion size distributions determined by Pargeter for these two welds are shown in Fig. 8.4 (a) and (b). The higher oxygen deposit is again characterized by predominantly grain boundary nucleated ferrite sideplates, whereas the lower oxygen level comprises a typical acicular ferrite microstructure. Though the austenite grain sizes were not reported, examining the published micrographs, it is evident that a smaller austenite grain size is apparent at the higher oxygen level.

On the basis of these results, it seems reasonable to suggest that given constant chemical composition and cooling rate, austenite grain size controls the development of the final microstructure. It is clear that this observation has been frequently masked by variations in composition, cooling rate and, in many cases, failure to assess austenite grain size accurately (if at all) in experimental work. Further, if the observation regarding a shift in the inclusion size distribution at higher oxygen levels represents a general trend, a qualitative argument has been developed to explain the original proposal by Abson et al., (1978) that the actual size distribution could be an important factor in determining the final microstructure.

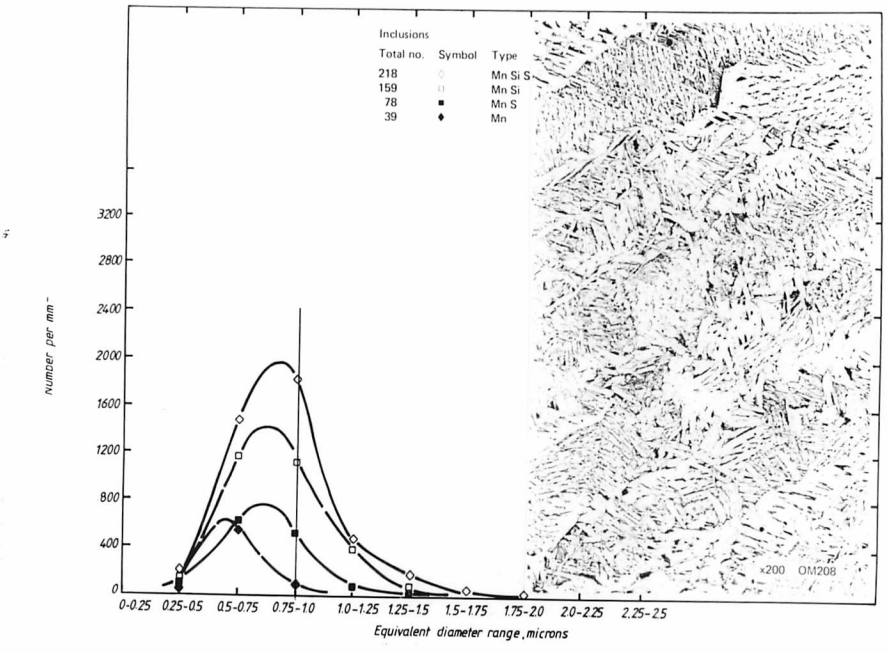

(a)

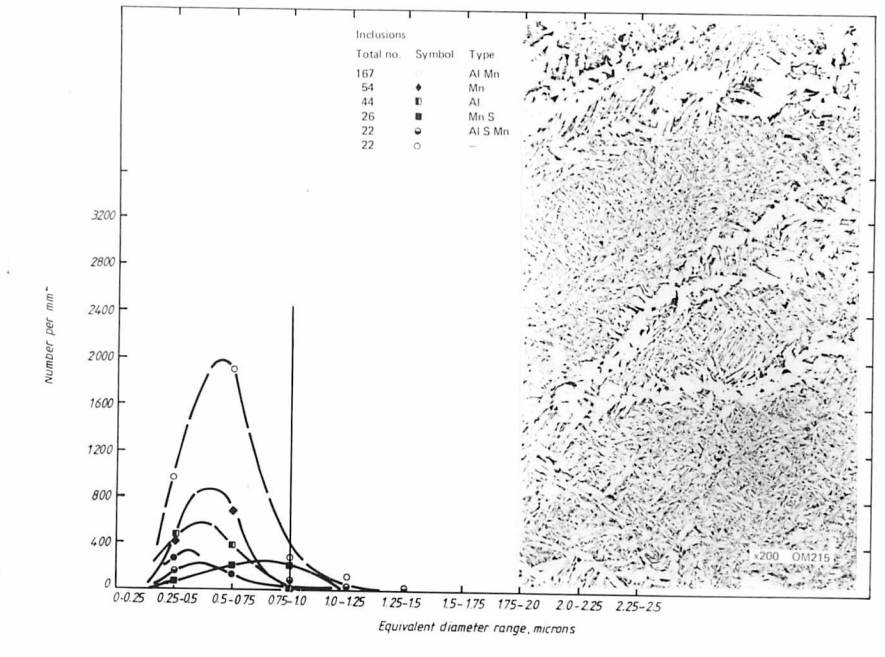

(b)

Fig.8.4 Microstructure and size distribution of weld metal inclusions observed by Pargeter (1981) in submerged arc weld deposits.
(a) High oxygen weld metal (0.06% O_2)
(b) Medium oxygen weld metal (0.03% O_2)

(Courtesy R. Pargeter, the Welding Institute).

8.3 THE ROLE OF MANGANESE IN THE DEVELOPMENT OF MICROSTRUCTURE IN LOW ALLOY STEELS AND WELD METALS.

8.3.1. INTRODUCTION AND METALLURGICAL BACKGROUND.

Traditionally, manganese has always been regarded as a 'friendly' element in steel metallurgy. Originally, it was added to deoxidise, and to fix sulphur in cast steel, preventing hot shortness by replacing the low melting point iron sulphide which gave serious problems in subsequent hot working. In recent years, its low price and relative abundance has made it an attractive alloying element for improving the properties of structural steels. For example, increasing manganese levels have been utilised in the pipeline industry in controlled rolled and microalloyed steels, eg Mintz (1974). In weld materials, a natural division is apparent between submerged arc and manual metal arc processes. In the former case, the role of manganese in promoting strong, tough materials is well established, eg. Tuliani et al., (1972), Farrar and Watson (1979). In contrast, only recently has an attempt been made to improve toughness via manganese alloying in manual metal arc welding, eg. Evans (1980), Taylor (1981).

Initially, it is interesting to note the effect of manganese on the calculated TTT curves described in Chapter 5. For the C-Mn-Mo steels considered in the subsequent investigation, Fig. 8.5 shows the predicted effect of increasing manganese in the range 0.6% to 1.5%. Clearly, manganese should have a powerful effect on the incubation time for both the diffusional and displacive transformations.

8.3.2. EXPERIMENTAL RESULTS

(a) Submerged arc welding

Two series of submerged arc welds are considered in this investigation. In both cases, two nominal oxygen levels were achieved, using BOC 80R and Oerlikon OP121TT fluxes. At each nominal oxygen level,

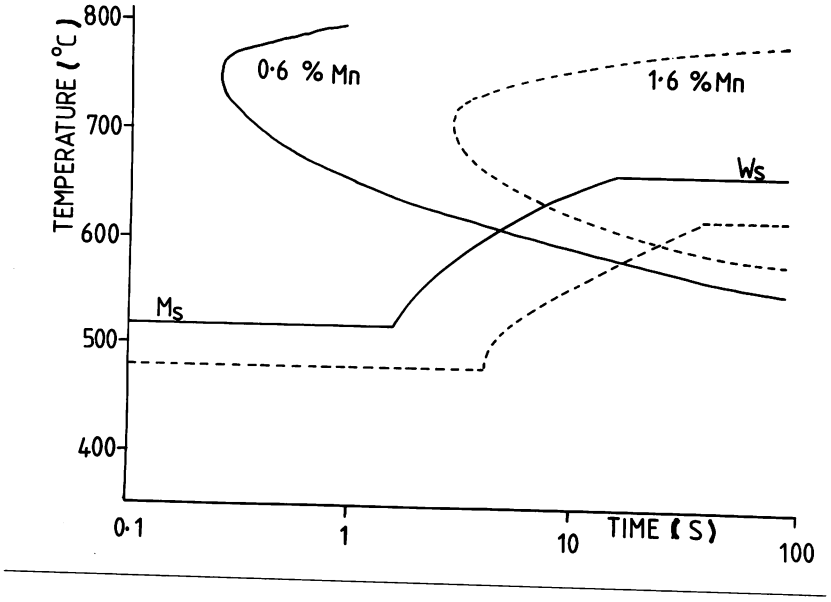

Fig.8.5. Calculated T.T.T. diagrams for alloy A- (0.6%Mn) and alloy C (1.6 % Mn) illustrating the pronounced effect manganese has on the incubation time for both the diffusional and displacive 'C' curves.

two distinct levels of manganese were investigated, by employing commercial S1 (or S1 Mo) and S4 (or S4Mo) welding wires containing 0.5% Mn and 2.0%Mn respectively.

The optical microstructure of the four C-Mn welds (SA 11, 13, 12, 14) are shown in Figs. 8.7 (a), (b), (c), (d). Increasing manganese under the OP121TT flux has reduced the oxygen level and produced a marked increase in the proportion of the fine interlocking acicular ferrite constituent. In contrast, at the higher level of oxygen produced by the BOC 80R flux, increasing manganese over the same range has produced no major microstructural change and the grain boundary ferrite sideplate microstructure is still predominant. The austenite grain sizes of these welds confirm the previous observations detailed in section 8.2. Financial limitations precluded the investigation of the Charpy impact properties of these welds as planned, but previous experience would suggest that only in the case of the medium oxygen deposits (welds SA11 and 13) would a marked improvement in toughness be achieved with increasing manganese content.

The optical microstructure of the four C-Mn-Mo welds (SA 7, 9, 8, 10) are shown in Figs 8.6 (a), (b), (c), (d). Although these welds were produced with the same batches of flux as the C-Mn series, lower oxygen levels (at the same manganese level) were achieved. This is particularly evident in the 'high' oxygen deposit welds SA 8,10, where the oxygen concentrations were less than 500ppm for both manganese levels. The only indication as to the possible causes of this effect were in the aluminium levels observed in the final deposits, which were higher (0.024% Al), in the C-Mn-Mo welds than the C-Mn series (0.018% Al) indicating a slightly higher deoxidation potential.

The predominant microstructure observed at low manganese levels (welds SA 7,8) closely resemble the observations in the C-Mn series. However, comparing the microstructure of welds SA7 (Fig. 8.6 (a)) and

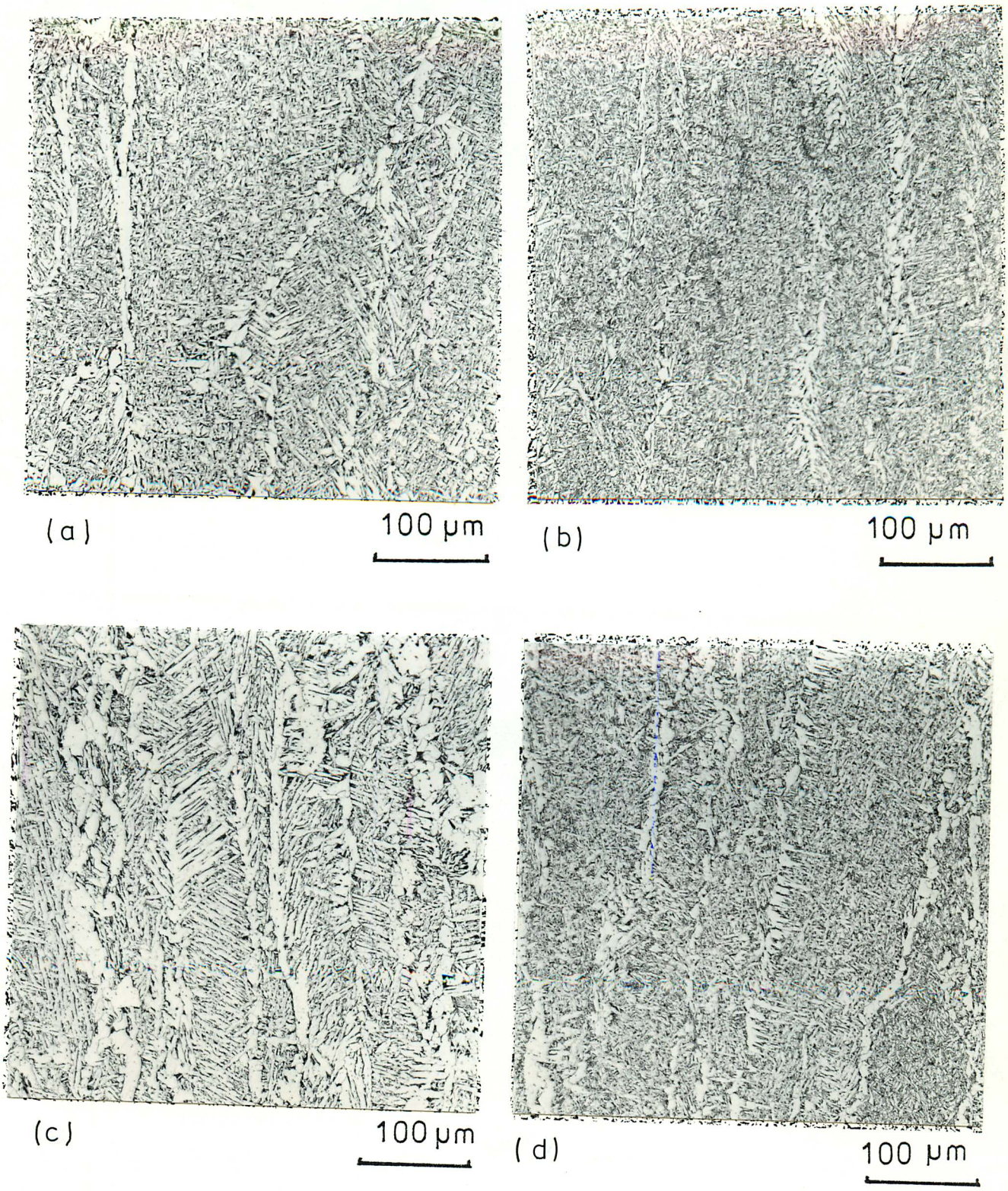

Fig.8.6 Microstructure of C-Mn-Mo submerged arc welds.

(a) Weld SA 7, Low Mn, Low O_2

(b) Weld SA 9, High Mn, Low O_2

(c) Weld SA 8, Low Mn, High O_2

(d) Weld SA 10, High Mn, Low O_2

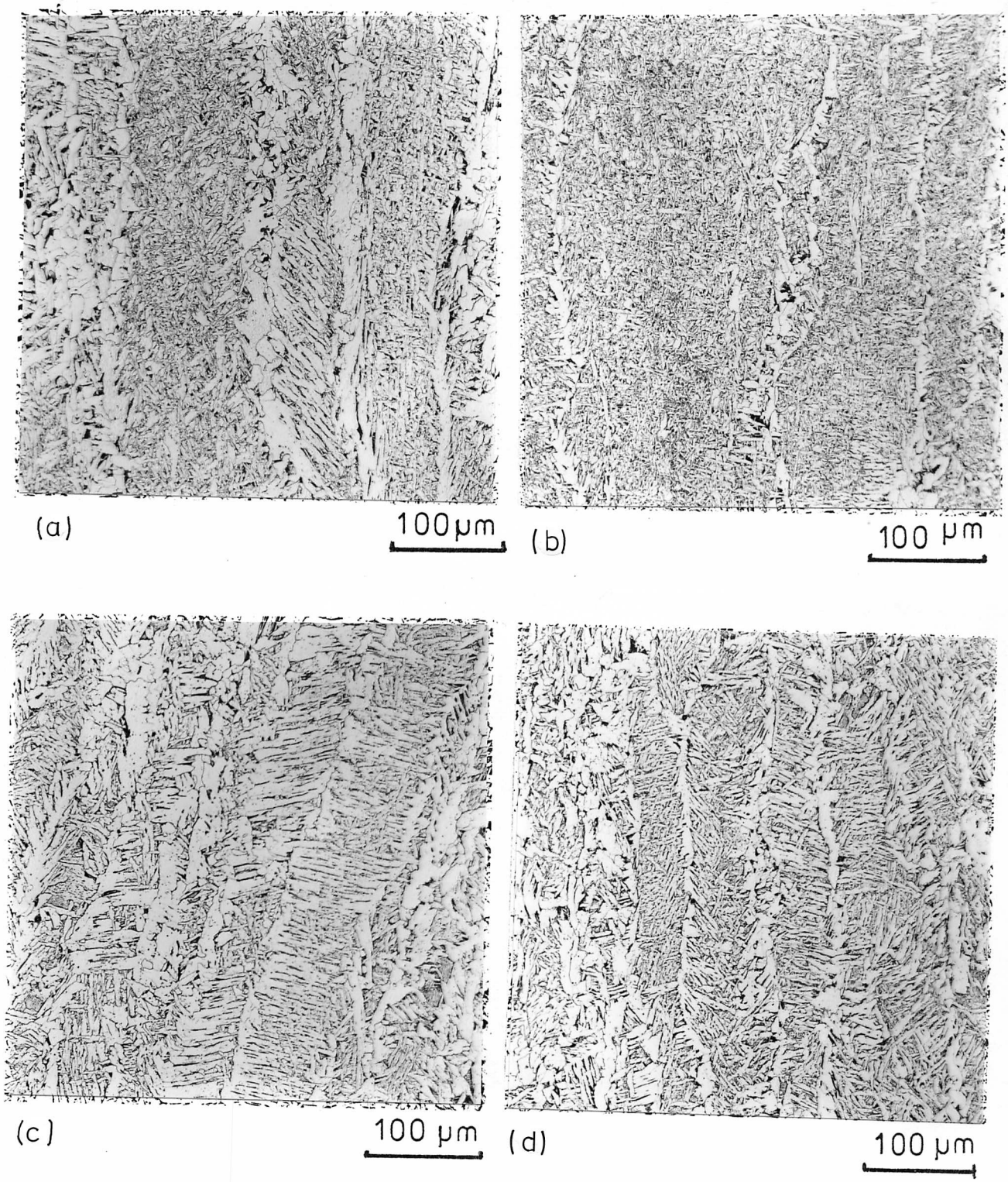

Fig.8.7 Microstructure of C-Mn submerged arc welds.

(a) Weld SA 11, Low Mn, Low O_2

(b) Weld SA 13, High Mn, Low O_2

(c) Weld SA 12, Low Mn, High O_2

(d) Weld SA 14, High Mn, High O_2

SA11 (Fig.8.7(a)), which have nominally the same manganese and oxygen levels, indicates that molybdenum has itself promoted the development of the acicular ferrite microstructure. At higher manganese levels (welds SA 9,10), a distinct difference in microstructure is observed in comparison with the C-Mn series, since both deposits now exhibit typical acicular ferrite microstructure. The mechanical properties for the C-Mn-Mo series of deposits are summarised in Figs. 8.8 (a) and (b). Increasing manganese under the BOC 80R flux has produced a distinct improvement in Charpy impact properties, whereas with the OP121TT flux the toughness is relatively insensitive to the manganese level.

(b) High purity steels.

To model the behaviour of the submerged arc welds previously described, a series of four high purity C-Mn-Mo steels were investigated. The chemical analysis is given in Table 3.11, which reveals that although a systematic increase in manganese has been achieved, unfortunately two levels of carbon were observed in the final ingots, ie alloys A and C (0.09% C), alloys B and D (0.14%C).

The continuous cooling diagrams derived for three of these alloys (alloys A,B, and C) are shown in Figs. 8.9 (a)(b)(c), referring to nominally 0.6% Mn, 1.1% Mn and 1.6%Mn respectively. The general effect of manganese in this system is to suppress transformation throughout the cooling range considered. At any fixed cooling rate, the effect is to suppress the ferrite field and bainite field to longer times.

The investigation of alloy D revealed several interesting features which deserve further comment. The overall kinetics of this alloy are summarised in Fig. 8.10, which shows the C.C.T. diagram. A marked increase in hardenability is observed, with a distinct flat top appearing in the diagram. The microstructure observed at selected cooling rates (designated A-G) are shown in Figs. 8.11 (a) to (f).

(a) OP121TT

● Low Mn

■ High Mn

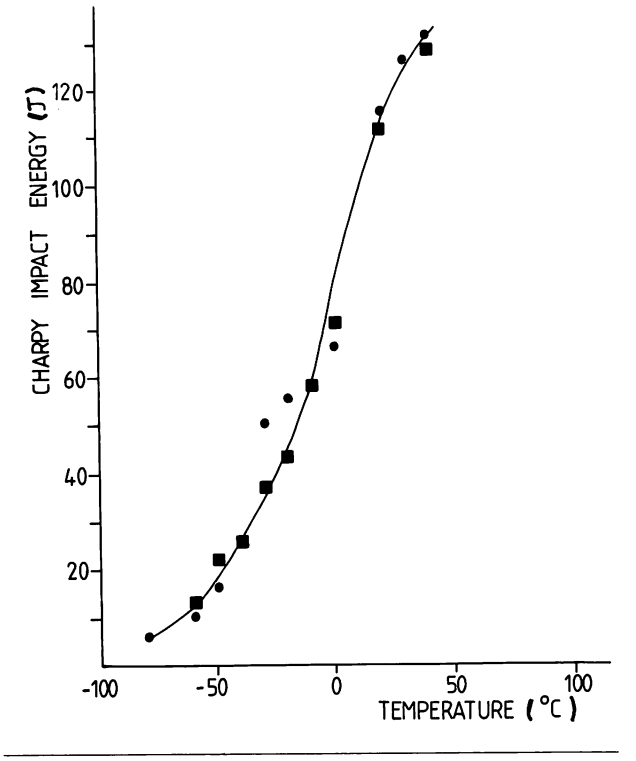

(b) BOC 80R FLUX

● Low Mn

■ High Mn

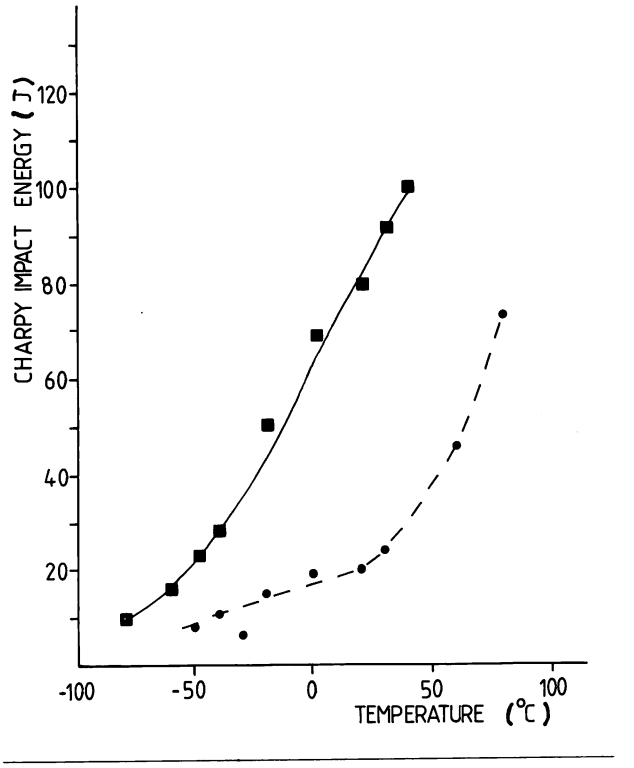

Fig.8.8 Charpy impact properties for C-Mn-Mo submerged arc weld metals.

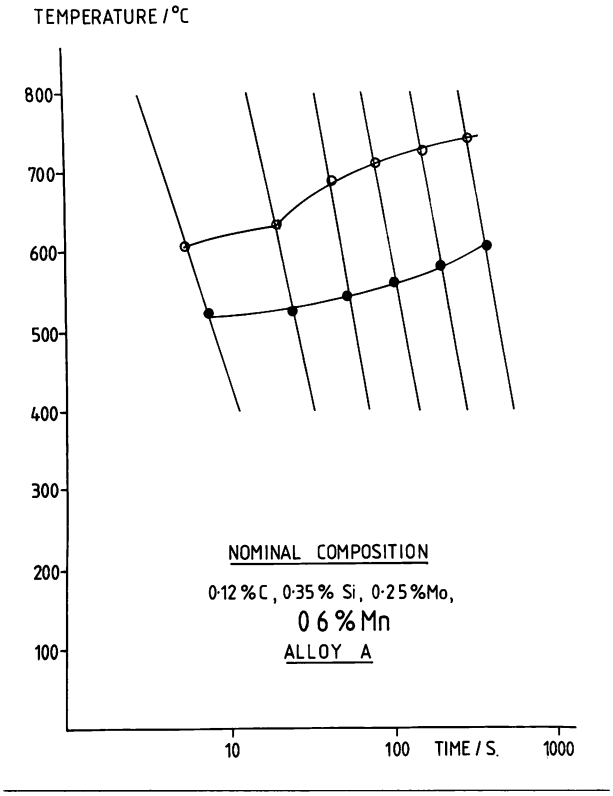

(a)

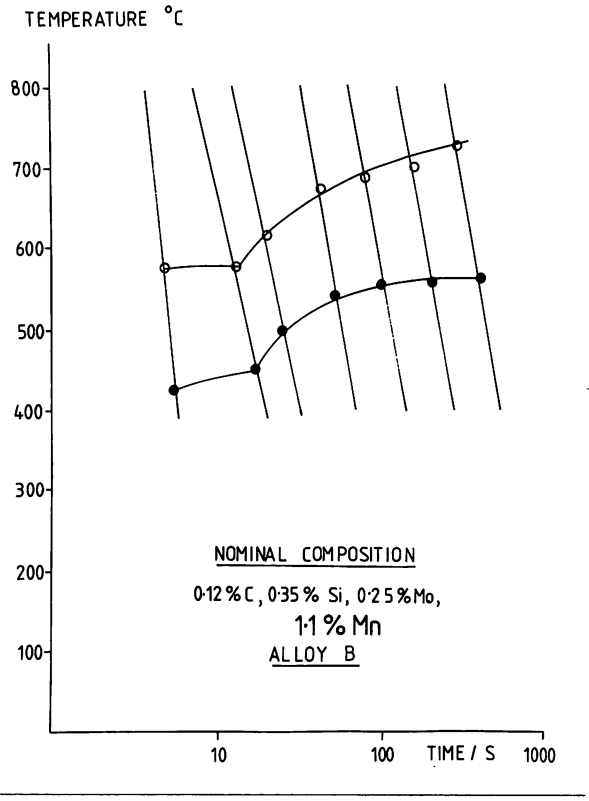

(b)

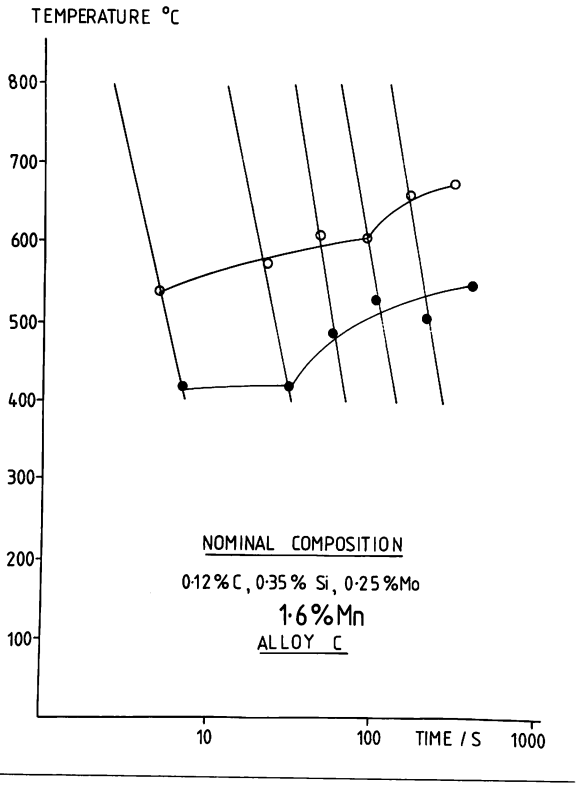

(c)

Fig.8.9 C.C.T. diagrams for alloys containing - 0.6% Mn - Fig.8.9 (a), 1.1 % Mn - Fig.8.9 (b) 1.6 % Mn - Fig.8.9 (c). At a fixed cooling rate manganese supresses the transformation temperature and moves the ferrite reaction C-curve to longer times.

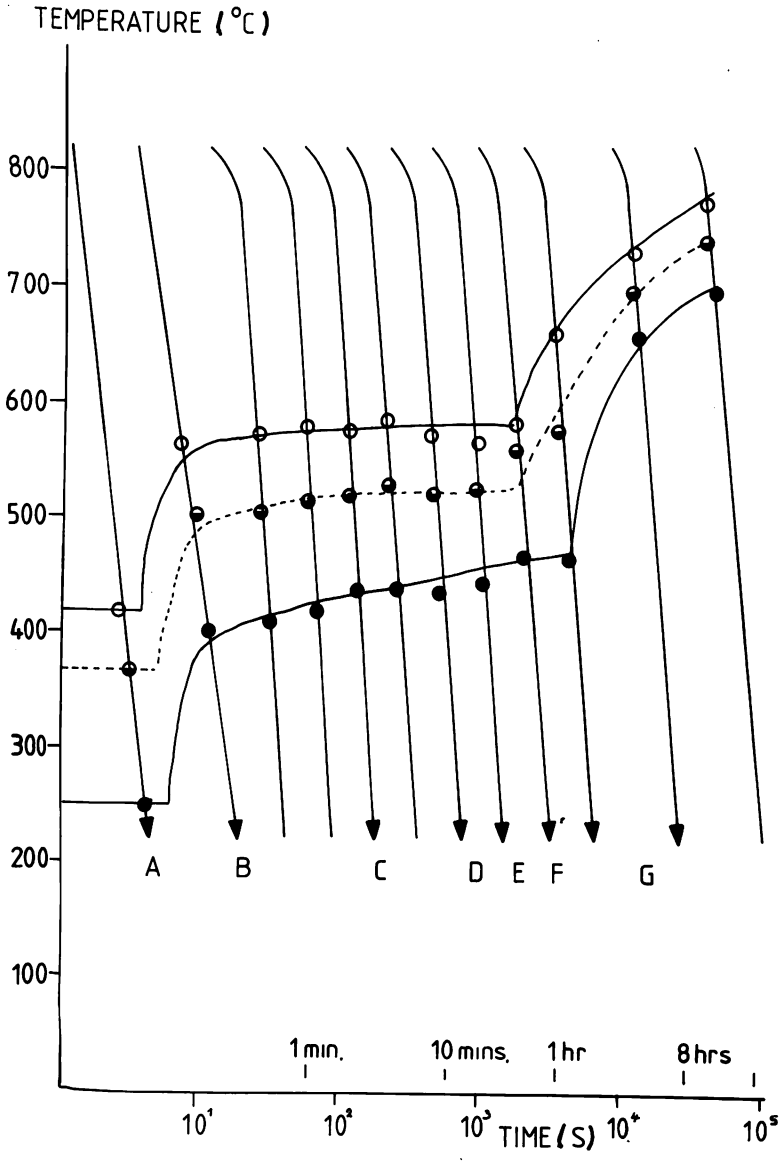

Fig.8.10 Continuous cooling diagram for alloy D. (Nominally 2.1 % Mn). At this level of manganese a distinct 'flat top' appears in the lower 'C' curve extending over a wide range of cooling rates. (For discussion see text)

This alloy system was the only one of the steels investigated where it was possible to quench directly to martensite in the dilatometer. The lath martensite so produced is shown in Fig. 8.11 (a). At slightly slower cooling rates (eg those designated B), a classic upper bainite microstructure is observed, as illustrated in Fig. 8.11 (b). This microstructure was uniquely identifiable up to cooling rate C, whereas at slower cooling rates, eg D, the resultant product (Fig. 8.11(c)) is less distinct, due to the extensive impingement. This complex microstructure persists until cooling rate E, where there is still no evidence for the classic grain boundary ferrite morphologies. The first indication of such boundary ferrite is found at cooling rate F, as shown in Fig. 8.11(d). At all cooling rates (eg G) slower than this, grain boundary ferrite is observed, as shown in Fig. 8.11 (e), where additionally, a Widmanstatten ferrite morphology is observed. If, at this cooling rate, the cooling cycle is interrupted by helium quenching, the residual austenite transforms to a classic upper bainite microstructure, as shown in Fig. 8.11 (f). This transformation occurs 60°C below the normal transformation temperature (as observed dilatometrically) and lends practical support to the concept of an 'effective' bainite start temperature discussed in Chapter 5.

(c). Manual metal arc welding

In both series of electrodes examined, a progressive refinement of microstructure occurred as manganese was increased in the weld deposit. This can be summarised in Fig. 8.12 (a),(b), which shows the substantial increase in the proportion of the acicular ferrite constituent for welds MMA 7 and 9 (ie the E7018 series). In acting as a weak deoxidising agent, increasing manganese in these electrodes has resulted in a systematic decrease in the oxygen level in the final deposit, as shown in Fig. 8.13 for both series of electrodes.

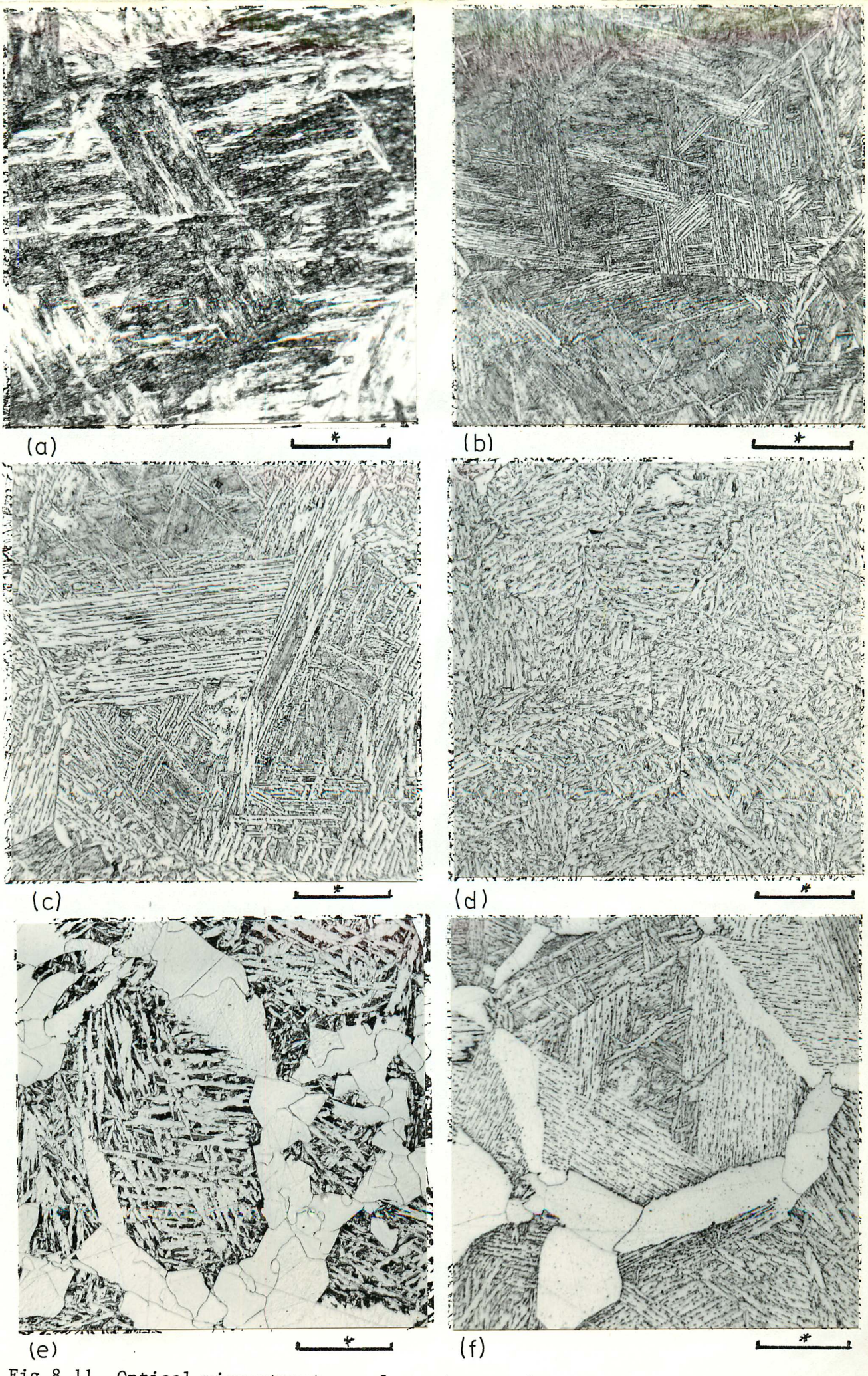

Fig.8.11 Optical microstructure of specimens subject to continuous cooling treatments - alloy D. For discussion see text.

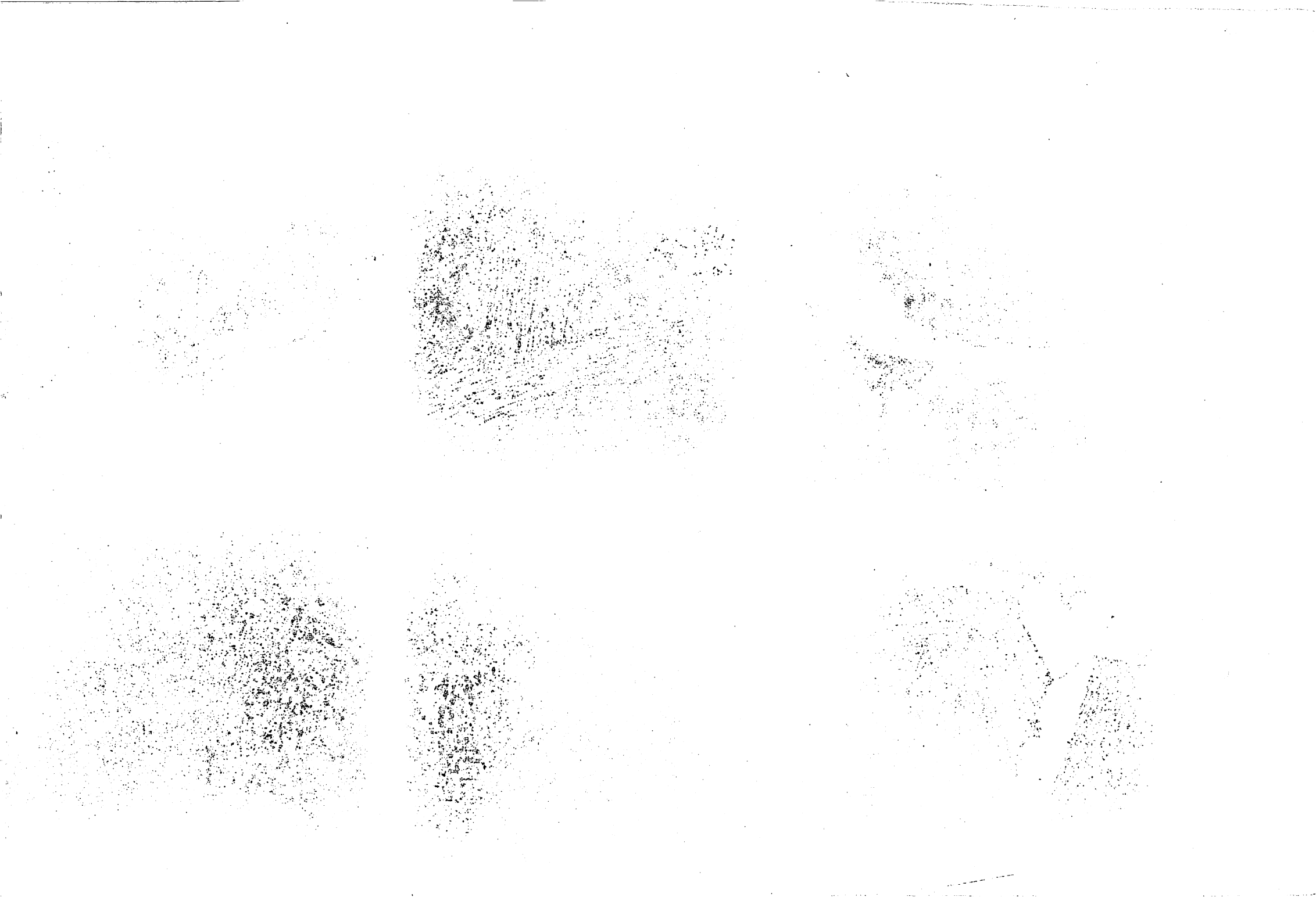

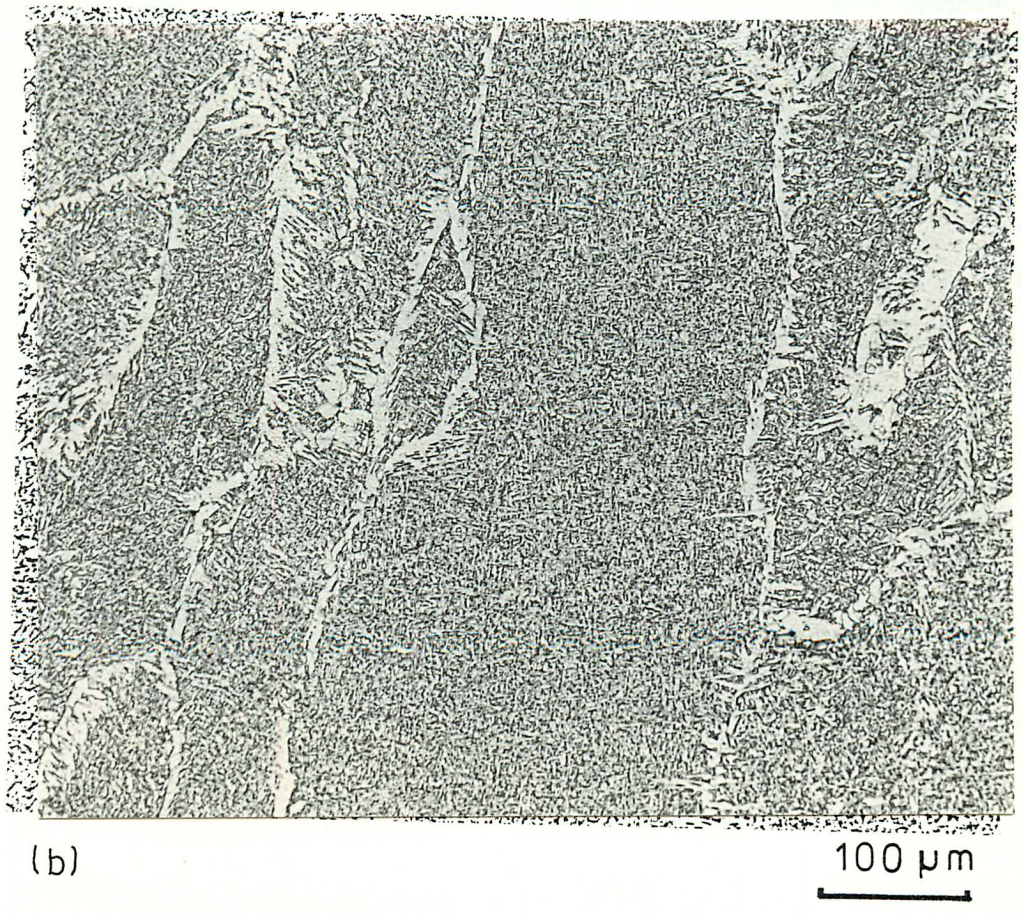

Fig.8.12 Effect of manganese on the microstructure of manual metal arc welds (MMA). Low manganese levels (Fig.(a)) are characteristically associated with grainboundary nucleated microstructures whereas high manganese levels (Fig.(b)) have a large proportion of the acicular ferrite microstructure. (MMA welds 7 and 9).

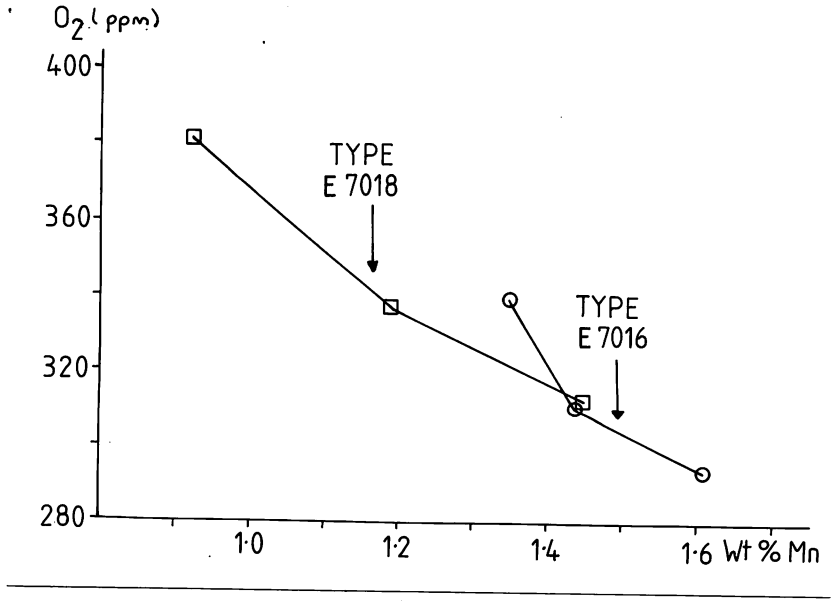

Fig.8.13 Consistent with its role as a weak deoxidant, increasing manganese causes a reduction in oxygen level in the final weld deposit for both E7016 and E7018 type electrodes.

E.D.X. analysis of the inclusions in these welds showed that corresponding with the increase in manganese, there was no major change in the inclusion type present in these materials. As previously reported in Chapter 7, the inclusions are complex oxides/sulphides and silicates, with typically Al, Si, S, Mn, Ti, all being present. There is, however, a slight change in the average composition of the inclusions, as shown in Fig. 8.14 (a), where a slight increase in manganese and corresponding decrease in silicon level was observed in the E7018 type electrodes. The other elements detected in the inclusions showed no systematic variation as manganese was increased in the weld deposit, as summarised in Fig. 8.14 (b).

In the partially transformed regions of these welds, the sequence of intragranular nucleation again comprised both inclusion nucleation and sympathetic nucleation of ferrite. However, increasing manganese has increased the relative proportion of sympathetically nucleated ferrite, as illustrated qualititively in Fig. 8.15 (a) and (b), which shows the intragranular regions of welds MMA 7 and 9.

8.3.3. DISCUSSION AND CONCLUSIONS

Considering the role of manganese as a whole, it is clear that it has a powerful effect in the development of microstructure in these low alloy materials. Its function in terms of hardenability is relatively simple to understand, in that at a given cooling rate, it promotes transformation to Widmanstatten ferrite. This is consistent with the expected effects on the calculated T.T.T. diagrams and the experimentally determined C.C.T. diagrams.

In considering weld materials, its role as deoxidant must also be considered, since, in principle, it can have at least three powerful effects.

1) reduce the total number of inclusions present

2) change the size distribution of the inclusions present

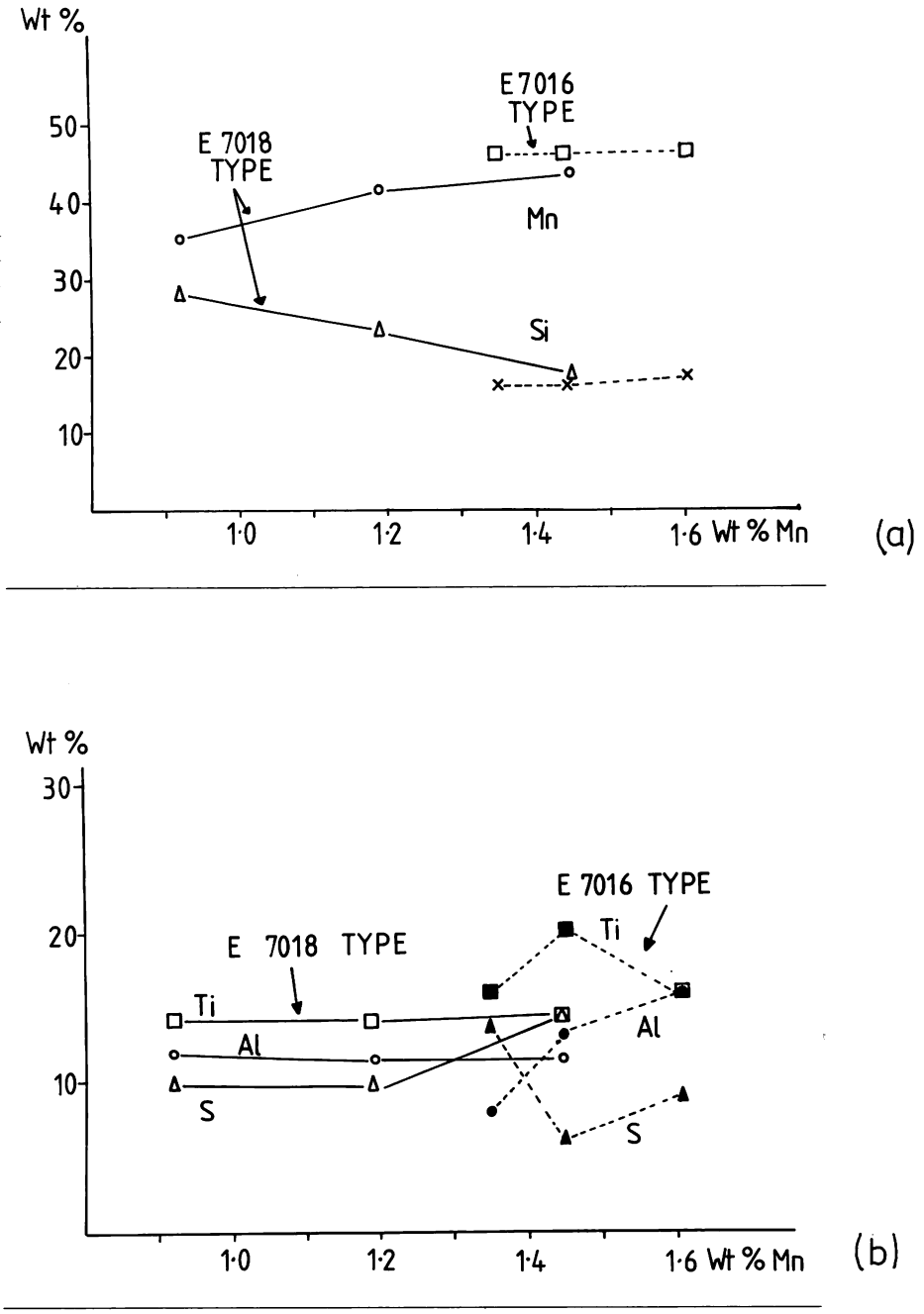

Fig.8.14 The effect of increasing manganese on average inclusion compositions in E7016 and E7018 type electrodes. A slight change in manganese and silicon levels occurs (Fig.8.14(a)) whereas the other elements present (Fig.8.14(b)) remain relatively unchanged.

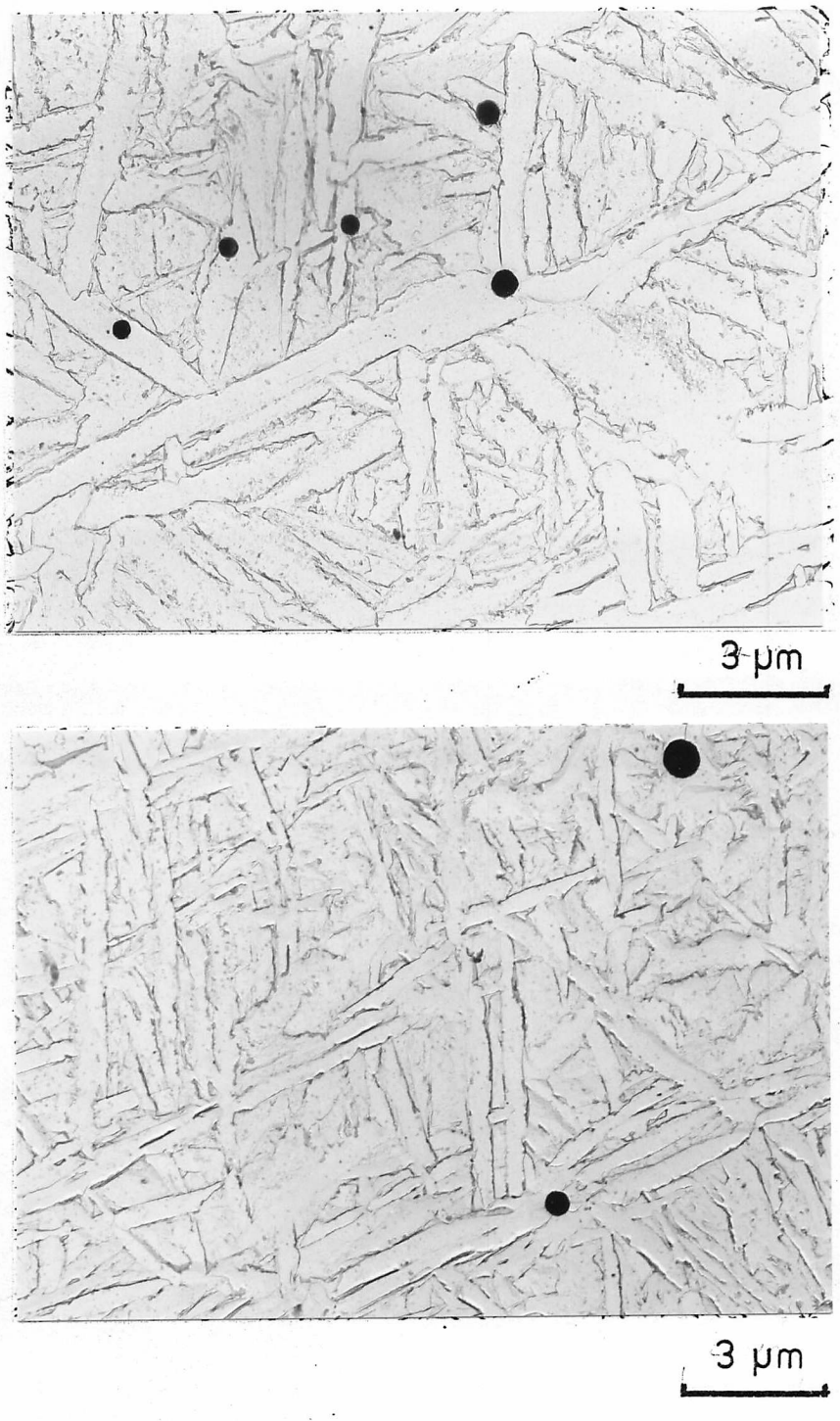

Fig.8.15 Transmission electron micrograph of the intragranular regions of welds MMA 7 and 9. Increasing the manganese level of the weld deposit has increased the proportion of sympathetically nucleated Widmanstatten ferrite.

(a) Weld MMA 7
(b) Weld MMA 9

3) change or modify the inclusion type.

The significance of the first two points has been discussed qualititively in the previous section. At first sight, decreasing the total inclusion content in the weld deposit seems incompatible with the increasing proportion of acicular ferrite in the final microstructure, as they have been shown to act as the primary nucleation sites for the intragranular reaction. However, this decrease in oxygen content is also accompanied by an increase in austenite grain size, eg. Figs. 8.12(a), (b), therefore favouring the possibility of enhanced intragranular reactions. Further, since by improving the hardenability, decomposition to Widmanstatten ferrite is favoured, this could explain the qualitative observation that the proportion of sympathetically nucleated ferrite increases.

The microstructural observations for both series of C-Mn and C-Mn-Mo series of submerged arc welds must be put in context by considering their chemical analysis. The marked improvement in microstructure produced as manganese was increased could be interpreted as support for the work of Farrar and Watson (1979). However, it is clear that increasing manganese reduces the oxygen level in a given system. It therefore seems likely that a critical degree of deoxidation is required rather than a critical level of manganese (as proposed by Farrar and Watson, 1979)) - though the two are obviously related.

Summarising, manganese contributes towards both the hardenability and the deoxidation reactions and thus has a dual role to play in the development of microstructure in weld materials.

8.4 THE EFFECT OF PREHEAT ON SUBMERGED ARC WELD METAL MICROSTRUCTURE AND TOUGHNESS

8.4.1. INTRODUCTION

The three welds supplied by the Welding Institute for microstructural studies were transverse sections from two pass tandem submerged arc deposits. They had been welded using the same flux (Oerlikon OP121TT) and an SD3 Mo wire at a heat input of 4.9kJ/mm. The welds were designated A,B,C, as follows :-

Weld A - 20°C preheat

Weld B - 100°C preheat

Weld C - 300°C preheat

The compositions were closely matching, centred on the following; 0.15%C, 0.30%Si, 1.36% Mn, 0.18% Mo, 0.022% Nb, 0.026% O_2.

8.4.2. EXPERIMENTAL RESULTS

The microstructure of the three welds A,B,C, are shown in Figs. 8.16 (a)(b)(c). The proportion of grain boundary nucleated ferrite increases as the preheat temperature increases, as does the average ferrite grain size. The various preheat treatments have not significantly changed the prior austenite grain size - though this is difficult to judge, as those boundaries are not distinct. The Charpy impact properties for these welds are shown in Fig. 8.17, where a marked decrease in toughness is observed with increasing preheat. In order to estimate the volume fraction of cementite in the final microstructure, deep-etched carbon extraction replicas were prepared from equivalent positions in all three welds. A typical microstructure is shown in Fig. 8.18, which shows the areas of cementite following a 100°C preheat. The measured volume fraction of cementite was determined directly using a Quantimet - 720 image analyser as follows:-

(a) 0° C Preheat

(b) 100°C Preheat

(c) 300°C Preheat.

Fig.8.16 Optical microstructure of submerged arc welds with different preheats. As the cooling time is increased (a to c) the proportion of grain boundary ferrite increases with a corresponding decrease in the acicular ferrite content.

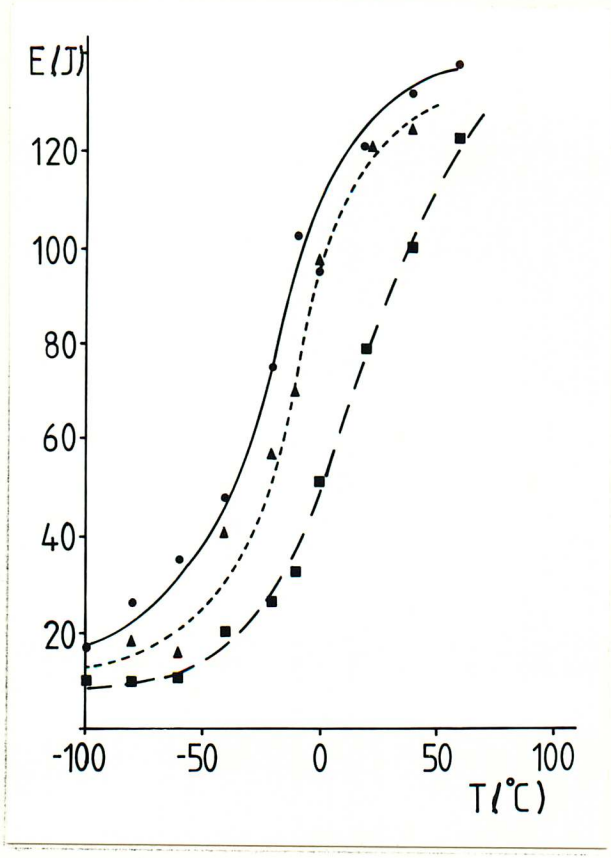

Fig.8.17 Charpy impact properties for submerged arc welds with different levels of preheat. As the preheart increases (0°C • , 100°C ▲ 300°C ■) a marked deterioration in toughness occurs.

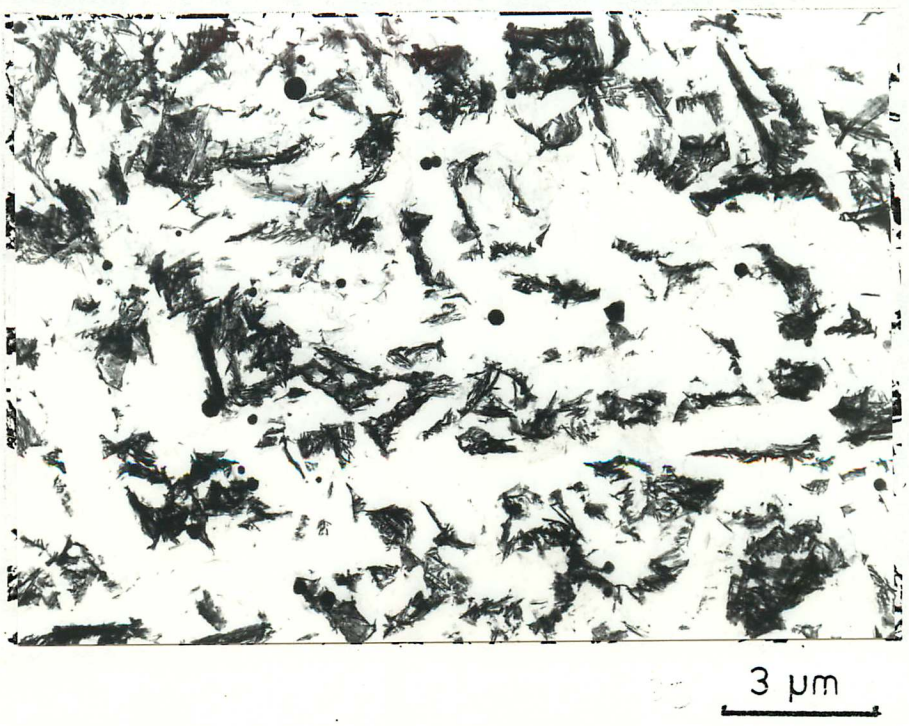

Fig. 8.18. Carbon extraction replica from submerged arc weld following 100°C preheat. The sharp black/white contrast between the extracted cementite and matrix allows quantitative analysis.

0°C Preheat - 12.3 ± 3.1 %

100°C Preheat - 18.1 ± 2.8 %

300°C Preheat - 20.1 ± 3.4 %

8.4.3. DISCUSSION AND CONCLUSIONS

Preheat is generally regarded as a necessary evil with respect to weld metal microstructure and mechanical properties. The overall effect of the slower cooling rate induced is to promote coarser microstructure. In this system, grain boundary ferrite has been promoted, with a resultant decrease in impact properties. There seems no evidence to support the original proposal by Abson and Dolby (1977) that preheat had increased the proportion of bainite in the microstructure.

8.5 THE EFFECT OF INCLUSION TYPE ON FERRITE NUCLEATION IN HIGH STRENGTH LOW ALLOY STEEL WELD METALS.

8.5.1. INTRODUCTION

The subject area covered in this section is perhaps one of the most speculative areas of development in welding research. Alchemists once sought the ingredients to change lead into gold, whereas welding metallurgists, rightly or wrongly, now seek the inclusions which are the most effective nucleants for the intragranular ferrite reaction.

The addition of innoculants and specialised deoxidants to commercial consumables represents an extremely complex problem, both in terms of experimental design and analysing the results. In principle these materials can have many effects, eg pinning austenite grain boundaries, modifying grain boundary reactions, changing the overall oxygen level, in addition to any direct effects on weld metal inclusions. At present, the most limiting feature of assessing work in this field is the lack of any direct experimental evidence to substantiate the various claims. For example, of the workers in this field, eg. North et al (1979), Mori et al. (1981), only Funakoshi et al (1977) have provided any experimental evidence to support their claims.

Experimentally, two approaches have been adopted in this section to investigate the effect of inclusion type on ferrite nucleation. Section 8.5.2 describes a brief investigation into the effect of parent plate deoxidation practice on microstructural development in manual metal arc welds. A single electrode type (OK Hytrode 7016-1) and four base steels (plates D-G) are investigated. Section 8.5.3 reports an investigation into the effect of particular inclusion types on ferrite nucleation in a series of model alloys (based on Alloy J). This work proved unsuccessful and will be only briefly described.

8.5.2. THE ROLE OF PARENT PLATE DEOXIDATION PRACTICE IN THE DEVELOPMENT OF MICROSTRUCTURE

This investigation centres on examining the effect of parent plate dilution on four manual metal arc deposits (MMA 13-16). The base steels were supplied by the Welding Institute, where an investigation is currently in progress studying the effects of parent plate deoxidation on the microstructure and toughness of submerged arc deposits.

Bead on plate welds were produced, which resulted in approximately 50% dilution with the parent plate. The optical microstructures of the four welds so produced are shown in Figs. 8.19 (a) to (d). The markedly different proportion of the acicular ferrite microstructure so produced must be put in context of the chemical analysis (see Table 3.9) which reveals that although the carbon content of each deposit remains reasonably constant, wide variations in the other major constituent elements have arisen. For example, the silicon level systematically increases in the deposits, as does the aluminium level. However, in response to these observations, there seems no direct or simple reflection in the observed total oxygen content of the weld deposit. Clearly, in this case, there is a complex interaction of Mn, Al, Si and oxygen, which is responsible for the improvement in microstructure which

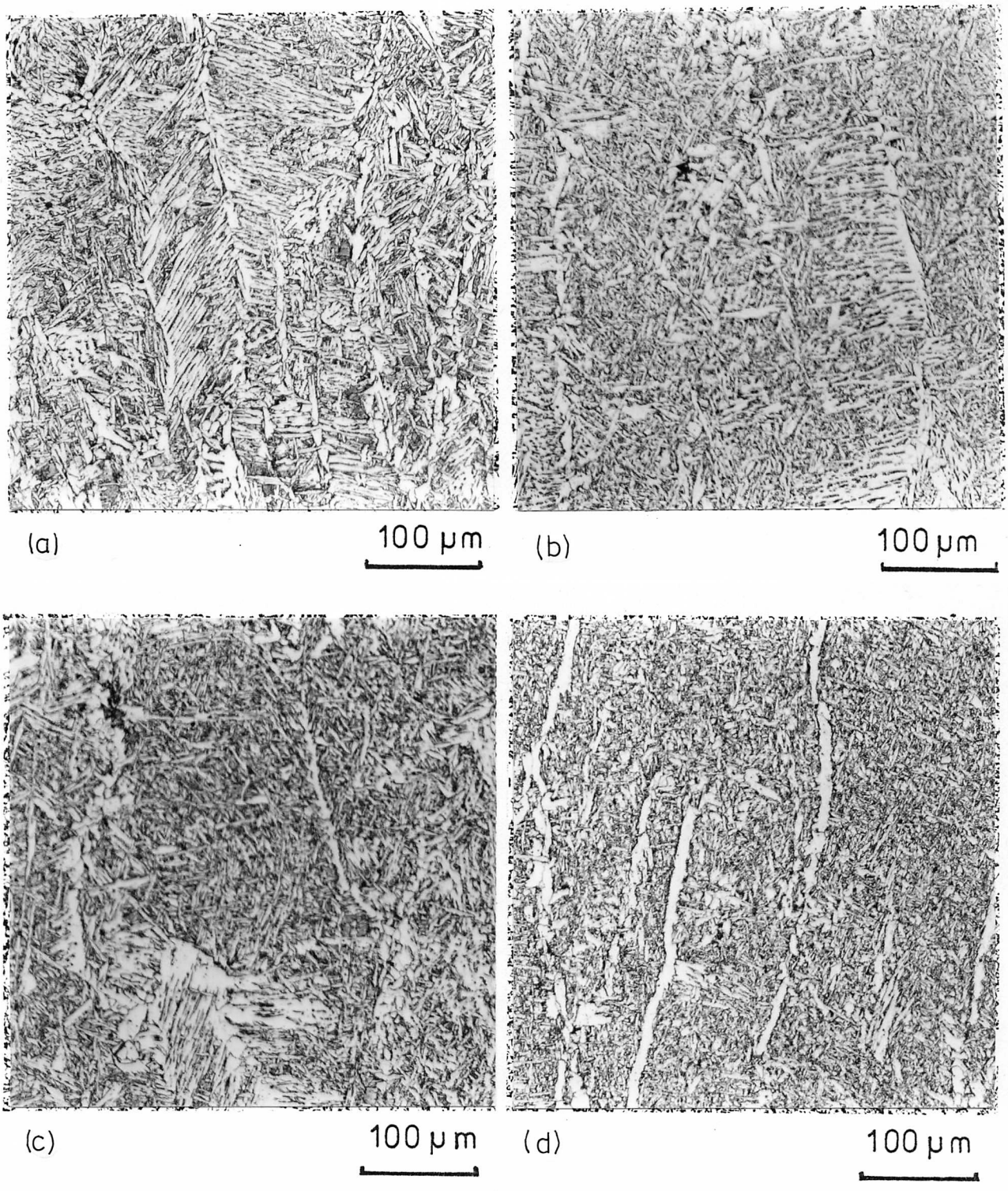

Fig.8.19. Optical micrographs showing the effect of parent plate deoxidation practice on the microstructure of manual metal arc welds.

(a) Rimming steel base plate
(b) Silicon killed base plate
(c) Silicon killed, Al treated base plate (Low AL)
(d) Silicon killed, Al treated base plate (High AL)
(For discussion see text).

Table 8.1. Composition of the inclusions observed in manual metal arc welds MMA 13-16. Since no quantitative method of analysis is available only the apparent compositions are reported.

	INCLUSION COMPOSITION				
BASE STEEL	Wt % Mn	Wt % Si	Wt % Al	Wt % Ti	Wt % S
D - RIMMING	42	23	<1	26	8
E - Si KILLED	46	16	<1	26	11
F - LOW Al	41	18	9	24	8
G - HIGH Al	27	14	26	27	6

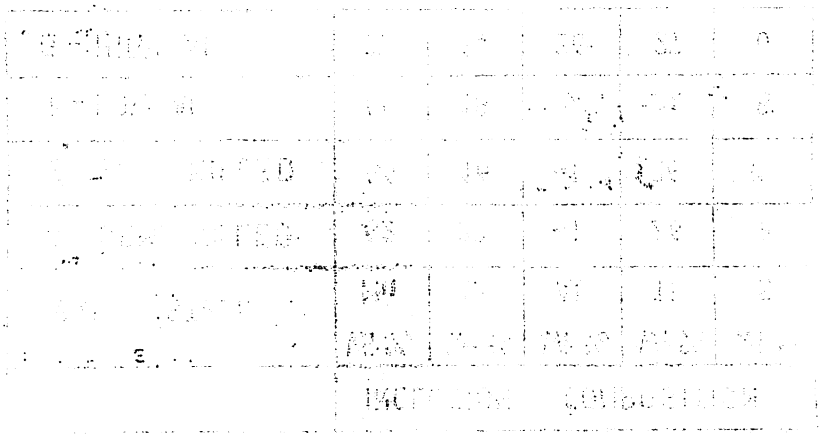

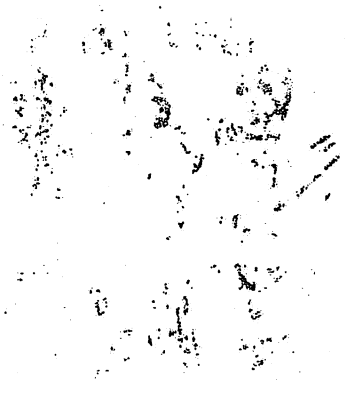

must be resolved if the role of plate deoxidation practice is to be fully understood.

The increasing level of aluminium observed in these four welds is clearly reflected in the composition of the resultant inclusions. Table 8.1 shows the relative proportion of the various constituent elements established using a STEM/EDS technique.

8.5.3. THE ROLE OF INNOCULANTS IN MICROSTRUCTURAL DEVELOPMENT IN A HIGH PURITY STEEL

This investigation centres on the addition of innoculants to a high purity C-Mn-Mo steel (Alloy J). Two experimental techniques were adopted with the intention of examining in isolation the possible effect on ferrite nucleation of a carbide, a nitride, an oxide and a sulphide. Individual innoculants were selected after examination of steel casting literature, eg Turnbull et al (1961), where grain refinement reagents have been sought for many years, and recent welding literature, eg Mori et al., (1981), where innoculants have been added to fluxes and electrode coatings to promote the intragranular ferrite reaction. This resulted in titanium carbide, titanium nitride and titanium oxide innoculants being selected for study. Additionally, manganese sulphide was investigated, as this had been observed in Chapter 4 to have acted as a nucleation site for the ferrite reaction.

The innoculant powders were supplied by the Welding Institute, where two had previously been employed in a recent investigation into electron beam welding (Robinson and Derossa (1981)). Initially, preparation of these alloys was attempted in the copper hearth of an Edwards argon arc furnace under a partial pressure of argon, but subsequently proved only a limited success. In the case of the nitride innoculant, TiN cuboids could occasionally be observed in the final cast ingot, as shown in

Fig. 8.20 Optical micrograph showing the presence of TiN cuboids in the innoculated alloy steel J. Following a light nital etch the TiN cuboids appear bright orange in colour. The as-cast microstructure comprises a predominantly upper bainite constituent.

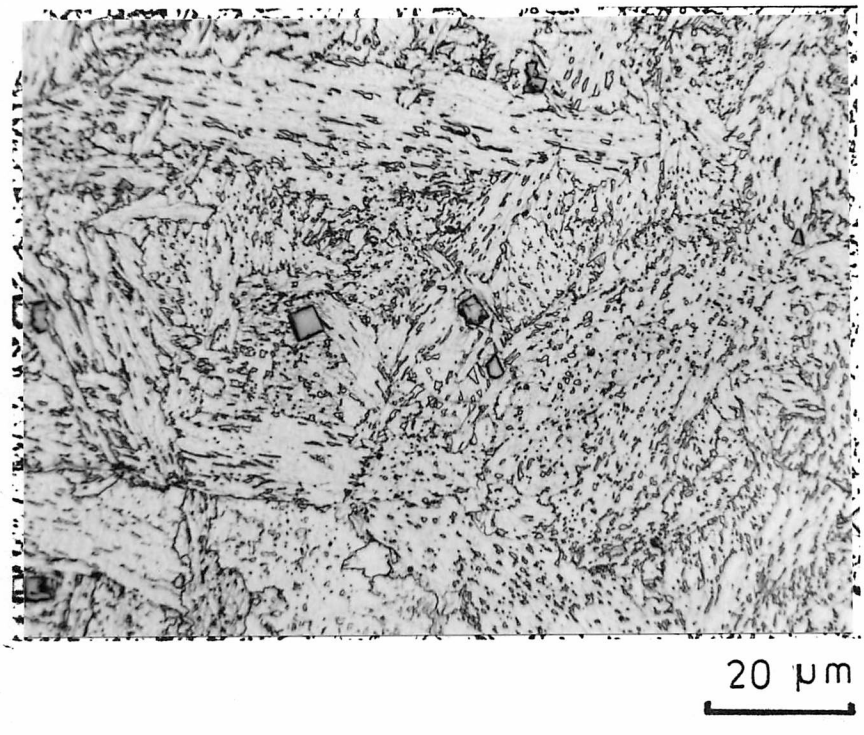

Fig.8.20. However, the cooling rate induced was such that a predominantly bainitic microstructure was developed in the final ingot and there appeared no obvious relationship between these TiN particles and the final microstructure. Preparation with the TiC and TiO_2 powders proved impossible by this method, due to the vigorous outgassing from the powder, and consolidation of the final ingot could not be achieved.

In the case of the manganese sulphide innoculants, the low oxygen level induced in the remelting process resulted in the development of dendritic type II MnS inclusions. Further trials with the same powder and alloys using tungsten-inert-gas remelting in an alumina crucible again proved unsuccessful, as the degree of oxidation could not be easily controlled.

Summarising, though unsuccessful in this brief investigation, the principle of isolating distinct inclusion types and examining the effects on ferrite nucleation could lead to exciting results.

8.5.4. THE EFFECT OF CRYSTALLOGRAPHY ON FERRITE NUCLEATION IN WELD METALS

Several authors, eg North et al (1979) Mori (1981) have speculated as to possible effects of a crystallographic relationship between the ferrite nucleus and inclusions. They rightly note that if a low energy interface exists between these phases, the overall effect would be to reduce the barrier ΔG^* to nucleation. The approaches involve calculating the minimum disregistry (S) between the ferrite nucleus and a series of distinct inclusion types.

For example, with NaCl type structures, eg TiO, TiN, TiC, they propose that minimum disregistry is observed when a Baker/Nutting (1959) relationship exists between the ferrite nucleus and the inclusions. This is consistent with predictions based on the R parameter discussed in Chapter 2 (Ecob and Ralph, 1980) and experimental

evidence in alloy steels (Howell and Honeycombe, 1981). This inclusion-ferrite crystallography also allows the austenite and ferrite to be related by the Kurdjumov-Sachs (1930) orientation relationship. However, a major discrepancy arises when the likely austenite/inclusion crystallography is considered. The most likely austenite/inclusion crystallography would be a cube/cube relationship, since these are the elastically 'soft' directions in cubic materials. This would preclude a three phase crystallography between the austenite / ferrite / inclusion, since the inclusion could not be cube/cube related to the austenite, Baker-Nutting (1959) related to the ferrite, while allowing a Kurdjumov-Sachs (1930) orientation between the austenite and ferrite.

In the case of hexagonal inclusions, eg AlN or Al_2O_3, a three phase crystallography is possible as follows:-

(0001) INCLUSION // $(111)_\gamma$ // $(110)_\alpha$

[1120] INCLUSION // $[110]_\gamma$ // $[111]_\alpha$

In the case of Al_2O_3, this would lead to a disregistry of 16% (Mori, 1981), whereas Ce_2O_3 (a rare earth metal oxide) would be 5%, (Bramfitt, 1970).

All of the proposals in this area will need careful experimental work, probably involving High Voltage Electron Microscopy, to establish if any such crystallographic effects play a role in ferrite nucleation. To date, there is no direct experimental evidence which has satisfactorily separated the possible effects of these particles on solidification, austenite grain size or directly on ferrite nucleation in weld materials.

8.6. THE EFFECT OF STRESS ON FERRITE NUCLEATION ON WELD METAL INCLUSIONS

Throughout the experimental work described in this thesis, weld quenching has been used to investigate the characteristics of the intragranular ferrite reaction. It is interesting to note, that often,

two adjacent inclusions have acted as the primary nucleation sites for the ferrite reaction. These observations were described in Chapter 6 for a typical manual metal arc deposit and are shown in Fig.8.21 for the study of submerged arc deposit SAQ2. This suggests that the conditions for favourable nucleation may be enhanced at such sites which could further follow if tessellated stresses were influencing the ferrite nucleation process.

Jones and Alberry (1977) have shown that for C-Mn weld metals, tensile stresses are present in the austenite prior to the ferrite transformation. Superimposed on this tensile stress would be the tessellated stresses around the inclusions, as a result of the differential contraction rates of the inclusion and the matrix. Andrews and Brooksbank (1971), (1972) have calculated the magnitude of these tessellated stresses for a series of oxide and sulphide inclusions. The most relevant of these calculations to the present situation considers the stress distribution around a duplex oxide/ sulphide inclusion similar to the type observed in this study. This predicts that both tensile and shear stresses would be present in the matrix adjacent to such inclusions. They further consider the interaction of these tessellated stresses where two inclusions are in close proximity. Using a photoelastic analogue, they illustrated the interaction of the stress fields, indicating that both zero stress regions and enhanced stress concentrations would be associated with two such inclusions. This is shown schematically in Fig. 8.22.

It is unlikely that the magnitude of the strain energy term and hence its contribution towards the free energy of activation for formation of a critical ferrite nucleus (ΔG^*) can be quantitatively assessed. However, it seems reasonable to suggest that the volume strain energy for ferrite nucleation could be less when associated with the inclusion stress fields described above, which when coupled with the

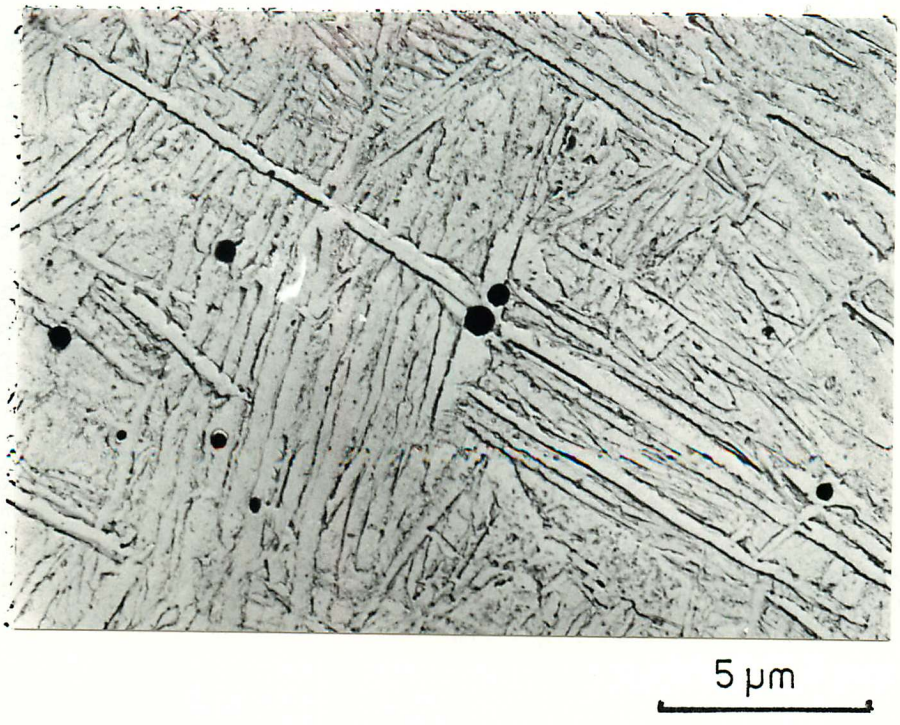

Fig.8.21 Transmission electron micrograph showing association of Widmanstatten ferrite with two weld inclusions (weld SAQ2).

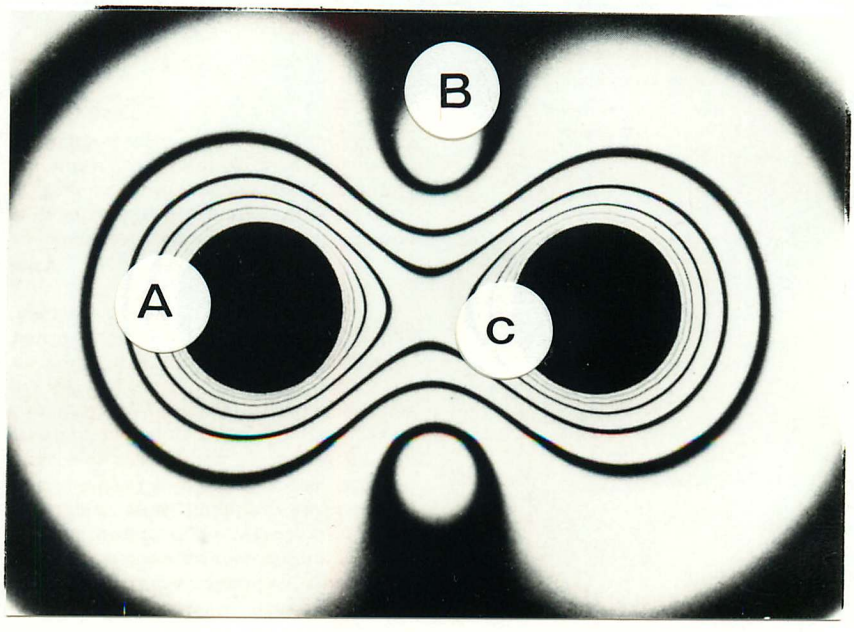

Fig. 8.22 Photoelastic analogue of the stress distribution around two inclusions in close proximity, after Andrews and Brooksbank (1972). Both stress concentrations (eg. at A), zero stress points (eg at B) and enhanced interactive fields (eg at C) are observed.

reduction of the inclusion/matrix interfacial energy, may help to explain why intragranular inclusions act as such favourable nucleation sites.

8.7 CONCLUSION

This chapter has investigated several of the factors affecting the development of microstructure in H.S.L.A. steel weld metals.

The role of inclusions in this respect is clearly complex. Given any particular cooling rate and alloy composition, there are two important and interrelated factors which control the final microstructure: (I) inclusion content (II) austenite grain size. Inclusions have been shown to be essential to initiate the intragranular ferrite reaction. However, if the size distribution/volume fraction of these particles is high, then the inclusions can actually suppress the operation of these intragranular nucleation sites by pinning austenite grain boundaries and promoting grain boundary ferrite reactions.

Since manganese contributes both towards the deoxidation of the weld metal and towards the hardenability during subsequent transformation, it has a dual role to play in the final development of microstructure. To a limiting point, both of these effects are beneficial, since increasing manganese promotes Widmanstatten ferrite formation from a hardenability point of view and reduces grain boundary pinning by its deoxidation reaction.

Several other factors which could be affecting the development of intragranular ferrite have been investigated eg, local stress distributions around inclusions and inclusion type. All of these parameters are likely to promote the ferrite reaction at inclusions.

It is interesting to speculate if the microstructural observation of the model steel D ($\triangleq$ 2% Mn) could be translated into commerical practice. This system seems ideal for thermomechanical treatment and is inherently 'weldable' due to the high manganese content.

CHAPTER 9

CONCLUSIONS AND SUGGESTIONS FOR FUTURE WORK

9.1 INTRODUCTION

This chapter will summarise the principal results of the dissertation and detail some suggestions for future work.

9.2. SUMMARY OF RESULTS

The results described in the previous chapters may be summarised as follows.

1) The decomposition of austenite to ferrite in H.S.L.A. steel weld metals investigated reproduces closely the morphological variants of the Dubé classification of proeutectoid ferrite. The nature of the constituent previously termed 'acicular ferrite' has been shown to comprise intragranular Widmanstatten ferrite. Nucleation of this intragranular ferrite occurs at lower transformation temperatures than that characteristic of austenite grain boundary nucleation and after site saturation has occurred at those boundaries. Weld metal inclusions have been shown to be the primary nucleation sites for the intragranular reaction and it is thought that their major role is to reduce the energy barrier to nucleation by acting as an inert substrate. Sympathetic nucleation of ferrite has been observed on existing inclusion nucleated ferrite laths and leads to the fine interlocking nature of acicular ferrite. Growth of Widmanstatten ferrite occurs until the remaining austenite is sufficiently enriched in carbon to decompose to a ferrite/carbide aggregate, or less frequently to high carbon twinned martensite (or retained austenite).

2) The nature of the inclusions observed in commercial manual metal arc and submerged arc weld deposits have generally been shown to be complex oxides, silicates and sulphides. Six principal elements, aluminium, silicon, sulphur, titanium, manganese and oxygen were usually observed in the majority of inclusions, the sulphide constituent being present as an outer coating. In the submerged arc deposits of specific interest, the average composition of inclusions formed under an acidic flux (BOC 80R) was consistent with a glassy phase in the Al_2O_3/ SiO_2/ MnO system. In contrast, the inclusions deposited under a typical basic flux (Oerlikon OP121TT) were rich in aluminium and well removed from the glassy region. In neither flux did the inclusions affect either the matrix chemistry or the composition of the austenite adjacent to the inclusions.

3) The extent to which inclusions nucleate ferrite (i.e. the proportion of acicular ferrite in the final microstructure) is a complex function of many variables. Given any particular welding technique, cooling rate and alloy composition, the results of this investigation have shown the further importance of two interrelated factors which control the development of the final microstructure: (i) inclusion content (ii) austenite grain size. If the inclusion volume fraction is high, then inclusion pinning of grain boundaries occurs, resulting in a small austenite grain size. Under these circumstances, the nucleation of intragranular ferrite is suppressed, due to the enhanced grain boundary reactions.

4) The contribution of two important factors which are likely to directly promote nucleation of ferrite on inclusions in weld materials cannot be quantified at this stage. However, qualitatively, the role of local, tessellated stresses, known to exist around inclusions and the

possibility that the ferrite nucleus could adopt a rational orientation relationship with the inclusion, are both likely to promote nucleation at these sites.

5) In considering the role of alloying additions to weld deposits, it is clear that elements such as manganese can have a dual role to play in the development of microstructure. In acting as a weak deoxidising agent, manganese decreases the total inclusion content of the deposit. This reduces the total number of intragranular nucleation sites, but can be accompanied by an increase in austenite grain size consistent with less inclusion pinning. In terms of hardenability increasing manganese over the the range considered can be rationalised in that, in essence, it promotes transformation to Widmanstatten ferrite. This is consistent with the predicted behaviour from the calculated T.T.T. diagrams presented and the dilatometric investigation of C - Mn - Mo steels under conditions of continuous cooling.

6) The effect of manganese on impact properties of C-Mn-Mo submerged arc weld deposits has been shown to be critically dependent on the oxygen level. At medium oxygen levels (250 ppm), the toughness properties are relatively insensitive to variations in manganese levels. At higher oxygen levels (400ppm), increasing manganese can dramatically change the microstructure and impact toughness of these materials.

7) The decomposition of austenite under isothermal heat treatment conditions in two submerged arc welds was investigated over the range 750°C to 500°C. Three principal morphologies, termed ferrite, Widmanstatten ferrite and upper bainite, have been investigated and the early stages of each reaction studied. The observed temperature ranges for each of these products were found to be in good agreement with calculated start temperatures for the Widmanstatten (W_s) and bainite (B_s) reactions.

8) Widmanstatten ferrite was observed under isothermal conditions at temperatures between 700°C and 570°C in the alloys investigated. At a definite and distinct temperature of 570°C, the morphology and reaction kinetics changed, corresponding to the development of an upper bainite microstructure. The morphology of this microstructural constituent has been identified unambiguously for the first time in HSLA weld metals, comprising alternate laths of bainitic ferrite separated by islands of retained austenite or cementite.

9) The thermodynamic analysis of transformations occurring under isothermal heat treatment conditions has been shown to be an accurate representation of the morphology and reaction kinetics of the various products observed experimentally. As a whole, the experimental results support the concept that there are two distinct 'C' curves, describing diffusional and displacive transformations under isothermal heat treatment conditions. The application of a similar analysis to transformations on continuous cooling has introduced the concept of an 'effective' or 'operative' bainite start temperature. At the cooling rate and alloy composition considered, transformation has been shown to proceed at temperatures consistently higher than this calculated B_s start temperature at all stages of transformations.

9.3. SUGGESTIONS FOR FUTURE WORK

The investigation described in this thesis has used a variety of experimental techniques, each of which individually could have formed a basis for intensive study. Specific areas where future research could be concentrated in the investigations of microstructure in weld metals are as follows:-

1) High voltage electron microscopy should be used to establish if weld metal inclusions adopt a rational orientation relationship with ferrite in commercial weld materials.

2) The principle of isolating individual inclusion types and investigating their effects on austenite decomposition should be investigated and could lead to exciting results.

3) The relative composition of inclusions should be studied, using an EDX technique, as a function of flux or coating formulation with reference to the $Al_2O_3/SiO_2/MnO$ and $Al_2O_3/SiO_2/MnO/TiO_2$ systems.

As a final comment, perhaps one of the most limiting factors in progressive study of phase transformations is the lack of experimental evidence regarding nucleation - perhaps the study of weld materials can provide the necessary driving force for this reaction.

References

Aaronson, H.I. (1962) 'The Decomposition of Austenite by Diffusional Processes', Interscience, New York.

Aaronson, H.I. (1969) 'The Mechanism of Phase Transformation in Crystalline Solids', Inst. Metals, London p.270.

Aaronson, H.I. and Domain, H.A. (1966) Trans. A.I.M.E. 236 781.

Aaronson. H.I. and Kinsman, K.R. (1967) Discussion to paper by Oblak J.M. and Hehemann, R.F. in 'Transformation and hardenability in steels'. Climax Moly. (1967)

Aaronson, H.I., Plichta, H.R., Franti, G.W. and Russell K.C. (1978) Metall. Trans. 9A p.363.

Aaronson, H.I. and Wells, C. (1956) Journal of Metals, 10, p.1216.

Abson, D.J. (1978.1) Written Discussion in 'Trends in Steels and Consumables for Welding', Proc. Conf., Welding Inst., London.

Abson, D.J. (1978.2) Welding Institute Research Report 68/1978/M

Abson, D.J. (1980) Private Communication

Abson, D.J. and Dolby, R.E. (1978) Welding Institute Res. Bulletin 19(7)

Abson, D.J. and Dolby, R.E. (1980) Welding Institute Res. Bulletin 21(4).

Abson, D.J., Dolby, R.E. and Hart, P.H.M. (1978) in 'Trends in Steels and Consumables for Welding' Proc. Conf., Welding Inst. London.

Abson, D.J. and Hart, P.H.M. (1980) Welding Institute Research Report 122/1980

Almqvist, G., Polgary, S., Rosendalh, C.H. and Valland, G., (1972) in 'Welding Research Related to Power Plants'. Proc. Conf. C.E.G.B. p.204, Marchwood.

Andersen, C.A. (1973) 'Microprobe Analysis'. A. Wiley Interscience Publications, New York.

Ashby, M.F. and Ebeling, T. (1966) Trans. Met. Soc. A.I.M.E. 236 p.1396

Atkinson, C., Aaron, H.B., Kinsman, K.R. and Aaronson, H.I. (1973) Met. Trans. 4 783.

Baker, R.G. and Nutting, J. (1959) in 'Precipitation Processes in Steels'. I.S.I. Special Report No.64, p.1.

Baker, T.J. and Charles, J.A. (1972) J.I.S.I. 210, p.702.

Batte, A.D. and Honeycombe, R.W.K. (1973) J.I.S.I. 284.

Bagaryatski, Y.A. (1950) Dokl. Akad. Nauk. SSSR 72, 1161.

Berry, F.G. and Honeycombe, R.W.K. (1970) Met. Trans. 1, p3279

Bhadeshia, H.K.D.H. (1979) Ph.D. Thesis, University of Cambridge, England.

Bhadeshia, H.K.D.H. (1980.1) Acta Metall. 28., p.1103.

Bhadeshia, H.K.D.H. (1980.2) Scripta Metall. 14, p.821.

Bhadeshia, H.K.D.H. (1981.1) Acta Metall. 29, p.1117.

Bhadeshia, H.K.D.H. (1981.2) Metal Science, in press.

Bhadeshia, H.K.D.H. (1981.3) Metal Science, 4, p.175.

Bhadeshia, H.K.D.H. (1981.4) Report 4 Dept. of Met. Cambridge.

Bhadeshia, H.K.D.H. and Edmonds, D.V. (1979) Met. Trans. A, 10, p.895.

Bhadeshia, H.K.D.H. and Edmonds, D.V. (1980) Acta Met. 28, 1265.

Bhadeshia, H.K.D.H. and Waugh, A.R. (1981) Acta Met., in press.

Boniszewski, T. (1979) The Metallurgist and Materials Technologist. Part 1., p.567, Part 2, p.640, Part 3, p.697.

Bosansky, J., Porter, D.A., Astrom, H. and Easterling, K.E. (1977) Scandanavian Journal of Metallurgy, 4, p.125.

Bowles, J.S. and Mackenzie, J.K. (1954) Acta Met. 2, p.224.

Brooksbank, K.J.B. and Andrews, K.W. (1972,1) J.I.S.I. 7, p.210.

Brooksbank, K.J.B. and Andrews, K.W. (1972,2) in 'Production and Application of Clean Steels', 134, The Iron and Steel Institute, London.

Bramfitt, B.L. (1970) Met. Trans. Vol. 1 July, p 1987.

Cahn, J.W. and Hagel, W.C. (1962) 'Decomposition of Austenite by Diffusional Processes'. Interscience, New York, p.131.

Campbell and Honeycombe, R.W.K. (1974) Met. Sci. 8, p.197.

Christian, J.W. (1962) in 'Decomposition of Austenite by Diffusional processes'. Interscience, New York.

Christian, J.W. (1965) 'The Theory of Transformations in Metals and Alloys'. Pergamon Press.

Cochrane, R.C. (1977) British Steel Research Report. T/PDM/462/1/77/C.

Cochrane, R.C. (1978) Written Discussion in 'Trends in Steels and Consumables for Welding'. Proc. Conf., Welding Inst., London.

Cochrane, R.C. and Kirkwood, P.R. (1978) in 'Trends in Steels and Consumables for Welding'. Proc. Conf., Welding Inst., London.

Darken, L.S. and Fisher, R.M. (1962) 'Decomposition of Austenite by Diffusional Processes', Interscience, New York, p.249

Davenport, A.T., Berry, F.G. and Honeycombe, R.W.K. (1968) Met. Sci. 2, 104.

Davis M.L.E. and Coe, F.R. (1977) Welding Inst. Res. Rep. 39/1977/M

Dickson, M.J. (1969) J. Appl. Cryst. 2,p.176

Dippenar, R.J., and Honeycombe, R.W.K. (1973) Proc. Royal Soc. London A. 335, p.455

Dolby, R.E. (1976) Welding Inst. Res. Rep. 14/1976/M

Dolby, R.E. (1980) I.I.W. Doc. IX-1175-80.

Dolby, R.E. (1981) I.I.W. Doc. IX-1213-81

Dubé, C.A., Aaronson, H.I. and Mehl, R.F. (1958) Rev. Met. 55, p201

Dunlop, G.L., Carlsson, C-J, and Frimodig, G. (1978) Met. Trans. 9A, p.261.

Ecob, R.C., and Ralph, B. (1980) Proc. Natn. Acad. Sci. U.S.A. 77, p.1749.

Ecob, R.C. and Ralph, B. (1981) Acta. Met. 29 p.1037.

Evans, G.M. (1980) Welding J. Res. Suppl. 59, p.67

Farrar, R.A., Tuliani, S.S. and Norman, S.R. (1974) Weld. Metal. Fab. 42 p.68

Farrar, R.A. and Watson, M.N. (1979) Metal. Const. 11, p.285

Funakoshi, T., Tanaka, T., Ueda, S., Ishikawa, M., Koshizuka, N. and Kobayashi, K. (1977) Transactions I.S.I.,J. 17, p.419

Garland, J. (1978) Written Discussion in 'Trends in Steels and Consumables for Welding' Proc. Conf. Welding Inst. London.

Garland, J. and Kirkwood, P.R. (1975) Metal Construction 5, p.275

Goodenow, R.H. and Hehemann, R.F. (1965) Trans. A.I.M.E. 233, p.1777

Habraken, L.T. and Economopoulos, M. (1967) in, 'Transformation and Hardenability in Steels' Proc. Conf. Climax, Moly. Co. Ann Arbor.

Hall, M, Kinsman, K.R. and Aaronson, H.I. (1972) Surf. Sci. 31, p.257.

Harrison, J. and De Rosa, S. (1981) Unpublished Research, Welding Institute.

Harrison, P.L. and Farrar, R.A. (1981) J. Mat. Sci. 8, p916

Harrison, P.L., Watson, M.N. and Farrar, (1981) Welding and Met. Fabrication. 4 p.117

Hehemann, R.F., Kinsman, K.R. and Aaronson, H.I. (1970) Met. Trans. 3 p.1077

Heikken, U.K. (1973) Acta. Met. 21 p.709

Hren, J.J., Goldstein, Ji. and Joy D.C. (1979) Introduction to Analytical Electron Microscopy. Plenum Press, London.

Hillert, M. (1962) 'The Decomposition of Austenite by Diffusional Processes ' Interscience, New York, p.197

Honeycombe, R.W.K. and Pickering. F.B. (1972) Met. Trans. 3, p.1099

Honeycombe, R.W.K. (1976) Met. trans. 7A, 915.

Howell, P.R. and Honeycombe, R.W.K. (1981) in 'Phase Transformations' Pittsburgh.

Howell, P.R. and Ricks, R.A. (1981) submitted for publication

Howell, P.R., Ricks, R.A. and Southwick, P. (1981) submitted for publication.

Ito, Y. and Nakanishi, M. (1976) The Sumitomo Search. No. 15

John, R., Kemp, P.R. and Welland, W.G. (1976) Metal Construction, 11, p.488.

Johnson, W.C., White, C.L., Marth, P.E., Ruf, P.K., Tuominen, S.M., Wade, K.D., Russell, K.C. and Aaronson, H.I. (1975) Met. Transactions. 6A, p.911

Jones, G.J. and Trivedi, R.K. (1971) J. App. Phys. 42, p.4299

Jones, W.K.C. and Alberry, P.J. (1977) C.E.G.B. Research Report R/M/R244.

Kelly, P.M. and Nutting, J. (1960) Proc. Royal Soc. London A. 259, p.45

Kennon, N.F. (1974) J. Aust. Inst. Metals. 19, p.3-18

Kiessling, R. and Lang, N. (1978) 'Non-metallic Inclusions in Steel' 2nd Edition, The Metals Society.

Kinsman, K.R., Eichen, E. and Aaronson, H.I. (1975) Met. Trans. 6A, p.303.

Kirkwood, P.R. (1978). Met. Const. 5, p.260.

Ko, T. and Cottrell, S.A. (1952) J. Iron Steel Inst. 172 p307.

Koshio, T., Ootawa, M., Tanigaki, T., Takino, T., Horii, Y., Tsunetomi, E. and Imai, K. (1981) I.I.W. Doc. 11.955.81

Krahe, P.R., Kinsman. K.R. and Aaronson, H.I., (1972) Acta Met. 20, p.1109

Kurdjumov, G. and Sachs. G. (1930) Z. Physik. 64 p.325

Lenel, U.L. (1980) PhD. Thesis, University of Cambridge, England.

Levine, E. and Hill, D.C. (1977) Metal Const. 9, p.346

Lui, Y.C., Aaronson, H.I., Kinsman, K.R. and Hall, M.G. (1972) Met. Trans. 3, p.1319

Masumoto, I. (1976) in 7th International Conference on Welding, Budapest.

Masumoto, I. and Ozaki, H. (1974) J. Japan Welding Soc. 43, p.1032.

Matas, S.J. and Hehemann, R.F. (1961) Trans. A.I.M.E. 221, p.179

Mehl, R.F. and Dubé, C.A. (1951) 'Phase Transformations in Solids' J. Wiley, New York.

Mintz, B. (1974) Metals Technology 1, no 5, p.226

Mori, N., Homma, H., Okita, S. and Wakabayashi, M. (1981) I.I.W. Doc. IX p.1196.

Mullins, W.W., and Sekerka, R.F. (1963) J. Appl. Phys. 34, p.323.

North, T.H. (1978) Written Discussion in 'Trends in Steels and Consumables for Welding' Proc. Conf. Welding Inst. London.

North, T.H., Bell, H.B., Kaikabi, A., and Craig, I. (1979) Welding Research Supplement 58, 12.

Oblak, J.M. and Hehamann, R.F. (1967) 'Transformation and Hardenability in Steels' Climax Molybdenum p.15

Ohmori, Y. and Honeycombe, R.W.K. (1971) Proceedings I.C.S.T.I.S. Suppl. Trans. I.S.I.J. 11, p.1160.

Pargeter, R. (1979) Private communication.

Pargeter, R. (1981) Research Report 151/1981, The Welding Institute.

Parsons, S.A. (1981) Ph.D. Thesis, University of Cambridge England.

Pickering, F.B. (1967) In 'Transformation and hardenability in Steel', Climax Molybdenum Inc.

Ricks, R.A. (1979) PhD. Thesis, University of Cambridge ,England.

Rigsbee, J.M. and Aaronson, H.I. (1979,1) Acta. Met. 27, p.365.

Ibid, (1979,2)

Russell, K.C. (1968) Acta Metall. 16, p.761.

Russell, K.C., Hall, M., Kinsman, K.R. and Aaronson, H.I. (1974) Met. Trans. 5, p.1503

Ryder, P.L. and Pitsch, W. (1966) Acta. Met. 14, p.1437.

Sakaki, H. (1959) 'Effect of Alloying Elements on Notch Toughness of Basic Weld Metals' Reports 1-7 J. Japan Weld. Soc. 28 (Welding Institute Translation).

Salmon-Cox, P. (1964) PhD. Thesis, University of Cambridge, England.

Signes, E.G. and Baker, J.C. (1979) A.W.S. Annual Meeting, April.

Smith, C.S. (1953) Trans. A.S.M. 45, p.533

Srinivasen, G.R. and Wayman, C.M. (1968) Acta. Met. 16, p.621.

Taylor, D.S. (1981) ESAB Research Report, No.26.

Thomas, G. (1973) Iron and Steel International 46, p.451

Townsend, R.D. and Kirkaldy, J.S. (1968) Trans. A.S.M. 61, p.605

Tuliani, S.S. (1972) in 'Welding Research Related to Power Plants' Proc. Conf., C.E.G.B., Marchwood.

Tuliani, S.S., Boniszewski, T. and Eaton, N.F. (1969) 37, p.327.

Tuliani, S.S. and Farrar, R.A. (1975) Weld. Metal. Fab. 43, p.553.

Tweed, J. and Knott, J.F. (1981) submitted for publication.

Underwood, E.E. (1970) 'Quantitative Stereology', Addison-Wesley.

Watson, J.D. and McDougall, P.G. (1973) Acta. Met. 21, p.961

Watson, N.W. (1980) Ph.D. Thesis, University of Southampton, England.

Watson, N.W., Harrison, P.L. and Farrar (1981) Welding and Met. Fab. 3, p101.

Widgery, D.,J. (1974) PhD. Thesis, University of Cambridge, England.

Widgery, D.J. and Saunders, G.G. (1975) Welding Inst. Research Bulletin, 16, p.277.

Zener, C. (1946) Metall. Soc. Aime, 167, 550.

Zener, C. (1949) J. App. Phys. 20, p.950.

ABBREVIATIONS

The following abbreviations have been used in this text.

K-S = The Kurdjumov - Sachs orientation relationship (G Kurdjumov and G. Sachs Z. Phys 64 325 (1930))

N-W = The Nishiyama-Wassermann orientation relationship

(Z Nishiyama, Scient. Rep Tohuku Univ. 23, 637 (1934))

(G Wassermann, Arch. Eisenhuttwes 16 647 (1933))